

UNIVERSITY OF SOUTHAMPTON

FACULTY OF ENGINEERING AND THE ENVIRONMENT

School of Engineering Science

Severely Plastically Deformed AZ80 Magnesium Alloy:

Microstructure and mechanical properties

by

Saad A. Alsubaie

Thesis for the degree of Doctor of Philosophy

2017

ABSTRACT

UNIVERSITY OF SOUTHAMPTON

FACULTY OF ENGINEERING AND THE ENVIRONMENT

School of Engineering Science

Saad A. Alsubaie

In this study the evolution of microstructure and the mechanical properties of an AZ80 magnesium alloy were investigated. It examined prepared samples of AZ80 magnesium alloy before and after processing by severe plastic deformation (SPD) using the High-Pressure Torsion (HPT) technique.

An AZ80 magnesium alloy with a chemical composition of Mg-8.7% Al-0.5% Zn was processed using HPT. The processing was conducted at room temperature, 296 K, and at the elevated temperature of 473 K under quasi-constrained conditions, using an imposed pressure of 6.0 GPa at a speed of one revolution per minute (rpm) through different numbers of turns: 1/4, 1, 3, 5 and 10. Processing magnesium alloy by HPT produced excellent grain refinement in the alloy, and it prevented the samples from developing cracks and segmentation at ambient temperature better than the other popular technique of SPD, for instance Equal-Channel Angular Pressing (ECAP).

The initial microstructure and the microstructural development after HPT processing were subsequently examined by optical microscopy (OM), scanning electron microscopy (SEM) and Transmission Electron microscopy (TEM). Microstructural investigations for the as-received condition showed an average grain size of ~25 μm . Optical microscopy images revealed microstructural evolution at both room and elevated temperature after the HPT process. The small proportion of refined grains at the edges expanded towards the disc centre with consecutive increasing numbers of revolutions. The TEM images demonstrate an evolution toward homogeneity at increasing numbers of revolutions. The final average grain size after 10 turns when the alloy was processed at room temperature was ~200 nm and ~330 nm when the alloy was processed by HPT at 473 K. The selected area electron diffraction (SAED) images of HPT samples after 10 revolutions show a fully developed ring at room temperature, indicating a microstructure with high angles of misorientation grain boundaries, and a

less developed ring at 473 K. Microstructural observation through the disc thickness demonstrates more heterogeneity in the vertical than the radial direction.

Vickers microhardness (Hv) values were taken along the disc diameter (radial direction) and over the total surface of the discs (colour-coded contour mapping). The results of Vickers microhardness (Hv) measurements along the diameters of the discs verify the heterogeneity of HPT deformation at lower numbers of turns. In the samples, the microhardness values increased rapidly at the edges of the disc, while the centres showed a lower value, and this large difference confirms the heterogeneity of HPT deformation in the early stages. With further straining samples showed a significant increase in microhardness values from the edges towards the disc centre. The microhardness values of samples processed by 5 and 10 turns showed a reasonable homogeneity across the disc diameter, with an average value of ~120 Hv when AZ80 was processed at room temperature and an average value of ~110 Hv when processed at 473 K.

Likewise, three selected discs processed by HPT for 1, 3 and 10 turns at both 296 K and 473 K were sectioned vertically across their diameter to be tested by (OM) and Vickers microhardness (Hv) through their thickness (axial direction). The results of (OM) and Vickers microhardness (Hv) confirmed the high heterogeneity in the axial direction than the radial direction.

Subsequent to the HPT process at room temperature, tensile specimens were cut from the processed discs and pulled in tension to failure at different tensile test temperatures (473, 523 and 573 K) and strain rates of ($1.4 \times 10^{-4} \text{ s}^{-1}$, $1.4 \times 10^{-3} \text{ s}^{-1}$, $1.4 \times 10^{-2} \text{ s}^{-1}$ and $1.4 \times 10^{-1} \text{ s}^{-1}$). The superplasticity of AZ80 magnesium alloy was confirmed for the first time (to the author's knowledge) at a maximum elongation of 645% when the alloy was pulled in tension to failure at 573 K using strain rate of $1.4 \times 10^{-4} \text{ s}^{-1}$. Moreover, the alloy exhibited a lower temperature superplasticity when it attained 423% at 473 K. Despite this superplasticity, AZ80 magnesium alloy does not show the predicted behaviour of increasing ductility with increased imposed strain during HPT process and decreased average grain size. The maximum elongation was reached in a sample processed by HPT for one turn, in which a smaller average grain size and the homogenous microstructure were not achieved.

Declaration of authorship

I, **Saad A. Alsubaie**, declare that this thesis entitled:

Severely Plastically Deformed AZ80 Magnesium Alloy: **Microstructures and mechanical properties**

and the work presented in it are my own and has been generated by me as the results of my own original research.

I confirm that:

- 1- This work was done wholly or mainly while in candidature for the research degree at this University;
- 2- Where any part of this thesis has previously been submitted for a degree or any other qualification at the University or any other institution, this has been clearly stated;
- 3- Where I have consulted the published work of others, this is always clearly attributed;
- 4- Where I have quoted from the work of others, the source is always given. With the exception of such quotation, this thesis is entirely my own work;
- 5- I have acknowledged all main sources of help;
- 6- Where this thesis is based on work done by myself jointly with others, I have made clear exactly what was done by others and what I have contributed myself;
- 7- Part of this work has been published as:
 - *Evolution of microstructure and hardness in an AZ80 magnesium alloy processed by high-pressure torsion.* Saad A. Alsubaie, Piotr Bazarnik, Malgorzata Lewandowska, Yi Huang, Terence G. Langdon, *Journal of Material Research and Technology*, 5 (2016) 152-158.
 - *Hardness Homogeneity in an AZ80 Magnesium Alloy Processed by High-Pressure Torsion.* Saad A. Alsubaie, Yi Huang, Terence G. Langdon, *Materials Science Forum* 879 (2017) 139-144.
 - *Hardness evolution of AZ80 magnesium alloy processed by HPT at different temperatures.* Saad A. Alsubaie, Yi Huang, Terence G. Langdon, *Journal of Material Research and Technology*, doi:10.1016/j.jmrt.2017.05.004
 - *EMISS University of Southampton postgraduate presentations 2014, 2015, and poster 2016.*

Signed: _____

Date: _____

Acknowledgment

I would like to express my sincere appreciation of the following people, without whose support I would not have reached my goal and the work would not have been accomplished. It is a pleasure to recognize and thank them, and I appreciate their valuable help.

I am especially indebted to Professor Terence G. Langdon and Dr Yi Huang for their guidance, assistance and advice throughout my journey. Their guidance and supervision have helped me to have a better understanding of my research.

I would like to thank the Public Authority for Applied Education and Training (PAAET), Kuwait, for their financial support throughout the duration of my research.

My sincere gratitude to Professor Malgorzata Lewandowska, and Dr Piotr Bazarnik, Warsaw University of Technology, Poland, for their much-appreciated help in generating TEM images.

Many thanks to my friends, my colleagues in the materials research group, and the administrative and technical staff of the School of Engineering Science in the Faculty of Engineering and the Environment for their support and help over the past four years.

Finally, and most importantly, I want to thank my family – my loving and supportive wife and my precious children – who always inspired and supported me. Their sacrifices for me have been greatly appreciated and I thank them with all my heart.

Contents

ABSTRACT	i
<i>Declaration of authorship.....</i>	<i>iii</i>
<i>Acknowledgment.....</i>	<i>v</i>
<i>Contents</i>	<i>vii</i>
<i>List of tables.....</i>	<i>xi</i>
<i>List of figures</i>	<i>xiii</i>
1 Introduction.....	1
1.1 Introduction	1
1.2 Aims and Objectives.....	2
1.3 Thesis Structure	2
2 Literature Review.....	5
2.1 Severe Plastic Deformation (SPD)	5
2.1.1 Equal-Channel Angular Pressing (ECAP)	6
2.1.1.1 Principle of Equal-Channel Angular Pressing (ECAP)	6
2.1.1.2 Routes in equal-channel angular pressing (ECAP)	8
2.1.1.3 Models of microstructure development in ECAP	12
2.1.1.4 Experimental factors influencing ECAP	13
2.1.1.5 Advantages and disadvantages of ECAP	16
2.1.2 High-pressure torsion (HPT)	17
2.1.2.1 Principle of high pressure torsion (HPT)	17
2.1.2.2 Principle of unconstrained and constrained HPT.....	19
2.1.2.3 Variation in homogeneity across an HPT disc.....	20
2.1.2.4 Effect of applied pressure	22
2.1.2.5 Effect of numbers of turns	25
2.1.2.6 Influence of stacking fault energy (SFE).....	29
2.1.2.7 Microstructure evolution toward homogeneity in HPT.....	33
2.1.2.8 Model of hardness evolution across the disc diameter during HPT	34
2.1.2.9 New approaches in HPT	37
2.1.2.10 Advantages and disadvantages of HPT	39
2.2 Materials processed by SPD	39

2.2.1	Grain size and strength.....	39
2.2.2	Grain size and superplasticity.....	41
2.3	<i>Magnesium and magnesium alloys</i>	47
2.3.1	Introduction.....	47
2.3.2	Effect of alloying elements	50
2.3.3	Wrought alloy	52
2.3.4	Processing magnesium alloys by ECAP	52
2.3.5	Processing magnesium alloy by HPT	55
2.3.6	AZ80 Magnesium alloy	57
2.4	<i>Literature review summary</i>	59
3	Experimental Material and Procedures.....	61
3.1	<i>Material</i>	61
3.2	<i>HPT processing at room temperature and high temperature</i>	61
3.3	<i>Sample preparations for microstructure observations.</i>	63
3.3.1	Mounting	63
3.3.2	Grinding	64
3.3.3	Polishing	64
3.3.4	Etching.....	64
3.3.5	Sample preparations for microstructure observations by Transmission Electron Microscope	65
3.4	<i>Microstructural examination</i>	65
3.4.1	Optical Microscopy (OM)	65
3.4.2	Scanning Electron Microscopy (SEM)	66
3.4.3	Transmission Electron Microscopy (TEM)	66
3.5	<i>Mechanical properties examination</i>	66
3.5.1	Microhardness along the diameter of the disc	66
3.5.2	Microhardness through the disc thickness.....	67
3.5.3	Tensile testing	68
4	Experimental Results	71
4.1	<i>Initial microstructure and hardness</i>	71
4.2	<i>Microstructure development after HPT processing at 296 K</i>	76
4.2.1	Microstructure observation along the disc diameter.....	77
4.2.2	Microstructure observation through the disc thickness	92

4.3	<i>Microhardness evolution after HPT processing at 296 K</i>	94
4.3.1	Microhardness along the disc diameter	94
4.3.2	Microhardness through the disc thickness	102
4.4	<i>Microstructure development after HPT processing at 473 K</i>	104
4.4.1	Microstructure observation along the disc diameter	105
4.4.2	Microstructure observation through the disc thickness	114
4.5	<i>Microhardness evolution after HPT processing at 473 K</i>	116
4.5.1	Microhardness along the disc diameter	116
4.5.2	Microhardness through the disc thickness	123
4.6	<i>The evolution comparison in Microstructure and microhardness between alloy processed by HPT at 296 K and 473 K</i>	125
4.7	<i>Superplastic Behaviour of AZ80 Processed by HPT</i>	128
4.7.1	Stress-strain curves	129
4.7.2	The appearance of AZ80 samples after tensile testing	139
4.7.3	The effect of strain rate and tensile testing temperature on the final elongation	148
4.7.4	Strain rate sensitivity index (m) and the activation energy (Q)	153
4.7.5	Microstructure observation at the gauge length	161
5	Discussion	177
5.1	<i>Microstructure evolution after HPT process at room temperature</i>	178
5.2	<i>Microstructure evolution after HPT processing at elevated temperature</i>	185
5.3	<i>Microstructure evolution in vertical direction</i>	189
5.4	<i>Precipitation evolution during HPT process at 296 K and 473 K</i>	191
5.5	<i>Microhardness evolution after HPT processing at 296 K and 473 K</i>	193
5.6	<i>Hardness measurements through the thickness of the disc</i>	196
5.7	<i>Superplastic behaviour of AZ80</i>	196
6	Summary and conclusions	205
7	Future Work	209
	References	211

List of tables

Table 2. 1 Number of passes required to achieve same total strain for deferent internal angles [50]	14
Table 2. 2 Average grain size of ZK60 processed by HPT at ambient temperature for different numbers of turns and different positions of the disc [86].....	22
Table 2. 3 Stacking faults energy for different metals.	31
Table 2. 4 Percentage weight reduction in using magnesium alloy over other structural metals [149]. ..	47
Table 2. 5 Slip plane, direction, and system for many metals [92].	48
Table 2. 6 Values of stacking faults energy of pure magnesium and different AZ series magnesuim alloys.	51
Table 2. 7 Mechanical properties of different AZ series magnesuim alloys [165].	52
Table 3. 1 Chemical composition of AZ80 magnesium alloy (mass fraction %)	61
Table 5. 1 Final grain size and the maximum Vickers microhardness of pure magnesium and magnesium alloys processed by HPT at room temperature for different numbers of revolutions.	179
Table 5. 2 Final grain size of magnesium alloys processed by HPT at elevated temperature for different numbers of revolutions.	186

List of figures

Figure 2. 1 Schematic illustration of channel angle & angle of outer curvature of ECAP [34]	7
Figure 2. 2 Schematic illustration of the four main processing routes in (ECAP) [44].	9
Figure 2. 3 Schematic illustration of slip systems in X, Y & Z planes for different numbers of passes using processing routes A, B _A , B _C & C [40].	10
Figure 2. 4 TEM photographs of oxygen-free copper processed by ECAP at 20°C: (a) Route B _C ; N = 3 (b) Route B _C ; N = 5 (c) Route B _C ; N = 10 (d) Route B _C ; N = 15 (e) Route A; N = 10 (f) Route C; N = 10 [27].	11
Figure 2. 5 Schematic illustration of cubic element distortion on the X,Y and Z plane of material processed by ECAP up to 8 passes using different routes (A, BA, BC & C) [44].	12
Figure 2. 6 Model of grain refinement where different microstructures are produced after ECAP depending on the alloy initial microstructure, where d is the initial grain size & d _c is the critical grain size needed to achieve an homogeneous microstructure [49].	13
Figure 2. 7 ZK60 billets processed by ECAP for one pass at 473 K, using a die with $\Phi = 90^\circ$ for the upper billet and a die with $\Phi = 110^\circ$ for the lower billet [48].	15
Figure 2. 8 Effect of pressing temperature on grain size after ECAP for pure Al and Al-3%Mg & Al-3%Mg-0.2Sc alloys [63].	16
Figure 2. 9 Schematic illustration of HPT processing principle [74].	18
Figure 2. 10 Schematic illustration of the HPT process condition: (a) unconstrained; (b) constrained; & (c) quasi-constrained conditions [76].	20
Figure 2. 11 Cross-section of three samples processed by HPT under different configurations: (a) unconstrained; (b) constrained; and (c) quasi-constrained conditions [82]	20
Figure 2. 12 Microhardness distribution on surface of HPT discs processed for different numbers of turns through 3D plots: (a) N=0; (b) N=1/4; (c) N=1/2; (d) N=1; (e) N=5; & (f) N=15 [9].	21
Figure 2. 13 Three-dimensional meshes of microhardness of Ni processed with different applied pressures: (a) 1 GPa; (b) 3 GPa; (c) 6 GPa; & (d) 9 GPa [68]	23
Figure 2. 14 Vickers microhardness Hv, plotted as a function of position on discs processed through 1/4 and 5 turns under an applied pressure of 1.0 and 6.0 GPa at (a), the average grain size for both pressures for centre and the edge of the discs are shown in (b) [83].	24
Figure 2. 15 TEM images of Cu-0.1 wt%Zr showing the microstructure after processing by HPT at room temperature for (a) 1/4 turn, (b) 1 turn and (c) 5 turns [90].	25
Figure 2. 16 3D meshes of microhardness in Ni processed by HPT with different number of turns at a pressure of 6 GPa: (a) N =1/2 turn; (b) N =1 turn; (c) N =3 turns; & (d) N =7 turns [68].	26
Figure 2. 17 Microhardness vs distance of Ni processed by HPT for 5 turns at room temperature with different applied loads: 1 GPa & 9 GPa [91].	27
Figure 2. 18 Microhardness vs distance of Ni processed by HPT with pressure of 6 GPa at room temperature with different numbers of turns [91]	27

Figure 2. 19 Colour-coded contour mappings showing the variation of microhardness value through the whole disc of ZK60 magnesium alloy processed by HPT for: (a) 1/4, (b) 1/2, (c) 1 and (d) 5 turns at 2.0 GPa pressure [86]	28
Figure 2. 20 Colour-coded contour mappings showing the variation of microhardness value through the whole disc of Cu-0.1% Zr alloy processed by HPT for: (a) 1/4, (b) 1, (c) 5 and 10 turns at 6.0 GPa pressure [90]	29
Figure 2. 21 Stacking sequence of plane of atoms in (a) Face-Centered Cubic (FCC) materials and (b) Hexagonal Close-Packed (HCP) [92] (b) (Adapted from W.G. Moffatt, G. W. Pearsall, and J. Wulff, <i>The structure and properties of materials</i> , vol. I, Structure, p.51. Copyright © 1964 by John Wiley & Sons, New York.	30
Figure 2. 22 Two regions of high-purity aluminium processed for 1 turn with 1.25 GPa pressure by HPT: (a) the centre of the disc & (b) the edge of the disc [87]	32
Figure 2. 23 Trend of different materials with low and high stacking- fault energy in early stages of HPT using the Vickers microhardness values [87]	33
Figure 2. 24 Three types of behaviour of hardness with equivalent strain for materials processed by HPT (a) without recovery; (b) with recovery; & (c) material weakening [117].	36
Figure 2. 25 Colour-coded contour maps showing the Vickers' microhardness values distributions in: (a) upper; (b) centre; and (c) lower plane of a pure aluminium disc processed by HPT [118]	36
Figure 2. 26 Distribution of microhardness values as a function of location of AZ31 processed by HPT for 1/4 , 1 and 5 turns [119].....	37
Figure 2. 27 Schematic illustrate: (a) a sample size of a disc of diameter of 11 mm & thickness of 2.5 mm [120]; & (b) a cylinder of diameter of 10 mm & thickness of 8.57 mm [121].	38
Figure 2. 28 Facility for ring HPT [122]	39
Figure 2. 29 Variation of elongation to fracture (up) and flow stress (down) versus the strain rate for Zn-22% Al alloy processed by ECAP at (a) [136], and HPT at (b) [137] with a tensile testing temperature of T= 473 K.....	42
Figure 2. 30 Elongation of specimens of ZK60 processed by ECAP for different number of passes & tested to failure at 473 K. Upper specimen is the untested [146].	44
Figure 2. 31 Engineering stress against elongation % curve at (a) & in (b) HPT sample after tension to failure by tensile test. Upper sample is original length before testing. Both (a) and (b) were processed by HPT at 3.0 GPa for 10 turns and tensioned to failure using different strain rates at a temperature of 573 K [147].	46
Figure 2. 32 Slip systems in HCP materials [154].	49
Figure 2. 33 Part of the Mg-Al phase diagram showing the aluminium content and the melting point of AZ80 magnesium alloy [162].	51
Figure 2. 34 Structure evolution of extruded ZK60 alloy processed by ECAP using a die with an 90° angle (a) before ECAP, (b) after 2 passes and (c) after 6 passes [170].	54
Figure 2. 35 Structure evolution of annealed ZK60 alloy processed by ECAP using a die with an 110° angle: (a) before; (b) after 1 pass; (c) after 4 passes; & (d) after 6 passes [170].	54

Figure 2. 36 Differences in grain size when processing Mg alloy AZ31 by HPT at different temperatures through 1 turn [15].....	56
Figure 2. 37 Differences in grain size when process Mg alloy AZ31 by HPT at different temperatures through 5 turns [15].	56
Figure 2. 38 Distribution of microhardness value along the half- cross section of AZ31 processed by HPT at temperature 463 K by N=1/4 upper, N=1 centre, N=5 lower [119]	57
Figure 2. 39 Microstructure evolution at disc centre of AZ80 processed HPT at room temperature using 3.0 GPa applied pressure for: (a) 0; (b) 1; & (c) 15 turns [120].	59
Figure 2. 40 Microhardness at different numbers of turns as a function of distance from disc centre [120].	59
Figure 3. 1 Schematic illustration of the heating elements around the upper and lower anvils of HPT facility [66].....	62
Figure 3. 2 Schematic illustration the TEM foils obtained from HPT disc.	65
Figure 3. 3 Quarter of disc illustrating the location of the four separate points in the bottom & the rectangle points over the whole disc [190].	67
Figure 3. 4 Position selected through disc thickness for Vickers microhardness Hv measurements [119].	68
Figure 3. 5 Schematic illustration the miniature tensile specimens obtained from HPT disc using electro-discharge machining [148].	69
Figure 4.1 SEM image showing the grain distribution in the as-received condition at the surface of the disc.	71
Figure 4.2 OM images show the grain distribution of AZ80 at the disc surface in the initial condition: (a) at the centre of the disc; (b) at the edge of the disc.	72
Figure 4.3 OM grain distribution through the disc thickness (axial direction) in the as-received condition. The yellow arrow shows the extrusion direction.	73
Figure 4.4 SEM images showing the precipitates in the AZ80 magnesium alloy prior to HPT process in the as-received condition, distributed at the grain boundaries: at (a), (b), (c) and (d), as a form of lamellar; and at (f) as a form of granular.	75
Figure 4.5 SEM images of (a) α phase matrix and its chemical analysis; (b) β precipitates phase and its chemical analysis.....	76
Figure 4.6 Optical images showing centre (left column) and edge (right column) after HPT processing at room temperature through (a, b) 1/4 turn and (c, d) 1 turn.	77
Figure 4.7 Optical images showing the centre (left column) and edge (right column) after HPT processing at room temperature through: (a, b) 3 turns; (c, d) 5 turns; and (e, f) 10 turns.	78
Figure 4.8 Fragmentation of precipitates after one turn of HPT process at 296 K.	79
Figure 4.9 STEM-HD images illustrating (a) the distribution of precipitates within the material after 1/4 of HPT; (b) the precipitates in zoom 2 and zoom 3 at a higher magnification and from various angles. ..	80

Figure 4.10 EDX showing scale counts for the matrix at points 2 and 4, and for the precipitates at points 1, 3 and 5.	82
Figure 4.11 STEM images show the precipitates at the triple junction after (a) 1 and (b) 5 turns of HPT at room temperature.	83
Figure 4.12 Agglomerate of precipitates in the triple junction between the grains after 10 turns as the TEM images shows and line EDX demonstrating the analysis of the matrix and the precipitate phases. .	84
Figure 4.13 Images from STEM summarize the microstructural evolution of the AZ80 alloy after processing by HPT at room temperature for: (a) 1/4 turn; (b) 1 turn; and (c) 10 turns.	85
Figure 4.14 Three TEM images show the high dislocation density at (a) 1/4, (b) 1, and (c) 3 turns of HPT at room temperature.	87
Figure 4.15 Formation of dislocation cell, shown by the TEM images at (a) and (b) after 1/4 turn of HPT at room temperature.	88
Figure 4.16 Reasonably equiaxed dislocation cell after 5 turns of HPT process at room temperature, as illustrated by TEM imagery.	88
Figure 4.17 TEM images at (a) and (b) showing an equiaxed UFG with an average grain size of ~ 200nm after processing by HPT for 5 turns at room temperature.	89
Figure 4.18 Images from TEM combined with the diffraction patterns for the AZ80 alloy after processing by HPT at room temperature for: (a) 1/4 turn; (b) 1 turn; and (c) 10 turns.....	91
Figure 4.19 TEM images showing the microstructure of sample processed by HPT for one turn at room temperature. A twinning deformation is appearing at grain size ~ 50 nm.	91
Figure 4.20 Optical images showing the centre (left column) and edge (right column) for the whole thickness after HPT processing at room temperature through: (a, b) 1 turn; (c, d) 3 turns; and (e, f) 10 turns.	93
Figure 4.21 Vickers microhardness H_v , plotted as a function of position on disc processed by HPT at room temperature using an applied pressure of 6.0 GPa through 0 to 10 turns: the lower dashed line at H_v 63 shows the as-received condition.....	95
Figure 4.22 Vickers microhardness H_v , plotted against equivalent strain showing the development of saturation conditions at strains above ~ 30.	96
Figure 4.23 Comparison of the hardness evolution between the centre and the edge of discs processed by HPT for up to 10 turns at room temperature.	97
Figure 4.24 Variation in the average microhardness values H_v of AZ80 processed by HPT at room temperature, plotted against number of HPT process turns N.....	97
Figure 4.25 Average grain size and the average microhardness values of the alloy processed by HPT for different number of turns at 296 K.	98
Figure 4.26 Colour-coded contour maps showing the distribution of the Vickers microhardness values of processed AZ80 discs by HPT at room temperature at: (a) 1/4; (b) 1; and (c) 5 turns.....	99
Figure 4.27 Histogram of Vickers microhardness values distributed at the whole disc surface after processing by HPT at room temperature through (a) 1/4 turn; (b) 1 turn; and (c) 5 turns. Vertical lines denote the average value.	101

Figure 4.28 Microhardness values at different displacement from the centre as a function of distance from bottom to top of the disc processed by HPT at 296 K: (a) 1 turn; (b) 3 turns; and (c) 10 turns.	103
Figure 4.29 Optical image at (a) and SEM images at (b) showing formation of twinning when AZ80 is processed by HPT at 473 K with N = 0.....	105
Figure 4.30 Optical images showing centre (left column) and edge (right column) after HPT processing at 473 K through: (a, b) 1/4 turn; and (c, d) 1 turn.....	106
Figure 4.31 Optical images showing centre (left column) and edge (right column) after HPT processing at 473K through: (a, b) 3 turns; (c, d) 5 turns; and (e, f) 10 turns.	107
Figure 4.32 Images from TEM combined with the diffraction patterns for the AZ80 alloy after processing by HPT at 473 K for: (a) 1/4 turn; (3) 1 turn; and (d) 10 turns.	109
Figure 4.33 STEM images show a reasonably homogenous microstructure after: (a) 5 turns: and (b) 10 turns of processing by HPT at 473K.....	111
Figure 4.34 STEM images of the precipitate distribution in AZ80 alloy processed by HPT at 473 K for: (a) 1; and (b) 5 turns.	112
Figure 4.35 Points count maps to show the distribution of precipitates after processing by HPT at 473 K for: (a) 1 turn; and (b) 5 turns.	113
Figure 4.36 TEM image of AZ80 magnesium alloy processed by HPT at 473 K for 10 turns, showing equiaxed UFG grains with an average grain size of ~ 330 nm.....	114
Figure 4.37 Optical images showing the centre (left column) and edge (right column) for the whole thickness after HPT processing at 473K through: (a, b) 1 turn; (c, d) 3 turns; and (e, f) 10 turns.....	115
Figure 4.38 Vickers microhardness Hv, plotted as a function of position on discs processed by HPT at 473 K, using an applied pressure of 6.0 GPa through 0 to 10 turns: the lower dashed line at Hv 63 shows the as-received condition.....	117
Figure 4.39 Vickers microhardness Hv, plotted against equivalent strain, showing the development of saturation condition at strains above 30 of an AZ80 processed by HPT at 473 K.	118
Figure 4.40 Comparison of hardness evolution between the centre and the edge of discs processed by HPT for up to 10 turns at 473 K.	119
Figure 4.41 Variation in the average microhardness values Hv of AZ80 alloy processed by HPT at 473 K , plotted against numbers of HPT process turns N.	119
Figure 4.42 Average grain size and the average microhardness values of the alloy processed by HPT for different number of turns at 473 K.	120
Figure 4.43 Colour-coded contour maps showing the distribution of the Vickers microhardness values at: (a) 1/4; (b) 1; and (c) 5 turns of processed AZ80 discs by HPT at 473 K.	121
Figure 4.44 Histogram of Vickers microhardness values distributed at the whole disc surface after processing by HPT at 473 K through: (a) 1/4 turn; (b) 1 turn; and (c) 5 turns. Vertical lines denote the average value.	123
Figure 4.45 Microhardness values at different displacement from the centre as a function of distance from bottom to top of the disc processed by HPT at 473 K: (a) 1 turn; (b) 3 turns; and (c) 10 turns.	125

Figure 4.46 Results of Vickers microhardness values H_v , plotted individually for each processed turn at 296 K and 473 K for (a) $N = 0$, (b) $N = 1/4$, (c) $N = 1$, (d) $N = 3$, (e) $N = 5$ and (f) $N = 10$.	127
Figure 4.47 Average H_v values along the disc diameter against the number of HPT turns for sample processed by HPT at 296 and 473K.	128
Figure 4.48 Stress-strain curve of the AZ80 in the as-received condition tested by tensile test in (a) at 473 K and (b) at 573 K for different strain rates.	131
Figure 4.49 Stress-strain curve for the AZ80 alloy processed for $N = 1/4$ turn in HPT at room temperature using an applied pressure of 6.0 GPa and tested in tension for different strain rates at a testing temperature of 473 K at (a), 523 K at (b) and 573 K at (c).	133
Figure 4.50 Stress-strain curve for the AZ80 alloy processed for $N = 1$ turn in HPT at room temperature using an applied pressure of 6.0 GPa and tested in tension for different strain rates at a testing temperature of 473 K at (a), 523 K at (b) and 573 K at (c).	134
Figure 4.51 Stress-strain curve for the AZ80 alloy processed for $N = 5$ turn in HPT at room temperature using an applied pressure of 6.0 GPa and tested in tension for different strain rates at a testing temperature of 473 K at (a), 523 K at (b) and 573 K at (c).	136
Figure 4.52 Stress-strain curve for the AZ80 alloy processed for $N = 10$ turn in HPT at room temperature using an applied pressure of 6.0 GPa and tested in tension for different strain rates at a testing temperature of 473 K at (a), 523 K at (b) and 573 K at (c).	137
Figure 4.53 Elongation – strain rate curve for the AZ80 alloy processed for different number of turns in HPT at room temperature using an applied pressure of 6.0 GPa and tested in tension for different strain rates at a testing temperature of 473 K at (a), 523 K at (b) and 573 K at (c).	139
Figure 4.54 Appearance of AZ80 alloy tensile specimens processed by HPT at room temperature for $N = 1/4$ after tension to failure using different strain rates at testing temperature of 473K and 573 K, including the untested sample at the top.	140
Figure 4.55 Appearance of AZ80 alloy tensile specimens processed by HPT at room temperature for $N = 1$ after tension to failure using different strain rates at testing temperature of 473 K and 573 K, including the untested sample at the top.	141
Figure 4.56 Appearance of AZ80 alloy tensile specimens processed by HPT at room temperature for $N = 5$ after tension to failure using different strain rates at testing temperature of 473 K and 573 K, including the untested sample at the top.	142
Figure 4.57 Appearance of AZ80 alloy tensile specimens processed by HPT at room temperature for $N = 10$ after tension to failure using different strain rates at testing temperature of 473 K and 573 K, including the untested sample at the top.	143
Figure 4.58 Appearance of AZ80 alloy tensile specimens processed by HPT at room temperature for different number of turns after tension to failure using strain rates of $1.4 \times 10^{-1} \text{ s}^{-1}$ at testing temperature of 473 K, including the untested sample at the top.	144
Figure 4.59 Appearance of AZ80 alloy tensile specimens processed by HPT at room temperature for different number of turns after tension to failure using strain rates of $1.4 \times 10^{-2} \text{ s}^{-1}$ at testing temperature of 473 K, including the untested sample at the top.	145
Figure 4.60 Appearance of AZ80 alloy tensile specimens processed by HPT at room temperature for different number of turns after tension to failure using strain rates of $1.4 \times 10^{-3} \text{ s}^{-1}$ at testing temperature of 473 K, including the untested sample at the top.	145

Figure 4.61 Appearance of AZ80 alloy tensile specimens processed by HPT at room temperature for different number of turns after tension to failure using strain rates of $1.4 \times 10^{-4} \text{ s}^{-1}$ at testing temperature of 473 K, including the untested sample at the top.	146
Figure 4.62 Appearance of AZ80 alloy tensile specimens processed by HPT at room temperature for different number of turns after tension to failure using strain rates of $1.4 \times 10^{-1} \text{ s}^{-1}$ at testing temperature of 573 K, including the untested sample at the top.	146
Figure 4.63 Appearance of AZ80 alloy tensile specimens processed by HPT at room temperature for different number of turns after tension to failure using strain rates of $1.4 \times 10^{-2} \text{ s}^{-1}$ at testing temperature of 573 K, including the untested sample at the top.	147
Figure 4.64 Appearance of AZ80 alloy tensile specimens processed by HPT at room temperature for different number of turns after tension to failure using strain rates of $1.4 \times 10^{-3} \text{ s}^{-1}$ at testing temperature of 573 K, including the untested sample at the top.	147
Figure 4.65 Appearance of AZ80 alloy tensile specimens processed by HPT at room temperature for different number of turns after tension to failure using strain rates of $1.4 \times 10^{-4} \text{ s}^{-1}$ at testing temperature of 573 K, including the untested sample at the top.	148
Figure 4.66 Elongation to failure comparison between HPT samples processed up to 1/4 turn at room temperature and tested to fracture using tensile test at different strain rates at (a) and different tensile testing temperatures at (b).	149
Figure 4.67 Elongation to failure comparison between HPT samples processed up to 1 turn at room temperature and tested to fracture using tensile test at different strain rates at (a) and different tensile testing temperatures at (b).	150
Figure 4.68 Elongation to failure comparison between HPT samples processed up to 5 turns at room temperature and tested to fracture using tensile test at different strain rates at (a) and different tensile testing temperatures at (b).	151
Figure 4.69 Elongation to failure comparison between HPT samples processed up to 10 turns at room temperature and tested to fracture using tensile test at different strain rates at (a) and different tensile testing temperatures at (b).	152
Figure 4.70 Strain rate sensitivity of AZ80 alloy in the as-received condition and tested in tension for different strain rates at a testing temperature of 473 K and 573 K.	153
Figure 4.71 Strain rate sensitivity of AZ80 alloy processed for (a) ¼ turn, (b) 1 turn, (c) 5 turns and (d) 10 turns in HPT at room temperature using an applied pressure of 6.0 GPa and tested in tension for different strain rates at a tensile testing temperature of 473 K.	155
Figure 4.72 Strain rate sensitivity of AZ80 alloy processed for (a) ¼ turn, (b) 1 turn, (c) 5 turns and (d) 10 turns in HPT at room temperature using an applied pressure of 6.0 GPa and tested in tension for different strain rates at a tensile testing temperature of 523 K.	157
Figure 4.73 Strain rate sensitivity of AZ80 alloy processed for (a) ¼ turn, (b) 1 turn, (c) 5 turns and (d) 10 turns in HPT at room temperature using an applied pressure of 6.0 GPa and tested in tension for different strain rates at a tensile testing temperature of 573 K.	159
Figure 4.74 Difference in flow stresses with the reciprocal of the temperatures of samples processed by HPT for one turn and tested in tension at 473 K and 573 K using strain rates of $1.4 \times 10^{-4} \text{ s}^{-1}$ – $1.4 \times 10^{-3} \text{ s}^{-1}$ to determine the value of the activation energy (Q).....	160

Figure 4.75 Surface morphology of the tested tensile samples at the gauge lengths for the AZ80 alloy processed for N = 1/4 turn in HPT at room temperature using an applied pressure of 6.0 GPa and tested in tension to failure for different strain rates at a testing temperature of 473 K.	163
Figure 4.76 Surface morphology of the tested tensile samples at the gauge lengths for the AZ80 alloy processed for N = 1 turn in HPT at room temperature using an applied pressure of 6.0 GPa and tested in tension to failure for different strain rates at testing temperature of 473 K.	164
Figure 4.77 Surface morphology of the tested tensile samples at the gauge lengths for the AZ80 alloy processed for N = 5 turns in HPT at room temperature using an applied pressure of 6.0 GPa and tested in tension to failure for different strain rates at a testing temperature of 473 K.	166
Figure 4.78 Surface morphology of the tested tensile samples at the gauge lengths for the AZ80 alloy processed for N = 10 turns in HPT at room temperature using an applied pressure of 6.0 GPa and tested in tension to failure for different strain rates at a testing temperature of 473 K.	167
Figure 4.79 Surface morphology of the tested tensile samples at the gauge lengths for the AZ80 alloy processed for N = 1/4 turns in HPT at room temperature using an applied pressure of 6.0 GPa and tested in tension to failure for different strain rates at a testing temperature of 573 K.	169
Figure 4.80 Surface morphology of the tested tensile samples at the gauge lengths for the AZ80 alloy processed for N = 1 turn in HPT at room temperature using an applied pressure of 6.0 GPa and tested in tension for different strain rates at a testing temperature of 573 K.	170
Figure 4.81 Surface morphology of the tested tensile samples at the gauge lengths for the AZ80 alloy processed for N = 5 turns in HPT at room temperature using an applied pressure of 6.0 GPa and tested in tension to failure for different strain rates at a testing temperature of 573 K.	172
Figure 4.82 Surface morphology of the tested tensile samples at the gauge lengths for the AZ80 alloy processed for N = 10 turns in HPT at room temperature using an applied pressure of 6.0 GPa and tested in tension to failure for different strain rates at a testing temperature of 573 K.	173
Figure 4.83 SEM images of the grains at the gauge length of the tensile tested samples at (a), (b), (c) and (d) . The average grain size shows greater growth in the sample processed by HPT for 10 turns and tested at 573 K using strain rate $1.4 \times 10^{-4} \text{ s}^{-1}$ than the sample processed by HPT for one turn and tested under the same conditions.	174
Figure 4.84 Elongation to failure comparison between HPT samples processed for different number of turns at room temperature and tested to fracture using tensile test at different strain rate and different testing temperatures.	175
Figure 5.1 TEM image shows the bi-modal structure of the alloy after one turn of HPT at room temperature. The yellow arrow shows the formation of twinning in grains with a size smaller than ~100 nm.	183
Figure 5.2 The equivalent strain near the centre, at the half-radius and periphery of a disc processed by HPT for a 1/4, 1, 3, 5 and 10 turns.	184
Figure 5.3 New recrystallized grains nucleate at the original grain indicated by the yellow arrows.	189
Figure 5.4 Simulation of a compression test showing the restricted flow region and the distribution of the effective strain [237].	190

1 Introduction

1.1 Introduction

In past decades, insightful exploratory studies have been undertaken into the enhancement of the mechanical properties of metallic materials. To produce a material with better specifications, properties such as high strength and high ductility have been observed closely. Strengthening can be achieved through methods such as solid solution, precipitation hardening and grain refinement. Reducing the average grain size is essential, since the strength of a material is related to its grain size, and refinement has proved an effective way to increase a material's strength. This relationship is introduced in the Hall-Petch equation:

$$\sigma_y = \sigma_0 + K_y d^{-1/2} \quad (1.1)$$

In this equation, the yield stress σ_y is proportional to the σ_0 , which is the friction stress, and K_y , which is the constant of yielding [1,2]. Likewise, the yield stress σ_y is inversely related to the average grain size, d . It is clear from this equation that reducing the grain size will improve the strength of the material. This equation drives material scientists and researchers to manufacture materials with an ultra-fine grain and to study their unique properties. Producing an ultra-fine grain is approached in two different ways: 'bottom-up' and 'top-down' [3,4].

In the past thirty years, severe plastic deformation (SPD) has been the most important 'top-down' approach to producing ultra-fine grained (UFG) material. Although SPD has many techniques to produce material with a fine grain, two have been most developed: equal-channel angular pressing (ECAP) [5] and high-pressure torsion (HPT) [6]. Both techniques are effective, but HPT is better at producing materials with a smaller grain size by a factor of $\sim 2-4$ [7], or a higher factor [8,9]. Accordingly, in recent years interest in the HPT process has increased rapidly.

Magnesium alloys have received great attention recently for use in the automotive and aerospace industries. This is due to their low density, high specific strength and stiffness, making them an excellent choice for weight reduction [10]. Furthermore,

magnesium alloy has a dimensional stability, a high damping capacity, electromagnetic interference shielding and machinability. It is recyclable and low cost, making it attractive for various applications in electrical and electronic portable devices. Despite these excellent features, magnesium alloys are difficult to deform at room temperature due to their hexagonal close-packed (HCP) crystal structure and limited slip systems. This limits the utilization of magnesium alloy in many applications. Furthermore, the strength and other mechanical properties of magnesium alloy need to be improved if it is to compete with other materials [11]. By using HPT techniques, the strength of magnesium alloy can be raised to approximately double [12], its ductility increased and superplastic elongation achieved [13,14]. Moreover, HPT offers a deformation of magnesium alloy at room temperature to produce an ultra-fine grain without the development of cracks or segmentations [15].

1.2 Aims and Objectives

Many studies have been conducted on magnesium alloy processed by SPD. These have mainly been at elevated temperatures using the ECAP process, yet a few were conducted at ambient temperature using HPT. To this day, there is a lack of information about AZ80 magnesium alloy processed by SPD. Little information is available using ECAP and even less using HPT. The aim of this study is to establish a database of the AZ80 magnesium alloy processed by HPT at various temperatures and to investigate the microstructural evolution, the mechanical properties and the potential of the AZ80 magnesium alloy to achieve superplastic behaviour.

1.3 Thesis Structure

This thesis consists of seven chapters. Chapter 1 is the introduction, and Chapter 2 is a literature review where the fundamentals of SPD and the principles of ECAP and HPT are presented. Chapter 3 provides details of the experimental material and procedure conditions; work was performed using the facilities at the University of Southampton, involving cutting, processing by HPT machine, grinding, polishing, generating optical microscopy (OM) images, generating scanning electron microscopy (SEM) images, and testing the hardness of the alloy and the elongation of the specimen before failure using a tensile test. The transmission electron microscopy (TEM) images were generated in collaboration with Professor Malgorzata Lewandowska and her student, Dr. Piotr

Bazarnik, from the Faculty of Materials and Engineering, Warsaw University of Technology, Warsaw, Poland. The results of processing AZ80 magnesium alloy by HPT at room temperature and high temperature are illustrated in Chapter 4. In Chapter 5, the results of the HPT process are analysed and discussed: the evolution of the microstructure and the microhardness at room temperature; the evolution of the microstructure and microhardness at high temperatures; and the superplastic behaviour of AZ80 processed by HPT at room temperature. Chapter 6 highlights the most important conclusions from this study, and Chapter 7 points to further investigations that the author will pursue in the future for a better understanding of AZ80 magnesium alloy processed by SPD.

2 Literature Review

2.1 Severe Plastic Deformation (SPD)

Severe plastic deformation (SPD) is a successful process technique used in metals and metal alloys to produce bulk ultra-fine grained (UFG) materials. These materials can be defined as fully homogenous and equiaxed microstructure materials with an average grain size of less than $\sim 1\text{ }\mu\text{m}$ and with high angles of misorientation grain boundaries as a large fraction of its grain boundaries [16,17]. The high angles grain boundaries (HAGB) are boundaries with misorientation $> 15^\circ$, if the misorientation angle is lower than 15° the boundaries will represent low-angle grain boundaries (LAGB) [18,19]. The grain size of an ultra-fine grained materials falls into two scales of measurement: the submicrometer range from 100 nm to 1000 nm; or the true nanometer range of less than 100 nm. Achieving an exceptionally fine grain increases the hardness of materials in accord with the Hall-Petch relationship explained earlier. Likewise, a material with a fine grain has better mechanical properties than one with coarse [6]. Despite a few limited applications of material processed by SPD, until recently this procedure had been performed only at the scale of laboratories and research institutes, considered to be a major limitation to moving forward to industrial production. Up-to-date published results in severe plastic deformation (SPD) have opened a new era of metals specifications. SPD can be defined as a metal forming process to produce an ultra-fine grain (UFG) by applying an extensive hydrostatic pressure on bulk metal. This imposes an extremely high strain without any major change to the shape and dimensions of the sample [17].

It is well known that grains of metallic materials can be refined to the submicrometer or true nanometer range by using SPD techniques [20]. It is the most efficient process for refining material grains [21]. The reduction in grain size will produce a metal or metal alloys with better mechanical properties such as high strength and, since ductility increases with decreasing grain size, a material with ultra-fine grain has good ductility [22]. SPD is a ‘top-down’ method that can produce a bulk nanostructure material free from contamination and porosity. Because of its ability to produce an ultra-fine grain with a unique nanostructure and mechanical properties, SPD is encouraging scientists to undertake more studies and research. The work of Professor P. W. Bridgman at Harvard

University in the 1930s, applying high pressure to a bulk materials in a number of experiments, established the scientific principles of the SPD procedure [23,24]. The second important development was equal-channel angular extrusion by Dr V. M. Segal and his colleagues in the 1980s [25].

There are many SPD techniques applied around the world, such as accumulative roll-bonding (ARB), cyclic extrusion compression (CEC), twist extrusion (TE) and multi-directional forging (MDF). However, the most important, popular and feasible techniques are equal-channel angular pressing (ECAP) [5] and high pressure torsion (HPT) [6]. These two are the major SPD techniques and will be discussed in the following sections [26].

2.1.1 Equal-Channel Angular Pressing (ECAP)

Among the SPD methods, ECAP is an effective tool to produce extraordinary grain refinement in a wide range of bulk polycrystalline metals [5], such as AZ91 magnesium alloy [27], commercial pure aluminium [28] and oxygen-free copper [29]. It is capable of imposing a large strain on the material at a wide range of processing temperature [30–32]. The grain size of a material produced by ECAP falls into the submicrometer range, 100–1000 nm. ECAP has received much attention in recent years because it is a simple procedure and can be scaled up easily [33]; the larger the sample size, the greater the potential to move forward to industrial application [34]. The size of the billets produced by this procedure at present may easily be used for production of small parts such as dental crown implants [35]. The first scientists to introduce this procedure in the 1970s and 1980s were Segal and his co-workers [25].

2.1.1.1 Principle of Equal-Channel Angular Pressing (ECAP)

In the ECAP process, the die contains an internal channel with a square or circle cross-section, curved with an abrupt angle Φ , while Ψ is the outer arc of the curvature, as shown in Figure 2.1 [36]. In this procedure, a billet sample in a form of a rod or bar is pressed by a plunger through the die channel, curved to pass through a very sharp angle [5]. As the sample passes through the channel angle by applying pressure with a plunger, a high strain is applied in a square or circular cross-section by simple shear, with no change in cross-sectional area. The process may be repeated with the same

sample as many times as necessary. Passing through the channel many times will accumulate shear strain at the sample and produce a material with a UFG structure [17].

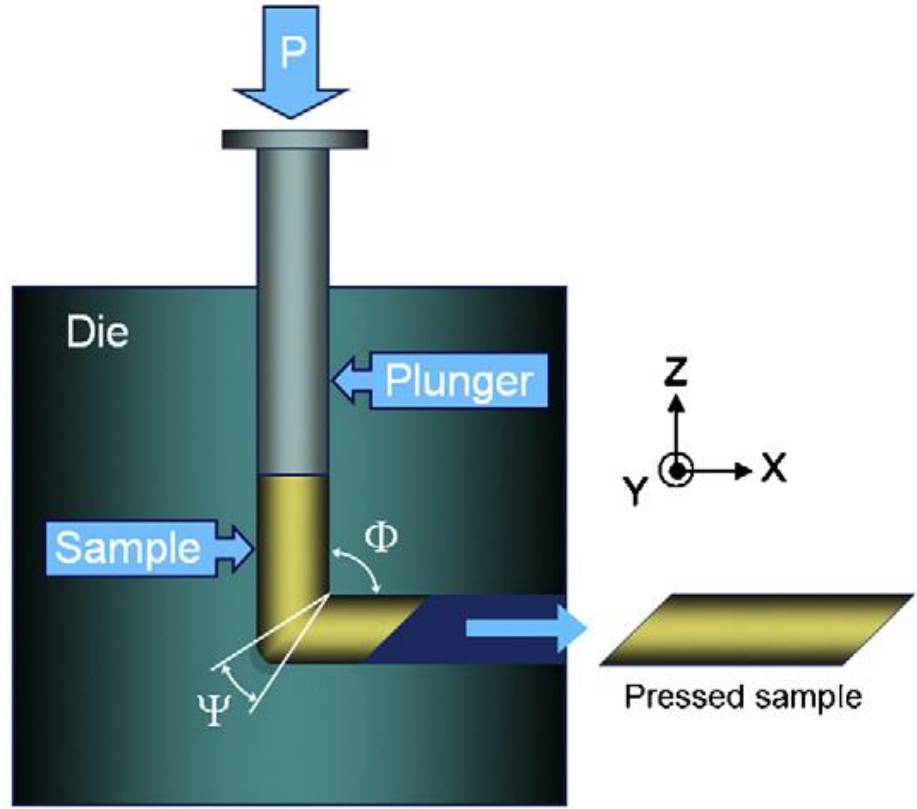


Figure 2. 1 Schematic illustration of channel angle & angle of outer curvature of ECAP [36]

The equivalent strain ε introduced to a sample when passed through the die during the equal-channel angular pressing (ECAP) process after a number of passes is [37]:

$$\varepsilon = \frac{N}{\sqrt{3}} \left[2 \cot \left\{ \left(\frac{\Phi}{2} \right) + \left(\frac{\Psi}{2} \right) \right\} + \Psi \operatorname{cosec} \left\{ \left(\frac{\Phi}{2} \right) + \left(\frac{\Psi}{2} \right) \right\} \right] \quad (2.1)$$

where N is number of passes, Φ is the channel angle and Ψ is the outer curvature angle. The calculation shows that the equivalent strain imposed on the material is $\varepsilon \sim 1$ after each individual pass, when the angle $\Phi = 90^\circ$ and the outer curvature $\Psi \sim 20^\circ$ [38].

Several experimental reports have revealed the potential for attaining a reasonable homogenous microstructure with equiaxed grains separated by a high-angle boundary using ECAP for a number of passes, N, having a final grain size of ~ 700 nm to $3 \mu\text{m}$

[27,39,40]. Although the final product of ECAP process has an ultra-fine grained microstructure, the mechanism for reaching that is different and depends on the material crystal structure. Due to the limited slip systems in hexagonal close-packed (HCP) materials, it is essential to activate additional slip systems to produce a homogenous ultra-fine grained microstructure. To verify the nature of grain refinement in ECAP, an experiment was conducted in aluminium as face-centre cubic (FCC) metal-represented, and magnesium as hexagonal close-packed (HCP) metal-represented [41]. The result proved that ECAP can produce an ultra-fine grain in two metals with different crystalline structures, using a different refinement mechanism. In FCC metals, the refinement mechanism starts uniformly all over the grains due to the availability of many slip systems with an array of cell development or subgrains, then it evolves to an equiaxed ultra-fine grained array with a reasonable fraction of high-angle grain boundaries all over the material. In HCP metals, the mechanism is different. Because of the limited slip system in HCP metals, the refinement is restricted. The newly-formed grains are located adjacent to the original grain boundaries and form many different final grain structures. The nature of the final grain structure depends on the initial grain structure and the size of the newly-formed grains after the first pass in ECAP. These grain structures can have either a multi-model or homogeneous distribution of ultra-fine grains.

2.1.1.2 Routes in equal-channel angular pressing (ECAP)

The same material processed by ECAP under the same conditions can produce a different microstructure if the processing route is different. There are four main processing routes in ECAP: A, B_A, B_C and C, as seen in Figure 2.2. The difference between these routes is specified by the way the sample rotates around its axis after each pass to start the next pass in the new position. The processing routes have a major influence on the material's final microstructure. Processing the material using different routes will produce different final microstructures [42–44]. It was shown that processing the materials with route B_C will develop a homogenous microstructure of grains with high-angle grain boundaries more rapidly than processing the material by Route B_A [45], and than Route A or C [46].

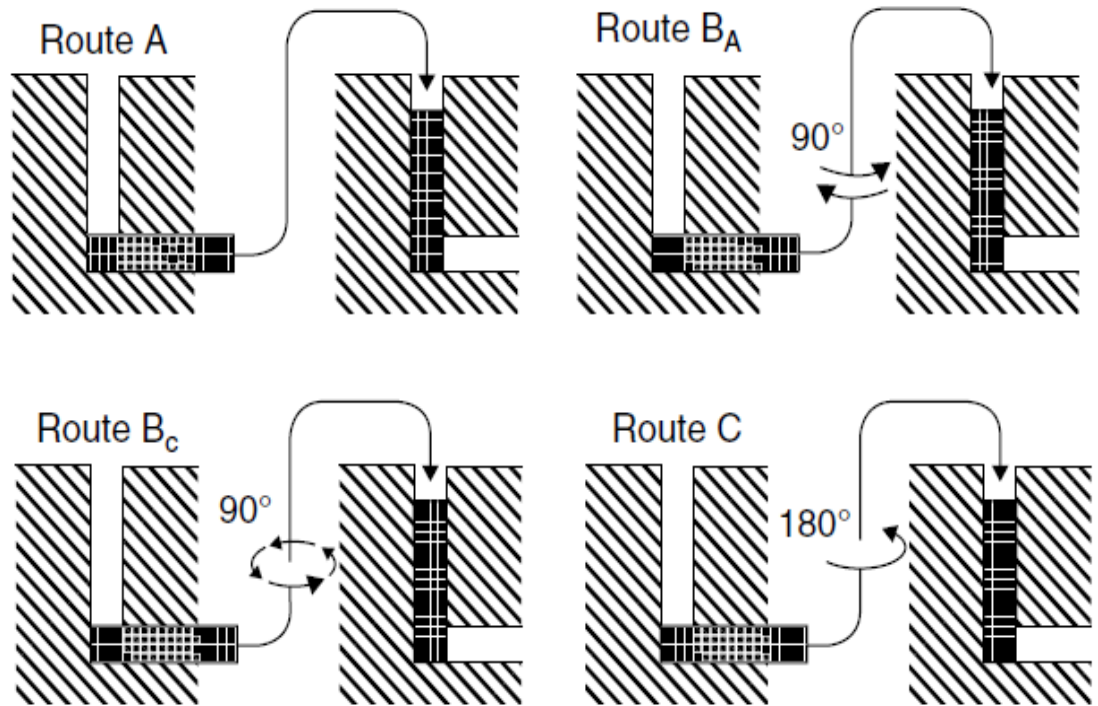


Figure 2. 2 Schematic illustration of the four main processing routes in (ECAP) [47].

In Route A, the sample is processed with no rotation in any direction between passes. In Route B_A, the sample is rotated through an angle of 90° in alternate directions in consecutive passes. In Route B_C, the sample is rotated through an angle of 90° in the same direction after each pass, and in Route C it is rotated through an angle of 180° after each pass [47]. Several reports have stated that Route B_C is the optimum to produce a uniform ultra-fine grain microstructure separated by high-angle grain boundaries [48,49]. In Route B_C the strain is redundant, which means that the strain is fully reversed after four passes [34]. Different slip systems are introduced by those routes, as illustrated in Figure 2.3.

An experiment was conducted on oxygen-free copper (99.99%) by ECAP at room temperature, using different routes for number of passes $N = 25$. The results of this experiment shows that Route B_C produced an equiaxed structure more rapidly than Routes A and C. Furthermore, the strength and ductility were better when using Route B_C than other routes [29]. Figure 2.4 shows the TEM images verifying the structure of oxygen-free copper processed by ECAP using different routes. As shown in Figure 2.5, distortion in the cubic elements is introduced for each processing route on the X, Y and

Z plane. Route B_C shows distortion in the cubic elements in all the planes and the cubic element is restored every four passes [47].

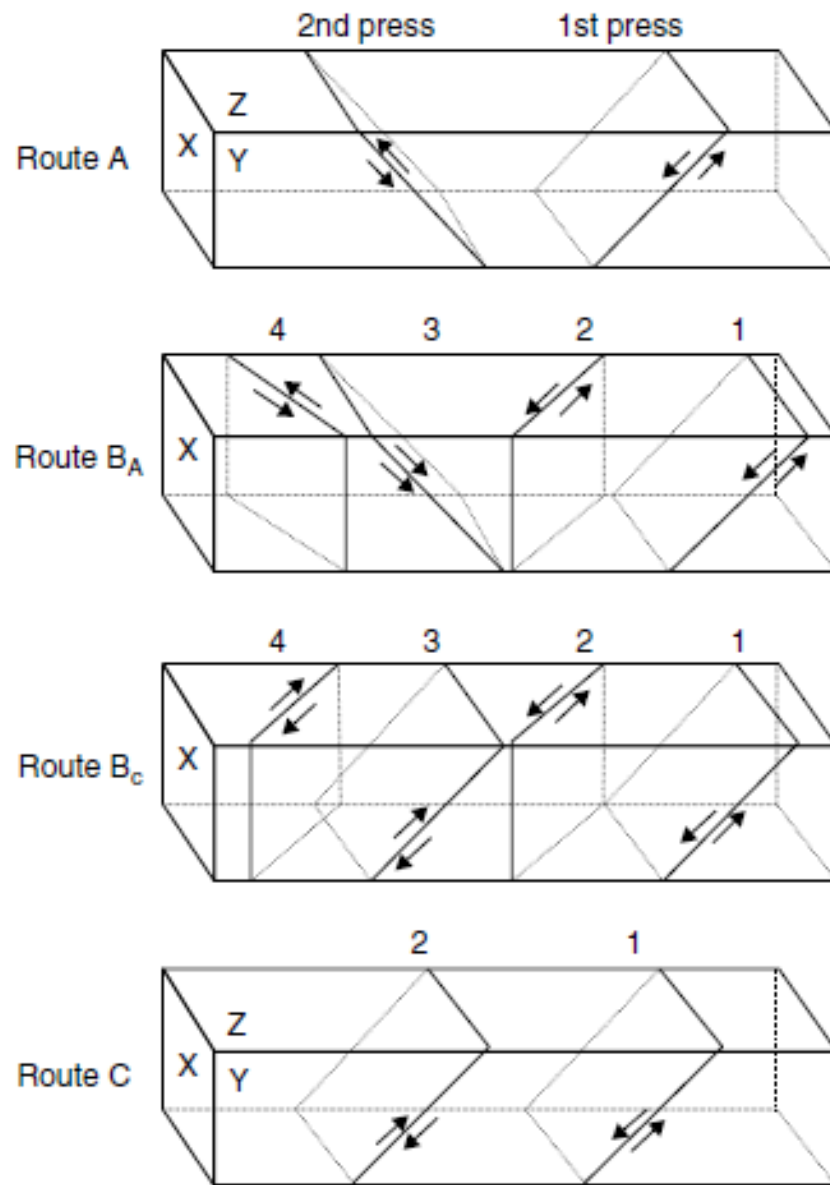


Figure 2. 3 Schematic illustration of slip systems in X, Y & Z planes for different numbers of passes using processing routes A, B_A, B_C & C [43].

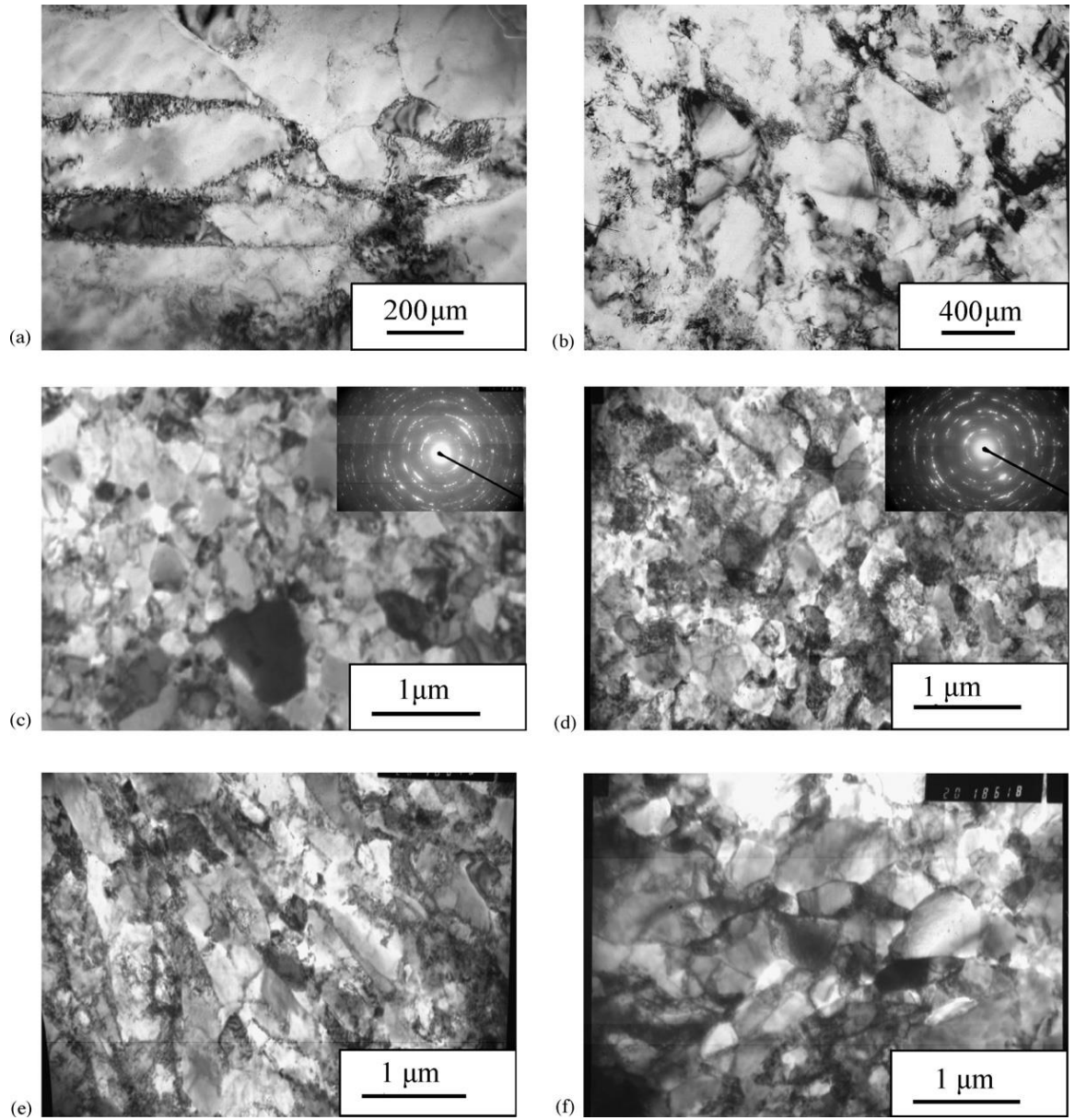


Figure 2. 4 TEM photographs of oxygen-free copper processed by ECAP at 20°C: (a) Route B_c; N = 3 (b) Route B_c; N = 5 (c) Route B_c; N = 10 (d) Route B_c; N = 15 (e) Route A; N = 10 (f) Route C; N = 10 [29].






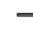







































































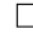






























Route	Plane	Number of pressings								
		0	1	2	3	4	5	6	7	8
A	X									
	Y									
	Z									
B _A	X									
	Y									
	Z									
B _C	X									
	Y									
	Z									
C	X									
	Y									
	Z									

Figure 2. 5 Schematic illustration of cubic element distortion on the X,Y and Z plane of material processed by ECAP up to 8 passes using different routes (A, B_A, B_C & C) [47].

2.1.1.3 Models of microstructure development in ECAP

The grain refinement and microstructure development of a material processed by ECAP have different mechanisms. These depend upon the crystal structure of the material, the initial microstructure and the average grain size after the first pass of ECAP.

In materials with a face centre cubic (FCC) structure, such as aluminium, grain refinement is simple. To be precise, there are bands of subgrains in the material's initial grains, and these evolve into a UFG structure when passed through the ECAP die [46]. In materials with a hexagonal close-packed (HCP) structure, such as magnesium and magnesium alloys, grain refinement is more complex. Different microstructures have been reported, depending on the initial microstructure [50]. Previous studies have illustrated that processing the same alloy using same conditions can produce a different microstructures, uniform or bi-modal, depending on the initial microstructure [51], as shown in Figure 2.6.

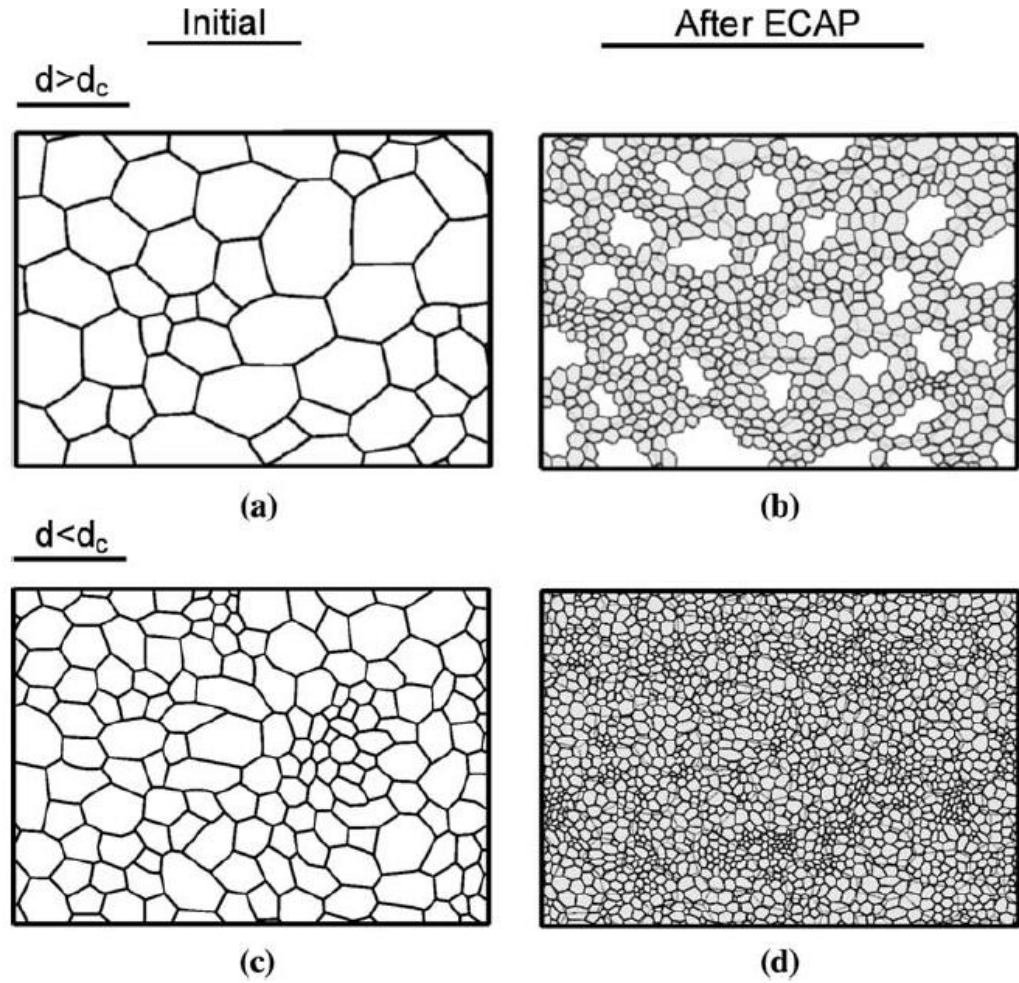


Figure 2. 6 Model of grain refinement where different microstructures are produced after ECAP depending on the alloy initial microstructure, where d is the initial grain size & d_c is the critical grain size needed to achieve an homogeneous microstructure [51].

2.1.1.4 Experimental factors influencing ECAP

As stated earlier and shown by Equation 2.1, the number of passes N through the channel is an important factor in accumulating the strain that affects the resultant microstructure. The other key factors are the channel angle, Φ , the curvature angle, Ψ and pressing temperature.

The degree of the internal channel angle, Φ , has a great experimental influence on the microstructure of the material processed by ECAP. It determines the magnitude of the imposed strain at each separate pass. Using an internal channel angle $\Phi = 90^\circ$ will impose a very high strain and produce a material with ultra-fine grain, having

boundaries with high angles of misorientations [38]. Increasing the internal channel angle $\Phi > 90^\circ$ will decrease the imposed strain on the ECAP sample at each pass. An experiment was conducted on pure aluminium (99.99%). After processing by ECAP using Route B_C through four different internal angles $\Phi = 90^\circ, 112.5^\circ, 135^\circ$ and 157.5° , it was seen how by increasing the internal angle, Φ , more passes are needed to impose the same high total strain on the sample when $\Phi = 90^\circ$, as in Table 2.1 [38]. By contrast, reducing the internal angle $\Phi < 90^\circ$ increases the imposed strain for each individual pass in the ECAP process and produce a slightly smaller grain size [52]. By decreasing the dead zone – the area or space where the sample billet is not in contact with the die channel outer wall during the process – the ECAP process will introduce a better strain homogeneity distribution to the sample [53].

Table 2. 1 Number of passes required to achieve same total strain for deferent internal angles [38]

Strain, ϵ	Number of pressings			
	$\Phi = 90^\circ$	$\Phi = 112.5^\circ$	$\Phi = 135^\circ$	$\Phi = 157.5^\circ$
~ 1	1 (1.05) [†]	2 (1.42)	3 (1.40)	6 (1.37)
~ 2	2 (2.1)	3 (2.13)	5 (2.34)	9 (2.05)
~ 4	4 (4.22)	6 (4.27)	9 (4.21)	19 (4.33)
~ 5	—	7 (4.98)	11 (5.15)	21 (4.78)

Increasing the internal channel has a major influence on processing difficult-to-work alloys. These are alloys that are hard to deform at ambient temperatures. A good example is magnesium alloy. Due to its structure, HCP magnesium alloy has limited slip systems. This leads to segmentation and cracks when the material is deformed at low temperatures using a die with an angle of $\Phi = 90^\circ$. Figure 2.7 shows two AZ60 magnesium alloy billets processed by ECAP using different dies. The upper billet used a die with channel angle $\Phi = 90^\circ$ so segmentations were created, while the lower billet used a die with channel angle $\Phi = 110^\circ$, so the billet avoided segmentation [50].

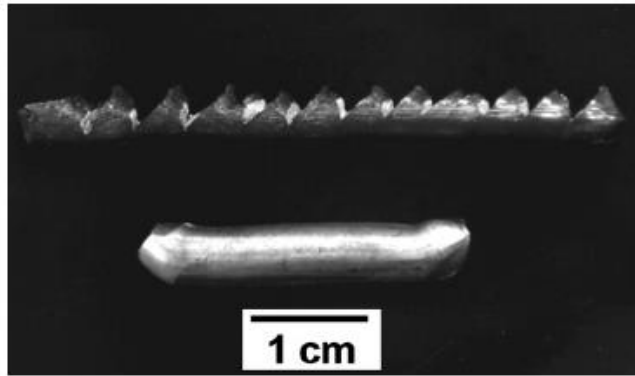


Figure 2. 7 ZK60 billets processed by ECAP for one pass at 473 K, using a die with $\Phi = 90^\circ$ for the upper billet and a die with $\Phi = 110^\circ$ for the lower billet [50].

The angle of outer curvature, where the die channel interconnects, has a minor influence on the imposed strain through the process, but it cannot be neglected. Studies have shown that, in order to increase the microstructure homogeneity, the outer angle curvature should be $\Psi \sim 20$ and the inner channel angle $\Phi = 90^\circ$ [5].

Pressing temperature has a significant influence on the ECAP process, and increasing the temperature is a major factor in helping to process difficult-to-work alloys [54]. Temperature can easily be controlled within the die; by increasing the process temperature, the non-basal slip system in magnesium alloy, for example, can be activated, which will increase the numbers of slip systems in the material, leading to enhanced ductility and workability. In consequence, the material can be processed by ECAP within a die having an inner channel angle of $\Phi = 90^\circ$ without inducing of cracks or segmentation. However, there is a disadvantage in increasing the pressing temperature; the material tends to form a larger average grain size than when processing at lower temperatures, due to the increment in the rate of recovery [5]. These results have been confirmed by several earlier investigations [55–58]. The lower the pressing temperature, the smaller the grain size, due to restriction to grain growth [59]. Figure 2.8 illustrates the increase in grain size associated with increased pressing temperatures.

Applying back pressure is another procedure that helps in processing difficult-to-work alloys at low temperatures using ECAP [31,32]. It can also improve the workability of a such alloys and attain a high number of passes in the ECAP process without introducing cracks or segmentation [60]. Using back pressure in ECAP leads to a finer grain size than without [61,62] Although back pressure has no clear effect on the level of the strain imposed to the sample, it can improve the strain homogeneity of the material processed

using ECAP by decreasing or removing the dead zone [53]. A dead zone is formed in the area where the billet is not in contact with the die wall, so the strain is no longer preserved.

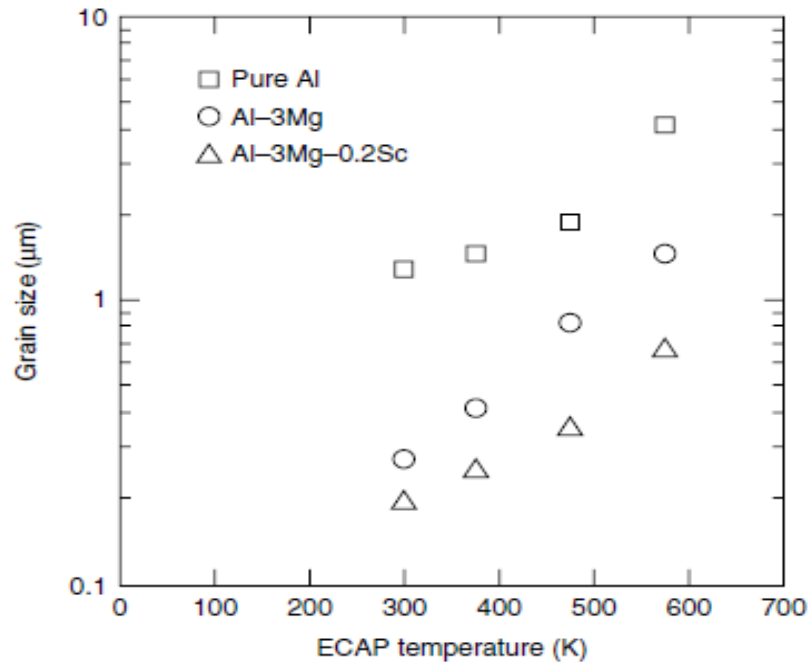


Figure 2. 8 Effect of pressing temperature on grain size after ECAP for pure Al and Al-3%Mg & Al-3%Mg-0.2Sc alloys [63].

2.1.1.5 Advantages and disadvantages of ECAP

There are many advantages to processing a material with ECAP. The ECAP process has the potential to enhance the strength and to achieve superplastic ductility by producing a bulk ultra-fine grain material, It is a procedure that uses simple facilities that can be easily scaled up to produce a large volume sample [5]. The facility of the ECAP process can be open to further simplification and the total strain can be increased by using multi-pass dies [64]. Furthermore, the ECAP principle can be integrated into a continuous process [65]. Inducing cracks and segmentations when processing difficult-to-work alloy at ambient temperature can be considered as a disadvantage.

2.1.2 High-pressure torsion (HPT)

Although ECAP has attracted more interest in recent decades because of the large sample size permitted, HPT has revealed an outstanding ability to refine grain [5,66]. It is considered to be the most effective SPD procedure to produce material with grain size in the nanometer range [6,49,67]. Both SPD techniques provide a high fraction of high-angle boundaries, but investigation shows that HPT produces an alloy with a finer-grained microstructure and a smaller fraction of lower-angle boundaries than the same alloy processed by ECAP [68]. A combination of external high pressure concurrent with torsional strain through the rotation of the lower anvil is applied to the sample. Massive hydrostatic pressure is imposed on the sample, up to several GPa. HPT is an SPD technique in which different materials with different crystal structures, such as Body-Centered Cubic (BCC) [69], Face-Centered Cubic (FCC) [70] and Hexagonal Close-Packed (HCP) [71], can be processed easily at different temperatures. In fact, it can process a material with limited slip systems or lack of ductility at room temperature or at a temperature below $0.2 T_m$ where T_m is the absolute melting temperature of a material without the development of segmentation or cracks [15,72,73]. This is one of the important advantages of HPT. It can increase the hardness of most metals and alloys by more than 100% in some areas of the sample [12,74]. Despite the advantages of HPT, one disadvantage should be well thought through, namely the variation of imposed strain along the diameter of the sample.

2.1.2.1 Principle of high pressure torsion (HPT)

In HPT, the sample is in the shape of a thin disc with a diameter of ~ 10 mm and a thickness of ~ 0.85 mm. This is placed in a circular cavity in the lower anvil, and the upper anvil has a similar circular cavity. The sample between the two cavities of the large anvils is subjected to a high compressive pressure, P , with several GPa. The upper anvil is stationary, while the lower anvil concurrently imposes a torsional strain on the sample through rotation, as illustrated in Figure 2.9. The combined depth of the cavities in the upper and lower anvils is 0.5 mm, which is less than the initial thickness of the sample, at 0.85 mm before processing. This difference in thickness allows a small amount of the material to flow out between the edges during the process. The free flow is restricted by the friction from the rough edge of the cavities. This limited flow of the processed material prevents the anvils from contacting each other and helps to build up

the hydrostatic pressure on the sample [75]. The disc is deformed plastically under quasi-hydrostatic pressure by shear force through the surface frictional forces [6]. The HPT procedure can be performed at room temperature or at elevated temperatures [17].

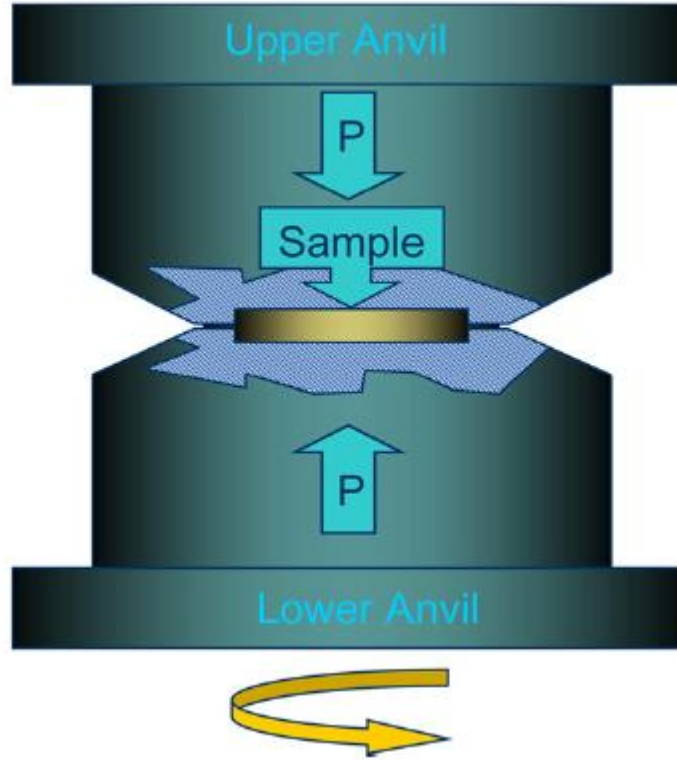


Figure 2. 9 Schematic illustration of HPT processing principle [74].

The relationship to estimate the shear strain, γ imposed on the HPT sample is given by [76]:

$$\gamma = \frac{2\pi Nr}{h} \quad (2.2)$$

where N is the number of turns, r is the distance from the centre of the disc and h is the disc thickness. This equation shows a variation in imposed strain along the diameter of the disc, where the maximum strain will be at the edge. This strain value will decrease gradually to the value of zero at the centre of the disc.

The relationship that calculates the strain according to von Mises is [77–79]:

$$\varepsilon_{vM} = \frac{\gamma}{\sqrt{3}} \quad (2.3)$$

To compare the strain produced by shear to the linear strain produced by extension, drawing and rolling [80,81], both equations can be combined and the true strain produced by HPT is [77]:

$$\varepsilon = \frac{2\pi Nr}{h\sqrt{3}} \quad (2.4)$$

2.1.2.2 Principle of unconstrained and constrained HPT

The three different types of conditions under which a sample may be processed by HPT [76] are shown in Figure 2.10 (a, b and c). The first is the unconstrained condition, in Figure 2.10 (a), where the sample is positioned in the lower anvil and the material can flow freely outwards. This type of configuration produces a very thin sample, developing an inhomogeneous pressure distribution. Moreover, there will be a continuous thickness reduction in the sample with increasing numbers of turns, leading to anvil contact and resulting in damage. The second condition is constrained Figure 2.10 (b), where the material is positioned in the lower anvil cavity and the material cannot flow freely outward from the anvils. The sample produced by this type of configuration has a greater thickness at the edge, due to the material flow between the anvil and the outer cylinder adding more friction to the anvils. Constrained conditions are difficult to achieve in reality, therefore most experiments (including this study) are undertaken in conditions where the material can flow outward from the anvil in a limited volume, as in Figure 2.10 (c). In this configuration, the combined depth of the cavities is less than the initial thickness of the sample before processing. This allows a limited volume of the material to flow between the anvils, due to friction, resulting in hydrostatic pressure to the sample located in the pressing area. This condition is known as quasi-constrained [17,82]. Moreover, the escaped material acts as a barrier between the anvils, protecting them from damage.

Figure 2.11 shows the result of copper samples being subjected to the three types of HPT configuration. At (a), the sample shows strong thinning when processed under unconstrained condition; at (b), the sample shows a greater thickness at the edge when processed under constrained conditions; and at (c), the sample shows a limited flow of material outward from the depression.

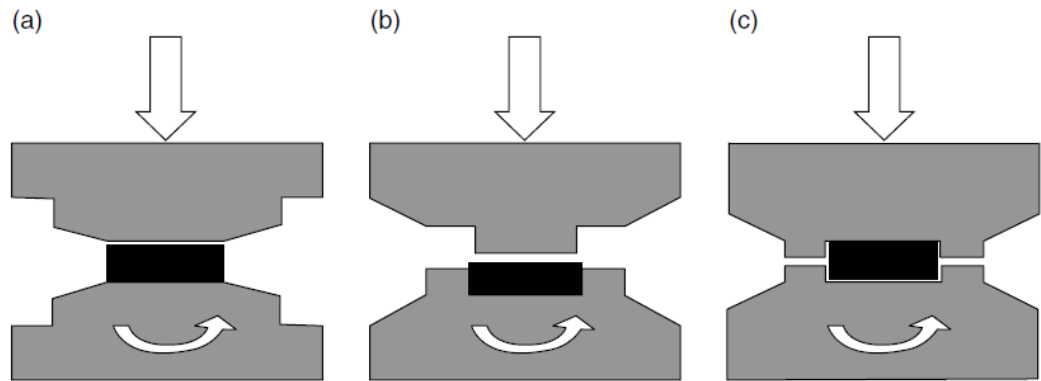


Figure 2. 10 Schematic illustration of the HPT process condition: (a) unconstrained; (b) constrained; & (c) quasi-constrained conditions [76].

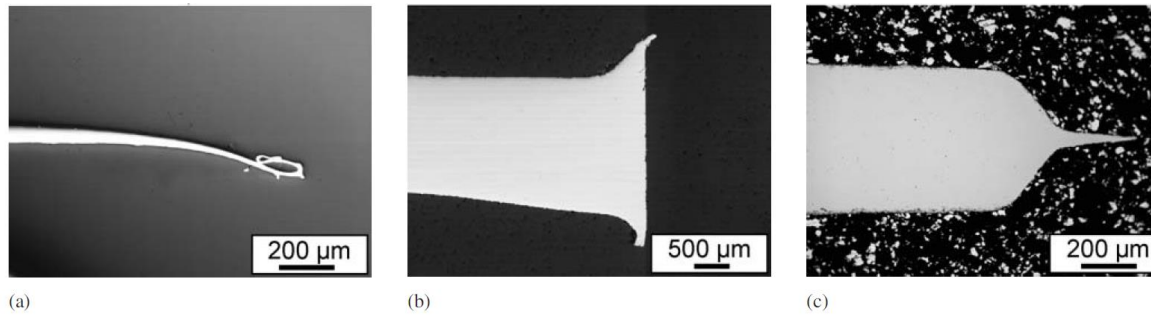


Figure 2. 11 Cross-section of three samples processed by HPT under different configurations: (a) unconstrained; (b) constrained; and (c) quasi-constrained conditions [82]

2.1.2.3 Variation in homogeneity across an HPT disc

The HPT process is able to produce an ultra-fine grained material in the submicrometer or nanometer ranges but, as introduced in Equation 2.4, the imposed strain on the sample disc during the HPT process is directly proportional to the distance from the disc centre. Therefore, the total imposed strain varies from the disc centre to the disc periphery. As a result of that expression, there is zero strain at the disc centre and it increases linearly to a maximum at the disc periphery. Because of this, it can be

anticipated that this variation in imposed strain will produce an inhomogeneous microstructure [83], which is considered to be an important limitation of the HPT process. However, this heterogeneity in the early stages of the HPT process can be reduced by increasing the number of revolutions [68,84]. Taking the microhardness values across the diameter of the disc has been the main prompt to study the evolution of the material microstructure [6,85]. An experiment conducted on AZ31 magnesium alloy using the HPT process and applying 2.5 GPa at the sample for 15 revolutions shows that the microhardness values increase rapidly at the disc periphery in the early stages of the HPT process, and with further strain the microhardness value at the centre will increase to reach the values at the disc periphery after 15 turns, as illustrated in Figure 2.12 [9]. This conclusion has been reported by many studies using the HPT process for only five turns, such as ZK60 [86] and high-purity aluminium [87], 8 turns for commercial purity aluminium [85] and 10 turns for pure tantalum [69].

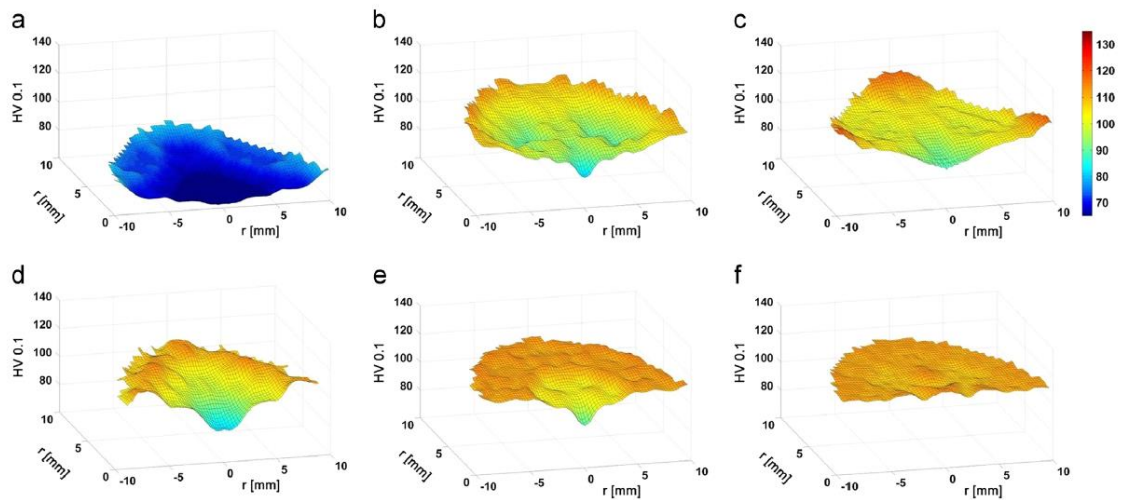


Figure 2. 12 Microhardness distribution on surface of HPT discs processed for different numbers of turns through 3D plots: (a) $N=0$; (b) $N=1/4$; (c) $N=1/2$; (d) $N=1$; (e) $N=5$; & (f) $N=15$ [9]

The average grain size of ZK60 shown in Table 2.2 demonstrates the variation in homogeneity during the HPT process. In the early stages the average grain size at the disc centre was relatively large compared to the disc's half-radius and disc periphery. Increasing the number of revolutions decreased average grain size at the centre of the disc more rapidly than other areas and the differences between the centre, half-radius and periphery become smaller. After five turns, the microstructure evolved and average grain size became more homogeneous over the entire disc, with a value of $\sim 1 \mu\text{m}$ [86].

Table 2. 2 Average grain size of ZK60 processed by HPT at ambient temperature for different numbers of turns and different positions of the disc [86].

<i>N</i>	Average grain size (μm)		
	Center	Half-radius	Periphery
1/4	4.1 ± 2.5	2.4 ± 1.3	2.0 ± 1.2
1/2	2.3 ± 1.3	2.0 ± 1.1	1.8 ± 1.0
1	1.4 ± 1.0	1.2 ± 0.9	1.1 ± 0.8
5	1.2 ± 0.8	1.0 ± 0.6	0.9 ± 0.6

2.1.2.4 Effect of applied pressure

Although there are many parameters affecting the evolution of microstructure, homogeneity and the resultant grain refinement of a material processed by HPT, applied pressure, P , and the imposed strain represented by the number of turns, N , are the most important.

The applied pressure and the unique geometry of the HPT anvils under quasi-constrained conditions allow the material to have a limited flow through the gap between them, which helps to build up hydrostatic pressure to impose great strain, leading to a high density of dislocations and further grain refinement [6]. This great hydrostatic pressure prevents the sample from cracking [88]. Moreover, it has a major effect in activating the non-basal slip systems in hard-to-work alloys [89]. This gives the HPT process an advantage over other, more conventional methods of SPD in processing those alloys at room temperature [15].

Many experiments have been performed to understand the influence of these parameters on a sample microstructure during the HPT process. Vickers microhardness, H_v , values along the diameter or over the whole cross-section of the disc are used to indicate the microstructural evolution of materials processed by HPT for differing numbers of turns. The smaller the variation in values, the greater the homogeneity in the microstructure.

An experiment was conducted using HPT techniques with different applied pressures of (a) 1 GPa, (b) 3 GPa, (c) 6 GPa and (d) 9 GPa, on pure nickel discs. All discs were processed at room temperature and torsionally strained to the same number of revolutions, five turns. The results show an increase in the microhardness value of the

material starting from the lowest pressure. Increasing microhardness values are associated with large variations in those values between the edge and the centre of the disc. The edge of the disc had the highest values, and the lowest were at the centre. Considerable variation in microhardness values between the centre of the disc and the disc periphery was found at the lowest applied pressure, when $P = 1$ GPa [68].

Increasing the pressure gradually to 3, 6 and 9 GPa led to increases in the overall value of microhardness over the whole disc. At the same time, the variation in microhardness values between the edge and the centre of the disc was reduced. These data were plotted and are represented in the three-dimensional meshes shown in Figure 2.13. The colors represent the variation of the microhardness values.

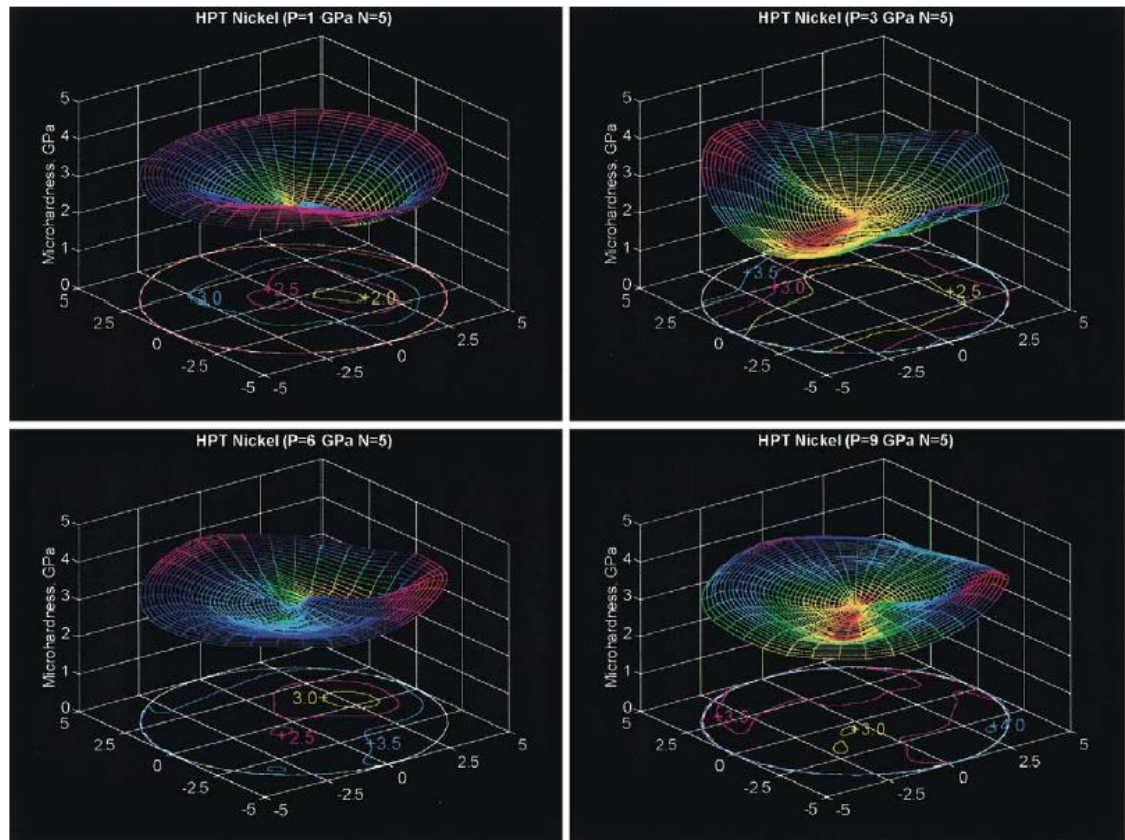
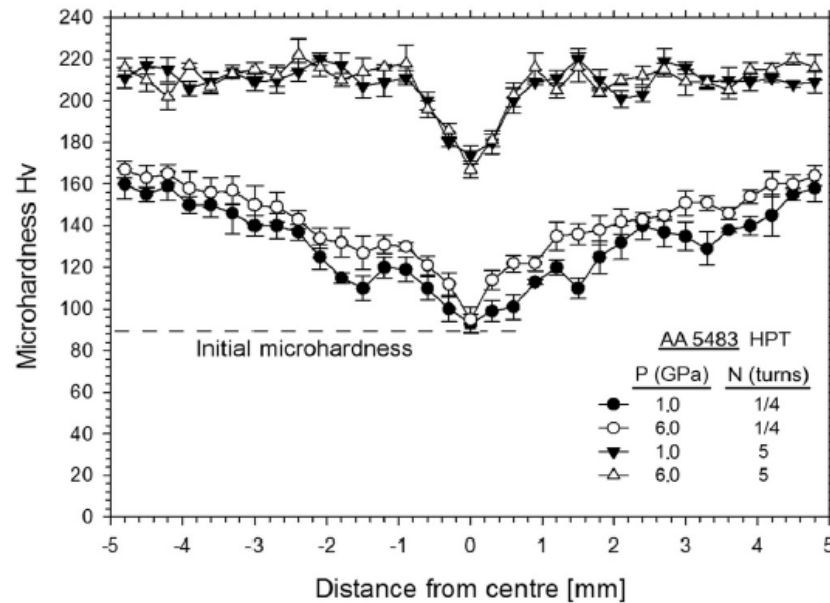


Figure 2. 13 Three-dimensional meshes of microhardness of Ni processed with different applied pressures: (a) 1 GPa; (b) 3 GPa; (c) 6 GPa; & (d) 9 GPa [68]

In a recent study, the effect of applied pressure on aluminium alloy during the HPT process was investigated. The alloy was processed at room temperature using an applied pressure of 1.0 and 6.0 GPa for 1/4, 1/2, 1, 3 and 5 revolutions. The results of the study indicate that the effect of different applied pressure is obvious in the early stages of

HPT, when a lower number of turns is applied; although it is small, it can be measured. Increasing the torsional straining to a higher number of revolutions leads to almost the same degree of deformation, and the differences in results become smaller, no matter what value of applied pressure is used [83]. This minor effect of the applied pressure was confirmed by Vickers microhardness values and average grain size, as shown in Figures 2.14 (a) and (b).



(a)

Pressure (GPa)	Location	Number of revolutions				
		1/4	1/2	1	3	5
1.0	Centre (nm)	—	—	—	310	250
	Edge (nm)	200	170	140	135	110
6.0	Centre (nm)	—	—	—	285	235
	Edge (nm)	175	155	135	130	120

(b)

Figure 2. 14 Vickers microhardness Hv, plotted as a function of position on discs processed through 1/4 and 5 turns under an applied pressure of 1.0 and 6.0 GPa at (a), the average grain size for both pressures for centre and the edge of the discs are shown in (b) [83].

The magnitude of applied pressure to the sample should be three times higher than the value of the yield stress of the undeformed alloy as a lower limit, and should not exceed the value of three times the yield stress of the anvil's material as an upper limit [82].

2.1.2.5 Effect of numbers of turns

The total number of revolutions, N , is another important factor, because it represents the total imposed strain on the sample as shown by Equation 2.4. Increasing the number of revolutions will increase the total imposed strain, therefore the microstructure will evolve with a greater grain refinement, as shown in Figure 2.15. Cu–0.1% Zr alloy was processed by HPT using up to 10 turns with an applied pressure of 6.0 GPa. The results show a gradual evolution toward homogeneity with increasing number of turns [90].

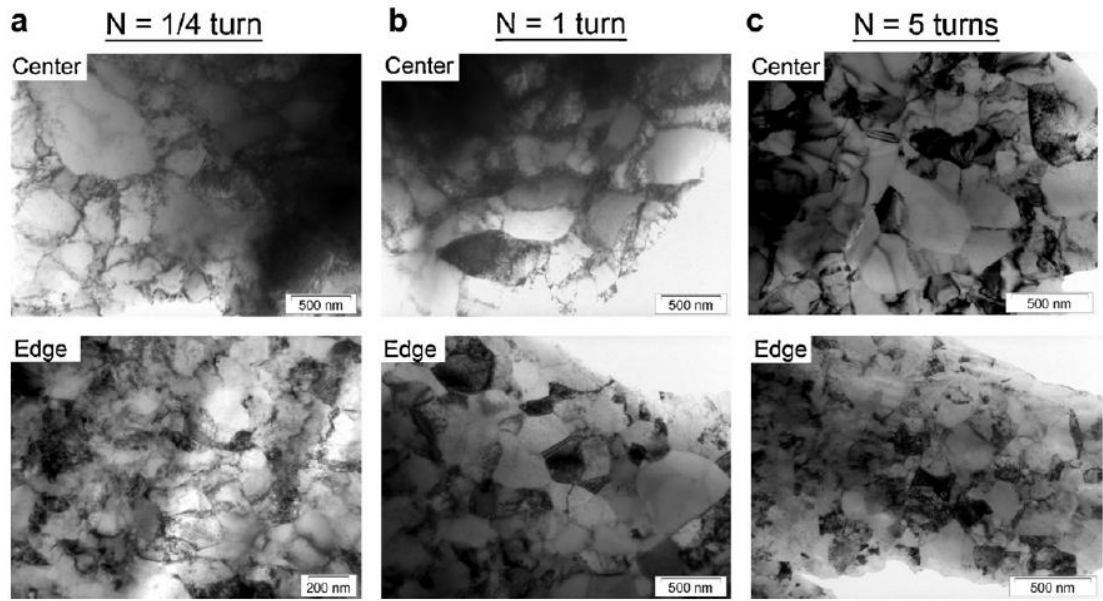


Figure 2. 15 TEM images of Cu-0.1 wt%Zr showing the microstructure after processing by HPT at room temperature for (a) 1/4 turn, (b) 1 turn and (c) 5 turns [90].

In another HPT experiment, pure nickel discs were subjected to a constant applied pressure at 6.0 GPa, but with a different number of turns: 1/2, 1, 3, and 7. The results show a large variation in microhardness values between the centre and the edges of the disc in the lower number of turns. As number of turns increases, the microhardness values over the whole disc increase and the variation in values between the edge and the centre of the discs decreases to achieve reasonable homogeneity after 7 turns [68], as shown in Figure 2.16.

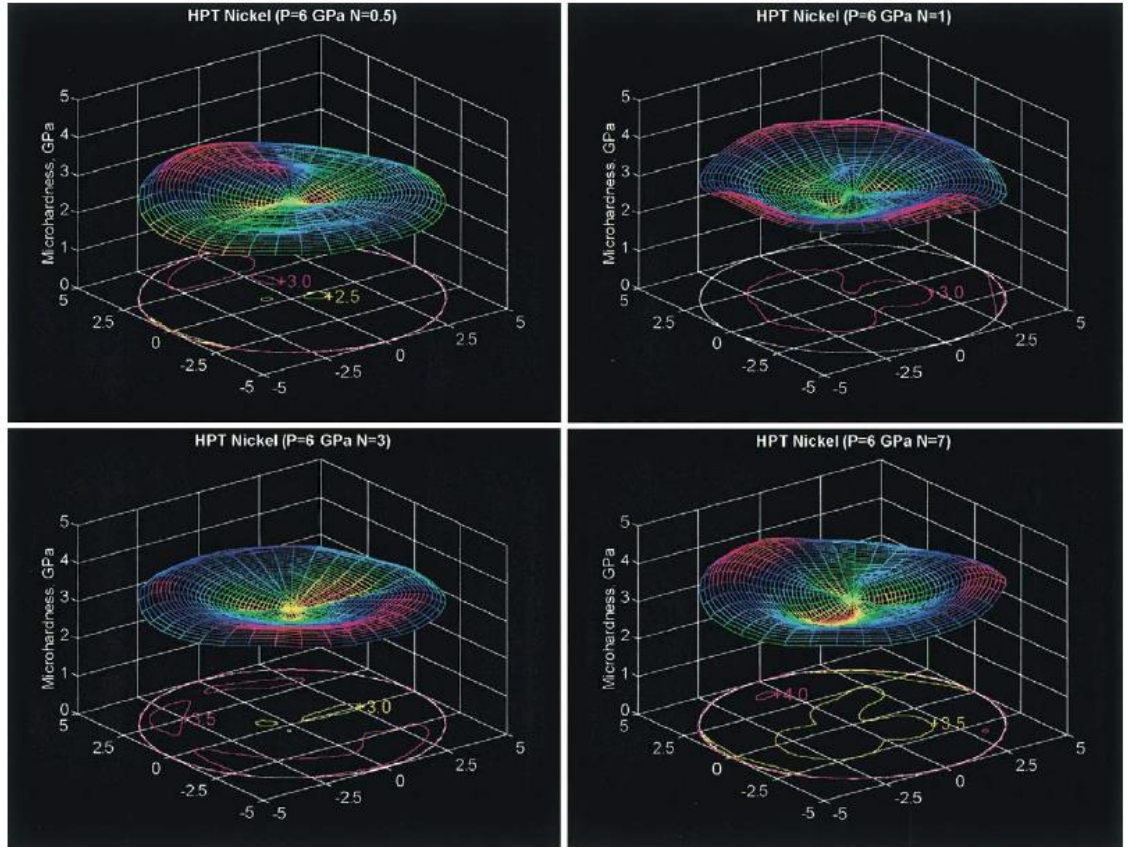


Figure 2. 16 3D meshes of microhardness in Ni processed by HPT with different number of turns at a pressure of 6 GPa: (a) $N=1/2$ turn; (b) $N=1$ turn; (c) $N=3$ turns; & (d) $N=7$ turns [68]

Figures 2.17 and 2.18 illustrate the influence of both the applied load and number of turns on the homogeneity of high-purity nickel, using a microhardness test as a function of distance. Both figures show a wide variation in homogeneity between the centre and the periphery of the disc. In Figure 2.17, the microhardness value at the centre of the disc increased from almost 2.4 to 3.3 GPa when the applied pressure increased from 1 GPa to 9 GPa, while at the edge the increase in the microhardness value was small in comparison to the centre. The heterogeneity was reduced and reasonable homogeneity achieved. Increasing the number of turns had the same influence: homogeneity increased in the whole disc [91]. When increased from a single turn to 7 turns, as shown in Figure 2.18, microhardness values increased and heterogeneity decreased. Although the applied pressure is an important parameter in the evolution toward homogeneity of a material processed by HPT, it should be noted that Equation 2.4 neglects the effect of applied pressure and only embodies the influence of imposed strain, represented by the number of turns.

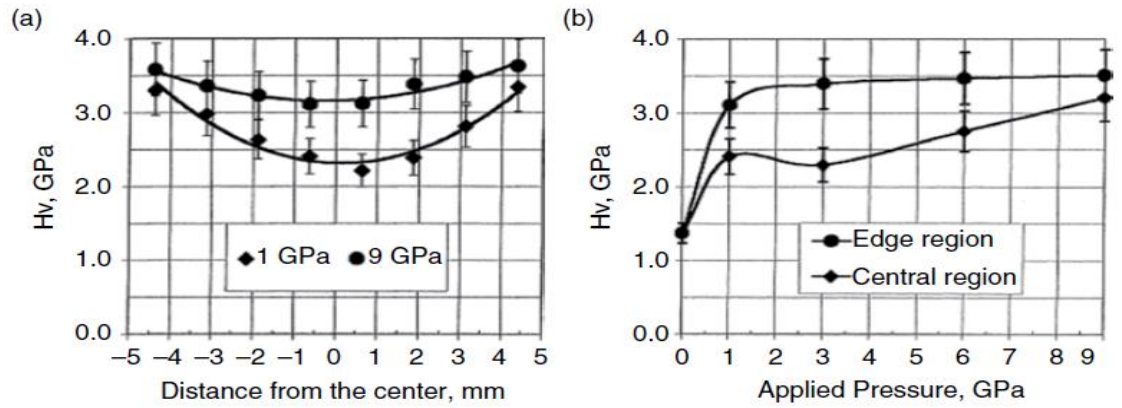


Figure 2. 17 Microhardness vs distance of Ni processed by HPT for 5 turns at room temperature with different applied loads: 1 GPa & 9 GPa [91]

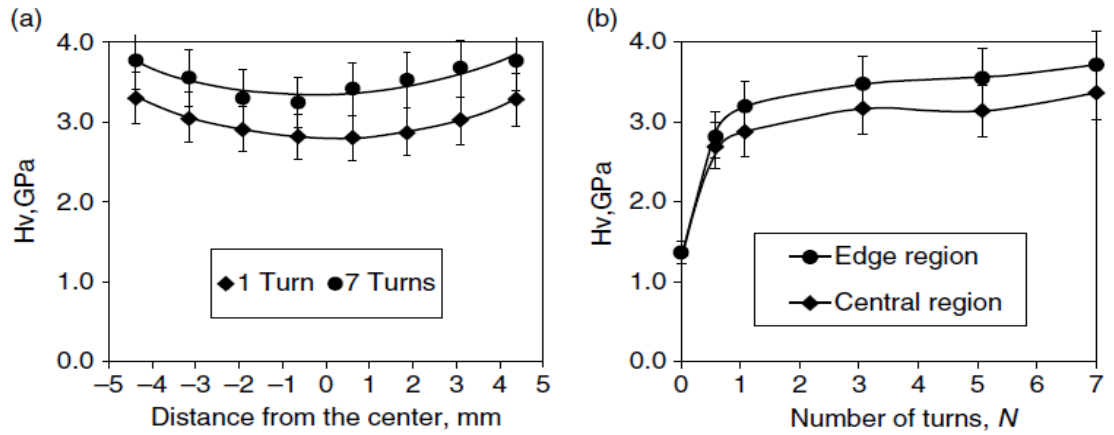


Figure 2. 18 Microhardness vs distance of Ni processed by HPT with pressure of 6 GPa at room temperature with different numbers of turns [91]

An alternative technique is used to evaluate and examine the effect of applied load, P , and the number of rotations, N , on the microstructural inhomogeneity of a material processed by HPT. In this technique, the microhardness values collected from a rectilinear grid pattern are used to construct a colour-coded contour mapping for each disc. This map visualizes the whole disc surface. Areas with lower and higher hardness values are presented in different colours for ease of recognition. The variation in colour indicates a variation in the microhardness value, which is a sign of inhomogeneity of the disc processed by HPT and verifies the HPT heterogeneous mode of deformation that is considered an important limitation of HPT [17]. Many studies have used this technique to understand the evolution of the material during HPT process [86,87,90], as shown in Figures 2.19 and 2.20.

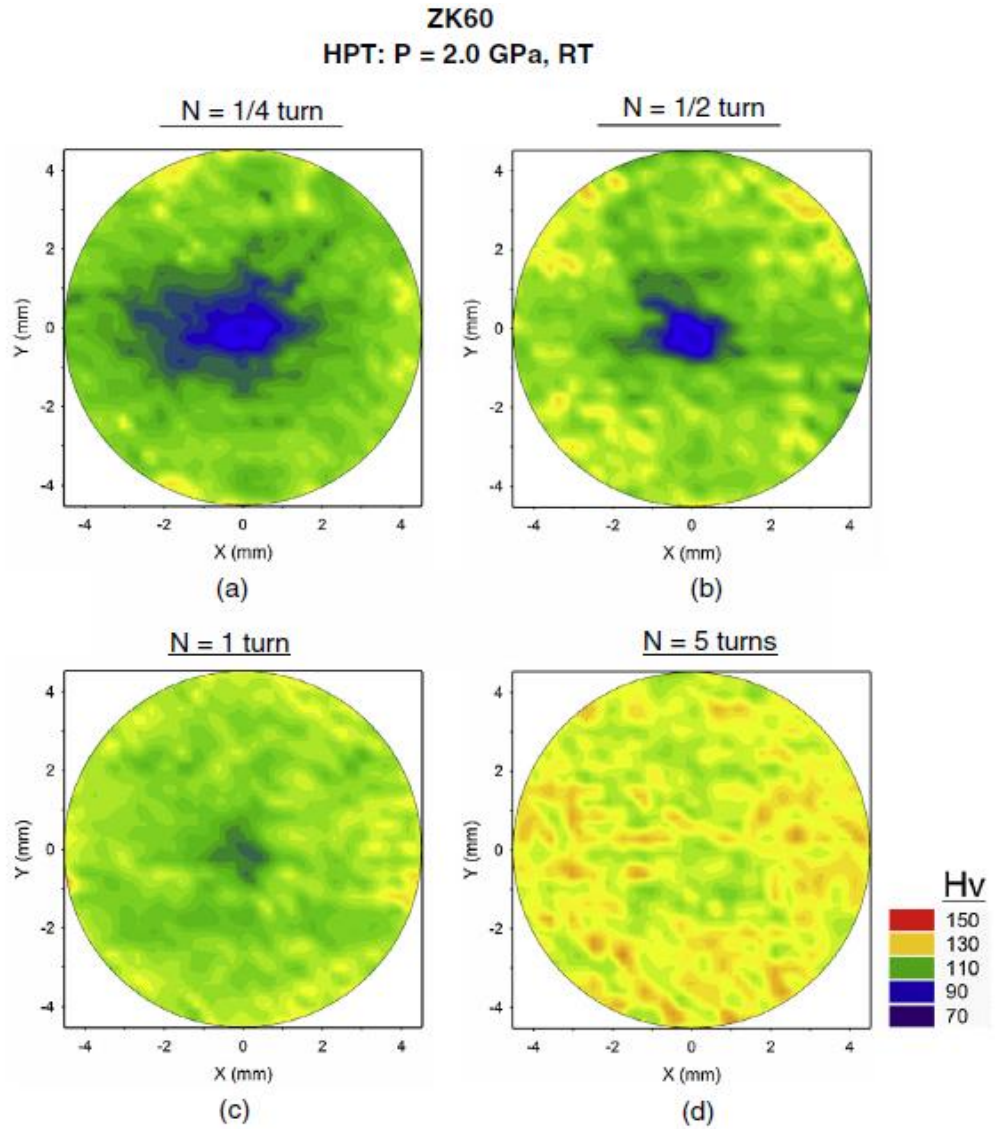


Figure 2. 19 Colour-coded contour mappings showing the variation of microhardness value through the whole disc of ZK60 magnesium alloy processed by HPT for: (a) 1/4, (b) 1/2, (c) 1 and (d) 5 turns at 2.0 GPa pressure [86]

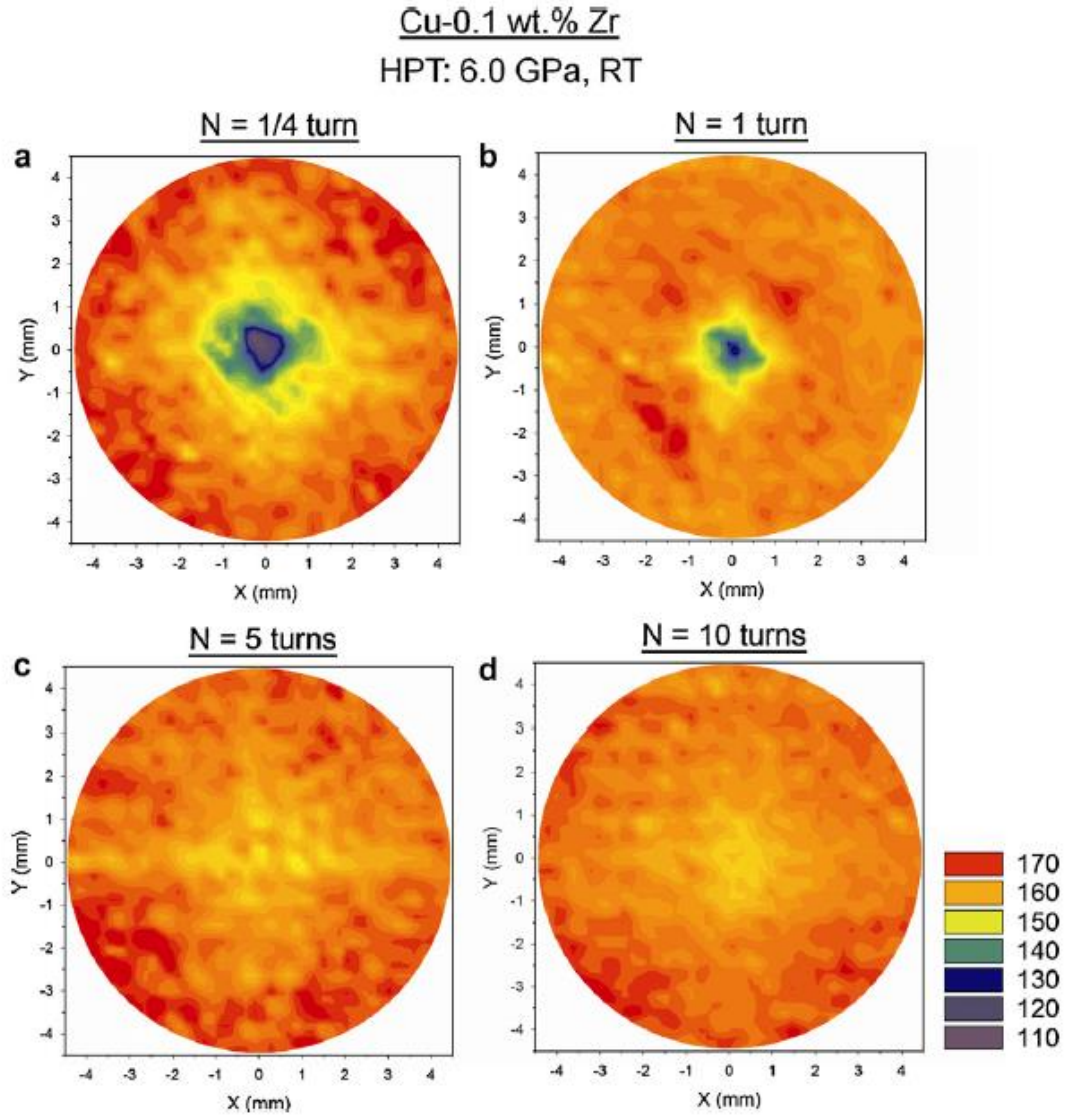


Figure 2. 20 Colour-coded contour mappings showing the variation of microhardness value through the whole disc of Cu-0.1% Zr alloy processed by HPT for: (a) 1/4, (b) 1, (c) 5 and 10 turns at 6.0 GPa pressure [90]

2.1.2.6 Influence of stacking fault energy (SFE)

Stacking fault energy (SFE) also has a great influence on the evolution toward homogeneity in a material processed by HPT in the early stages. Each crystal structure in a material has a plane of atoms, and this plane has maximum atom density. These closely-packed planes of atoms lie on top of each other in a stacking sequence, and this sequence differs between different crystal structures. In the FCC crystal structure, the stacking sequence is ABC ABC ABC, while for a HCP crystal structure it is AB AB AB. Figures 2.21 (a) and (b) show a stacking sequence for FCC and HCP materials.

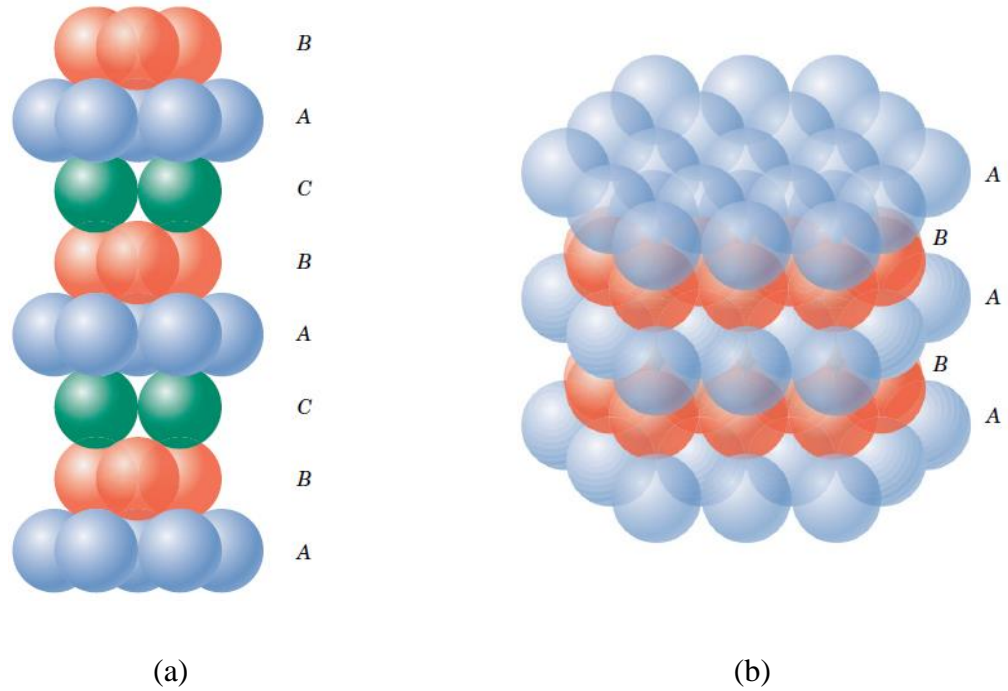


Figure 2. 21 Stacking sequence of plane of atoms in (a) Face-Centered Cubic (FCC) materials and (b) Hexagonal Close-Packed (HCP) [92] (b) (Adapted from W.G. Moffatt, G. W. Pearsall, and J. Wulff, *The structure and properties of materials*, vol. I, Structure, p.51. Copyright © 1964 by John Wiley & Sons, New York.

An error can occur in the regular order of the stacking sequence of the atomic layers, and these planar or two-dimensional defects are called stacking faults. These can be created during plastic deformation. In HCP magnesium alloy, three basal stacking faults can be formed: I_1 with stacking sequence ABABCBCB; I_2 with stacking sequence ABCACAC; and E with stacking sequence ABABCABAB [93]. These faults have an energy that affects the deformation mechanism in a material, termed the stacking fault energy (SFE).

SFE indicates how easily slip can occur in a material, and it determines the mode of deformation during the HPT process. In a material with high SFE, dislocation slip is the primary mode of deformation, because of the small separation between the partial dislocations, while, in a material with a low SFE, twinning is an important mode, because it is difficult for slip to act in a larger separation [94,95]. The lower SFE materials are susceptible to rapid strain hardening, because of the widely separated dislocations that inhibit cross-slip, resulting in a low rate of dynamic recovery [96,97]. Table 2.3 presents the magnitude of a SFE for different metals.

Table 2. 3 Stacking faults energy for different metals.

Material	Stacking Fault Energy (mJ/m²)
magnesium	125 [98]
copper	78 [99]
aluminium	200 [96]
nickel	150 [96]
gold	50 [96]

Moreover, stacking fault energy has an influence on the final average grain size of a material processed by HPT, as the average grain size of a material with a high stacking fault energy is larger than one with lower [100]. Investigations show that material refinement in the nanometer range can be achieved if the material has a low SFE, due to a slow rate of dynamic recovery, resulting a smaller grain size after processing by HPT [100]. An experiment conducted on pure copper and copper–zinc alloys shows that the microhardness values were low at the disc centre and high at the edges, since these alloys have a very low stacking-fault energy and a slow rate of recovery [97]. The final average grain size, on other hand, was smaller in Cu-10% Zn alloy than the pure Cu, when both were subjected to five turns in HPT under 6.0 GPa applied pressure. Because Cu-10% Zn alloy has a lower stacking fault energy than pure Cu, the final average grain size was smaller [100]. By contrast, a material with high SFE, such as high purity-aluminium, will have a high rate of recovery that annihilates dislocations, meaning that the material will have variations in homogeneity, with a higher microhardness value at the centre of the disc in the initial stages of HPT. This higher microhardness value indicates a more deformed area at the centre of the disc. The lower microhardness values were at the edges, because of the presence of dynamic recovery at a high rate

[87]. As shown in Figure 2.22, the TEM microstructure was recorded for high-purity aluminium processed by one turn under pressure of 1.25 GPa by HPT, where the finer grains were at the centre of the disc and the larger were at the edge.

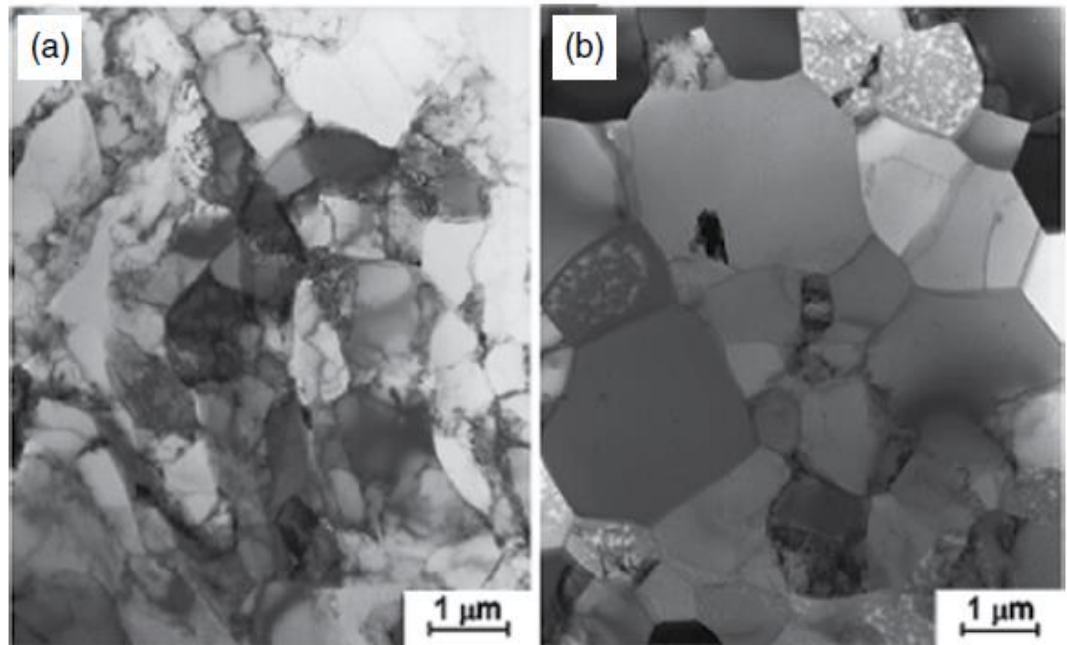


Figure 2. 22 Two regions of high-purity aluminium processed for 1 turn with 1.25 GPa pressure by HPT: (a) the centre of the disc & (b) the edge of the disc [87]

Figure 2.23 shows the material behaviour in the early stages of HPT, when it has a different stacking fault energy and rates of recovery. Both materials will develop a homogeneous microstructure throughout the disc with an increasing number of turns [87]. It can be seen from the graph that materials with a fast recovery rate developed a higher microhardness value at the disc centre, while materials with slow recovery rate developed a higher microhardness value at the disc periphery.

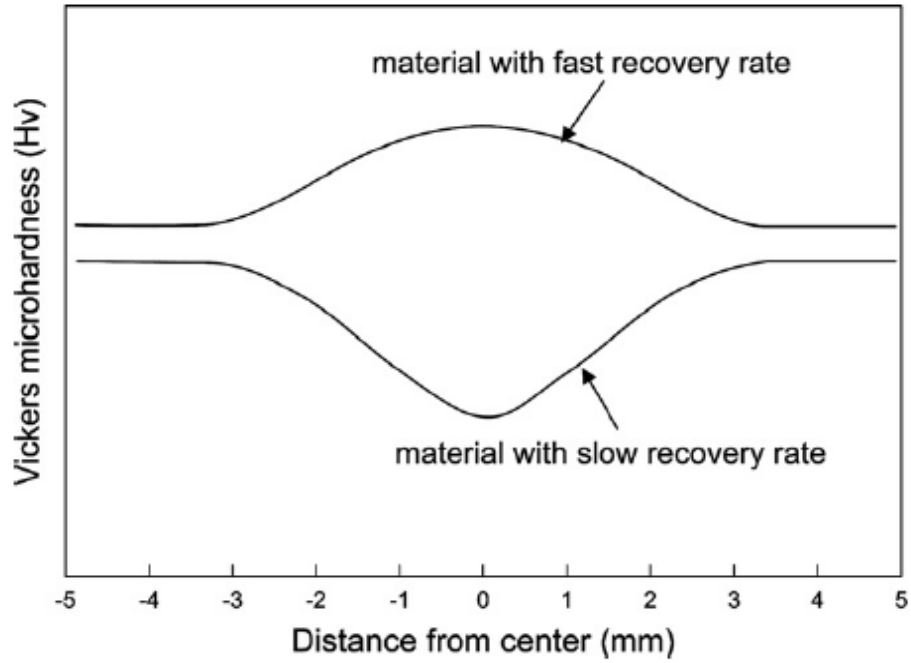


Figure 2. 23 Trend of different materials with low and high stacking- fault energy in early stages of HPT using the Vickers microhardness values [87]

2.1.2.7 Microstructure evolution toward homogeneity in HPT

As illustrated earlier, the HPT process induces a heterogeneous microstructure and hardness across the disc diameter of deformation due to the induced inhomogeneous strain during the HPT process [87,101]. According to Equation 2.4, the torsional strain applied to the disc depends on the distance from the disc centre, therefore the disc periphery will be subjected to the maximum strain, while areas near the centre will be subjected to the minimum [18,75,84]. Furthermore, this inhomogeneity appears in the axial direction or through the disc thickness of a material processed by HPT [102]. It decreases gradually with greater imposed strain by increasing the number of revolutions as shown in earlier reports [9,66,101]. This evolution toward homogeneity was observed, recorded and analysed through Vickers microhardness values, optical microscopy (OM), scanning electron microscopy (SEM) and Transmission Electron Microscopy (TEM) [9,83,103–105].

This microstructural evolution toward homogeneity across the disc diameter during HPT process was first explained by a simple model. The disc periphery is exposed to a higher strain in the early stages as the friction coefficient is high, and this area of the

disc will be subjected to higher shearing deformation, resulting in local hardening and a stiffer region, the shearing transferring to adjacent regions because of the reduction in frictional force. By increasing the number of turns, the deformation will develop in a repetitive manner and shearing will extend from the periphery to the centre of the disc. This explains the grain refinement of the disc centre and the resultant reasonably homogenous microstructure achieved with increasing numbers of revolution [68,85].

The second justification involves the combination of two models of plasticity of strain gradient. These are the geometrically necessary dislocations, leading to first-order strain gradients and incompatibilities of plastic strain between neighbouring grains, leading to second-order strain gradients [106]. These two models give an explanation of the deformation of the central area of the disc and the reasonable homogeneity of microstructure and uniformity of microhardness along the disc diameter. There is higher accumulated plastic strain at the disc periphery than at the disc centre in the early stages of the HPT process, leading to a strain gradient. The area of higher strain at the edge of the disc starts to expand with further strain toward the centre of the disc, leading to a decrease in the strain gradient between the disc areas. By increasing the number of turns, the accumulated strain rate increases at the disc centre more than at the disc edge. At this stage, refinement starts to take place across the centre area, and after five turns reasonable homogeneity is obtained.

A recent study using finite element modeling explained the microstructure evolution in the disc centre [107]. It was demonstrated that, with further torsion of HPT at high pressure, under quasi-constrained conditions the material will flow outward from the anvils and the thickness of the sample will be continuously reduced. This reduction in sample thickness leads to an increase in the value of effective compressive strain at the disc centre [108].

2.1.2.8 Model of hardness evolution across the disc diameter during HPT

Metals processed by HPT achieve a significant grain refinement. Nevertheless, microhardness evolution differs between various metals and alloys. The evolution of microhardness during HPT is of three types, as illustrated in Figure 2.24, where microhardness is plotted against the calculated equivalent strain at each point of measurement using the relationship for strain given in Equation 2.4. This approach is

useful in categorizing the evolution of hardness with increasing equivalent strain. This categorization depends on the magnitude of SFE and the rate of recovery in the materials. The plot outlines the microhardness evolution up to the development of a saturated or steady-state condition in which hardness remains constant over a wide range of strain.

The first model, Figure 2.24 (a), is the general model in which strain hardening behaviour accrues at the beginning of the HPT process. The central area of the disc has lower Hv values, and these increase with increasing distance from the centre. As the number of revolutions increases, the hardness gradually increases and is saturated at higher level of strain, as in most metals [84,109,110]. This behaviour takes place when the material has low SFE and no or little recovery.

The second model, Figure 2.24 (b), is when a material's hardness outline forms a bell-shaped curve. In the early stages of HPT, the material shows rapid strain hardening, followed by significant strain softening, until saturation. This type of behaviour is seen in materials with a very high SFE, which causes the dislocations to cross-slip easily with rapid recovery [87]. High-purity aluminium, magnesium and zinc confirm this type of behaviour [111–113].

The third model, Figure 2.24 (c), is when the hardness value decreases with increasing strain. This material weakening can occur in different pure metals processed by HPT at room temperature such as pure Pb (99%), Sn (99.9%) and In (99.999%) [113], or different alloys such as Zn-Al and Pb-62% Sn eutectic alloy [114,115]. Notice that the unprocessed condition, 'annealed', is marked by a bar on the vertical axes.

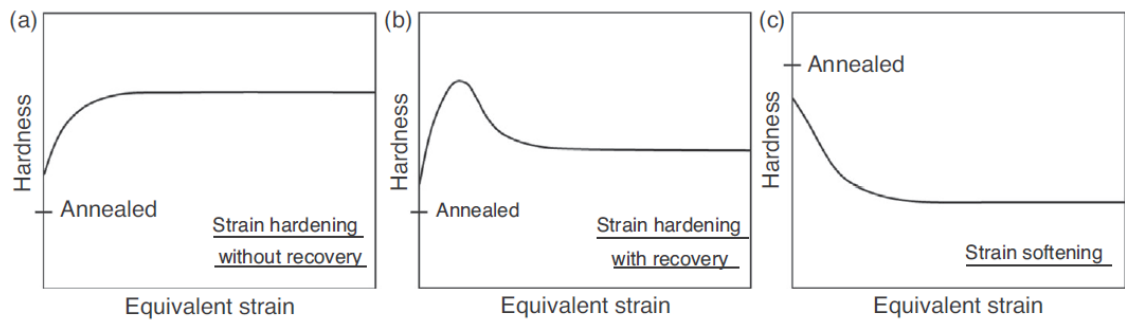


Figure 2. 24 Three types of behaviour of hardness with equivalent strain for materials processed by HPT (a) without recovery; (b) with recovery; & (c) material weakening [116].

To investigate through-thickness hardness homogeneity of a material processed by HPT, an earlier experiment was conducted on many pure aluminium discs of the same thickness at room temperature. The imposed pressure was 6.0 GPa and different numbers of rotations were applied, from 1/4 to 20 turns. The discs were carefully sectioned to upper, centre and lower planes. The Vickers microhardness values show the same measurements for the upper, centre and lower planes, also that there was a steady evolution to homogeneity with all planes [117]. Figure 2.25 shows contour maps of the sectioned discs.

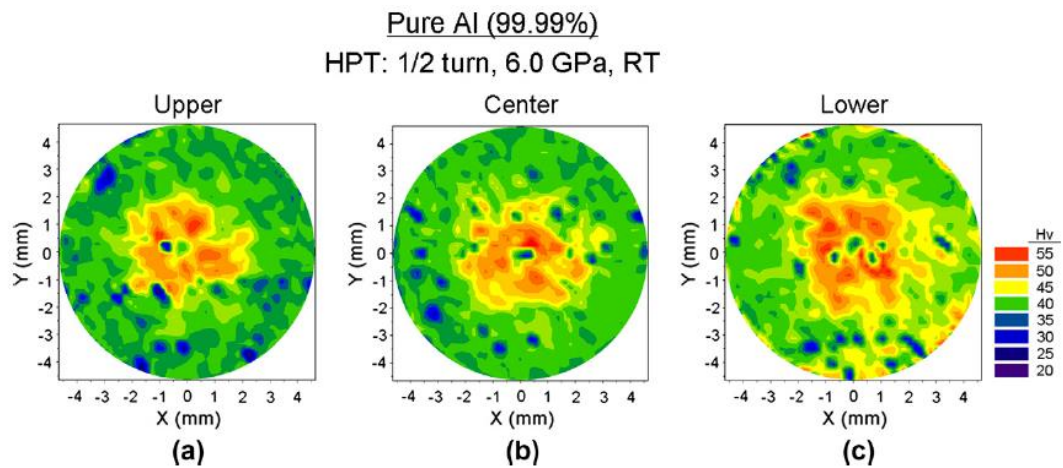


Figure 2. 25 Colour-coded contour maps showing the Vickers' microhardness values distributions in: (a) upper; (b) centre; and (c) lower plane of a pure aluminium disc processed by HPT [117]

Second, an AZ31 magnesium alloy was processed by HPT at elevated temperatures of 463 K using an applied pressure of 6.0 GPa for a number of revolutions up to five turns. The discs were cut vertically along their diameter and examined using an optical microscope and scanning electron microscope. The Vickers microhardness values show

that deformation was not homogeneous throughout the thickness, because of differences in grain size distribution through the disc thickness and the variation in microhardness values in different position [118]. Figure 2.26 shows the variation in microhardness distribution through the thickness of the alloy. There is a pronounced heterogeneity in the axial direction; this is more than the heterogeneity in the radial direction in discs processed for 1/4, 1 and 5 turns.

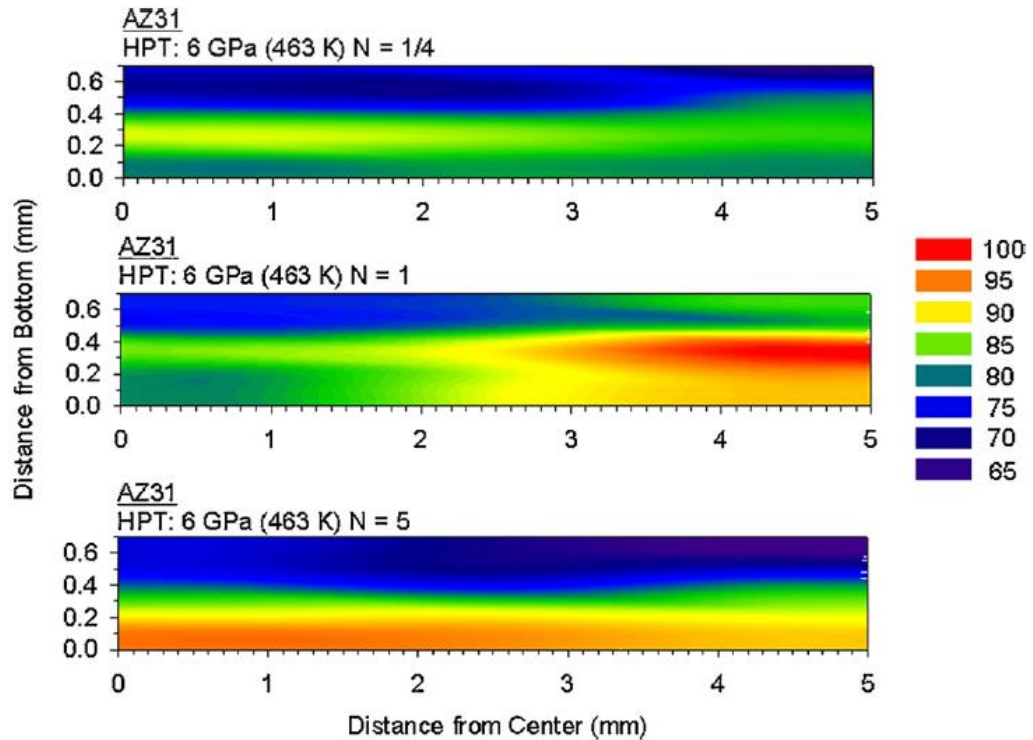


Figure 2. 26 Distribution of microhardness values as a function of location of AZ31 processed by HPT for 1/4 , 1 and 5 turns [118]

2.1.2.9 New approaches in HPT

The very small sample size of the HPT sample disc, with a diameter of ~10 mm and thickness of less than 1 mm, represents an important limitation of the HPT process [6]. To cope with this limitation there have been many attempts to increase the diameter or thickness in many studies [119,120]. A disc of AZ80 magnesium alloy having a diameter of 11 mm and a thickness of 2.5 mm was successfully processed by HPT using pressure of 3.0 GPa for 15 revolutions, the produced microstructure had an average grain size of ~100 nm [119]. Another successful attempt to increase the size of the sample was the processing of Al-Mg-Sc alloy by HPT up to one revolution.; In this case the specimen was a cylinder of diameter 10 mm and thickness 8.57 mm, and the

resultant microstructure had an average grain size of ~ 200 nm [120]. Both samples sizes shown in Figure 2.27.

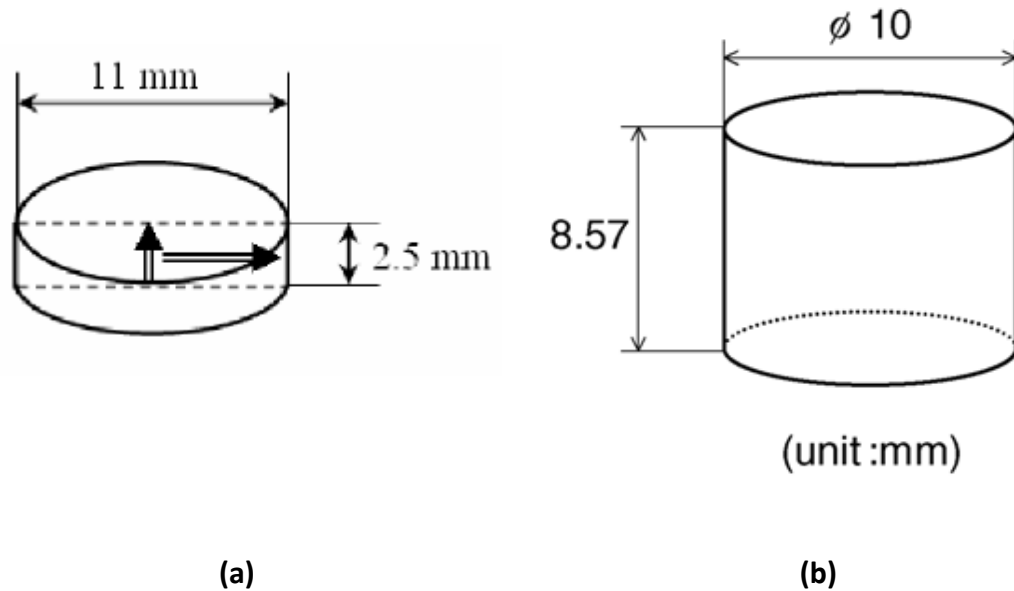


Figure 2. 27 Schematic illustrate: (a) a sample size of a disc of diameter of 11 mm & thickness of 2.5 mm [119]; & (b) a cylinder of diameter of 10 mm & thickness of 8.57 mm [120].

Although increasing the size of the sample was successful, there was greater variation in microhardness values throughout the sample, contrary to the prediction of Equation 2.4 that imposed strain is constant through the disc thickness, and only varies with distance from the disc centre and number of turns.

To overcome the variation in imposed strain at the disc surface during HPT process, an attempt was made by designing a HPT sample in the shape of a ring. Figure 2.28 shows the ring HPT facility. As an alternative to the classic HPT disc, ring samples were processed by HPT and proved to be more effective in obtaining a homogeneous microstructure easily throughout the disc sample [121]. Synthesizing bulk hybrid metals is a new potential for HPT, as a multilayer alloy consisting of two or more commercial metals. In recent study, two discs of commercial Al-1050 alloys and one of ZK60A were piled up in Al/Mg/Al sequence without any chemical or mechanical bonding and processed by conventional HPT at room temperature [122]. The successful mixing of the two commercial metals by HPT will allow the introduction of a new alloy system in the near future.

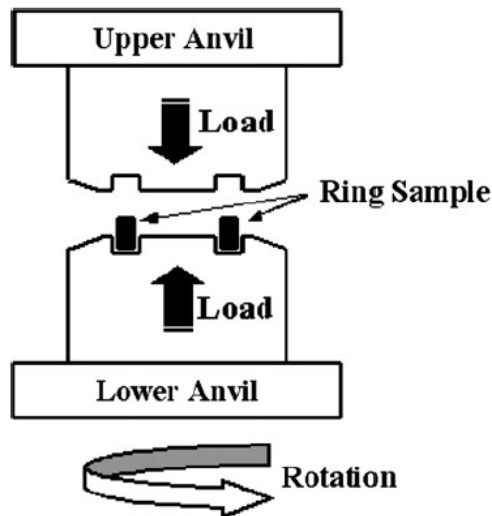


Figure 2. 28 Facility for ring HPT [121]

2.1.2.10 Advantages and disadvantages of HPT

The HPT process has many advantages. It is a simple and fast process, can be applied to a different crystal structure materials and has benefits over ECAP by avoiding the problems associated with processing materials with limited slip systems, or less ductile materials at ambient temperatures [6]. Moreover, HPT can produce a material with a grain size much finer than other SPD processes, such as ECAP [18,123]. Although HPT is limited to very small samples [97], the materials produced by HPT can be used in small electronic devices. However, this restriction does prevent materials from being used in structural applications, despite attempts to scale the sample up [120]. The variation in strain along the diameter of the sample leads to an anticipation of an inhomogeneous microstructure produced by HPT, but many investigations confirm a reasonable homogeneity after five turns of HPT across the disc diameter [15,124].

2.2 Materials processed by SPD

2.2.1 Grain size and strength

The main objective of processing materials using SPD is to increase their strength by reducing their grain size, based on the Hall-Petch relationship (Equation 1.1). Grain size has a major influence on the strength of materials [1,2], and many studies show that reducing grain size to the submicrometer or nanometer scale by SPD will increase the

strength of the material [125]. Reducing the grain size and having a large fraction of high-angle grain boundaries are important features in obtaining advanced and unique properties [16,126].

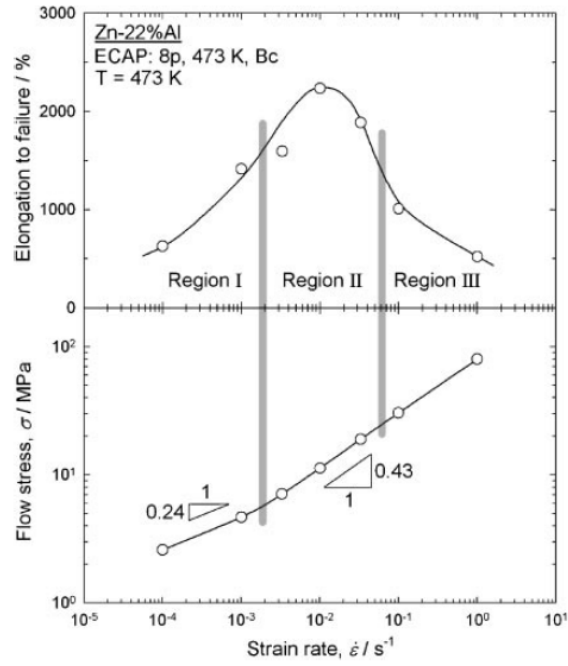
HPT is the most effective SPD procedure to refine the grain size of the bulk material to the nanometer range [6,67]. A high purity nickel (99.99%) was processed by HPT using an applied pressure of 6.0 GPa for 5 revolutions [68]. The results show not only a smaller average grain size but also a lower fraction of low-angle grain boundaries after HPT than the same material processed by ECAP [123]. An Al–3 wt.% Mg–0.2 wt.% Sc alloy and pure copper were processed by HPT using an applied pressure of 6.0 GPa for 5 revolutions [127]. A significant grain refinement was produced by the HPT process for both materials, with an average grain size of ~150 nm and ~140 nm, respectively. The microhardness values measurement increased by a factor of approximately two and three from the initial condition.

The average grain size results from the HPT process are influenced by homologous temperature; the higher the HPT processing temperature, the larger the resultant grain size. AZ91 magnesium alloy was processed by HPT using an applied pressure of 3.0 GPa for up to 10 turns at 296, 423 and 473 K [104]. HPT successfully produced an extensive average of ultra-fine grain size for the three processing temperatures: ~35 nm at room temperature, ~180 nm for 423 K and ~250 nm for 473 K. Another magnesium alloy AZ61 showed the same behaviour. The alloy was processed by HPT using an applied pressure of 3.0 GPa for up to 7 turns, and the resulting average grain sizes were ~110 nm when the alloy was processed at room temperature and ~220 nm when it was processed at 423 K [66].

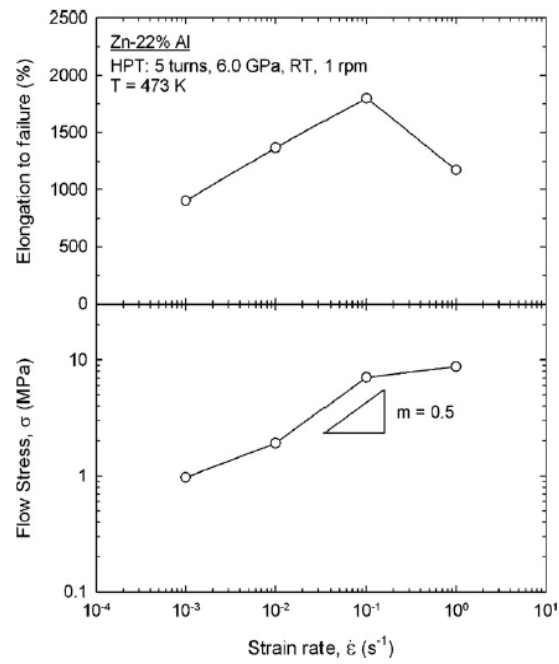
SFE is another factor influencing the resultant average grain size. Materials with low SFE tend to have smaller grain sizes when processed by HPT under the same conditions. Pure copper and a Cu–10% Zn alloy were processed by HPT using an applied pressure of 6.0 GPa for five turns, and the resultant average grain size was smaller in Cu–10% Zn alloy than pure copper, due to the lower SFE of the alloy [100]. The applied pressure in the early stages, the number of turns and the distance to the disc centre are other factors determining the degree of grain refinement [74].

2.2.2 Grain size and superplasticity

Superplasticity is the ability of a material to display a very high tensile elongation to fracture [128], to at least 400% of the original length, with measured strain rate sensitivity close to ~ 0.5 without the development of necking [17]. In order for a material to exhibit superplastic behaviour, it should first have a grain size of less than $10\ \mu\text{m}$. Second, the testing temperature must be above $0.5\ T_m$, where T_m is the absolute melting temperature of a material [128]. Metals undergo strain hardening when pulled in tension at temperatures of less than $0.4\ T_m$, but at elevated temperatures above $0.5\ T_m$ the rate of strain hardening decreases and the metal flows plastically without necking [129]. This steady-state flow promotes the metal exhibiting a superplastic behaviour. The main flow mechanism for achieving superplastic behaviour at elevated temperature is grain boundary sliding (GBS) [130]. In GBS, the elongation of the polycrystalline material comes from the flow of each individual grain over each other without any change in its equiaxed shape during deformation [131]. The strain rate sensitivity, m , can be defined as the slope of a logarithmic plot of the flow stress versus the strain rate [132]. Strain rate sensitivity is an important parameter to determine the main flow mechanism controlling the flow behaviour of the material. The strain rate sensitivity of most metals exhibits a sigmoidal relationship between the flow stress and the strain rate, as shown in Figure 2.29. This behaviour can be divided into three regions: In Regions I and III, the strain rate sensitivity is relatively low ~ 0.2 and the grains of the materials shows an elongated shape along the tensile axis. Here, the materials show a very small elongation, and in Region II, where the strain rate sensitivity ~ 0.5 , the grains retain their equiaxed shape and are not elongated during the tensile test and the material shows excellent elongation. It has been found that the maximum elongation associated with the maximum grain boundary sliding is in Region II, where the strain rate sensitivity is ~ 0.5 . Grain boundary sliding will initiate cavities within the material due to the grain displacement. Moreover, any stress concentration site, such as the triple junction between the grains, can develop a cavity [133] and, to eliminate the cavity development during deformation, grain boundary sliding must operate with an accommodation mechanism [132].



(a)



(b)

Figure 2. 29 Variation of elongation to fracture (upper) and flow stress (lower) versus the strain rate for Zn-22% Al alloy processed by ECAP at (a) [134], and HPT at (b) [135] with a tensile testing temperature of T= 473 K.

The steady-state strain rate, $\dot{\epsilon}$, can be described by the following relationship [132]:

$$\dot{\varepsilon} = A \frac{D.G.b}{k.T} \left(\frac{b}{d} \right)^p \left(\frac{\sigma}{G} \right)^n \quad (2.5)$$

where A is a dimensionless constant, D is the diffusion coefficient, G is the shear modulus at the testing temperature, b is the Burgers vector, k is Boltzmann's constant, T is the absolute temperature, d is the spatial grain size, σ is the applied stress, and p and n are the inverse grain size exponents and the stress exponent, respectively. Equation (2.5) demonstrates the inverse proportion relationship between strain rate and grain size: the smaller the grain size, the faster the strain rate [136]. This means that optimum superplasticity will occur at a faster strain rate [135]. Moreover, a finer-grained metal can have superplastic behaviour at lower temperatures when pulled in tension at a constant rate than its coarse-grained equivalents. It has been found that grain boundary sliding can be enhanced by reducing the grain size, which enhances the ductility of the materials [137]. Many coarse magnesium alloys show reasonable elongation when pulled in tension, while fine-grained magnesium alloy extends this elongation to 47% when pulled in tension at room temperature [138]. The fraction of high-angle grain boundaries (HAGB) has an influence in grain boundary sliding, and it was found that its presence promotes grain boundary sliding, while the presence of low-angle grain boundaries (LAGB) restricts it [139].

The testing temperature is another important factor in superplastic behaviour. The testing temperature should be at least $\sim 0.5 T_m$, and increasing it can enhance the ductility and achieve superplastic behaviour at a higher strain rate. Doing so can lead to grain growth in the material when testing it at slow strain rate, which reduces the elongation and inhibits the material from achieving superplastic behaviour. In materials exhibiting superplastic behaviour, usually a two-phase alloy or material with a second phase, this second phase acts to stabilize the grain and suppress grain growth [140].

Awareness is growing of the wide potential application of superplastic materials in industrial forming and the development of fabricating complex shapes and curved parts, increasing the interest in superplastic materials. Recently, the commercial superplastic forming (SPF) industry has produced complex shapes as metallic parts for many aerospace and automotive applications [141]. This forming of complex parts is usually carried out at slow strain rates within the range of $\sim 10^{-3}$ - 10^{-4} s^{-1} , which extends the

forming time. Reducing the grain size of a material can increase the strain rate to achieve high-strain rate superplasticity (HSRS), which can be defined as superplastic elongation of a materials when drawing in tension at strain rate of 10^{-2} s^{-1} or higher [142]. Complex shapes have been successfully formed using HSRS [20].

Both popular SPD techniques, ECAP and HPT, have successfully produced ultra-fine grained materials exhibiting superplastic behaviour. High-strain rate superplasticity was achieved by processing two commercial aluminium alloys using the ECAP technique for 12 passes. The maximum elongation that the alloy reached when pulled in tension to failure by tensile test was higher than 1000% at a strain rate of $1.0 \times 10^{-2} \text{ s}^{-1}$ [143]. Further, a commercial ZK60 magnesium alloy processed by ECAP has an exceptional record for superplasticity, with elongation of 3050% when subjected to 2 passes and pulled in tension to failure by tensile test at 473 K at slow strain rates of $1.0 \times 10^{-4} \text{ s}^{-1}$ [144]. This is another example of the success of materials processed by ECAP to reach superplasticity. Figure 2.30 shows the elongation of ZK60 magnesium alloy at different numbers of passes [144].

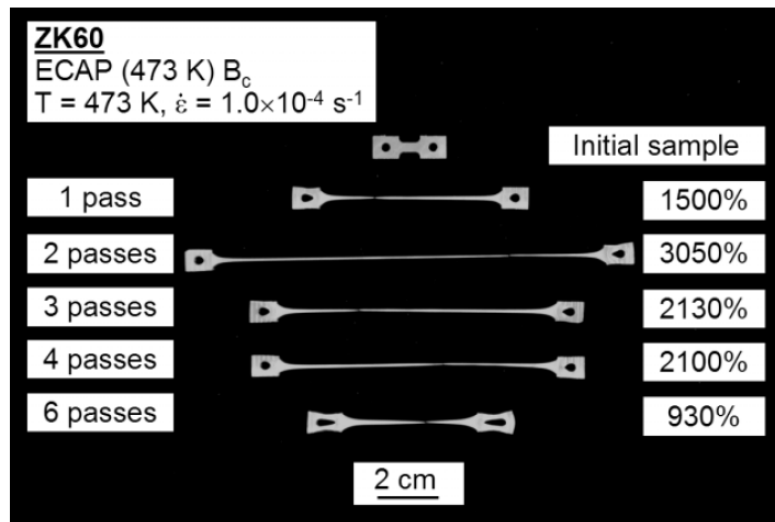


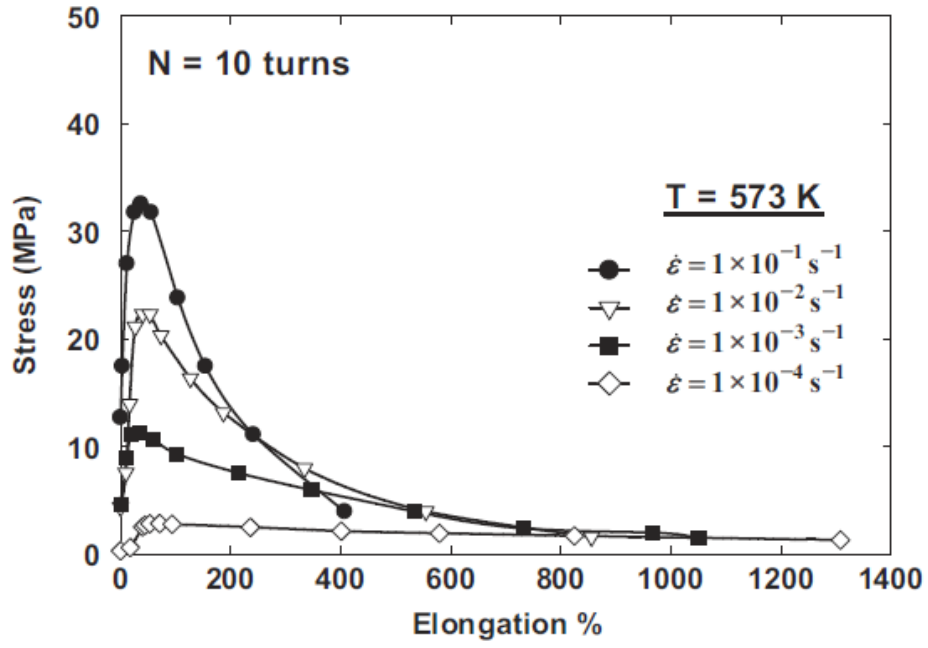
Figure 2. 30 Elongation of specimens of ZK60 processed by ECAP for different number of passes & tested to failure at 473 K. Upper specimen is the untested [144].

In recent years, several studies of materials processed by SPD using HPT technique have demonstrated this superplastic behaviour. A Zn-22% Al alloy shows an

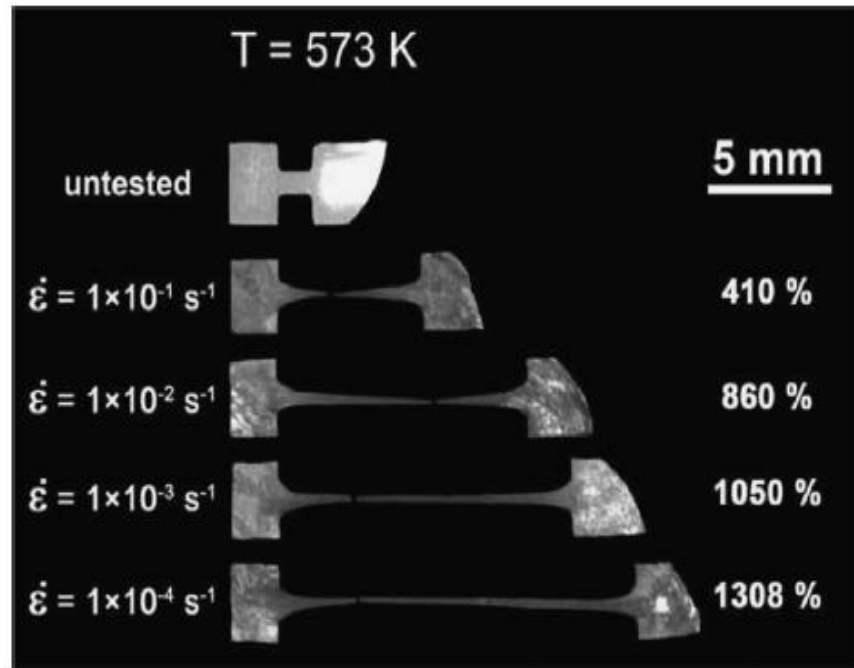
extraordinary superplastic elongation of 1800% when pulled in tension to failure at a temperature of 473 K, using $1.0 \times 10^{-1} \text{ s}^{-1}$ as the strain rate after being processed by HPT at room temperature for five turns [135]. In another study, a Al–33% Cu alloy processed by HPT at room temperature for 10 turns exhibited a maximum elongation of 1250% when at tensile testing temperature of 723 K using a strain rate of $1.0 \times 10^{-4} \text{ s}^{-1}$.

AZ61 magnesium alloy was processed by HPT up to 7 turns using imposed pressure of 3 GPa, at room and elevated temperatures, and the material exhibited superplastic behaviour when pulled in tension, reaching a maximum elongation of 620% [66]. AZ91 is another magnesium alloy processed by HPT that features superplastic elongation. AZ91 was processed by HPT up to 10 turns at room temperature using an applied pressure of 3.0 GPa. The tensile test was conducted at different temperatures and strain rates. The alloy showed good HSRS, with an elongation of 590% at temperatures of 473 K and 860% at temperature of 573 K using $1.0 \times 10^{-2} \text{ s}^{-1}$ as the strain rate, while the maximum elongation of the alloy, 1308%, was achieved using a strain rate of $1.0 \times 10^{-4} \text{ s}^{-1}$ at temperatures of 573 K [145]. Figure 2.31 shows the maximum elongation of AZ91 processed by HPT and pulled in tension to failure at a temperature of 573 K using different strain rates.

As demonstrated previously, the HPT process induces a heterogeneous microstructure in the early stages of deformation. This is due to the induced inhomogeneous strain distribution during the HPT process, where the disc centre has a value of zero strain and the disc periphery has a maximum value of strain, as shown in Equation 2.4. This heterogeneity decreases gradually by raising the imposed strain, by increasing the number of revolutions [9,66,101]. To avoid an area of heterogeneous microstructure in the centre of the disc, the tensile specimen is usually machined away from the HPT disc centre. The central point of tensile specimen is 2 mm from the disc centre, and this allows two specimens from each HPT disc [146] and a more homogenous microstructure.



(a)



(b)

Figure 2. 31 Engineering stress against elongation % curve at (a) & in (b) HPT sample after tension to failure by tensile test. Upper sample is original length before testing. Both (a) and (b) were processed by HPT at 3.0 GPa for 10 turns and tensioned to failure using different strain rates at a temperature of 573 K [145].

2.3 Magnesium and magnesium alloys

2.3.1 Introduction

Magnesium is the lightest structural metal in current use. Because of its low density (1.74 gm/cm^3), compared to aluminium and steel, and its high specific strength (158 kN.m/kg), it has great potential in automotive and aerospace applications where the weight of the structural materials has a major influence on fuel consumption and CO_2 emissions. Table 2.4 shows the weight reduction in kilograms when using magnesium alloys in the automobile industry [147].

Table 2. 4 Percentage weight reduction in using magnesium alloy over other structural metals [147].

	Component							
	Engine block		Gear box + clutch housing (Al alloy)	Oil pan (Al alloy)	Four wheels		Engine cradle	
	Cast iron	Al alloy			Steel	Al alloy	Steel	Al alloy
Traditional solution (kg)	32	23.5	21.5 + 5	3	36	23	25	17.5
Magnesium alloy solution (kg)		19	15 + 3	2	18	18	15	15
Weight reduction (kg)	13	4.5	6.5	1	18	5	10	2.5
Weight reduction (%)	40	19	30	33	50	22.5	40	30

Moreover, magnesium alloys have dimensional stability, excellent sound damping, electromagnetic interference shielding, machinability, are recyclable without environmental pollution and are low-cost. Magnesium can be alloyed with many elements through solid solution [148]. Those features make it suitable for different applications in electrical and electronic portable devices. However, magnesium has an HCP structure, which indicates poor workability and low ductility at room temperature due to the limited slip systems [149]. In HCP crystal structure materials, deformation at room temperature can be achieved by two dominant mechanisms: slip in the basal plane and mechanical twinning [148,149]. A slip system can be defined as a combination of slip plane and slip direction, where the slip plane is the plane with the greatest atomic density and the slip direction is the direction that is closest-packed in that plane [96]. Slip starts when the applied shearing stress on the slip plane in the slip direction exceeds the critical resolved shear stress (CRSS).

Due to the large differences in CRSS in the basal plane slip, twinning has a lower value and the non-basal plane slip system has higher values [150]. Basal slip and mechanical

twinning are the primary deformation mechanisms in magnesium and magnesium alloy at room temperature. There are only three slip systems at room temperature in the basal plane in magnesium alloy, only two of which are independent [151]. Table 2.5 shows the number of slip systems for FCC, BCC and HCP metals [92]:

Table 2. 5 Slip plane, direction, and system for many metals [92].

<i>Metals</i>	<i>Slip Plane</i>	<i>Slip Direction</i>	<i>Number of Slip Systems</i>
Face-Centered Cubic			
Cu, Al, Ni, Ag, Au	{111}	$\langle 1\bar{1}0 \rangle$	12
Body-Centered Cubic			
α -Fe, W, Mo	{110}	$\langle \bar{1}11 \rangle$	12
α -Fe, W	{211}	$\langle \bar{1}11 \rangle$	12
α -Fe, K	{321}	$\langle \bar{1}11 \rangle$	24
Hexagonal Close-Packed			
Cd, Zn, Mg, Ti, Be	{0001}	$\langle 11\bar{2}0 \rangle$	3
Ti, Mg, Zr	{10 $\bar{1}0$ }	$\langle 11\bar{2}0 \rangle$	3
Ti, Mg	{10 $\bar{1}1$ }	$\langle 11\bar{2}0 \rangle$	6

In polycrystalline materials, at least five independent slip systems are required to achieve homogenous deformation and avoid materials failure, according to von Mises criterion [152]. Since material having a HCP structure such as magnesium alloy has three slip systems in the basal plane, of which two are independent, this limited slip system results in brittleness and a lack of ductility, and these materials are considered to be hard-to-work materials. Because of that, a homogenous deformation at room temperature without producing cracks is hard to achieve.

Twinning is an important deformation mechanism in HCP materials, such as magnesium and magnesium alloy, at ambient temperatures. When atoms are located in a mirror-image position of an atom on the other side of a plane because of the applied shear force, twinning occur [92]. When slip systems are restricted or when the stress for twinning is lower than critical resolved shear stress for slip, twinning also occurs. Furthermore, twinning occurs at low processing temperatures or a high strain rate in HCP materials, the later called mechanical twins [96], and there is a second type of twinning as a result of the annealing process in FCC metals and alloys, known as annealing twinning [92]. Figure 2.32 demonstrates the slip systems in HCP metals [153]. As it shown in Figure 2.32, a and c represent the short and the long unit cell dimensions, the ideal ratio c/a for HCP structure is 1.633, however there are many HCP

materials that have different c/a ratio value than the ideal [92]. Magnesium has a c/a ratio of 1.624 which is lower than the ideal value [154], this value can effect which twinning mode is activated in HCP metals, if the c/a value is larger than 1.732 a compression twinning will appear , but if c/a value is lower than 1.732 a tension twinning will appear [155].

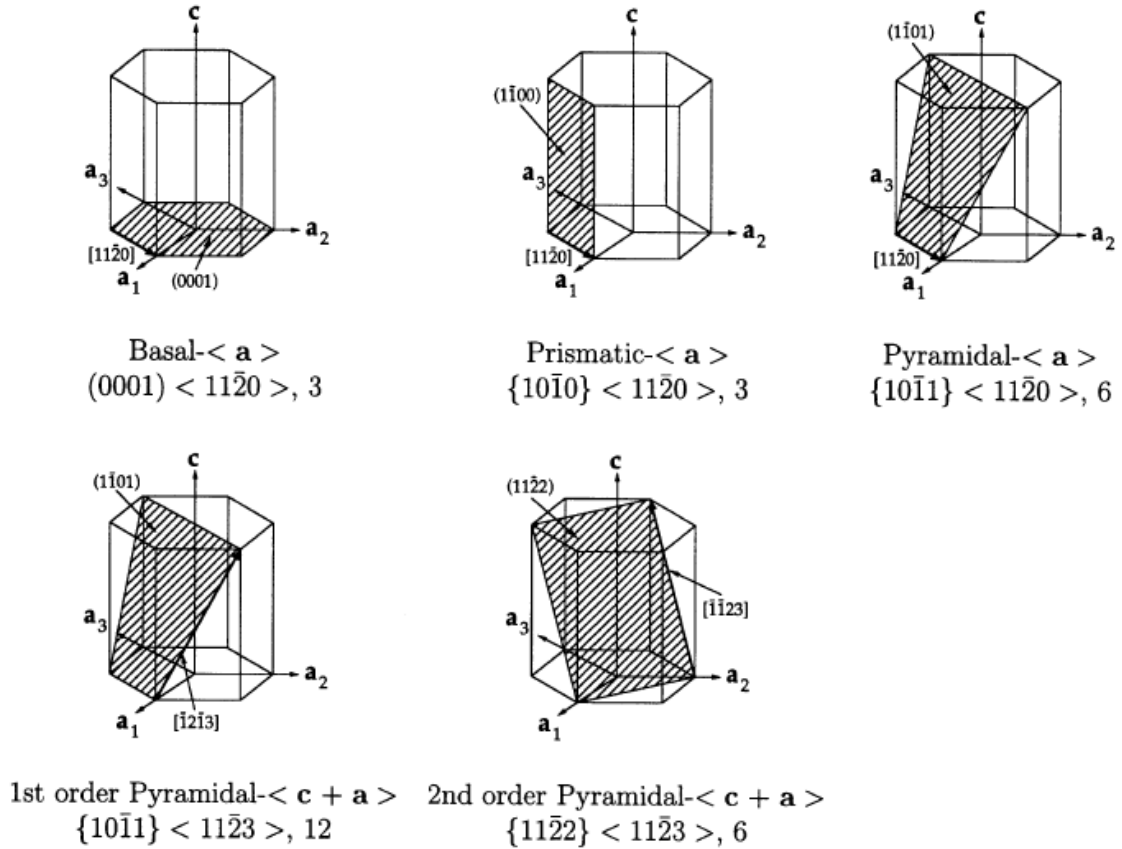


Figure 2. 32 Slip systems in HCP materials [153].

The activation of the non-basal slip systems in magnesium alloy can help in homogenous deforming of the material and producing a finer grain. The activation of pyramidal slip systems can provide five independent deformation modes and fulfill von Mises criteria. Processing magnesium alloy by SPD can activate the non-basal slip systems. AZ31 magnesium alloy was processed by ECAP with and without back pressure, and back pressure was used to produce a hydrostatic pressure on the sample. The results show that finer grains were produced after one pass when using back pressure and an expansion of a non-basal slip systems dislocation within the sample,

which points to the influence of using hydrostatic pressure in the activation of the non-basal slip systems [89].

Temperature is another factor that activates the non-basal slip systems and increases the ductility of magnesium. New slip systems are activated when magnesium is deformed at elevated temperatures $\sim 225\text{ }^{\circ}\text{C}$ [156]. At ambient temperatures, the CRSS for basal slip system in magnesium single crystal is lower by 100 times than the non-basal slip systems [157], so deformation is limited to basal slip system and twinning mode. By increasing the processing temperature above $200\text{ }^{\circ}\text{C}$, the CRSS for non-basal slip systems decreases and it becomes more favourable to deformation than twinning [158].

2.3.2 Effect of alloying elements

Magnesium alloy can be classified into five basic systems, depending on the main alloying element: aluminium; manganese; zinc; zirconium; or rare earth. Magnesium's mechanical properties vary with the alloying element; aluminium is the most important element for alloying with magnesium. Some 12.7 wt% is the maximum solid solubility of aluminium in magnesium, as shown in the Mg-Al phase diagram in Figure 2.33. Adding aluminium to magnesium forms an eutectic system at $437\text{ }^{\circ}\text{C}$ [148]. Moreover, the addition of aluminium will form the intermetallic β phase $\text{Mg}_{17}\text{Al}_{12}$, which has a high aluminium content of 43 wt%. This β phase increases the tensile strength of the alloy and reduces its ductility. While the matrix α phase is the HCP structure, the intermetallic β phase has a BCC structure [159] and is usually distributed as a network separated at the grain boundaries. The melting temperature of the β phase is 710 K [160]. This phase is stable when the alloy is deformed at temperatures of up to 573 K but, when increasing the deformation temperature to 673 K, it will start to dissolve partially. Increasing the aluminium content in the alloy will increase the fraction of β phase $\text{Mg}_{17}\text{Al}_{12}$ [161]. Moreover, increasing the aluminium content in the magnesium will lower the SFE value. Table 2.6 shows the SFE for pure magnesium and different magnesium aluminium alloys. The addition of zinc will also increase tensile strength, and the same will occur by adding manganese, which also enhances corrosion resistance, while the addition of zirconium increases tensile strength without decreasing ductility [148].

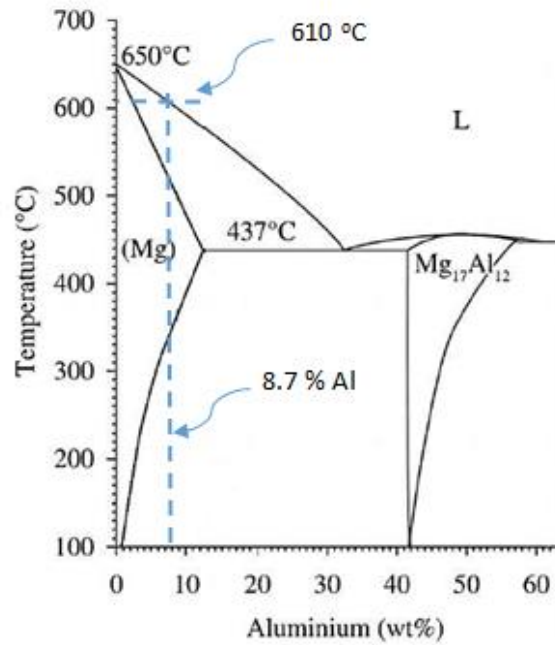


Figure 2. 33 Part of the Mg-Al phase diagram showing the aluminium content and the melting point of AZ80 magnesium alloy [162].

Table 2. 6 Values of stacking fault energies of pure magnesium and different AZ series magnesium alloys.

Materials	Stacking Fault Energy (mJ/m ²)
Pure magnesium	125 [98]
Mg-3wt.% Al	27 [163]
Mg-6wt.% Al	16 [163]
Mg-9wt.% Al	6 [163]

2.3.3 Wrought alloy

There is a further classification of magnesium alloy by the alloy processing type: low pressure die casting; high pressure die casting; and wrought [164]. Wrought alloys are considered to display the lowest workability of magnesium alloys at room temperature, yet have the greatest strength. In this category, the magnesium–aluminium system is the most important in alloys such as AZ31, AZ61, AZ80 and AZ91. Table 2.7 gives the values of yield strength, tensile strength and elongation to failure of different magnesium wrought alloys.

Table 2. 7 Mechanical properties of different AZ series magnesium alloys [165].

Alloy	0.2%-Yield Strength [MPa]	Tensile Strength [MPa]	Fracture Elongation [%]
AZ31	193	262	14
AZ61	228	317	17
AZ80	276	379	7

2.3.4 Processing magnesium alloys by ECAP

As mentioned earlier, processing magnesium alloys by ECAP can produce UFG. Different magnesium alloys such as AZ31 (Mg-3% Al-1% Zr), AZ91 (Mg-9% Al-1% Zn) and ZK60 (Mg-5.5% Zn-0.5% Zr) were processed by ECAP under different conditions: number of passes; different angles; and different temperatures. It is difficult to process magnesium alloy by ECAP at ambient temperatures because of the lack of ductility, due to limited slip systems, and this will cause cracks and segmentations in the billets [166]. Based on previous investigations, there are effective procedures to prevent these from developing, including reducing the strain induced in each pass by using a die with an angle larger than 90° [50,59], increasing the temperature during the process to activate non-basal slip systems [166,167], imposing back pressure to activate non-basal slip systems and improve the workability [31,89,168], and applying an earlier process than ECAP, such as extrusion, termed EX-ECAP. To study the nature of grain

refinement in HCP materials processed by ECAP, AZ31 and ZK60 magnesium alloys billets were pressed as HCP metal representatives by ECAP at 473 K. Due to limited slip systems and the processing temperature in the recrystallization range of magnesium alloy [169], the grain refinement will be based on the dynamic recrystallization principle, by which the formation of the newly recrystallized grains occurs adjacent to existing grain boundaries [41]. The resultant microstructure can vary, even if the same alloy is processed under the same conditions. In this experiment, ZK60 magnesium alloy formed two different models of microstructures. The first resultant microstructure was a homogenous UFG distribution, and the second had a bi-modal grain distribution Figures 2.34 and 2.35 [170]. Formation of these models depends on the grain structure before ECAP, the size of the newly formed grains after one pass of ECAP [169]. Several studies have shown that processing magnesium alloys by ECAP can enhance mechanical properties such as strength and ductility [54,171,172].

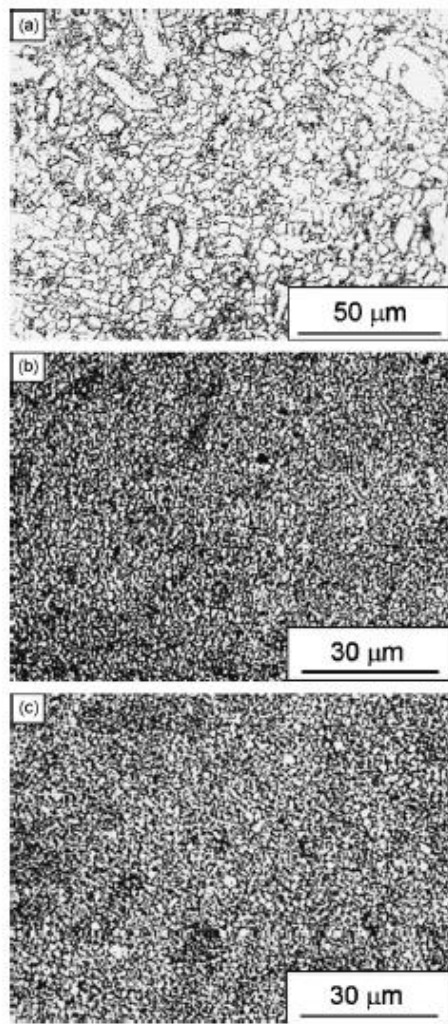


Figure 2. 34 Structure evolution of extruded ZK60 alloy processed by ECAP using a die with an 90° angle (a) before ECAP, (b) after 2 passes and (c) after 6 passes [170].

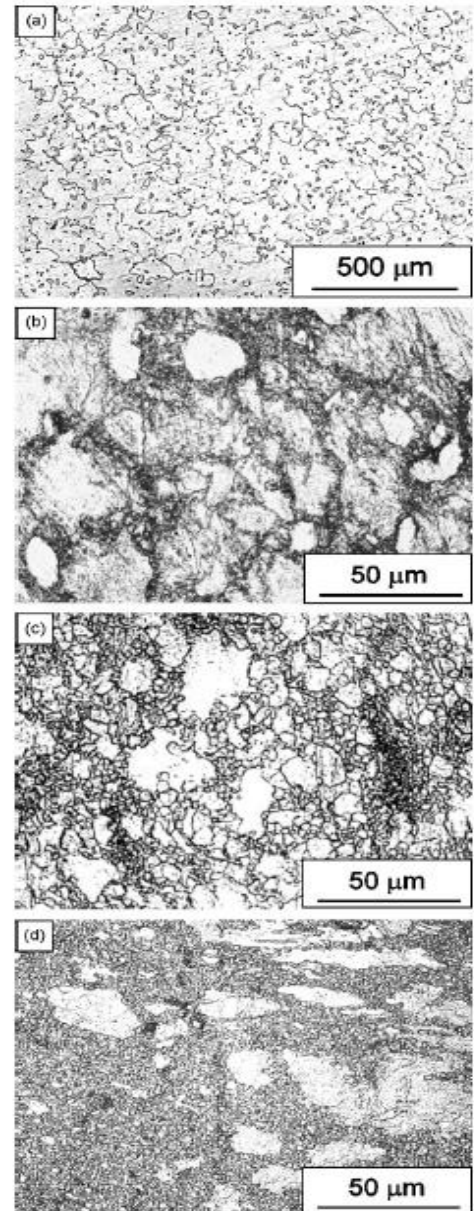


Figure 2. 35 Structure evolution of annealed ZK60 alloy processed by ECAP using a die with an 110° angle: (a) before; (b) after 1 pass; (c) after 4 passes; & (d) after 6 passes [170].

2.3.5 Processing magnesium alloy by HPT

Magnesium can be processed easily by HPT at room temperature without developing segmentation or cracking under the imposition of high hydrostatic pressure [15]. Because of the intensive pressure, applied by the pressing up to several GPa, and the geometry of the anvil, HPT shows more singularity to process magnesium alloy at room temperature than ECAP. An earlier experiment showed that an as-cast sample prepared from Mg-9% Al alloy was catastrophically broken after a single pass of the ECAP process at 473 K, however it was possible to process the material for two passes without visible cracking when it was in the extruded condition [173]. In other study, an alloy of Mg-9% Al prepared from high purity Mg and Al was processed successfully by HPT at room temperature and at a temperature of 423 K in both the extruded and as-cast condition [14], due to the imposition of compressive pressure during HPT process that protects the alloy from cracking [174]. Processing magnesium alloy by HPT at room temperature can produce substantial grain refinement, to the submicrometer or nanometer range [14,119], while increasing the processing temperature can lead to grain growth and produce larger grains [15].

To study the influence of different process temperatures and the imposed strain through number of rotations on the homogeneity and strength of magnesium alloys, an experiment conducted on AZ31 at 296, 373, 473 K shows that processing at 296 and 373 K forms a bi-modal structure at the centre and half radius of the discs. At the edges, the proportion of coarse grains was much lower and the size of the coarser grains was smaller. Increasing the number of turns decreases the average grain size at the centre and the half radius of the disc.

Increasing the processing temperature to 473 K forms a heterogeneous structure after one turn, with coarse grains at the centre of the disc. These become larger in size when moving up to five turns, so increasing the number of turns increases the average grain size of the centre, the half radius and the edge of the disc, as shown in Figures 2.36 and 2.37. The increase in grain size was attributed to the occurrence of grain growth at this temperature [15]: the longer that the samples are subjected to the elevated temperature during the process, the larger the grains grow, thus the grain size becomes larger after five turns than one turn at this temperature. As grain size increases with increasing process temperature, the microhardness values recorded after processing at 473 K for

one turn and five turns were the lowest among the three processed temperatures. In fact, the microhardness values after five turns of HPT process were lower than after one turn of the HPT process.

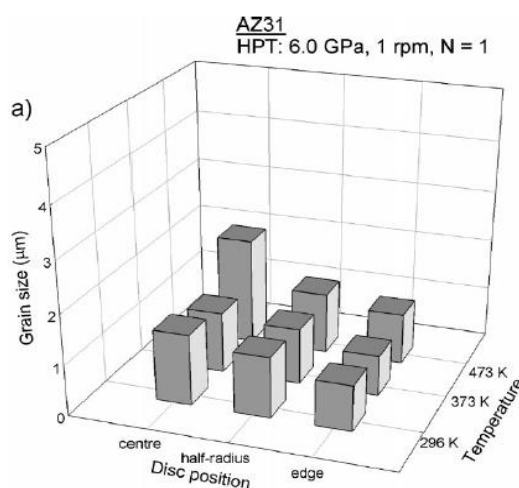


Figure 2. 36 Differences in grain size when processing Mg alloy AZ31 by HPT at different temperatures through 1 turn [15].

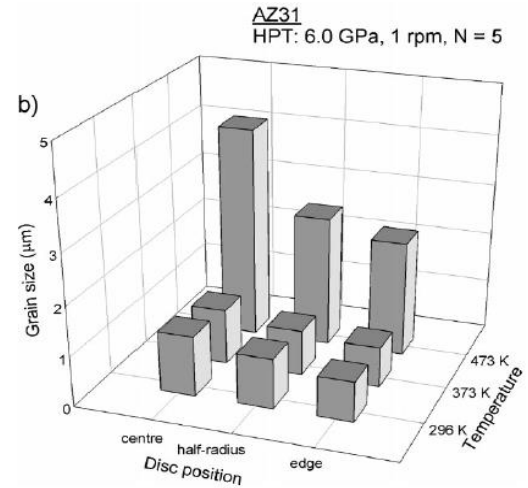


Figure 2. 37 Differences in grain size when processing Mg alloy AZ31 by HPT at different temperatures through 5 turns [15].

In recent years, investigations have been undertaken to investigate the homogeneity of magnesium alloys processed by HPT throughout the disc thickness. The results of these investigations verify that the deformation of magnesium alloy processed by HPT is not homogeneous through the thickness. This heterogeneity is confirmed by many observations such as variation in grain size, variation in microhardness values and the presence of shear bands through the disc thickness [102,118]. Figure 2.38 represents a colour map of microhardness distribution as a function of distance from bottom to top, through the thickness of half a disc of an AZ31 alloy processed by HPT.

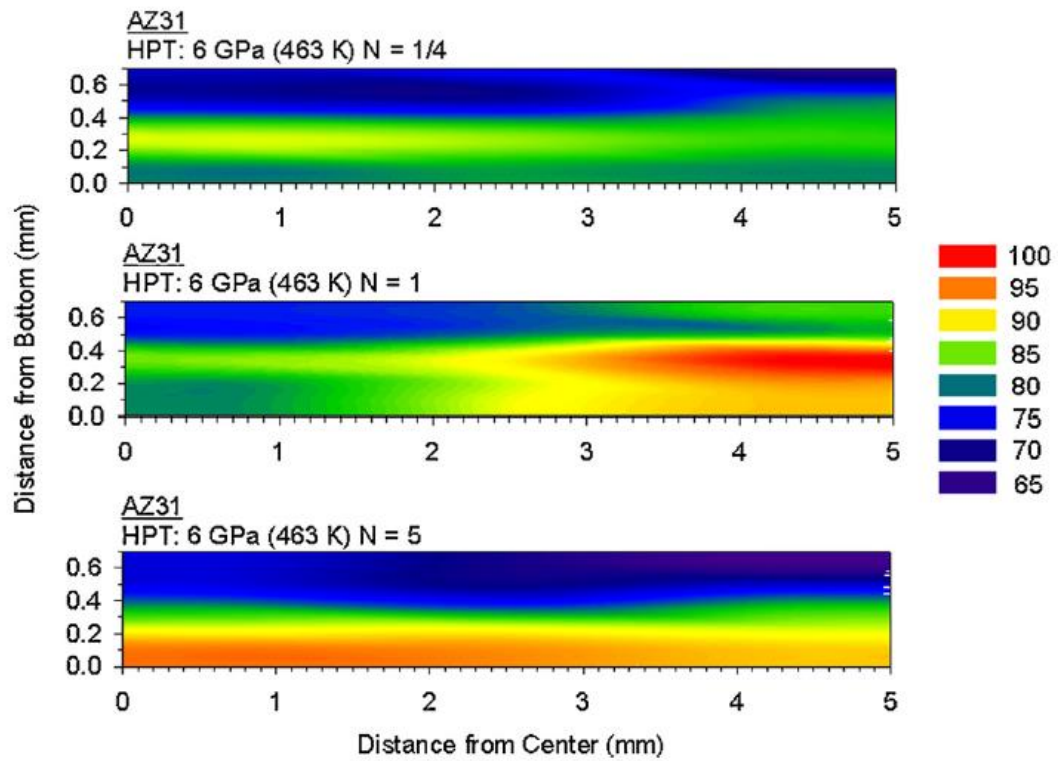


Figure 2. 38 Distribution of microhardness value along the half- cross section of AZ31 processed by HPT at temperature 463 K by N=1/4 upper, N=1 centre, N=5 lower [118]

2.3.6 AZ80 Magnesium alloy

In the group of Mg-Al-Zn wrought magnesium alloy, AZ80 has the highest tensile strength in this category, with a value of 380 MPa [175]. Because of its light weight, good corrosion resistance, comparatively low price and good mechanical properties, AZ80 is widely used as a structural material. For example, in the automobile industry it is one of the best choices for electric bus frameworks and as an alternative for ZK60 magnesium alloy [176–178] wheels in car racing. Aluminium is the main alloying element in the AZ80 magnesium alloy, and the composition of the alloy is Mg-8.7%wt Al-0.51%wt Zn-0.18%wt Mn. AZ80 magnesium alloy mainly comprises two phases: the α -Mg matrix solid solution phase and the β phase that is rich in aluminium.

Although AZ80 is a widely known magnesium alloy, there is still a lack of information on it as a material processed by SPD, especially ECAP and HPT. To date, few papers have been published about AZ80 processed by ECAP, and fewer by HPT.

Few ECAP experiments have been conducted on AZ80 to reduce grain size. One used a back pressure equal-channel angular pressing (BP-ECAP) [61], where the AZ80 magnesium alloy was pressed for 4 passes through a die with an internal channel angle $\Phi = 90^\circ$ and outer curvature angle $\Psi \sim 30^\circ$ using 100 MPa back pressure and two different routes, A and B_c, at 150 °C and 200 °C respectively. The results show that the average grain size was much smaller than when processing the same alloy without back pressure; furthermore, back pressure improved the AZ80 magnesium alloy's formability.

In another experiment, a combination of ECAP processing using different passes and temperatures, followed by an ageing treatment, was used to strengthen AZ80 magnesium alloy [179]. In this experiment, the best strengthening conditions for AZ80 were found by combining the ECAP process for 8 passes at 633 K, followed by an ageing treatment at 423 K.

The HPT experiment was conducted to evaluate the microstructure and mechanical properties of an AZ80 magnesium alloy [119]. In this experiment, the AZ80 extruded rod was solution heat treated for 11 hours at 400 °C, then water quenched before the HPT process. Then the rod of AZ80 of diameter of 11 mm was sliced into discs 2.5 mm thick. The experiment was conducted at room temperature using an applied pressure of 3.0 GPa for 0, 1, 3, 10 and 15 revolutions. The results show the evolution from coarser to finer grains at the edge of the disc at a lower number of turns in the HPT process. Increasing the number of turns spread the evolution towards the disc centre, and the structure became more homogenous, with a grain size in the nanometer range. The resultant grain size was ~50 nm after 15 turns in some parts of the disc, while the average grain size was ~100 nm. Figure 2.39 shows the evolution of microstructure with increasing numbers of turns. The measured hardness values in this experiment were interesting, as they showed no variation between the centre and the edge of the disc at any number of revolutions. Two explanations are proposed for this result: either that the indentation size was large and covered many fine grains; or that maximum hardness was

reached after one revolution. Figure 2.40 shows the microhardness at different numbers of revolution as a function of distance from the disc centre.

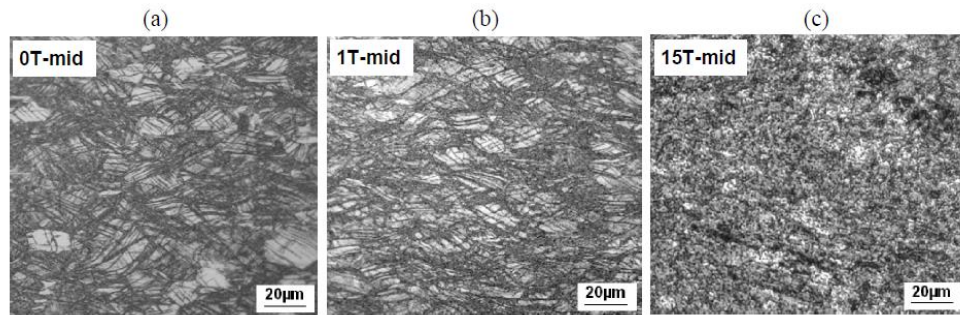


Figure 2. 39 Microstructure evolution at disc centre of AZ80 processed HPT at room temperature using 3.0 GPa applied pressure for: (a) 0; (b) 1; & (c) 15 turns [119].

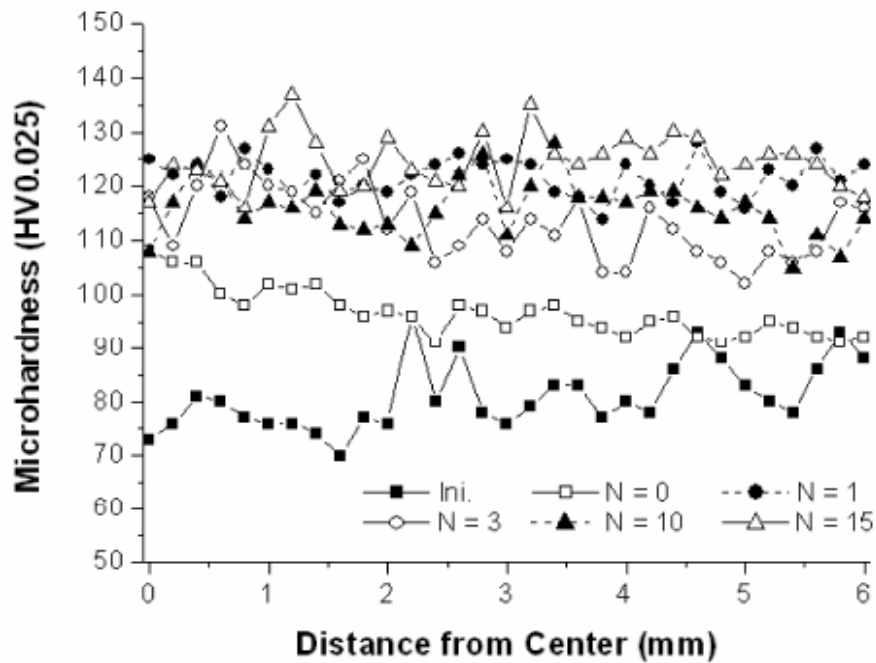


Figure 2. 40 Microhardness at different numbers of turns as a function of distance from disc centre [119].

2.4 Literature review summary

In summary, in recent years many magnesium alloys have been investigated through the two main SPD techniques of ECAP (ZK60 [50,170,180], AZ31 [31,169] and AZ80

[175]) and HPT (ZK60 [19,86,109], AZ31[9,15,181] and AZ80 [119]). These investigations included microstructure and microhardness evolution along the disc diameter. Few have gone further than that to investigate the microstructure and microhardness evolution through the disc thickness AZ31[118] and AZ91[102]. Due to the importance to industry of the superplastic behaviour of alloys, the tensile properties and superplasticity have been a part of these investigations, such as Mg-9% Al alloy [173], AZ91 [182] and AZ31 [183] in ECAP, and Mg-9%Al alloy [184] Mg-Li alloy with 8 wt% [185] and AZ91 [145] in HPT.

The lack of information about AZ80 magnesium alloy processed by HPT was the main motivation for this study. Only one published paper, to the author's knowledge, has described the behaviour of AZ80 processed by HPT at room temperature [119]. In that report, AZ80 was heat treated prior to the HPT process to avoid the initiation of cracks. This study is the first to describe the AZ80 processed by HPT at room temperature without a prior process, and the first to study the evolution of microstructure and microhardness through the disc thickness. In another part of this study, AZ80 was processed by HPT at an elevated temperature (473 K) for the first time, followed by investigation of the evolution of microstructure and microhardness of AZ80 along the diameter of the disc and through the disc thickness. Basically, it is a study of the microstructural and microhardness evolution of an AZ80 over a wide range of HPT processing temperatures.

In earlier investigations of the tensile properties and superplasticity potential of AZ80 magnesium alloy, two extruded coarse-grained alloys showed a maximum elongation of 239% and 246% when pulled in tension to failure [186,187]. To the author's knowledge, no study has reported superplastic behaviour in AZ80 magnesium alloy exceeding 400%, nor described elongation in ultra-fine grained AZ80 magnesium alloy processed by HPT. In this study, discs of AZ80 magnesium alloy with an initial grain size of $\sim 25\ \mu\text{m}$ were processed by HPT at room temperature, which resulted in an extensive reduction in the average grain size. Samples processed by HPT were subsequently pulled in tension to failure at different temperatures and strain rates, and the elongation exceeded 400% for the first time. As a result, the superplastic behaviour of AZ80 magnesium alloy was confirmed.

3 Experimental Material and Procedures

3.1 Material

The study was conducted using a commercial AZ80 magnesium alloy. The chemical composition of the material is listed in Table 3.1. AZ80 magnesium alloy was supplied by Magnesium Electron Ltd (Swinton, Manchester, UK) in the form of long 1000 mm extruded rods of 9.6 mm diameter.

Table 3. 1 Chemical composition of AZ80 magnesium alloy (mass fraction %)

	Al	Cu	Fe	Mn	Ni	Si	Zn	TO
AZ80	8.7	<0.001	0.005	0.18	0.0005	0.02	0.51	<0.30
TO = total others								

Using an abrasive cutting wheel, the AZ80 magnesium alloy rods were sliced into discs of ~1.5 mm thickness. Water was used to minimize thermal damage to the rod during the process. The discs were ground from both sides of the disc using SiC P800 (21.8 μm) abrasive paper to a required final uniform thicknesses of ~0.85 mm, so that the strained layer resulting from the cutting process was removed.

3.2 HPT processing at room temperature and high temperature

The AZ80 magnesium alloy discs were processed by HPT at room temperature (296 K) and at elevated temperature (473 K) under quasi-constrained conditions, as shown in Figure 2.9. The disc, with a diameter of 9.6 mm and a thickness of 0.85 mm, was placed in the shallow lower anvil cavity. The depth of each cavity in the upper and lower anvils is 0.25 mm, creating a small gap that allowed a limited outflow of material between the two anvils during the HPT procedure. Intense care was taken to mark the upper and lower surfaces of the discs before starting the process to check whether slippage was present. Cleaning of the cavity of the anvils using ethanol was carried out before and after each step of the process.

To compare the microstructural and microhardness evolution of AZ80 at high temperature to that at room temperature, samples of AZ80 were processed by HPT at 473 K using a small furnace placed around the upper and lower anvils, as shown in Figure 3.1. The temperature of the process was measured continuously through a thermocouple positioned in the upper anvil. The required temperature ($\pm 5\text{ }^{\circ}\text{C}$) was held for 10 minutes before HPT processing, while a sample was placed in the lower cavity to achieve homogenous temperature distribution between the anvils and the samples.

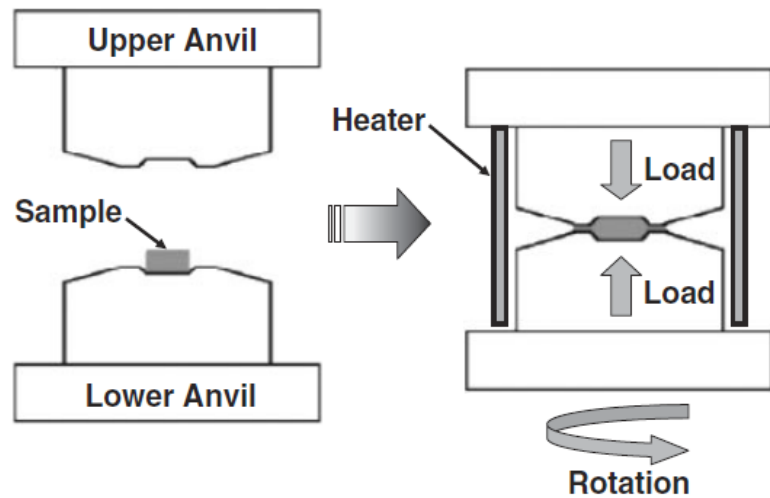


Figure 3. 1 Schematic illustration of the heating elements around the upper and lower anvils of HPT facility [66].

Under conditions of both room and elevated temperature, samples with different numbers of turns, N , namely 1/4, 1, 3, 5 and 10, were processed under an imposed pressure of 6.0 GPa at a speed of 1 rotation per minute. Samples labeled $N = 0$ are those which were subjected to hydrostatic compression pressure for one minute without torsion for any number of turns.

The applied pressure of 6.0 GPa was calculated using a conversion to change the applied load of HPT facility, as follows:

The applied load of the facility = 48 tonnes (48000 kg)

The area of the anvil cavity $A = \pi r^2$

To convert the kilograms to Newton's, then calculate the applied pressure:

$$\text{Applied Force} = \frac{48000 \text{ kg}}{0.102 \frac{\text{kg}}{\text{N}}} = 470588.2 \text{ N}$$

$$A = \pi r^2 = \pi \times (0.005)^2 = 7.854 \times 10^{-5} \text{ m}^2 = 7.854 \times 10^{-5} \text{ m}^2$$

$$\text{Pressure} = \frac{\text{Force}}{\text{Area}} = \frac{470588.2 \text{ N}}{7.854 \times 10^{-5} \text{ m}^2} = 6 \times 10^9 \frac{\text{N}}{\text{m}^2} = 6.0 \text{ GPa}$$

3.3 Sample preparations for microstructure observations.

Four discs were selected to examine the as-received condition prior to processing by HPT. The first disc was taken to measure the average Vickers microhardness (Hv) value, the second to determine the average grain size of the as-received condition using OM and SEM, the third was cut through the middle to examine the microstructure through the disc thickness and the fourth was examined by SEM to determine the α matrix and the distribution of the β phase (precipitates).

3.3.1 Mounting

After HPT processing, three selected discs with one, 3 and 10 turns were sectioned vertically to investigate the evolution of microstructure and hardness through the discs' thickness, and the rest were kept for surface investigation. Processed discs were mounted for easy handling using a cold mounting technique, Struers EpoFix Kit (resin + hardener). This technique was used because it generates little heat during polymerization. The ratio of the resin to the mixture is 25/28 and the ratio of hardener to the mixture is 3/28 parts per weight respectively. The mixture was blended for 3 minutes by hand. The moulds were sprayed with separation spray, for easy removal of the mounted material, then the mixture was poured in. The sample was left for 48 hours to solidify completely.

3.3.2 Grinding

The matrix and precipitate phases in magnesium alloy have two different hardness values [188]. Because of this, magnesium alloy is among the most difficult alloys to prepare for microstructural examination. Intense care must be taken when preparing a sample of magnesium alloy. Magnesium dust has the potential to ignite during grinding, causing a fire hazard, therefore water was used as a cooling fluid [164]. The samples were ground by SiC abrasive papers starting with P800 (21.8 μm), then with P1200 (15.3 μm) and finally with P4000 (5 μm). The grinding time and grinding wheel rotation speed need not be the same at each step and depend on the condition of the scratches on the surface. The grinding time can vary from one to two minutes and the rotation wheel speed between 70 rpm and 150 rpm. It is important to detect the sample surface after each step by eye or optical microscopy to ensure scratch reduction.

3.3.3 Polishing

Polishing is the second step of sample preparation and it is best to avoid water during this stage. Using an oil-based diamond lubricant as a coolant, initial polishing may be performed using a short-nap fibre pad with a diamond paste of 1 μm . For final polishing, a black napless porous synthetic cloth is used with an aqueous suspension of polishing alumina without any lubricant. Like grinding, the polishing time and rotation speed of the wheel depend on the final surface condition. The final surface must be mirror-like. Because of the difficulty in preparing magnesium alloy, it is preferable to use one's hands rather than grinding and polishing machines.

3.3.4 Etching

The final step before examining the material by optical microscopy and scanning electron microscopy is etching. The etchant used with AZ80 magnesium alloy is acetic glycol. The chemical composition of this etchant is 20 ml acetic acid, 1 ml HNO_3 , 60 ml ethylene glycol and 19 ml H_2O . Before etching and after final polishing, the sample should be cleaned with a solvent such as methanol or ethanol: because of magnesium's high reactivity, during etching it is best to avoid water [164]. Then, the sample is wiped with etchant for 3 to 5 seconds, then cleaned again with methanol or ethanol. Finally, the sample surface should be dried using a compressed air. It is now ready for the

optical microscopy test. It is preferable to keep the surface polished and smooth to reduce visual errors when making the Vickers microhardness readings.

3.3.5 Sample preparations for microstructure observations by Transmission Electron Microscope

TEM samples were prepared from half-radius position of HPT disc samples. The discs' thickness was reduced to 0.12 mm and four foils of a diameter of 3 mm were punched out using a special punch. The centres of these discs were 3 mm from the centre of the parent disc, as illustrated in Figure 3.2.

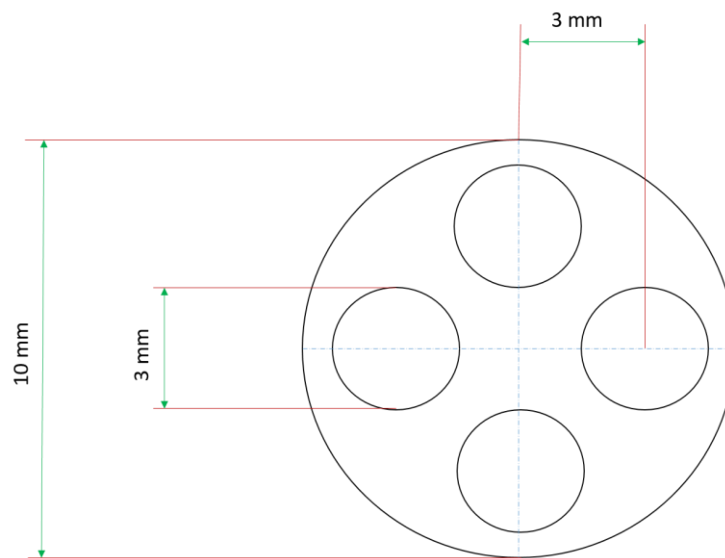


Figure 3. 2 Schematic illustration the TEM foils obtained from HPT disc.

3.4 Microstructural examination

3.4.1 Optical Microscopy (OM)

After HPT processing and sample preparation, the microstructural features of AZ80 magnesium alloy disc were examined and investigated using different techniques. To observe the initial microstructure and microstructure development after HPT processing for different numbers of turns, optical microscopy was used to generate images of each condition. After polishing, the discs' surfaces were etched using acetic glycol. This etchant was used to reveal the grain boundaries of the material, using an OLYMPUS-BX51 microscope. The average grain size in the as-received condition was specified using the linear intercept method, with a count of at least 300 grains, using ImageJ

software. OM images were taken at the discs' surface for the as-received condition and for each HPT process number of turns. Furthermore, OM images were taken of the vertically sectioned discs to investigate the microstructure development through the disc thickness.

3.4.2 Scanning Electron Microscopy (SEM)

Using a JEOL JSM-6500F, SEM images were made of the unprocessed and processed HPT samples to determine the morphology of the precipitates at the disc surface and to show the quantitative and chemical analyses of the elements in the α matrix and β precipitate phases, using energy-dispersive spectroscopy (EDS). Sample preparation, as explained in 3.3.1, was undertaken with the samples tested by SEM.

3.4.3 Transmission Electron Microscopy (TEM)

TEM images used in this study were taken using High Resolution STEM Hitachi HD-2700, STEM Hitachi S-5500 and conventional TEM microscope JEOL 1200 to investigate the microstructural evolution of AZ80 magnesium alloy after the HPT process, to include the morphology of the precipitate and the grain size after the HPT processing down to nanometer range. Selected area electron diffraction (SAED) was utilized in TEM observations. Furthermore energy-dispersive X-ray spectroscopy (EDX) was used to analyse the β precipitate phases.

3.5 Mechanical properties examination

3.5.1 Microhardness along the diameter of the disc

The mechanical properties were examined and investigated. Hardness measurements along the diameter of the disc were made using applied loads of 100 gf and a dwell time of 15 s. As shown in Figure 3.3, the values of four selected points along the diameter, separated by a distance of 0.3 mm in cruciform positions, were taken. To achieve a higher degree of accuracy, an average value of those four selected points was taken to determine the value of a point, represented by a circle, lying at the centre at a distance of 0.15 mm from each separate point. These average hardness values were used to provide the variation along the disc diameter and demonstrate the evolution of microhardness after each individual turn in the HPT process. The values were recorded

and used in the Vickers microhardness profile. The hardness value prior to HPT processing in the as-received condition was measured, and the average value was calculated and plotted as dashed line in the profile. As shown in Figure 3.3, the distribution of the microhardness values over the whole disc surface was recorded using a rectilinear grid pattern with 0.3 mm spacing between successive points.

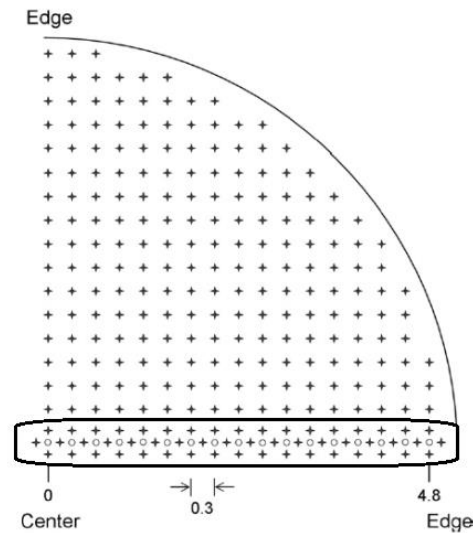


Figure 3. 3 Quarter of disc illustrating the location of the four separate points in the bottom & the rectangle points over the whole disc [189].

3.5.2 Microhardness through the disc thickness

For the hardness measurement through the thickness, selected discs processed by HPT for 1, 3 and 10 turns were sectioned vertically along their diameter. A rectangular net of five separate points was made at three specific distances, at 0.1, 0.5 and 0.9 of the disc's radius, starting from centre, using applied loads of 100 gf and a dwell time of 15 s in order to avoid any interference between the measurement points. The points were cautiously separated by a distance of 100 μm from each other. The average of the five separated points was measured, then plotted to show the Vickers microhardness distribution as a function of distance, from the bottom of the disc through the disc thickness, as shown in Figure 3.4. The machine used in testing the alloy along the diameter, over the whole surface of the disc and through the thickness of the discs, was the Vickers microhardness tester FM-300.

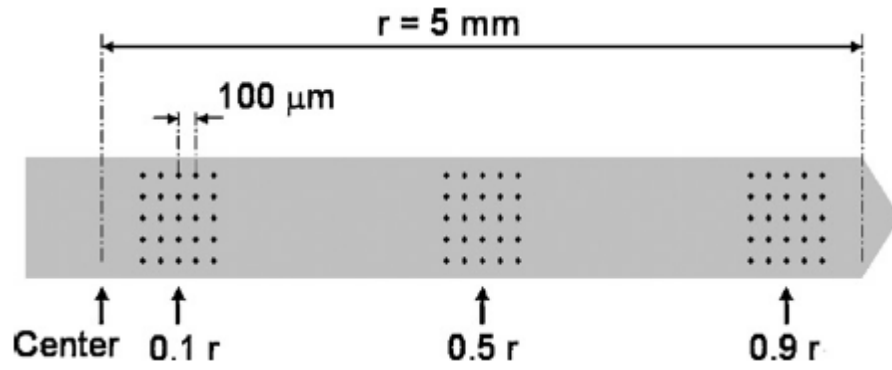


Figure 3. 4 Position selected through disc thickness for Vickers microhardness Hv measurements [118].

3.5.3 Tensile testing

The miniature tensile specimens were carefully cut using an electro discharged machine (EDM) from the processed discs after reducing their thickness to ~ 0.65 mm by SiC abrasive papers. To avoid the higher heterogeneous microstructure area at the disc centre, the off-centre position method was used to cut the micro-tensile specimens, where the centre of the miniature tensile specimen is located 2 mm from centre of the disc as described in Figure 3.5 [146].

This procedure allows two miniature tensile specimens to be cut from each processed disc. The gauge length and the width of the specimens were 1.1 mm x 1.0 mm. To give accurate data of the specimens before the tensile test was conducted, all sectional areas of the miniature were carefully measured, since there were minor differences in thickness between the specimens. In addition, for better analysis accuracy, the test was repeated three times for each sample.

The tensile test was conducted at three different temperatures of 473 K, 523 K and 573 K using an electric furnace surrounding the grips of Zwick/Roell tensile Z030 machine. This machine operates at a constant rate of cross-head displacement. Before starting the test, the samples were kept at the testing temperature for 10 minutes to achieve an homogenous temperature distribution. Samples were pulled in tension to failure using a strain rate of $1.4 \times 10^{-4} \text{ s}^{-1}$, $1.4 \times 10^{-3} \text{ s}^{-1}$, $1.4 \times 10^{-2} \text{ s}^{-1}$ and $1.4 \times 10^{-1} \text{ s}^{-1}$ for each testing temperature and for samples produced from discs processed for $N = 1/4, 1, 5$ and 10 turns. Test loads and displacement were recorded using testIIXpert testing software in a

computer-acquisition system. The data collected from the software were used to plot the stress versus strain curves, therefore to identify the maximum elongation of the tested samples and the strain rate sensitivity (m).

Following the tensile test, the microstructure of the samples was observed using SEM at the gauge surface near the tip of the fracture without any further grinding or polishing to the sample. The images were recorded using Wild Herrbrugg stereoscope for accurate measuring.

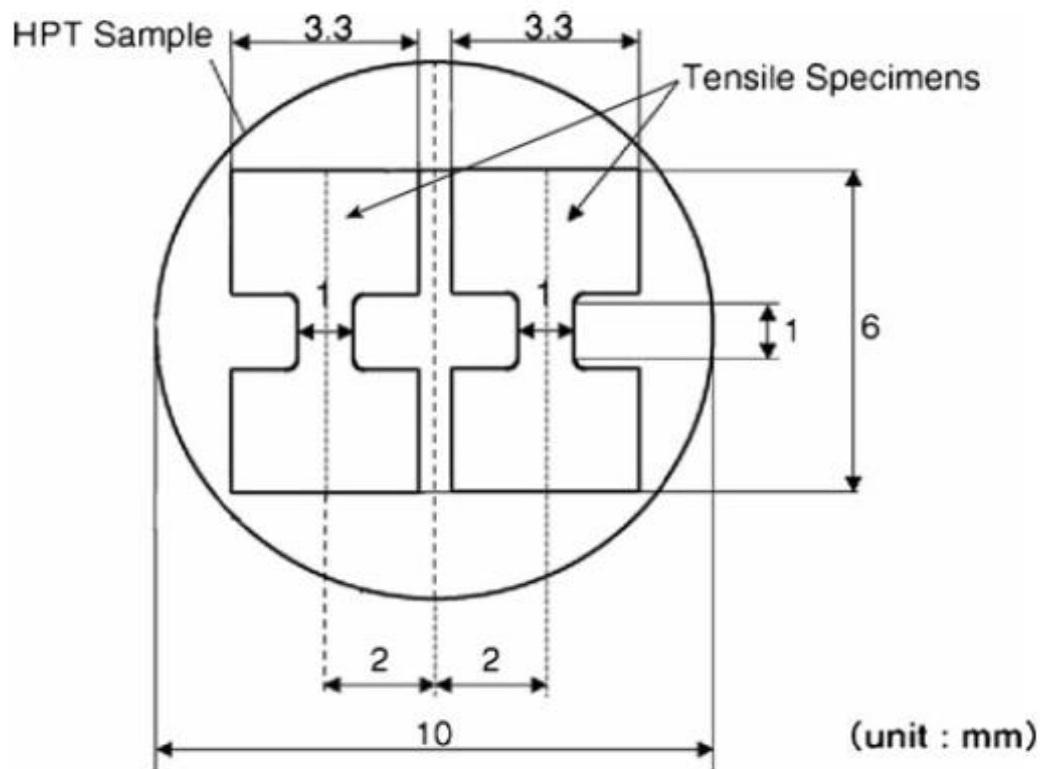


Figure 3. 5 Schematic illustration the miniature tensile specimens obtained from HPT disc using electro-discharge machining [146].

4 Experimental Results

4.1 Initial microstructure and hardness

The AZ80 magnesium alloy was examined in its initial condition. First, an inspection of the unprocessed disc revealed fairly equiaxed grains and a uniform structure with an average grain size of $\sim 25 \mu\text{m}$ and average Vickers microhardness value of 63 Hv. This homogeneity in the microstructure at the surface of the material was demonstrated by the distribution of microhardness values and the average grain size distribution across the entire disc surface. Figure 4.1 shows the SEM image of grain distribution in the disc surface. The microstructure shows a homogeneous distribution of fairly equiaxed grains. Figure 4.2 (a) and (b) shows the OM images of grain distribution in two areas, the centre and the edge of the disc, before the HPT processing this image confirms the homogeneity of the microstructure. Figure 4.3 shows the grain distribution in the as-received condition through the disc thickness in the axial direction. The yellow arrow runs in the direction of the extrusion. It is clear that the grains are fairly equiaxed in both the axial and radial direction.

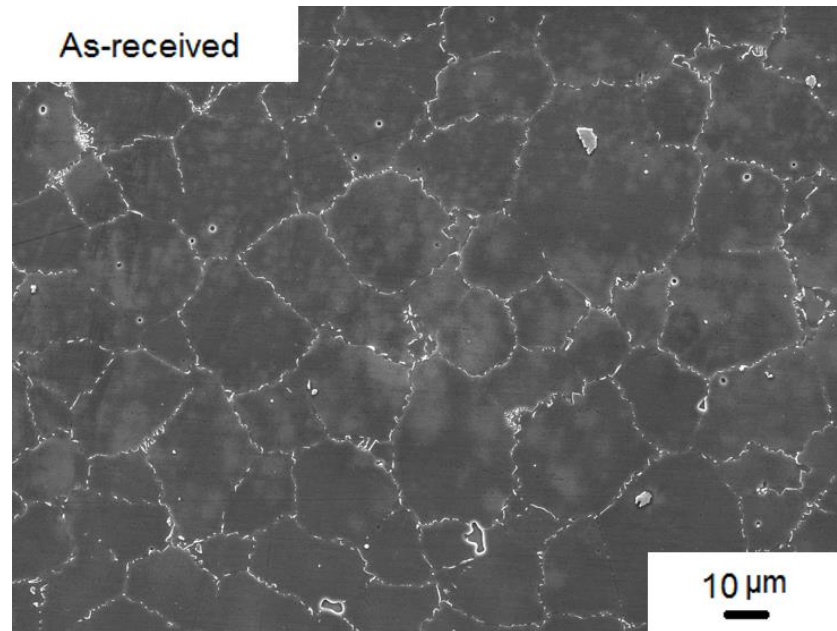
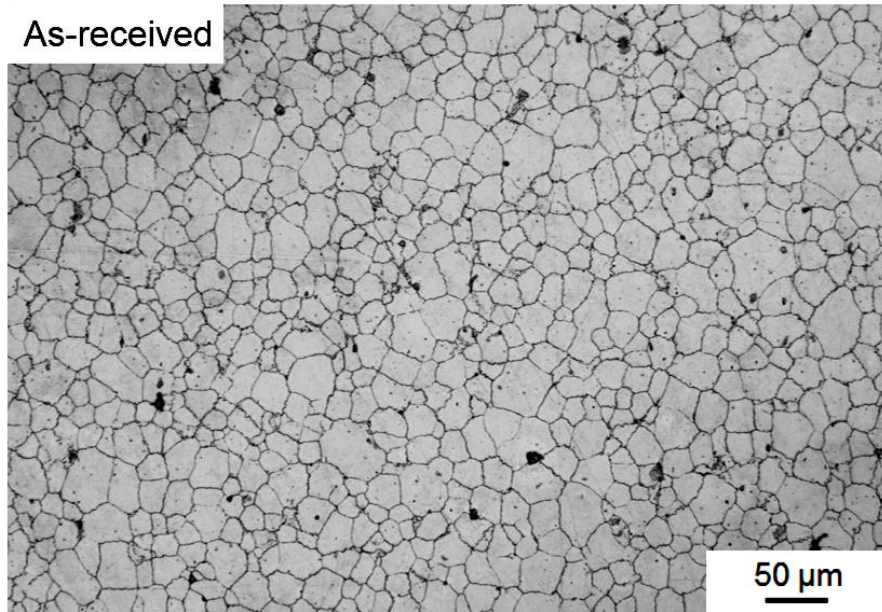
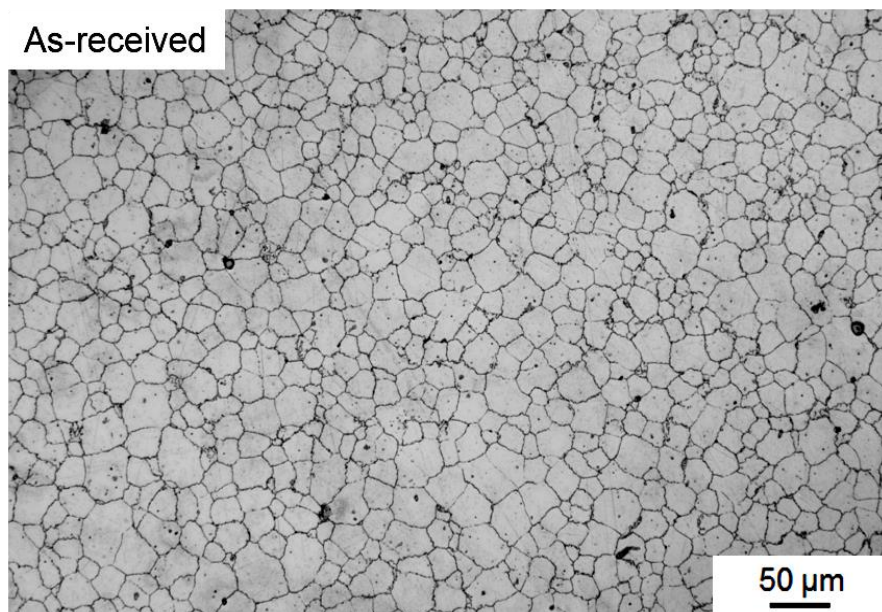


Figure 4.1 SEM image showing the grain distribution in the as-received condition at the surface of the disc.



(a)



(b)

Figure 4.2 OM images show the grain distribution of AZ80 at the disc surface in the initial condition: (a) at the centre of the disc; (b) at the edge of the disc.

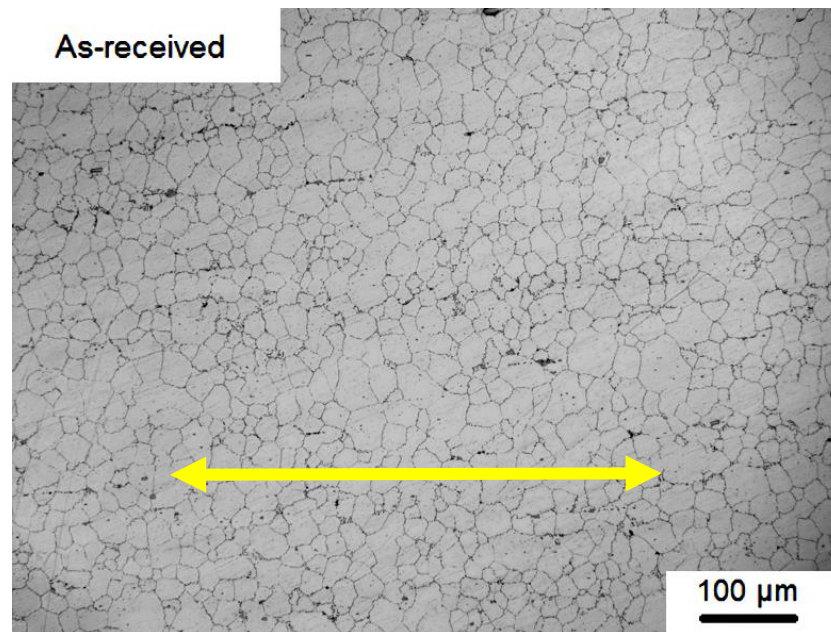
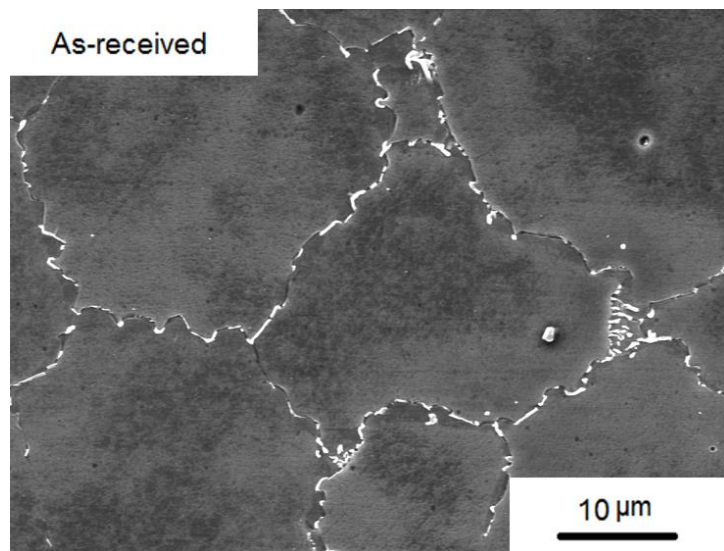
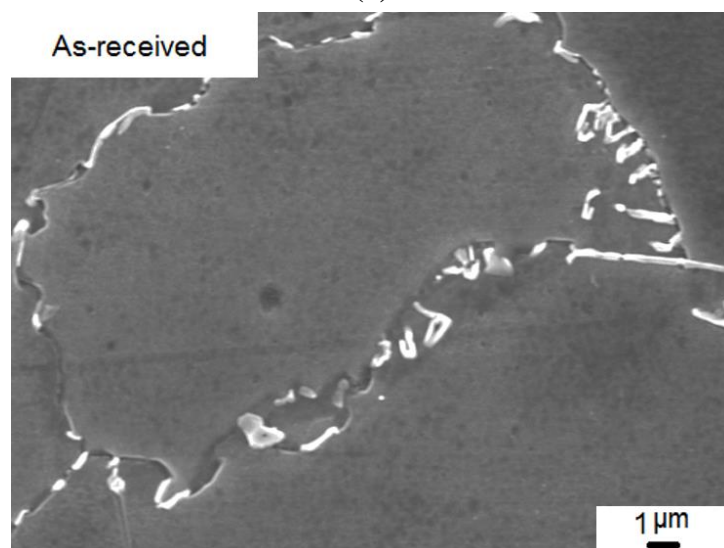


Figure 4.3 OM grain distribution through the disc thickness (axial direction) in the as-received condition. The yellow arrow shows the extrusion direction.

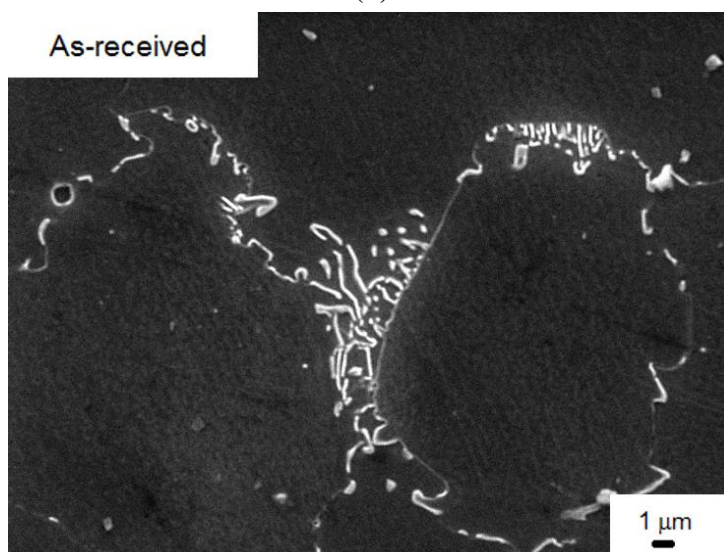
The microstructure of the extruded AZ80 sample disc has two phases: α matrix and the β phase. The distribution of the β phase was found to be widespread discontinuously at the grain boundaries, as shown in the OM Figures 4.2 and 4.3. The α matrix is in bright contrast to the β phase in the optical images, while in the SEM the α matrix is in dark contrast and the β phase is bright, as shown in Figures 4.1, 4.4 and 4.5. The precipitate, in a brighter colour, has a different form in the alloy. Precipitates mainly have lamellar and granular morphology; it can be seen from SEM image in Figure 4.1 that most of the precipitates are distributed mainly along the grain boundaries. Using a higher magnification, as shown in the SEM images in Figure 4.4, the precipitates show some agglomeration near the triple junctions. The average length of the lamellar precipitates is ~ 1 to $4\ \mu\text{m}$. Using energy-dispersive spectroscopy (EDS), the chemical composition of the as-received condition was evaluated. The chemical analysis of the matrix and the precipitates of the material prior to the HPT process are demonstrated in Figures 4.5 (a) and (b). It has been found from the (EDS) analyses that the β phase is rich in aluminium. Many previous studies have confirmed that the β phase spread along the grain boundaries in AZ80 magnesium alloy is $\text{Mg}_{17}\text{Al}_{12}$ intermetallic precipitates [159,190,191].



(a)



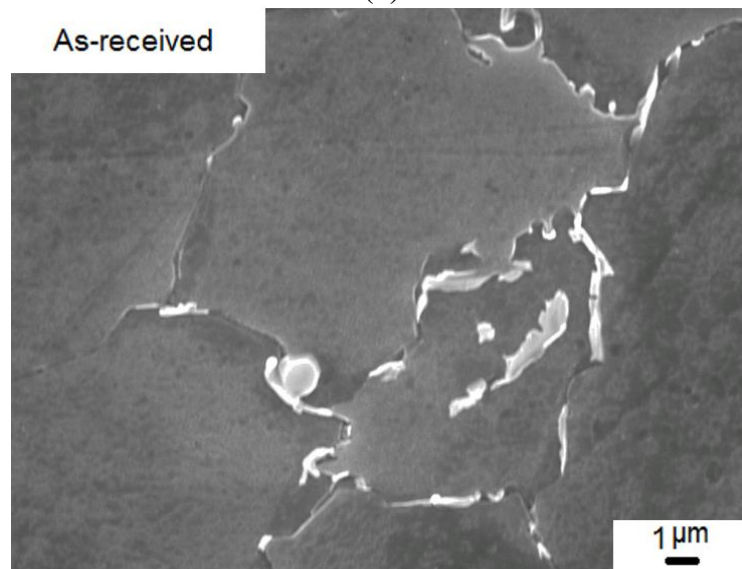
(b)



(c)



(d)



(f)

Figure 4.4 SEM images showing the precipitates in the AZ80 magnesium alloy prior to HPT process in the as-received condition, distributed at the grain boundaries: at (a), (b), (c) and (d), as a form of lamellar; and at (f) as a form of granular.

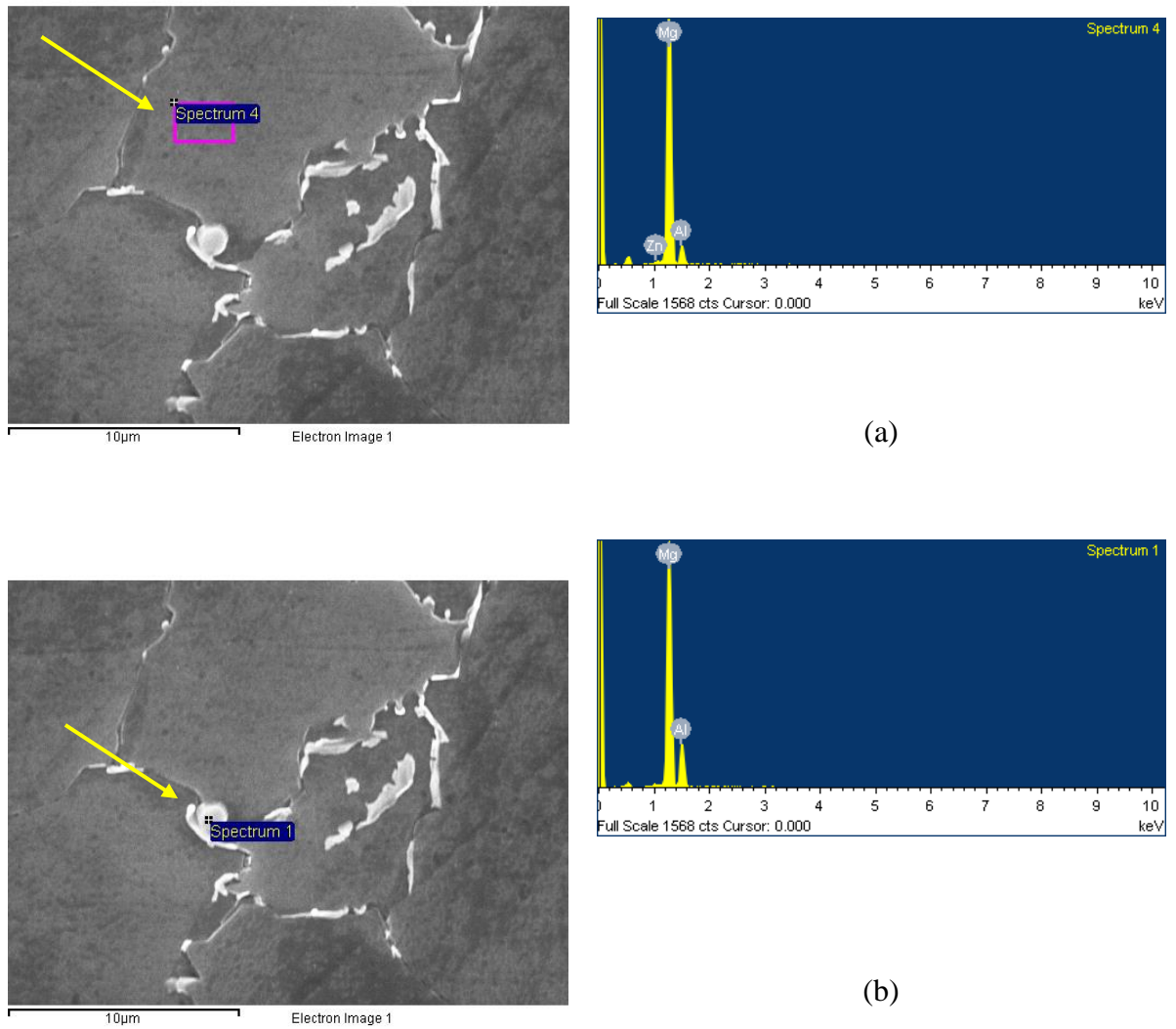


Figure 4.5 SEM images of (a) α phase matrix and its chemical analysis; (b) β precipitates phase and its chemical analysis.

4.2 Microstructure development after HPT processing at 296 K

Successful processing of AZ80 magnesium alloy by HPT for up to 10 turns took place without introducing obvious cracks or segmentation to the disc. The results show that the microstructure after HPT was significantly refined and that there was a gradual evolution into highly deformed grains. Even in the early stages of HPT at which the number of turns is small, the microstructure shows an excellent level of grain refinement.

4.2.1 Microstructure observation along the disc diameter

The microstructural observation started with optical microscopy (OM). The OM images were made at two areas of the discs, the centre and at the edge of the discs, after HPT processing beginning with a 1/4 turn, up to 10 turns, at room temperature. A close inspection of the microstructure after a 1/4 turn showed that there was a rapid development at the edge of the disc. Figure 4.6 shows clearly that the central areas of the discs were exposed to a lower deformation at a 1/4 turn in Figure 4.6 (a) and the deformation at the edges showed elongated grains properly in the torsion direction in Figure 4.6 (b). When the material was processed up to 1 turn, the elongated grains in some areas at the edge of the disc deformed to more refined smaller-sized grains, as shown in Figure 4.6 (d), while the disc centre had a proportion of coarse grains, as shown in Figure 4.6 (c).

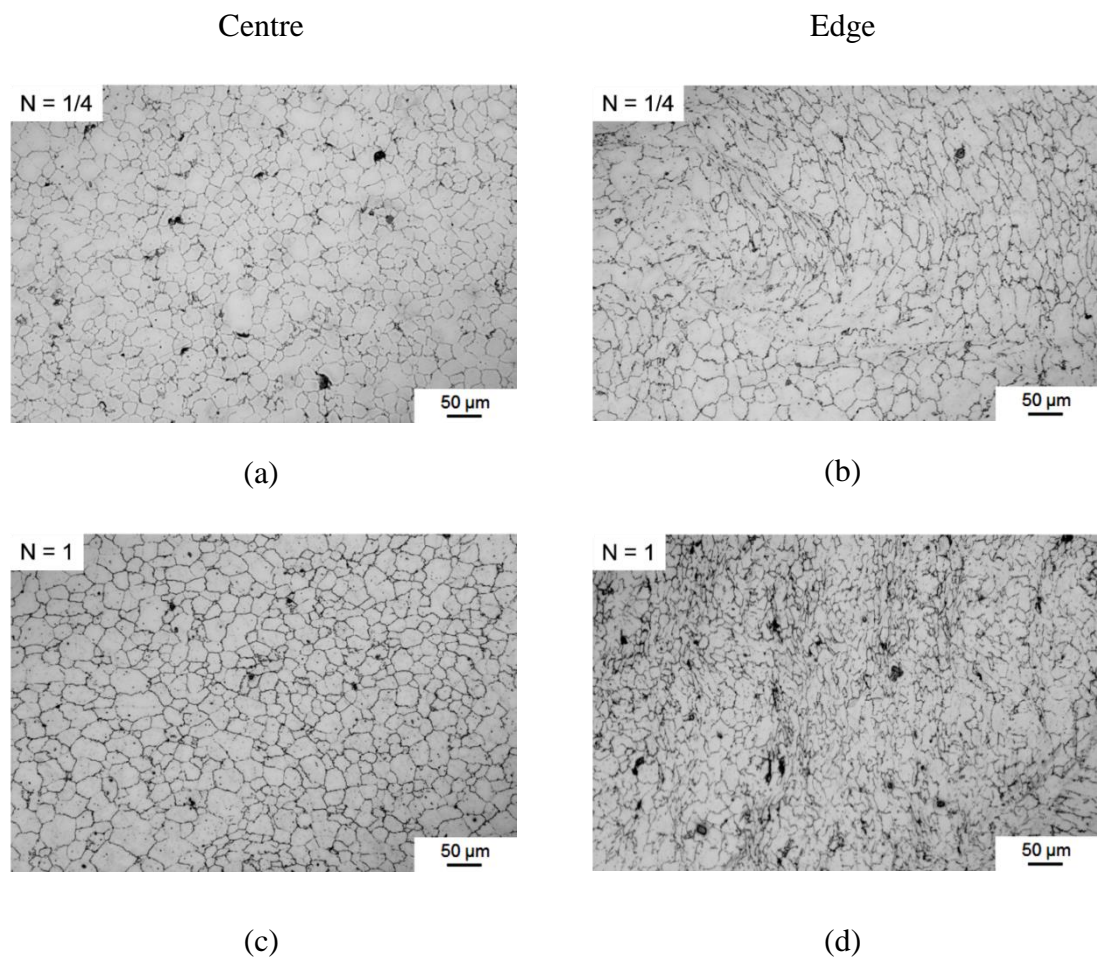


Figure 4.6 Optical images showing centre (left column) and edge (right column) after HPT processing at room temperature through (a, b) 1/4 turn and (c, d) 1 turn.

In Figure 4.7 (a) the central area of the processed disc up to 3 turns appears coarse, while the disc edge became highly refined In Figure 4.7 (b), which will be demonstrated to be consistent with the microhardness results presented in section 4.3.1 where there was a sharp drop in hardness values near and at the centre of a disc processed by 3 turns. When the AZ80 was processed up to 10 turns, the refinement dominated the central area and there was no great difference between the edge and the centre of the disc, showing a more reasonable uniform microstructure, as shown in Figures 4.7 (e) and (f).

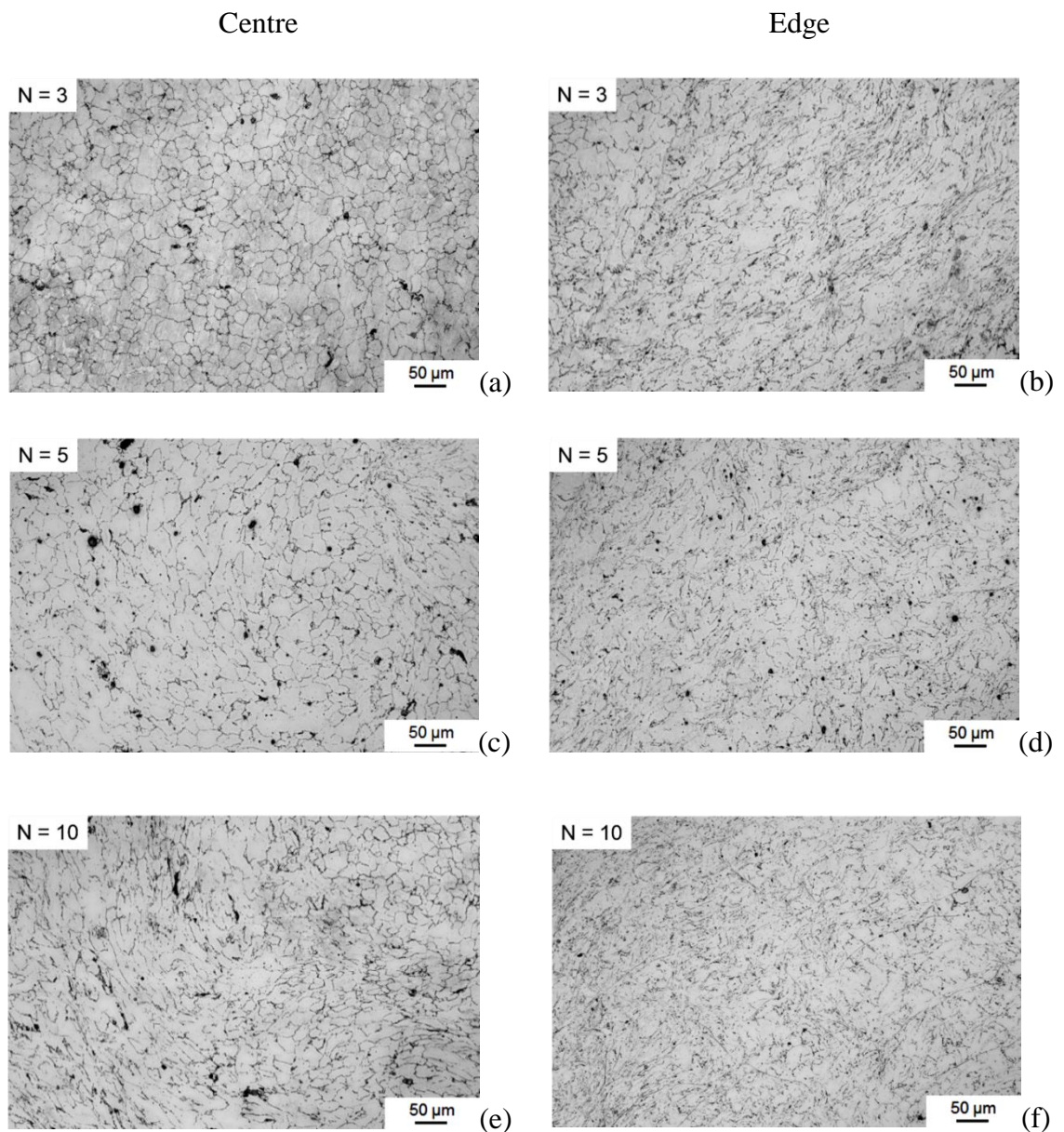


Figure 4.7 Optical images showing the centre (left column) and edge (right column) after HPT processing at room temperature through: (a, b) 3 turns; (c, d) 5 turns; and (e, f) 10 turns.

SEM images were taken at a higher magnification to observe the distribution of β phase after one turn of HPT process, as shown in Figures 4.4 and 4.5. The precipitates prior to HPT were in a granular and lamellar form, distributed along the grain boundary that appears as a brighter contrast between the darker contrast grains. In the early stage of HPT, the precipitates started to fragment and shatter into small particles, as shown in Figure 4.8. Earlier investigations showed that the precipitates aligned themselves probably in the direction of the torsion in the early stages of HPT process [104].

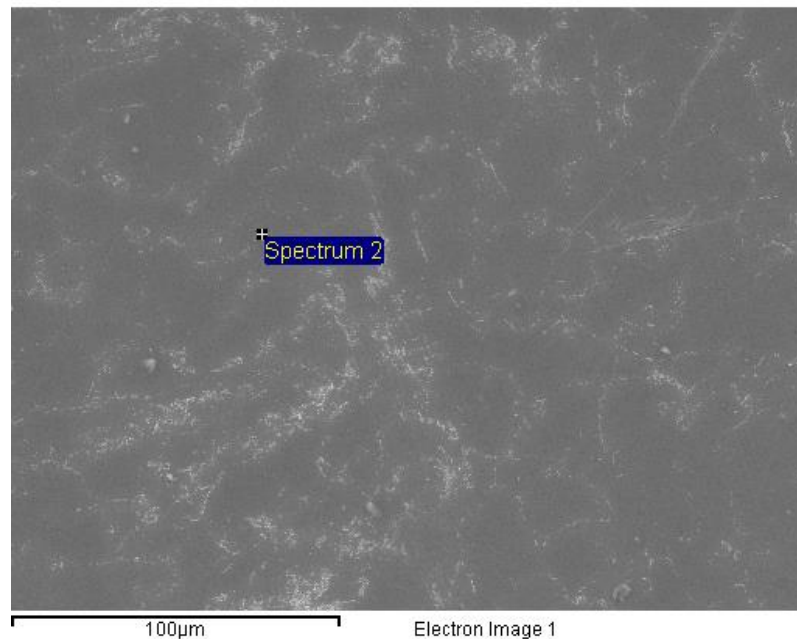


Figure 4.8 Fragmentation of precipitates after one turn of HPT process at 296 K.

After 1/4 turn of HPT, the precipitates started to fragment to smaller sizes. The size of the precipitates is now in the nanometer range; the STEM-HD images in Figure 4.9 shows the distribution of the β phase within the matrix at (a), and the fragmentation of the precipitates to a size smaller than 100 nm at (b) in a sample processed for 1/4 turn by HPT at room temperature, while the average length of the precipitates in the initial condition was in the micrometer range, as shown in the SEM images in Figure 4.4. After HPT, the precipitates were no longer distributed at the grain boundaries, but at this stage were randomly distributed within the matrix. Figure 4.10 shows the distribution of the precipitates within the matrix. The EDX scale count displays the precipitates at points 1, 3 and 5, and in the matrix at points 2 and 4.

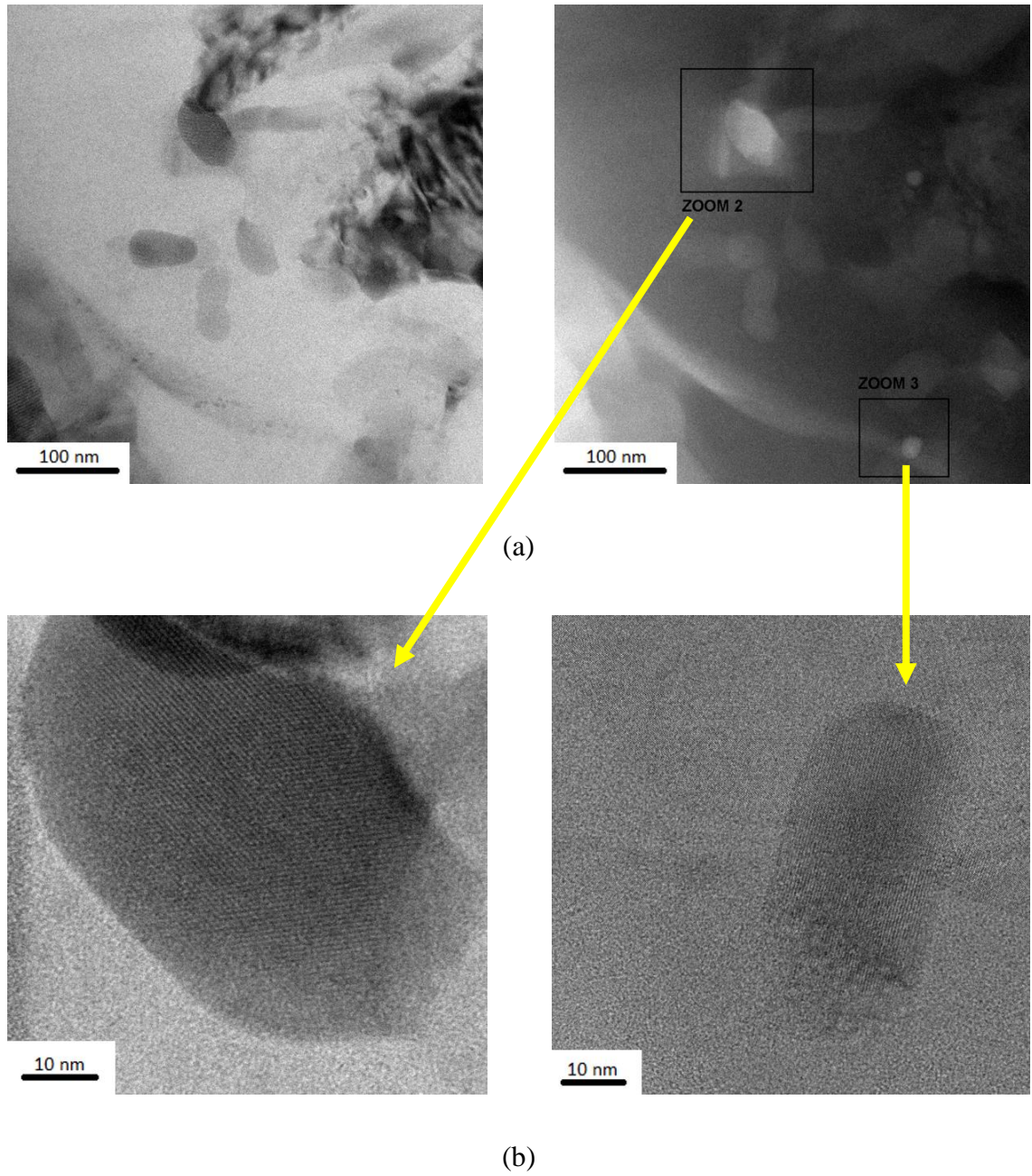
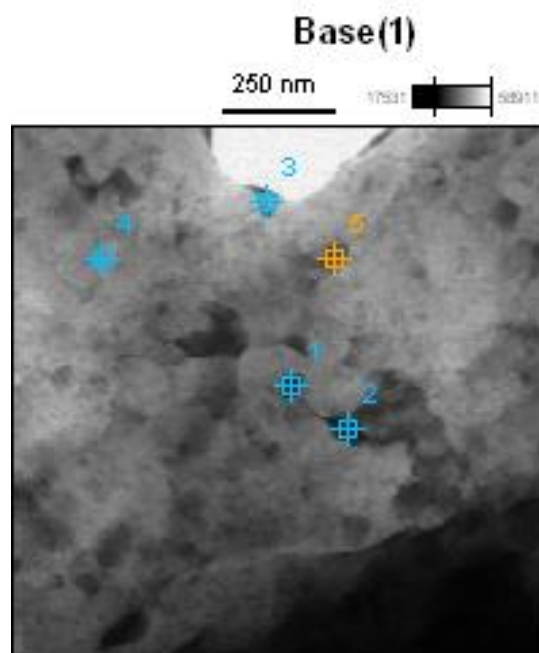
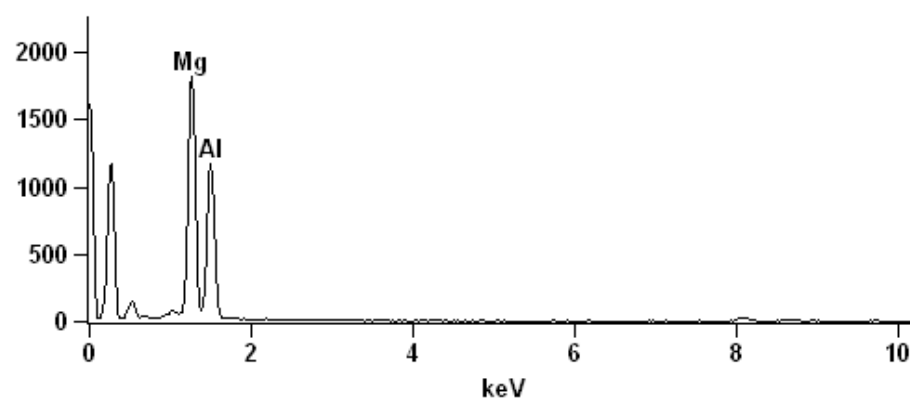


Figure 4.9 STEM-HD images illustrating (a) the distribution of precipitates within the material after 1/4 of HPT; (b) the precipitates in zoom 2 and zoom 3 at a higher magnification and from various angles.



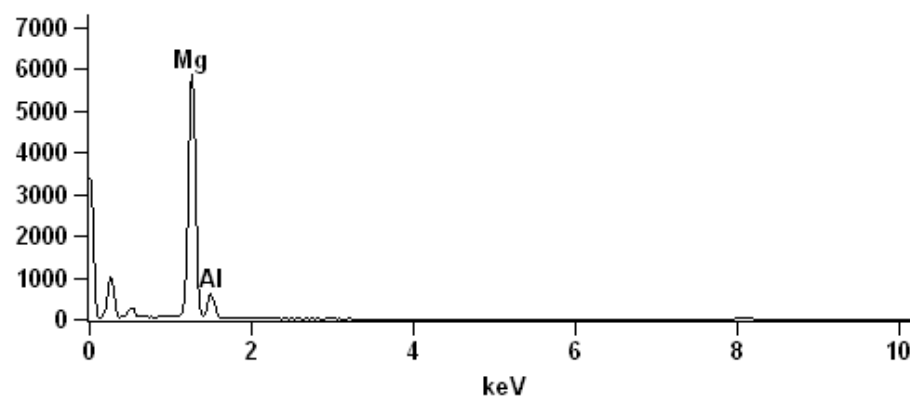
Full scale counts: 1813

Base(1)_pt1



Full scale counts: 5865

Base(1)_pt2



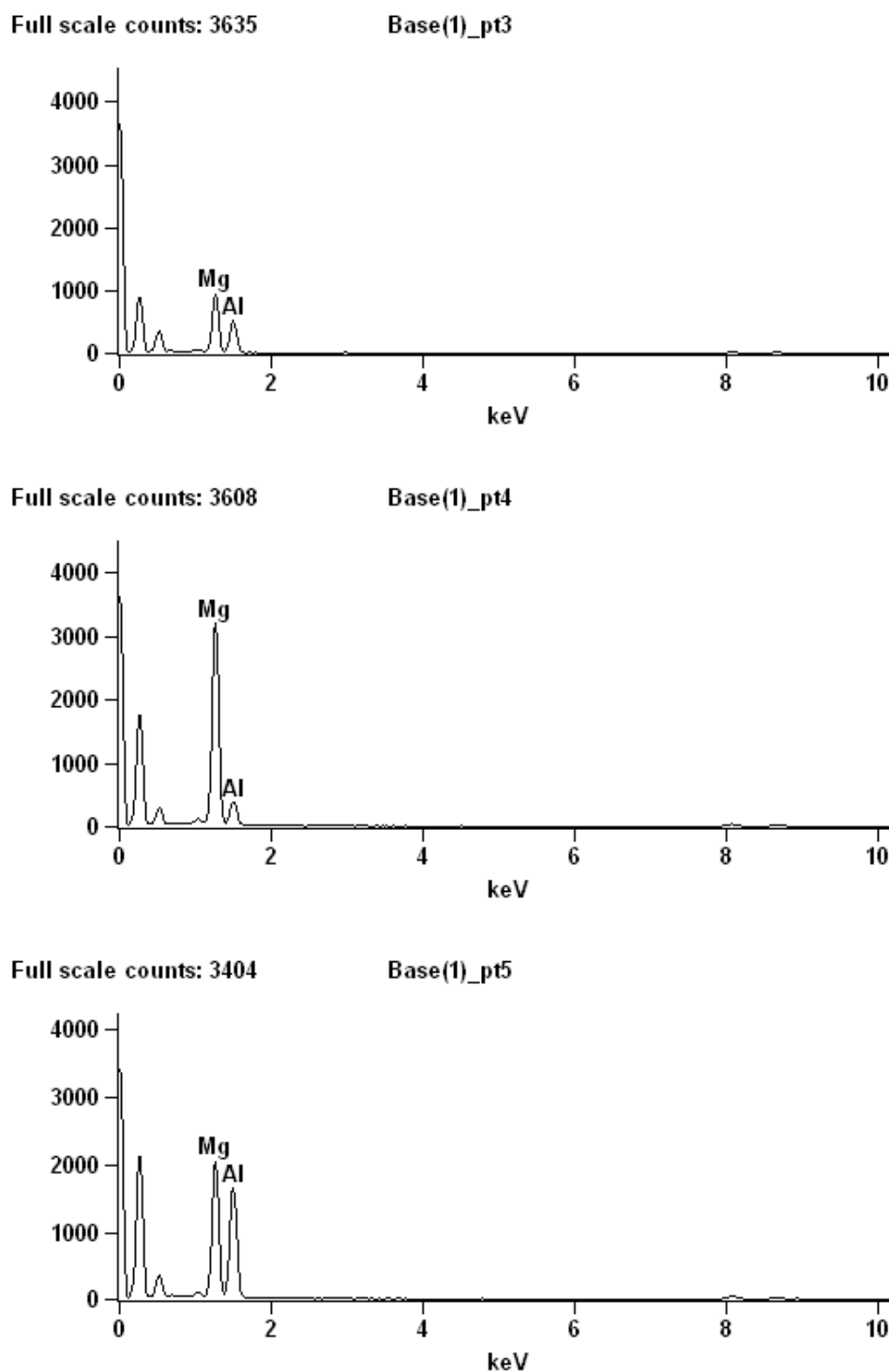
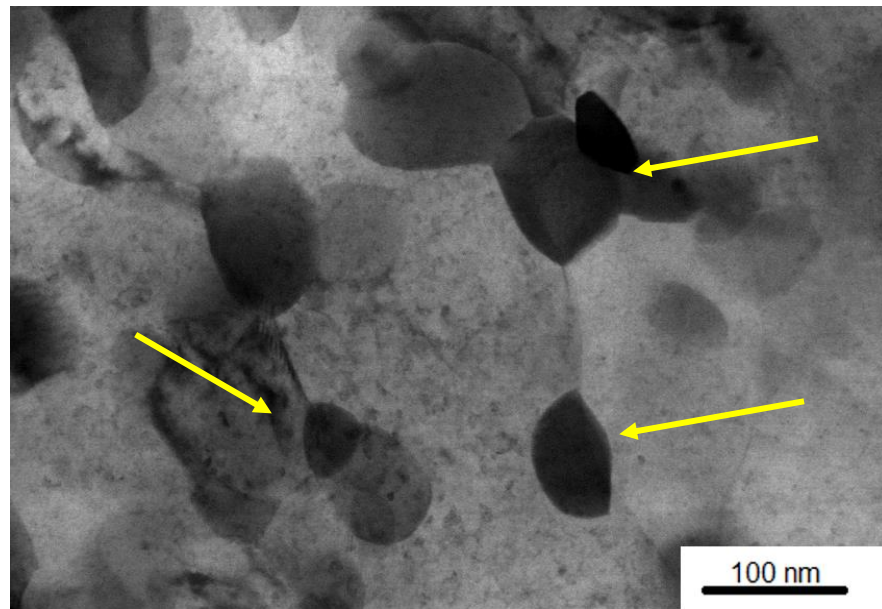


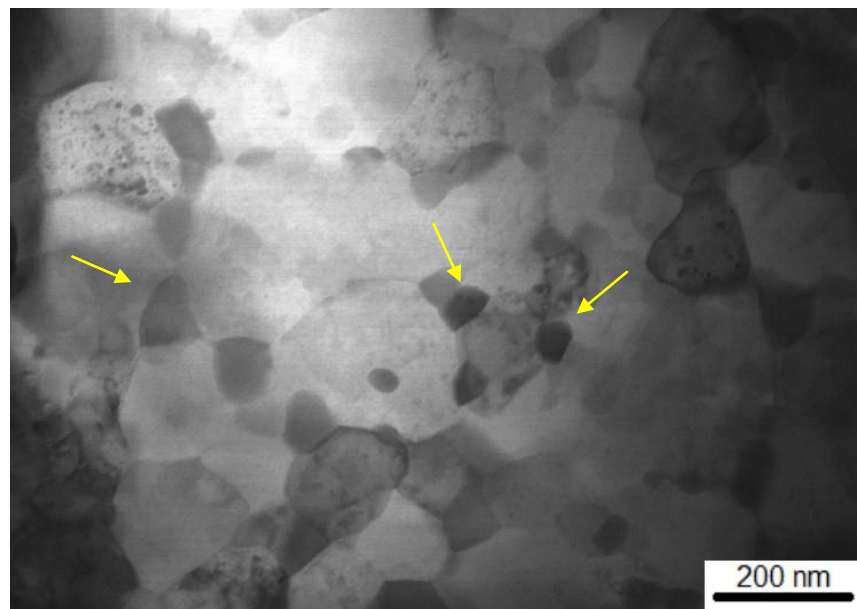
Figure 4.10 EDX showing scale counts for the matrix at points 2 and 4, and for the precipitates at points 1, 3 and 5.

After fragmentation and starting from a low number of HPT turns, precipitates started to form at the triple junction between the grain boundaries. The STEM images in Figures 4.11 (a) and (b) (indicated by yellow arrows) and 4.12 (indicated by a red arrow) show

precipitates located at the triple junctions after processing by HPT for up to 1, 5 and 10 turns. The presence of precipitates at the triple junctions was confirmed by the line EDX in Figure 4.12. It is clear from Figures 4.11 and 4.12 that the size of precipitates is reduced to less than 100 nm.



(a)



(b)

Figure 4.11 STEM images show the precipitates at the triple junction after (a) 1 and (b) 5 turns of HPT at room temperature.

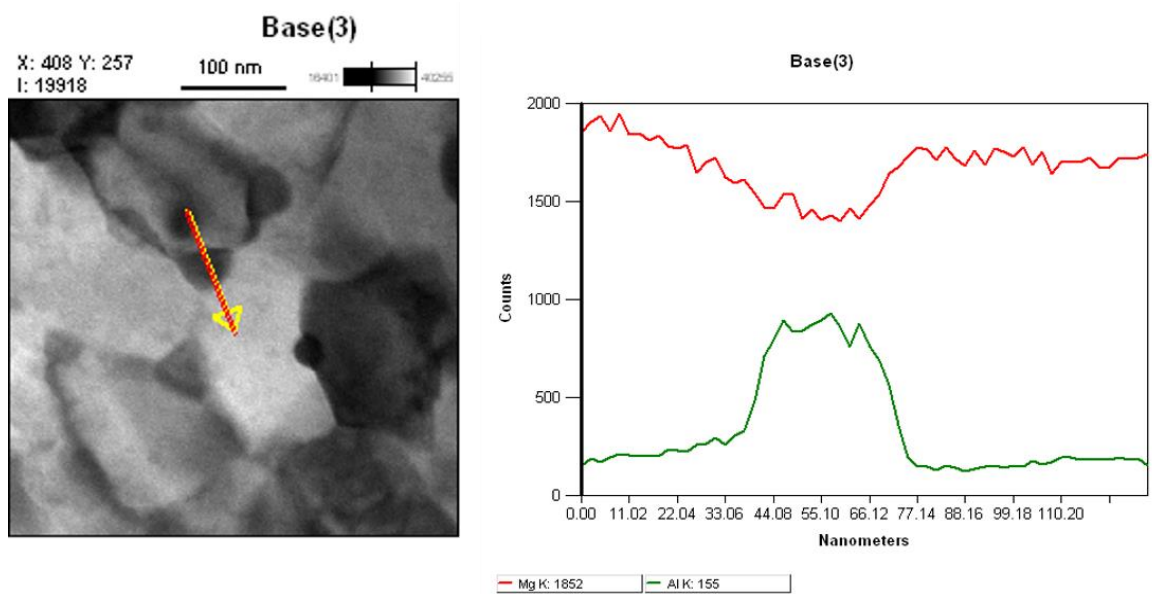
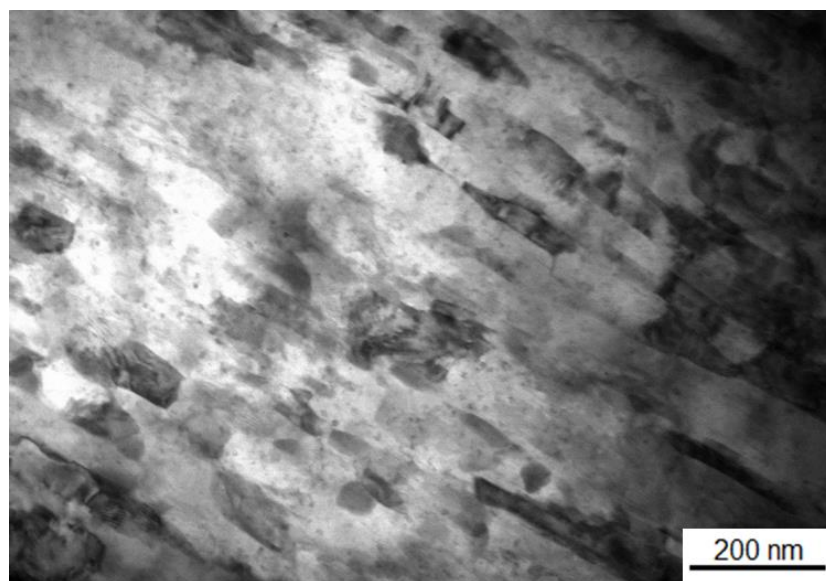
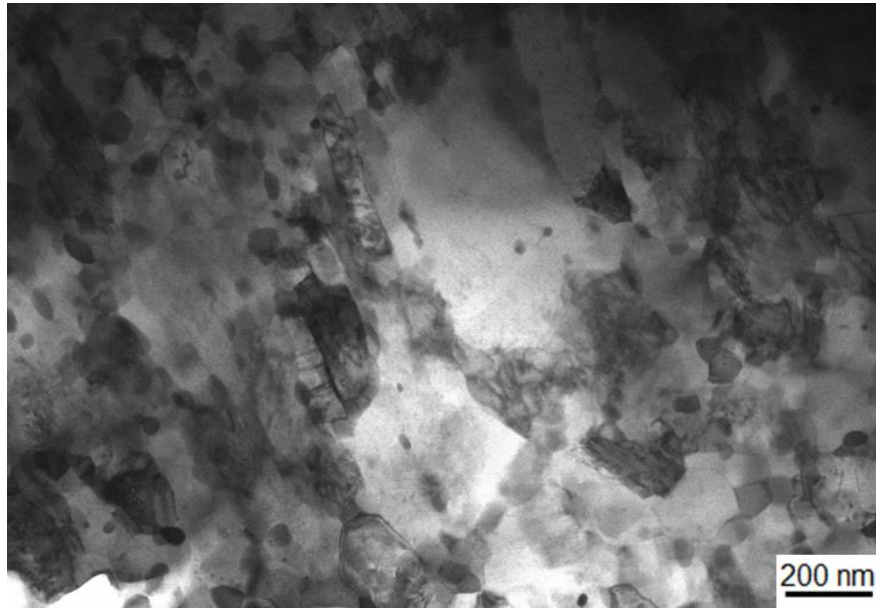


Figure 4.12 Agglomerate of precipitates in the triple junction between the grains after 10 turns as the TEM images shows and line EDX demonstrating the analysis of the matrix and the precipitate phases.

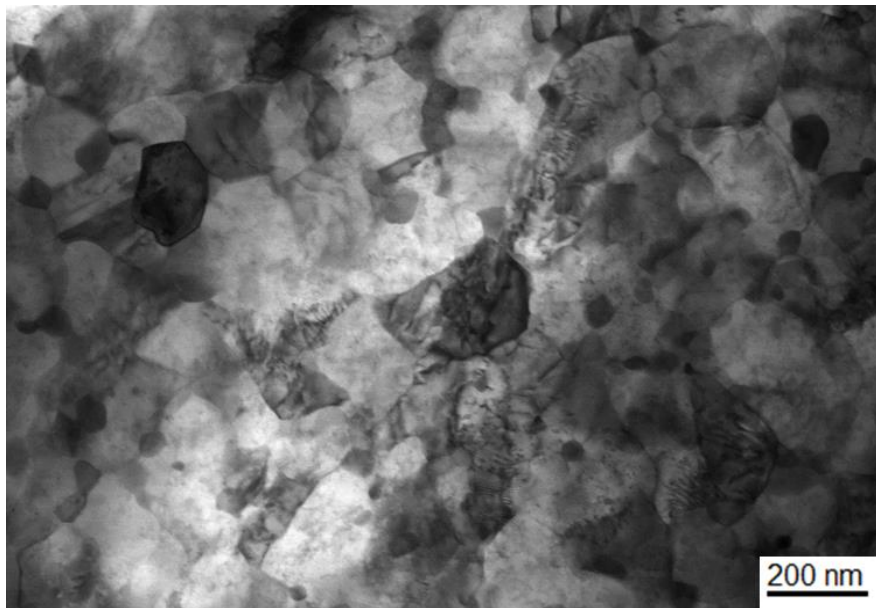
The STEM images of AZ80 in Figure 4.13 summarize the microstructural evolution after the HPT process at room temperature. It is clear from Figures 4.13 (a) and (b) that microstructural evolution shows an elongated grain, probably in the torsion direction at the early stages of HPT process at 1/4 and 1 turn, while images of AZ80 processed by HPT up to 10 turns show equiaxed grains and a reasonably homogeneous microstructure with an average grain size of ~200 nm.



(a)



(b)

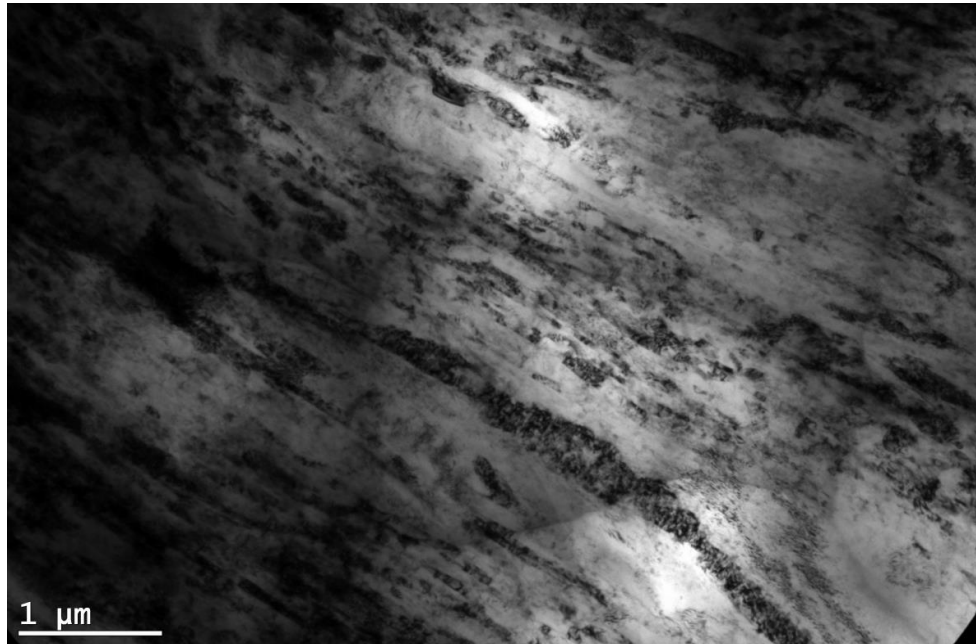


(c)

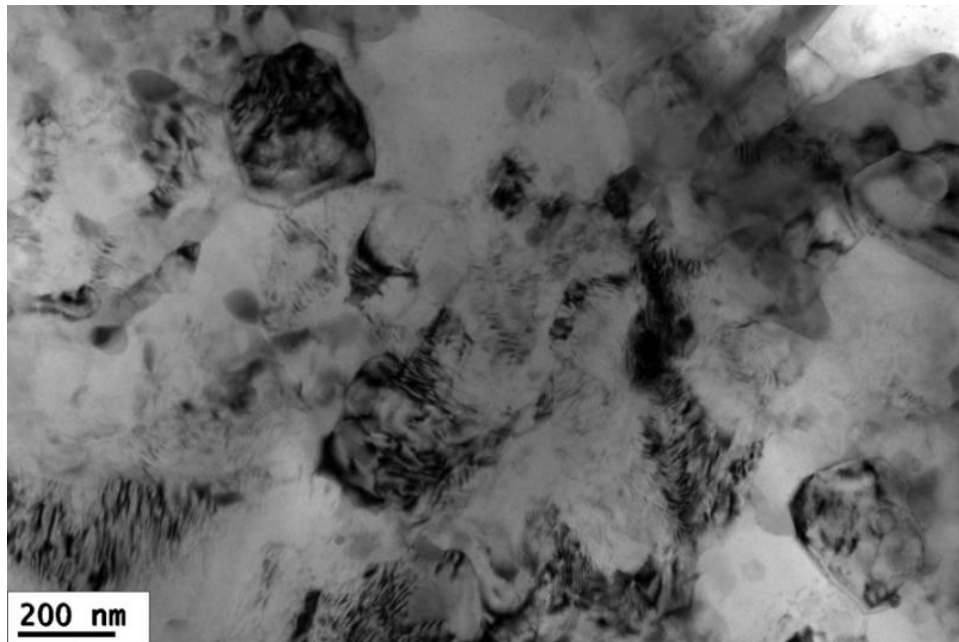
Figure 4.13 Images from STEM summarize the microstructural evolution of the AZ80 alloy after processing by HPT at room temperature for: (a) 1/4 turn; (b) 1 turn; and (c) 10 turns.

Starting at the early stages of HPT, the material generates many dislocations. This shows the amount of imposed strain on the material, and high dislocation density is shown in Figures 4.14 (a), (b) and (c). The high dislocation density is illustrated in Figure 4.14 for 1/4, 1, and 3 turns and the incomplete (SAED) ring is shown in Figure

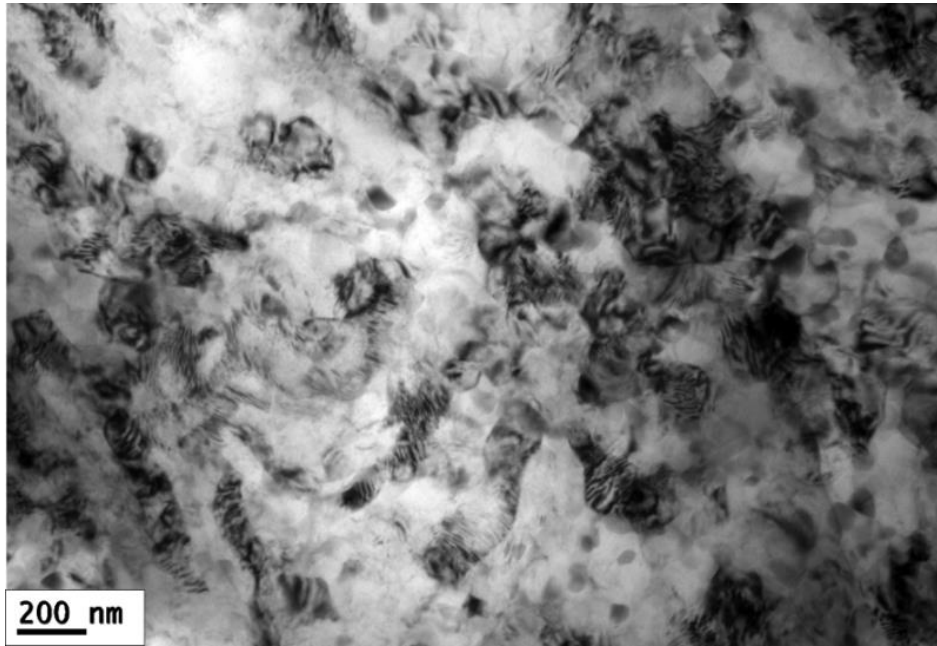
4.18 (a) and (b) for 1/4 and 1 turn, indicating that the material until this stage has a large fraction of large grains. At lower numbers of HPT revolutions, these dislocations arrange themselves as an elongated cell, as shown in Figures 4.15 (a) and (b), and with further strain these cells evolve to a more equiaxed shape, as shown in Figure 4.16.



(a)

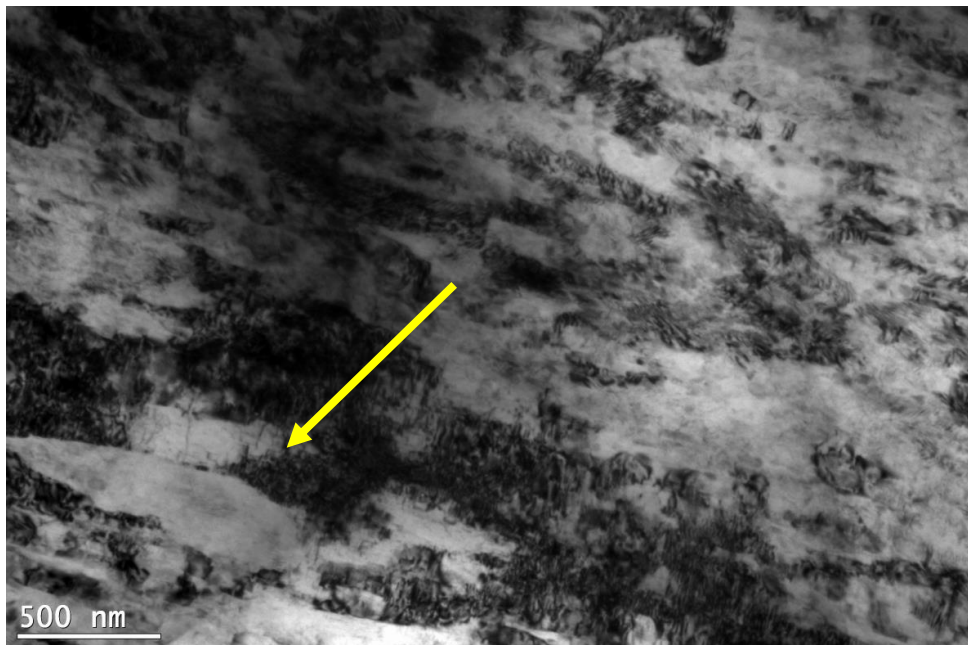


(b)

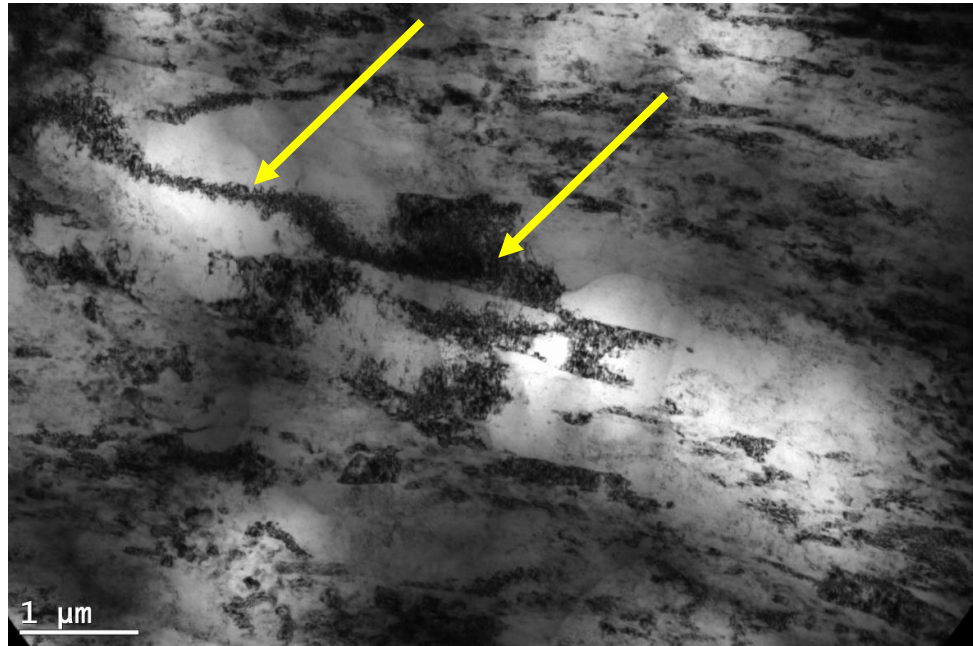


(c)

Figure 4.14 Three TEM images show the high dislocation density at (a) 1/4, (b) 1, and (c) 3 turns of HPT at room temperature.



(a)



(b)

Figure 4.15 Formation of dislocation cell, shown by the TEM images at (a) and (b) after 1/4 turn of HPT at room temperature.

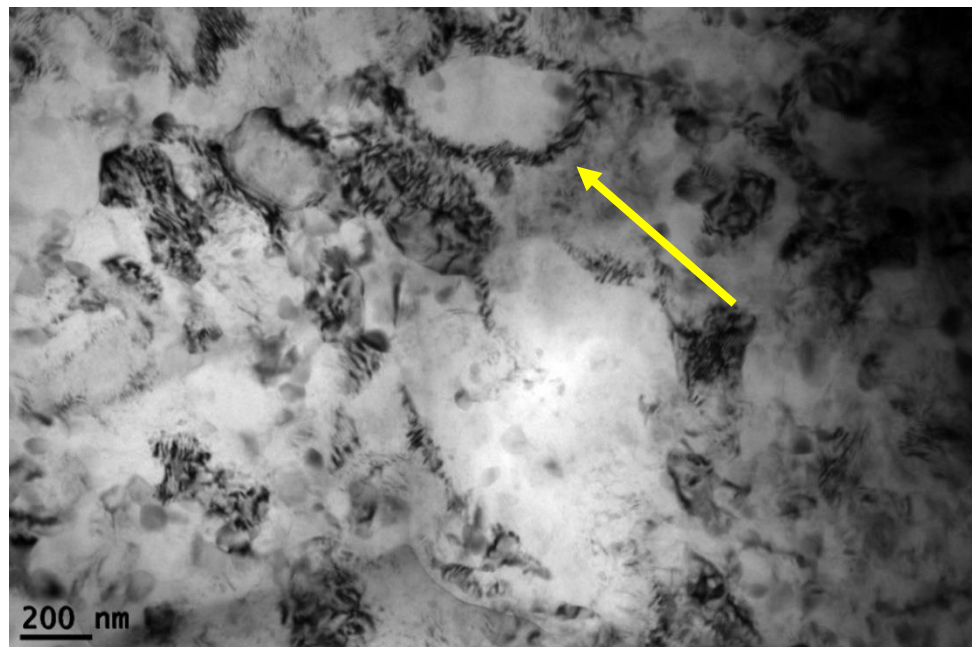
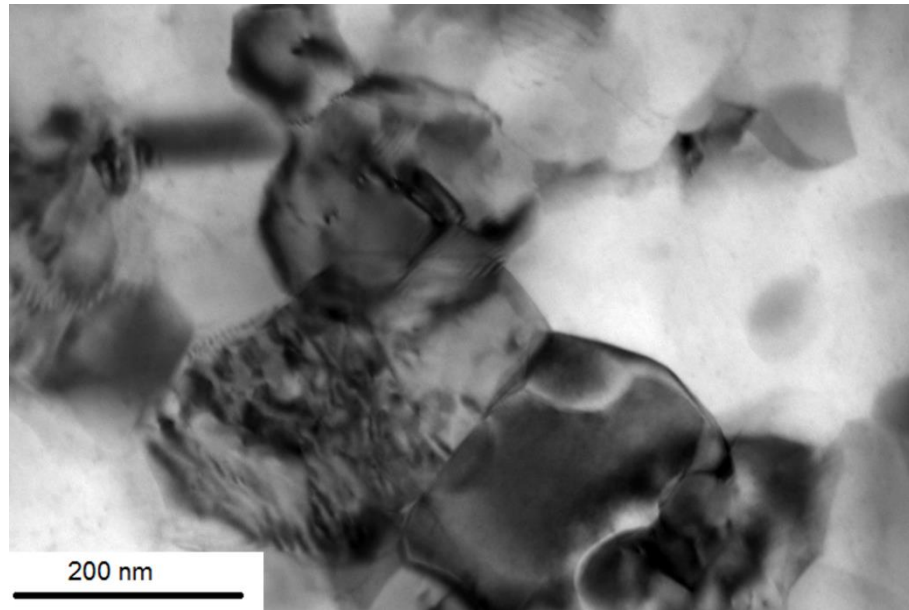
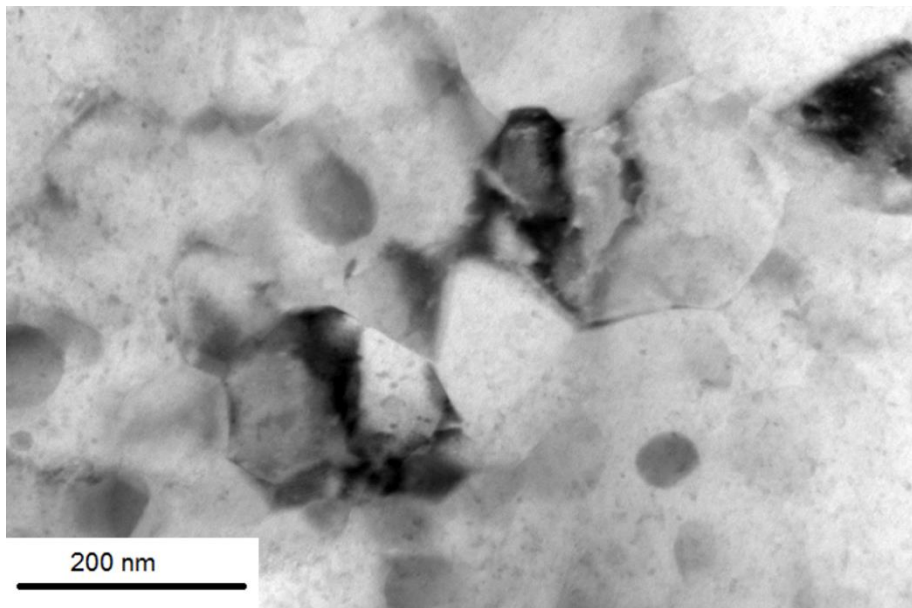


Figure 4.16 Reasonably equiaxed dislocation cell after 5 turns of HPT process at room temperature, as illustrated by TEM imagery.

At later stages of HPT, after a higher number of turns, the alloy reaches a level of saturation in grain size. At this stage, the rate of dislocation generation balances the rate of dislocation annihilation, equiaxed grains with a reasonable homogenous microstructure appears and a steady state is established. Figures 4.17 (a) and (b) show the equiaxed grains after five turns of HPT.



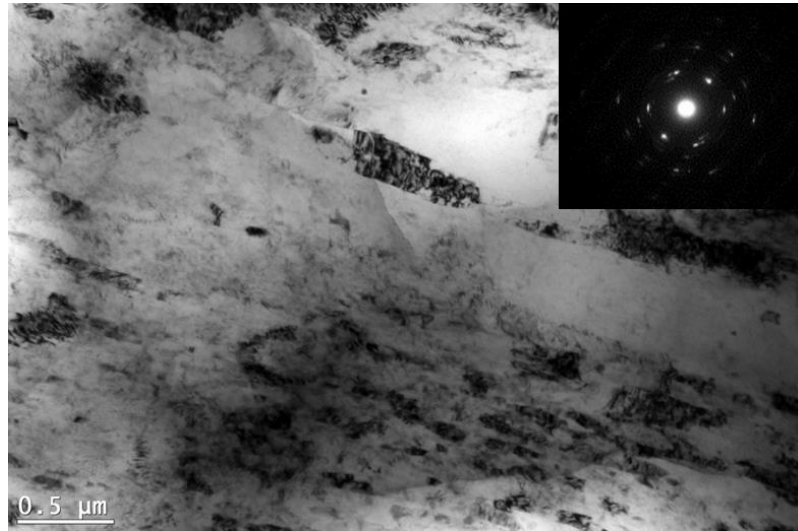
(a)



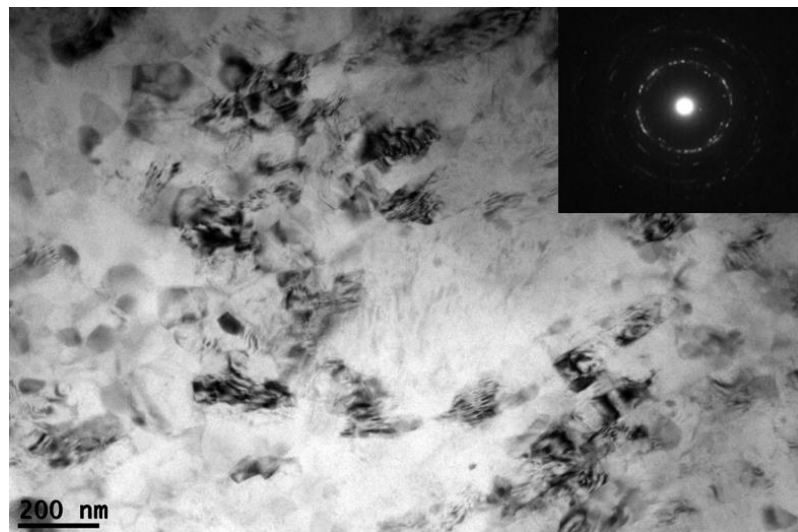
(b)

Figure 4.17 TEM images at (a) and (b) showing an equiaxed UFG with an average grain size of ~ 200nm after processing by HPT for 5 turns at room temperature.

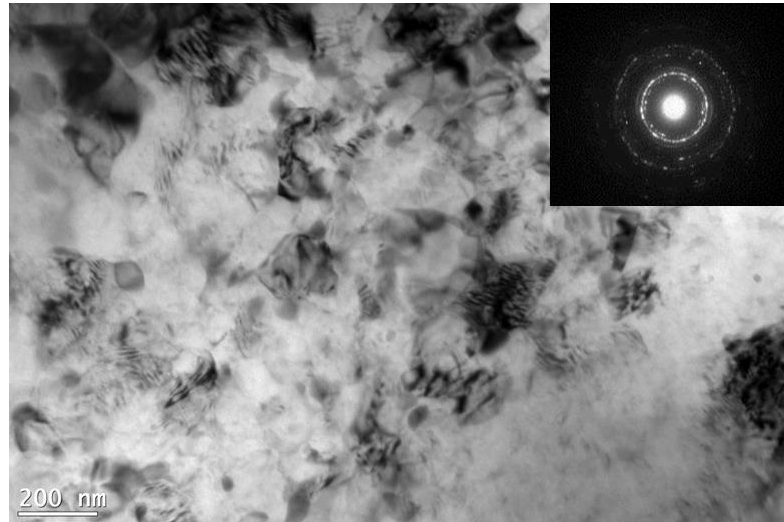
The resultant microstructure with a large fraction of high-angle grain boundaries was confirmed by selected area electron diffraction (SAED), as in Figure 4.18. This shows how the build-up of dots at 1/4 and 1 turn, (a) and (b), developed into circular rings after 10 turns in (c), which confirms the production of UFG separated by boundaries having high angles of misorientation.



(a)



(b)



(c)

Figure 4.18 Images from TEM combined with the diffraction patterns for the AZ80 alloy after processing by HPT at room temperature for: (a) 1/4 turn; (b) 1 turn; and (c) 10 turns.

Although the process was conducted at ambient temperatures, there is no evidence of twinning deformation in the OM or SEM images. The only evidence of twinning was found in grains of an average size of ~ 50 nm, as indicated by the yellow box in the TEM image in Figure 4.19, which shows the microstructure of the alloy after one turn of HPT at room temperature.

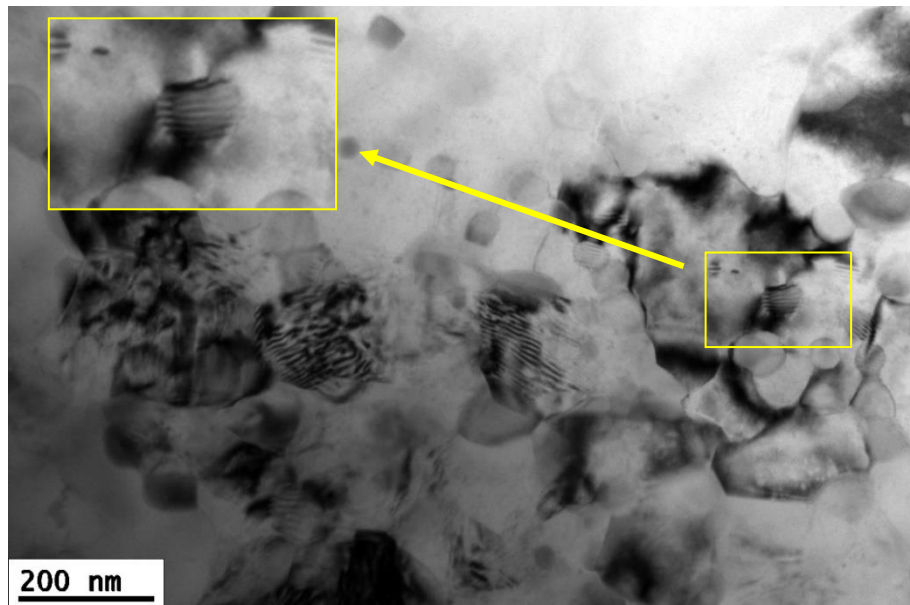


Figure 4.19 TEM images showing the microstructure of sample processed by HPT for one turn at room temperature. A twinning deformation is appearing at grain size ~ 50 nm.

4.2.2 Microstructure observation through the disc thickness

Figure 4.20 shows the microstructures through the disc's thickness. It was found that there is a dissimilarity of contrasts in different regions through the disc thickness. This difference lies in the brightness of the images, indicating differences in microstructure development and specifically plastic flow distribution through the disc thickness. Two different areas were observed in the microstructure, as presented in Figure 4.20. Areas with smaller grain size structure appear slightly darker than areas with coarse grains. The inspection through the thickness revealed a clear variation in microstructure, more than that along the diameter even at a high number of turns. A second observation that can be seen in Figure 4.20 is the presence of a coarse-grained structure at the top and the bottom surface of the disc, while the mid-thickness area has a finer-grained structure. This was observed in earlier experiments when AZ31 magnesium alloy was processed by HPT at 463 K [192]. This observation is contrary to the assumption in Equation (2.4) that a constant amount of imposed strain from the top surface to the bottom surface of the disc leads to homogenous deformation throughout the disc thickness. This area of finer grain indicates a higher plastic flow in the mid-thickness region, leading to a higher degree of deformation in that area than in the top and bottom surfaces. This difference in average grain size structure between neighbouring areas was found in both the centre and the edge of the discs.

As shown in Figures 4.20 (a) and (b), when the disc was processed for one turn the area of finer grains is larger in thickness at the edge of the disc than the centre, and this observation is found also in the disc processed by HPT up to 3 turns in Figures 4.20 (c) and (d). This suggests a higher imposed strain at the edge of the disc. This area of higher deformation expanded in a vertical direction at the centre region of the disc with increasing number of turns. When the disc was processed up to 10 turns, the difference in the size of the highly refined mid-thickness region between the centre and the edge of the disc was reduced, as shown in Figure 4.20 (e) and (f).

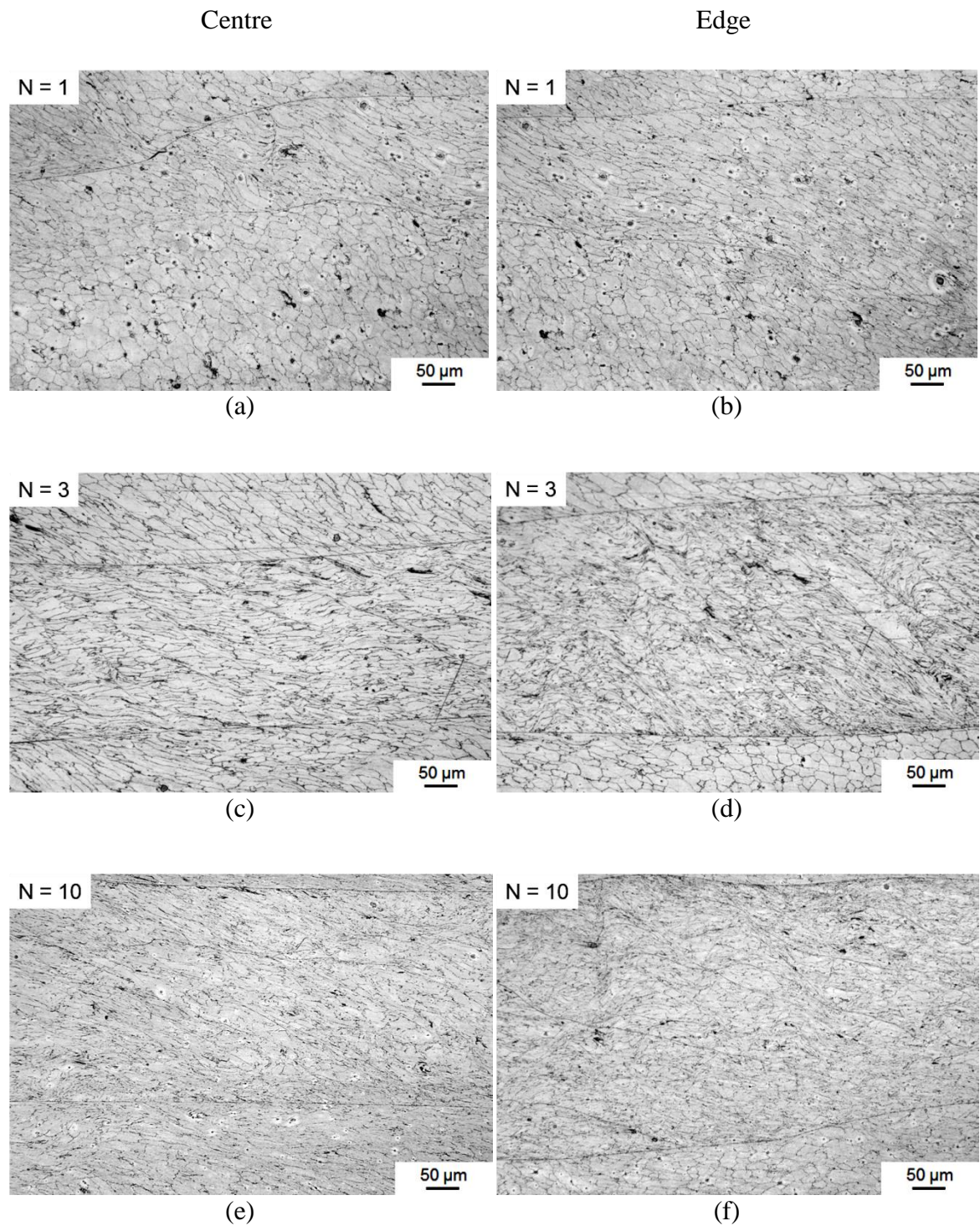


Figure 4.20 Optical images showing the centre (left column) and edge (right column) for the whole thickness after HPT processing at room temperature through: (a, b) 1 turn; (c, d) 3 turns; and (e, f) 10 turns.

4.3 Microhardness evolution after HPT processing at 296 K

4.3.1 Microhardness along the disc diameter

Hardness measurements were taken across the diameter of each processed disc. The results of Vickers microhardness, Hv, measurements along the disc diameter for various numbers of turns 1/4, 1, 3, 5 and 10 are depicted in Figure 4.21: N = 0 represents the disc pressed for one minute without rotation. The average microhardness values are plotted as a function of distance (r) to the centre of the disc. The lower dashed line symbolizes the average microhardness value obtained from the cross-diameter of the discs in the as-received condition of 63 Hv.

Inspection shows that the microhardness values are higher after processing by HPT at room temperature than in the as-received condition. The hardness profile showed a rise in hardness with increasing distance from the centre of the disc at early stages of HPT through 3 turns. This increase in hardness is especially evident around the edges of the discs. In practice, there are significant differences between the edges and the centre at lower numbers of turns. For example, after a 1/4 turn the microhardness value was ~110 Hv at the edge, but only ~88 Hv at the centre. There was a gradual increase in average microhardness values at the centre of disc samples processed by up to one turn, with an average value of ~92 Hv. Along the diameter, the difference in the microhardness profile between 1/4 and 1 turn is insignificant, and at the periphery it is essentially negligible. There is a constancy in Hv values of ~90 at $r = 0$, and ~110 at the disc periphery after processing by HPT for a 1/4 and 1 turn.

Samples processed by up to 3 turns developed significantly increased microhardness values from the edges toward the disc centre. The area of high microhardness values was wider in discs processed to a higher number of turns than with fewer turns, and the area of the higher microhardness values extended from $r > 1$ mm to the disc periphery, yet a sharply defined area showed that the minimum hardness value, average ~ 92 Hv, appeared at the centre, and that area started at $r < 1$ mm and extended to the disc centre. The microhardness values of samples processed by 5 and 10 turns were saturated to Hv ~120 through the total disc diameter and showed reasonable homogeneity across the disc diameter through 5 and 10 turns. The central region of the disc showed lower values of microhardness values in the early stages of HPT, which is compatible with the

imposed equivalent strain, as in Equation 2.4. The microhardness values are consistent with the microstructure evolution after processing the alloy by HPT for different number of turns, where the higher microhardness values and the finer grains are present at the edge of the disc in the early stages.

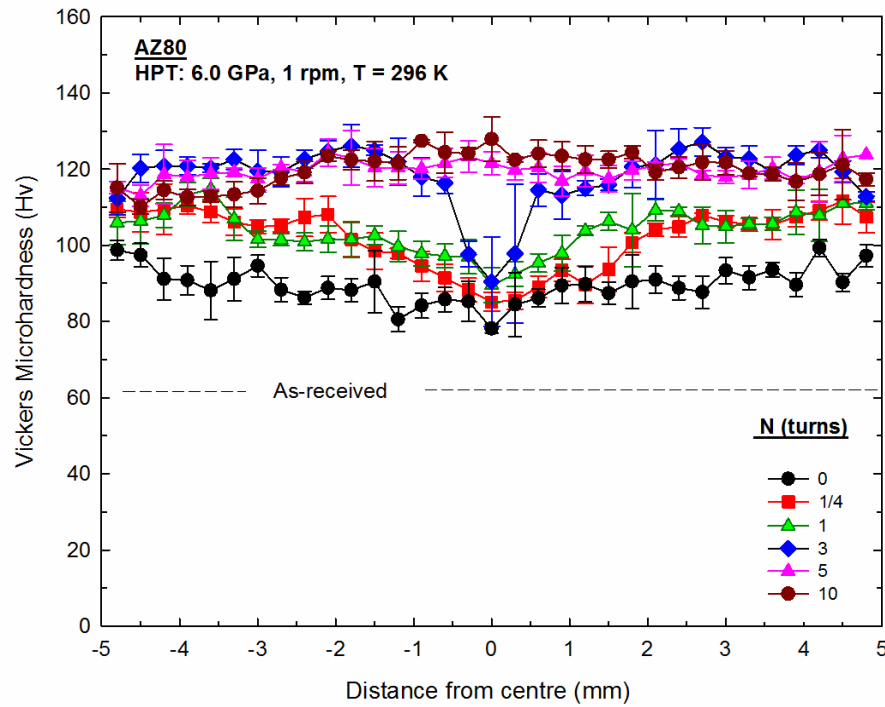


Figure 4.21 Vickers microhardness H_v , plotted as a function of position on disc processed by HPT at room temperature using an applied pressure of 6.0 GPa through 0 to 10 turns: the lower dashed line at $H_v \sim 63$ shows the as-received condition.

The material demonstrated strain-hardening behaviour during the HPT process. This is displayed in Figure 4.22 when plotting the microhardness values, H_v , against the calculated equivalent strain using the relationship in Equation 2.4. In Figure 4.22, all the individual datum points are plotted together and essentially delineate a single curve. Thus, the as-received microhardness value of H_v , 63 initially increases to >80 at the centre and the edge of the 1/4 turn disc, there is a continuous increase in microhardness values, up to ~ 120 H_v at an equivalent strain of ~ 30 and, thereafter, at even higher equivalent strains, hardness remains reasonably constant up to equivalent strains of >200 . This indicates the development of a steady-state, or saturated, condition. This behaviour was described in earlier studies as the standard model of hardness evolution, where microhardness values increases until saturated at high strain [193,194].

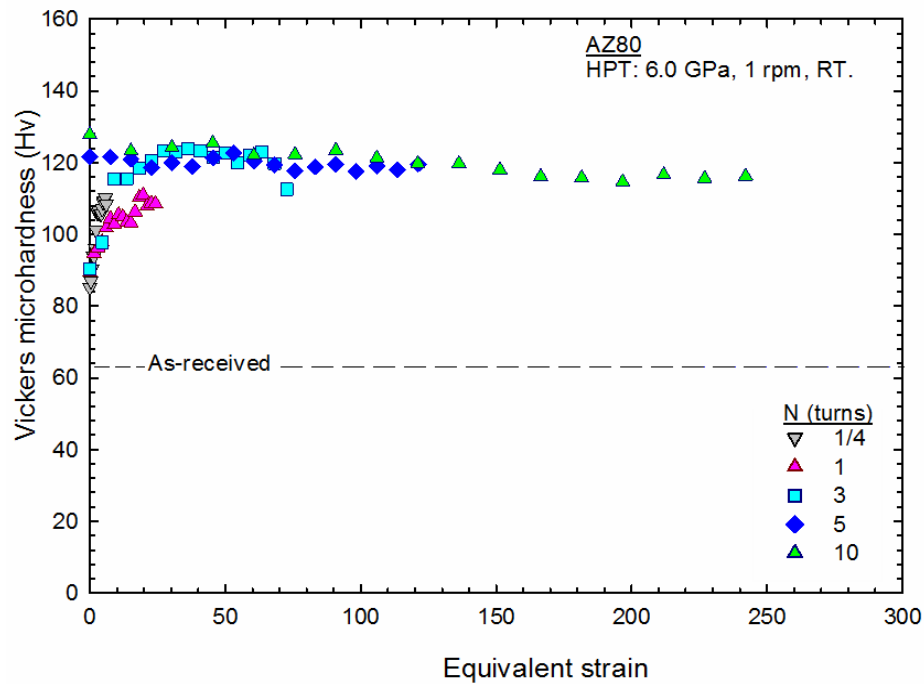


Figure 4.22 Vickers microhardness Hv, plotted against equivalent strain showing the development of saturation conditions at strains above ~ 30.

Figure 4.23 shows the hardness evolution occurring during the HPT process at the centre and the edges of the discs for up to 10 turns. The increase in microhardness values from the as-received condition at both the centre and the disc periphery started at the pressing stage. There was a difference in the microhardness values between the centre and the edge of the disc: an increasing number of turns decreases the difference, as shown when the alloy was processed for five turns. At this higher number of turns, the alloy shows a reasonable homogeneity and the difference in values between the centre and the edge of the disc becomes very small.

Figure 4.24 shows the average microhardness values plotted against the numbers of turns. This graph demonstrates the increase in average microhardness value along the disc diameter with increasing numbers of turns, where the average is ~101 Hv at a 1/4 turn, increasing to an average of ~104 Hv at 1 turn. The largest increment in the average value was when the AZ80 was processed up to 3 turns, when the average microhardness reached a value of ~118 Hv. As the material was processed by 5 and 10 turns, the average microhardness value did not change further and was saturated at an average of ~120 Hv.

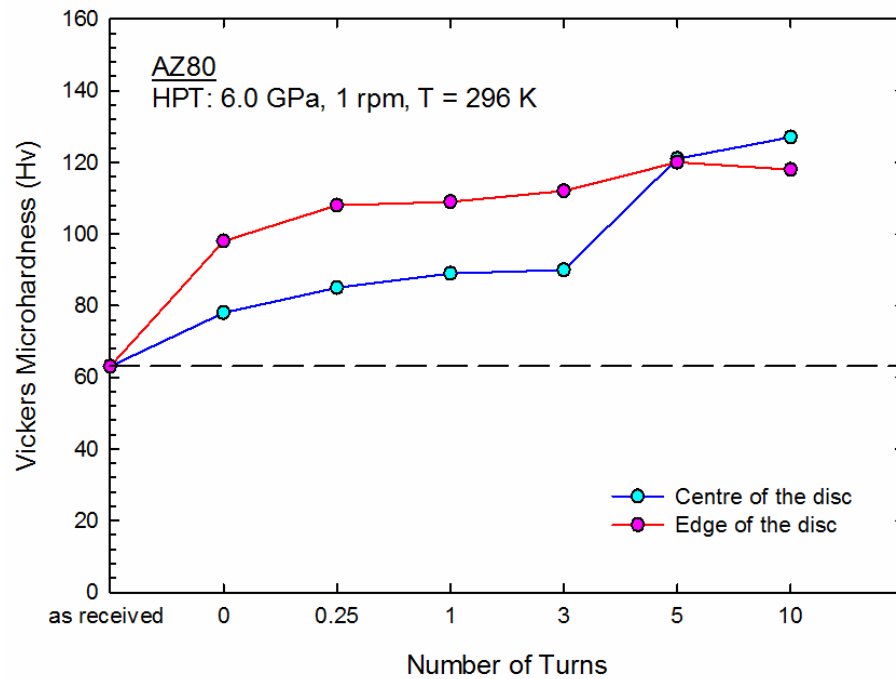


Figure 4.23 Comparison of the hardness evolution between the centre and the edge of discs processed by HPT for up to 10 turns at room temperature.

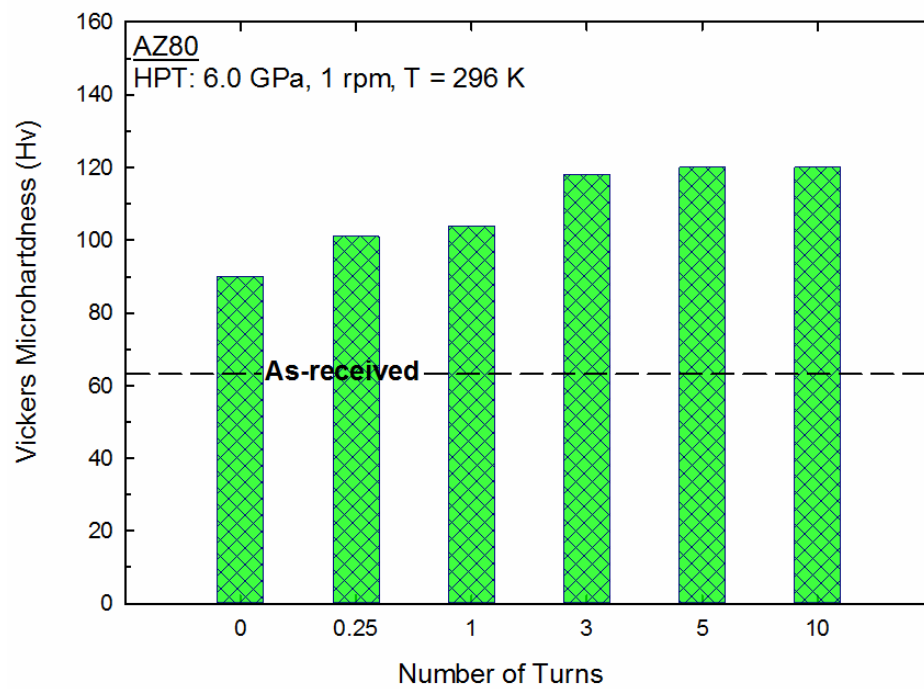


Figure 4.24 Variation in the average microhardness values Hv of AZ80 processed by HPT at room temperature, plotted against number of HPT process turns N.

The measurement of average grain size against the average Vickers microhardness (Hv) for 1, 3, 5 and 10 processed turns is plotted in Figure 4.25. The average grain size after one turn was ~ 370 nm. Increasing the number of turns imposed more strain on the sample and gave a further reduction to the grain size, up to a reasonable stability of grain size after 5 and 10 turns, with an average of ~200 nm.

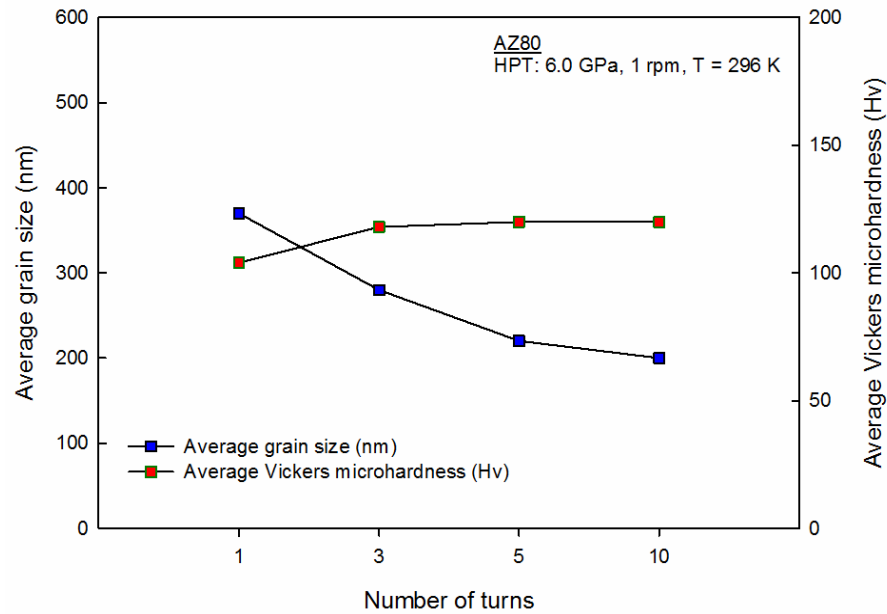


Figure 4.25 Average grain size and the average microhardness values of the alloy processed by HPT for different number of turns at 296 K.

The overall hardness evolution development for the whole disc surface is displayed using colour-coded contour mapping, as shown in Figure 4.26. The microhardness data were recorded using a rectilinear grid pattern at 0.3 mm spacing between each point. These maps provide attractive displays of the microhardness values distribution over the whole surface for processed discs. The two perpendicular axes X and Y are marked in mm, where the position (0, 0) is the midpoint of each disc. The microhardness values are in the range of 80 to 140 Hv, represented by a series of colour increases of 10 Hv.

These plots demonstrate the material tendency toward structural homogeneity with increasing numbers of revolutions. There is a large area in the centre of the disc where the microhardness values were lower in samples processed by HPT to 1/4 turn. The microhardness values were of an average of ~90 Hv at the centre, while higher hardness values at the edges of the disc were within the range of 120 to 130 Hv. The proportion

of the area having lower microhardness values fell in the sample processed by HPT for more than one turn, as at this stage the microhardness values gradually increased and expanded toward the disc centre. Discs processed by up to five turns show an increase in the microhardness values over the entire disc surface to an average value of ~ 120 Hv. The disc surface shows a reasonable homogeneity after five turns.

AZ80

HPT: 6.0 Gpa, 1 rpm, T =296 K

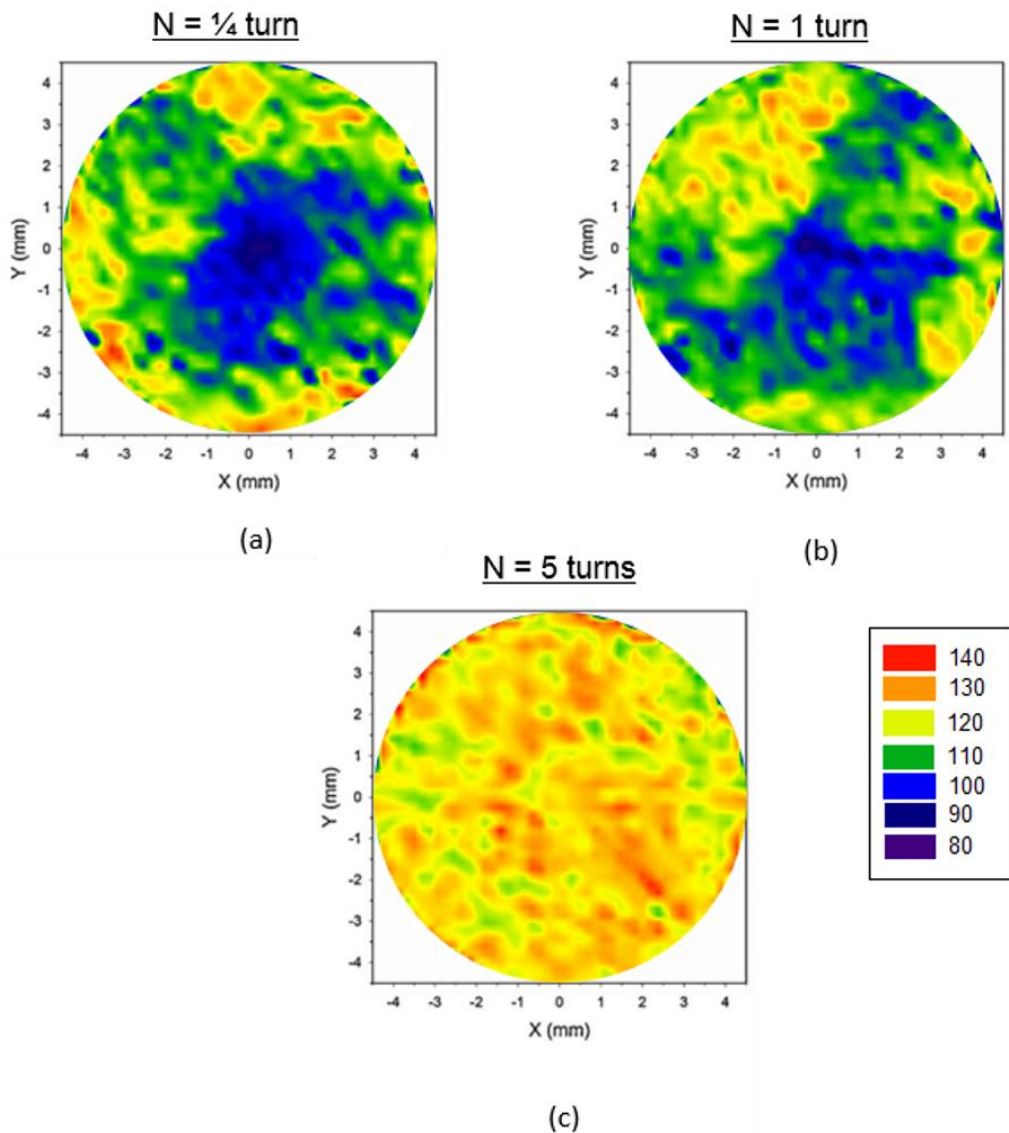
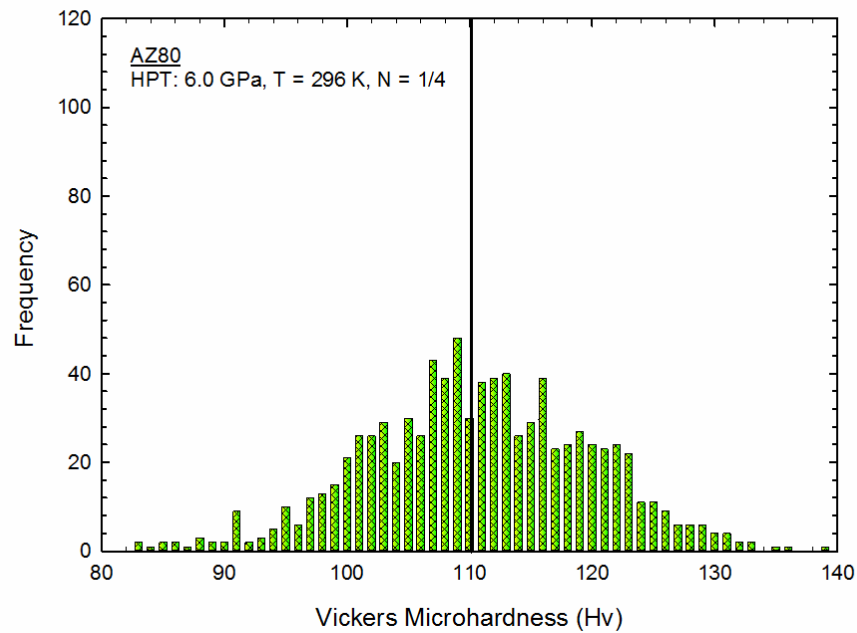
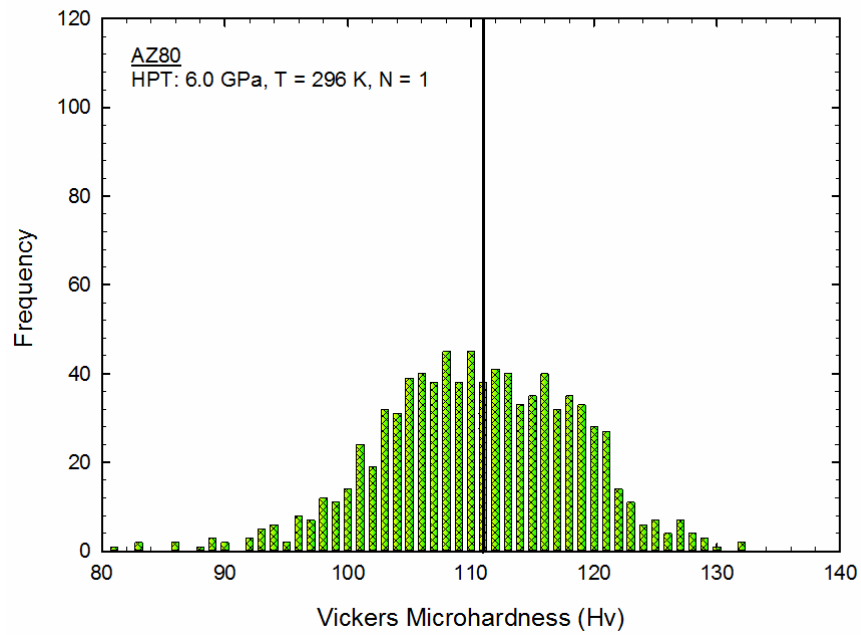


Figure 4.26 Colour-coded contour maps showing the distribution of the Vickers microhardness values of processed AZ80 discs by HPT at room temperature at: (a) 1/4; (b) 1; and (c) 5 turns.

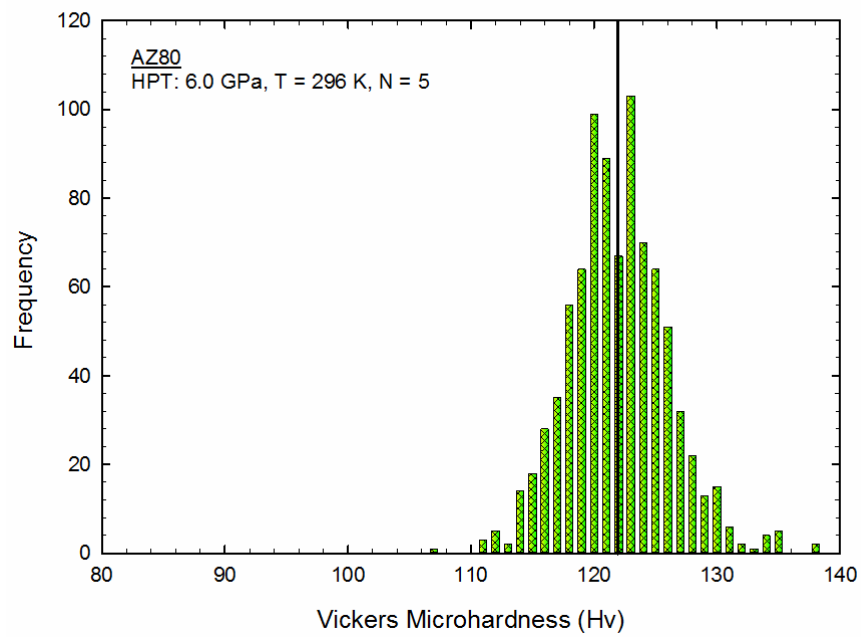
Figure 4.27 was generated by using the Vickers microhardness values used in Figure 4.26. The values were plotted against their frequency using the same data that were collected to generate the colour-coded mapping for the whole surface of the disc processed by HPT for 1/4, 1 and 5 turns. In this histogram, the average microhardness values is represented by a vertical line. The results of these data lead to two conclusions: first the width of the distribution is at a maximum at a 1/4 turn and this width becomes narrower when the material is processed to a higher number of turns. Second, the average value of the microhardness values collected over of the whole disc surface rises with increasing number of turns. In discs processed for a 1/4 turn, the average microhardness value was 110 Hv, while it was 122 Hv for a disc processed for 5 turns.



(a)



(b)

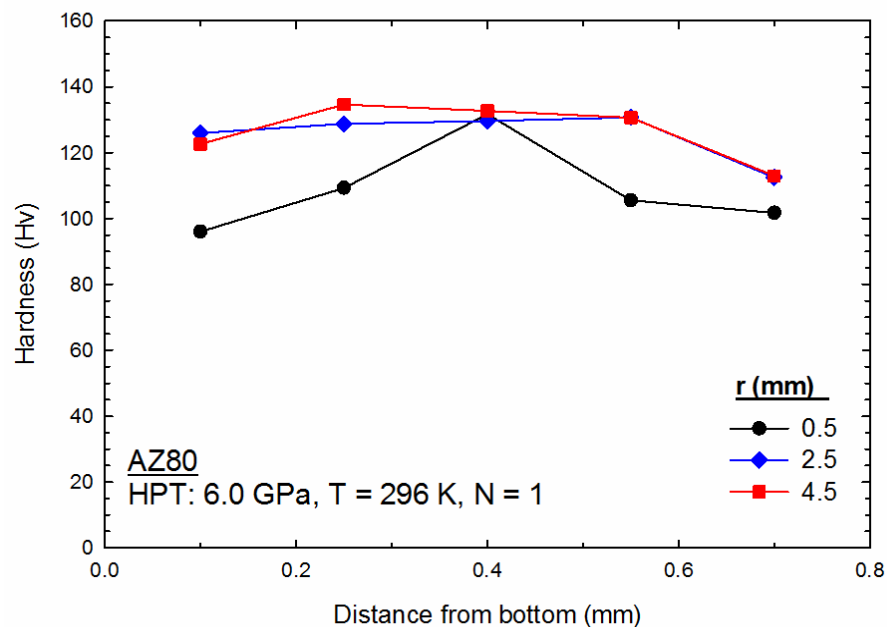


(c)

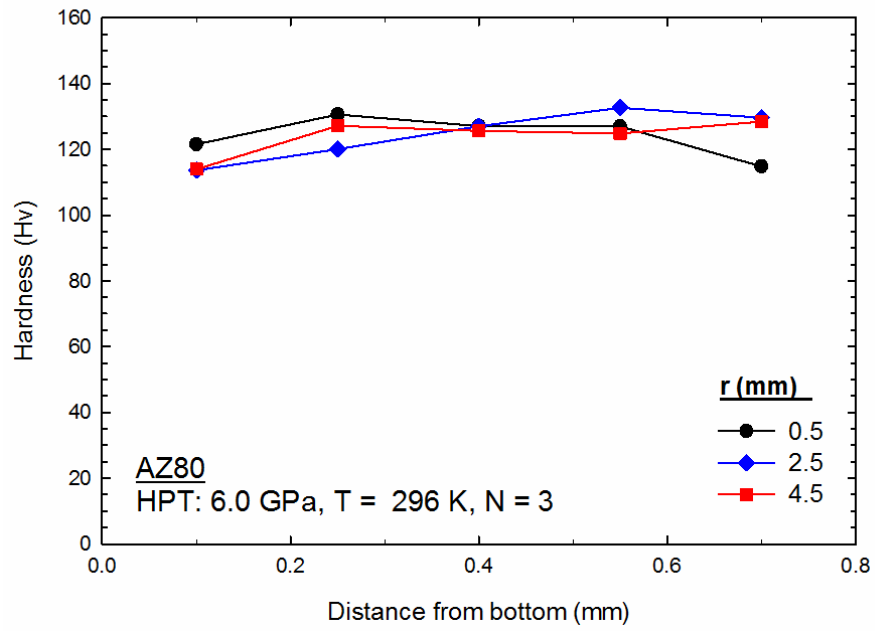
Figure 4.27 Histogram of Vickers microhardness values distributed at the whole disc surface after processing by HPT at room temperature through (a) 1/4 turn; (b) 1 turn; and (c) 5 turns. Vertical lines denote the average value.

4.3.2 Microhardness through the disc thickness

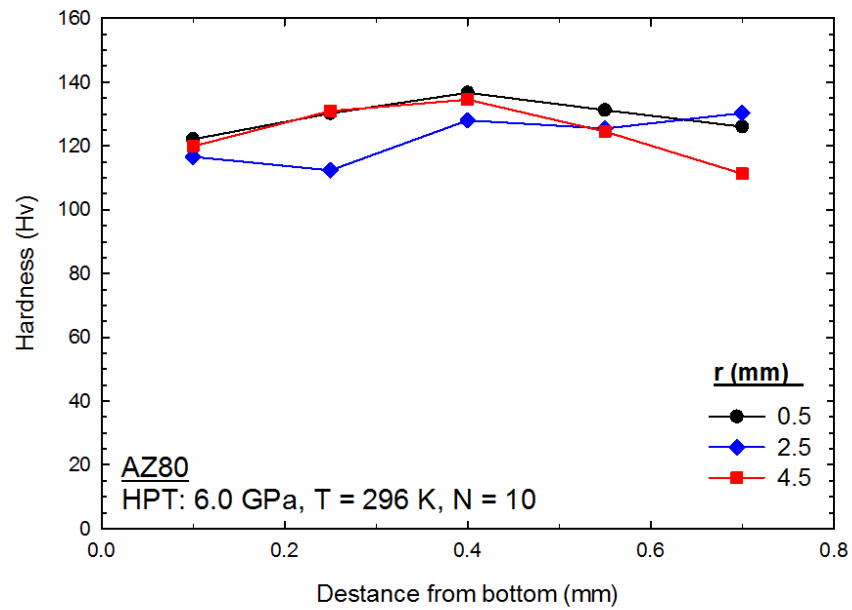
Samples processed by HPT for 1, 3 and 10 turns using an applied pressure of 6.0 GPa at room temperature were cut in a vertical direction and tested using the Vickers microhardness test. The microhardness values were used to determine the difference in homogeneity in the through thickness direction, as in Figure 4.28. These were measured at different radii from the centre, at 0.5 mm, 2.5 mm and 4.5 mm, and plotted as a function of distance from the bottom as described in Figure 3.4. At one turn, there was a clear variation in microhardness values near the centre between bottom, mid-thickness and top surface. The smaller values were found at the bottom and the top, with an average value of ~95 Hv, while higher values were at the mid-thickness, with an average value of ~125 Hv. At 3 turns, the variation in the microhardness values became less between the bottom, mid-thickness and top surface in the centre and at the edge of the disc. At 10 turns, there was difference in microhardness values between the higher values at the mid-thickness of the disc, and the lower values at the bottom and the top surface of the disc.



(a)



(b)

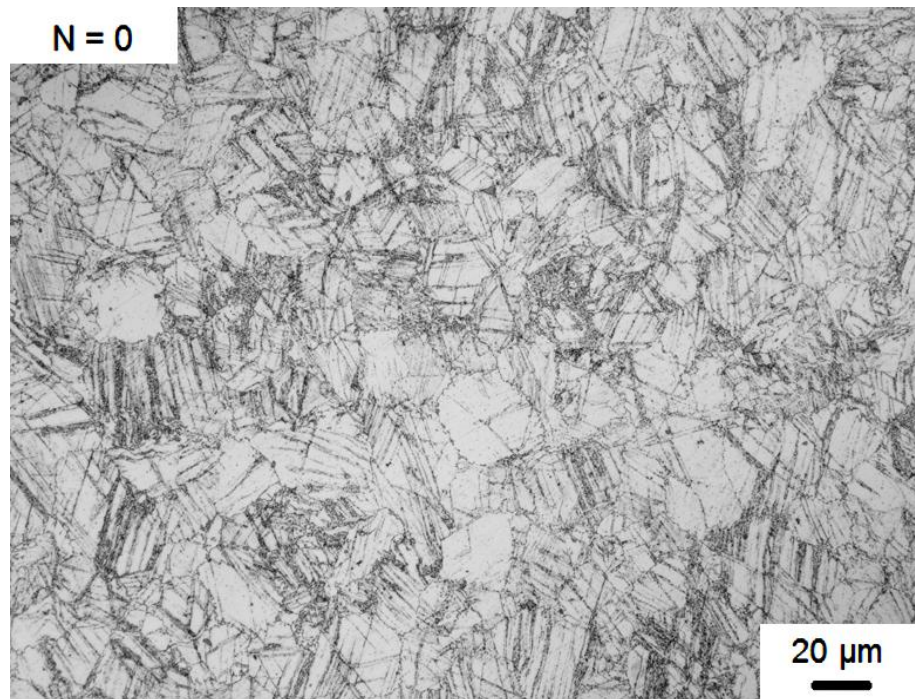


(c)

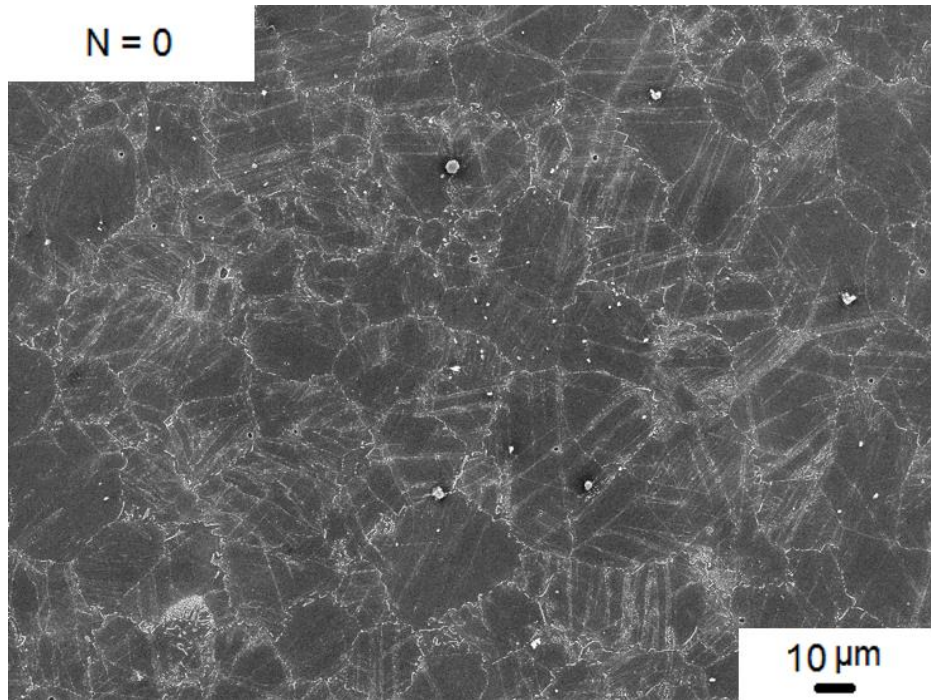
Figure 4.28 Microhardness values at different displacement from the centre as a function of distance from bottom to top of the disc processed by HPT at 296 K: (a) 1 turn; (b) 3 turns; and (c) 10 turns.

4.4 Microstructure development after HPT processing at 473 K

Processing AZ80 magnesium alloy by HPT at elevated temperature was successful; the microstructure evolved toward homogeneity with increasing numbers of turns. After 10 turns of the HPT process, it displays an excellent grain refinement with ultra-fine grains having a high angle of misorientation. An interesting observation in samples processed by HPT at 473 K was observed: while there was no obvious twinning in the OM and SEM images of samples processed by HPT at room temperature, twinning appears in the alloy processed by HPT at elevated temperature at the early stages of HPT process (the pressing stage), which indicates that the twinning was introduced to the alloy by the compression pressure. This twinning can be seen in OM and SEM images in Figure 4.29 (a) and (b) of samples processed by HPT for $N = 0$ at 473 K. In this condition, the sample was pressed by HPT for one minute without torsion for any number of turns.



(a)



(b)

Figure 4.29 Optical image at (a) and SEM images at (b) showing formation of twinning when AZ80 is processed by HPT at 473 K with $N = 0$.

4.4.1 Microstructure observation along the disc diameter

In order to undertake a systematic microstructure investigation of AZ80 processed by HPT at both room and elevated temperature, two areas at the centre and at the edge of the processed discs by HPT at elevated temperature (473 K) were selected for OM examination. The OM images in Figures 4.30 and 4.31 show the centre of the processed disc in the left column and the edge of the processed discs in the right. The images of the disc processed for a 1/4 and 1 turn showed an intense twinning in the microstructure at both the centre and the edge of the disc. It can be seen that twinning is spread over the whole disc surface. These images display no great differences between the centre and the edge when the alloy was processed by HPT for a few turns.

In contrast, the sample processed for up to 3 turns shows a clearer difference in microstructure between the centre and the edge of the disc, as shown in Figures 4.31 (a) and (b). The fraction of the refined grains is larger at the edge than the centre. The edge of the disc shows a bi-modal structure of ultra-fine grains mixed with coarse grains that are deformed by twinning, while the centre of the disc shows only coarse grains deformed by twinning. This transitional bi-modal structure was reported earlier when

AZ80 was processed by ECAP at elevated temperatures [195]. Figures 4.31 (c) and (d) represent the sample processed by HPT for up to 5 turns. The edge of the disc shows an ultra-fine microstructure. This area of ultra-fine grains has extended to the centre of the disc, as shown in Figure 4.31 (c). A close inspection of the microstructure at the centre after 5 turns (Figure 4.31 (c)) shows a small fraction of coarse grains present at the centre of the disc. These coarse grains are refined effectively with further straining. The microstructure after 10 turns of HPT at 473 K showed that the refinement dominating the central area, as well as the disc periphery, expanded to cover the whole disc from the edge toward the centre. Processing AZ80 by HPT for up to 10 turns at 473 K gave a reasonably homogeneous microstructure.

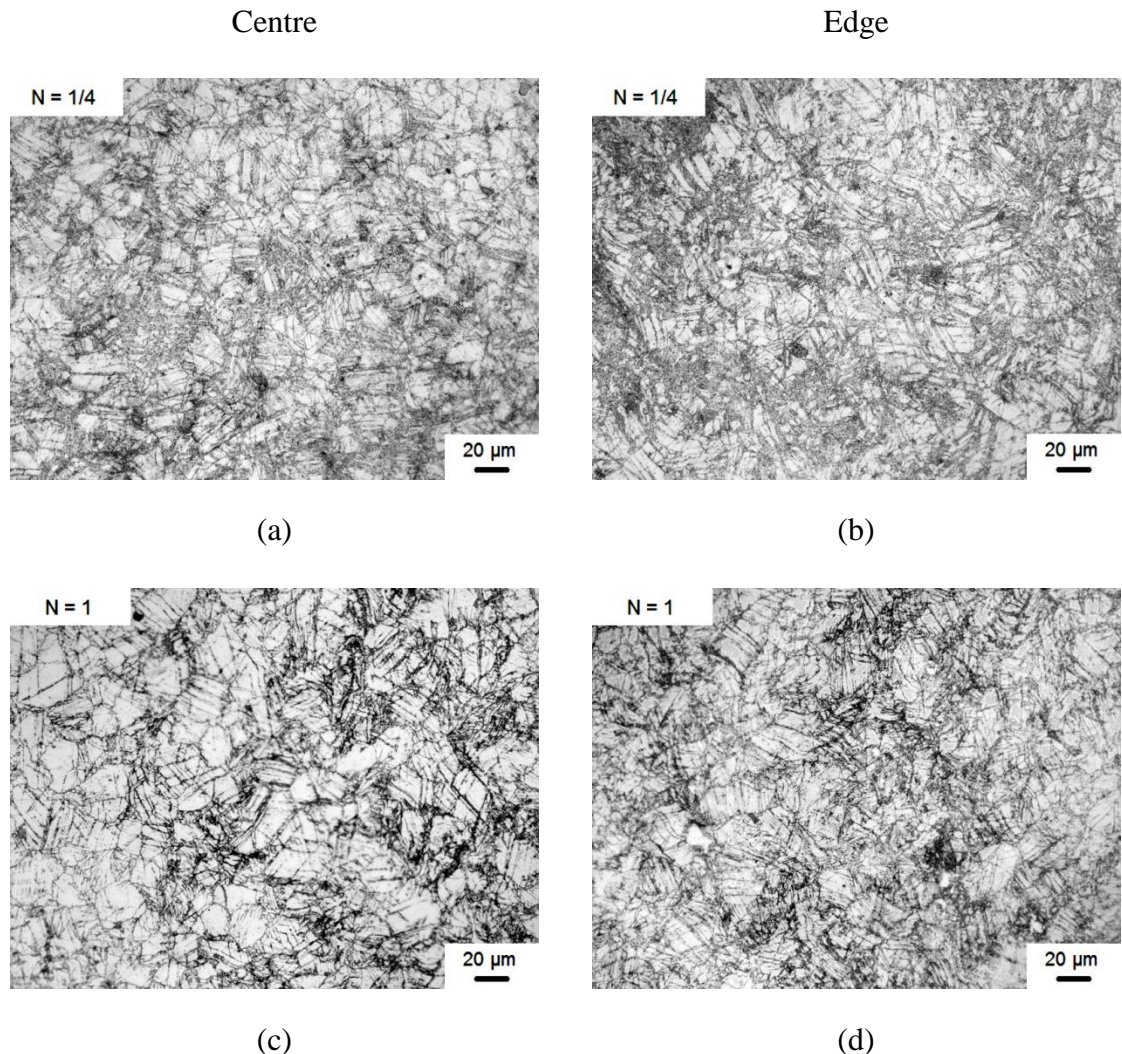


Figure 4.30 Optical images showing centre (left column) and edge (right column) after HPT processing at 473 K through: (a, b) 1/4 turn; and (c, d) 1 turn.

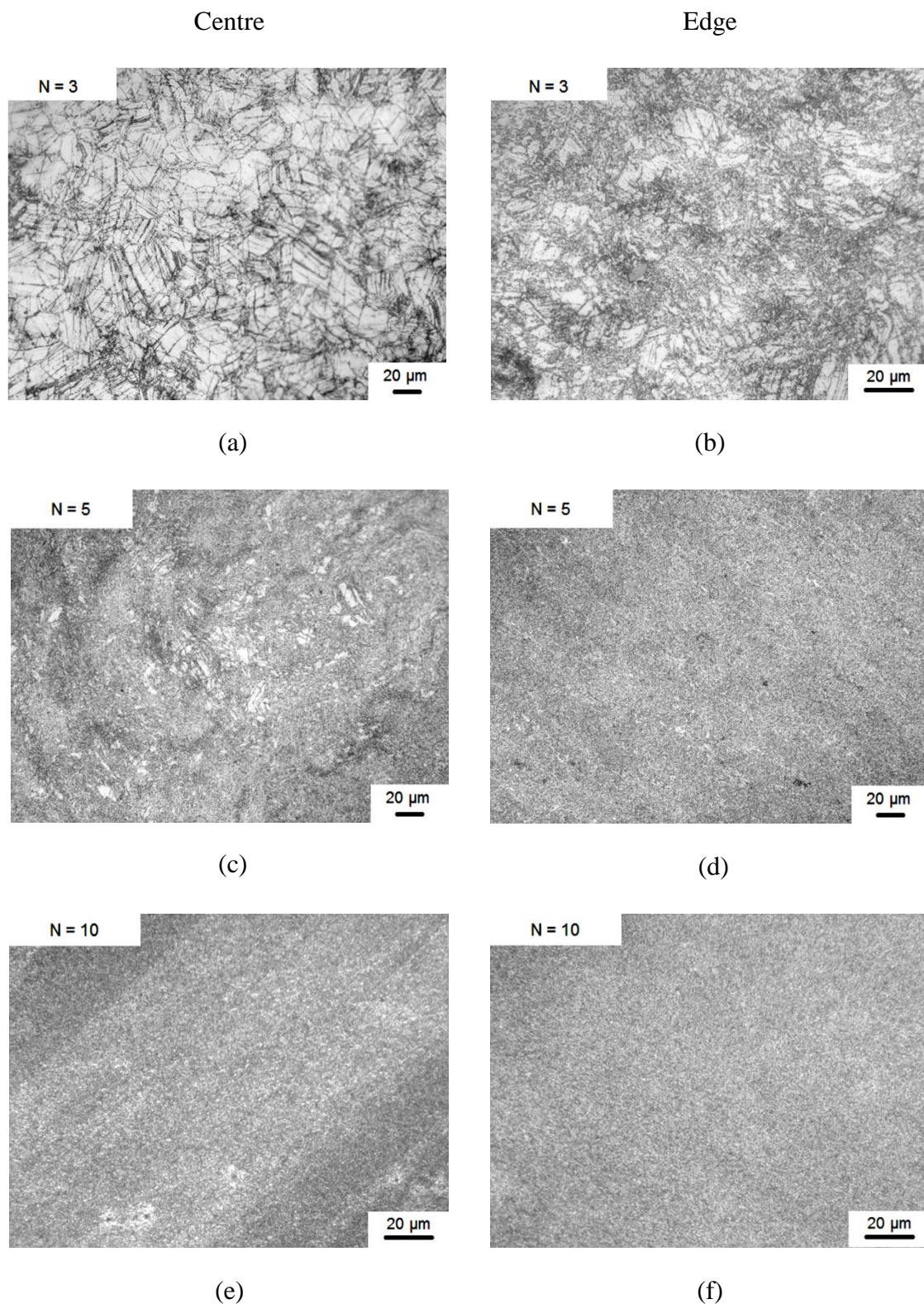
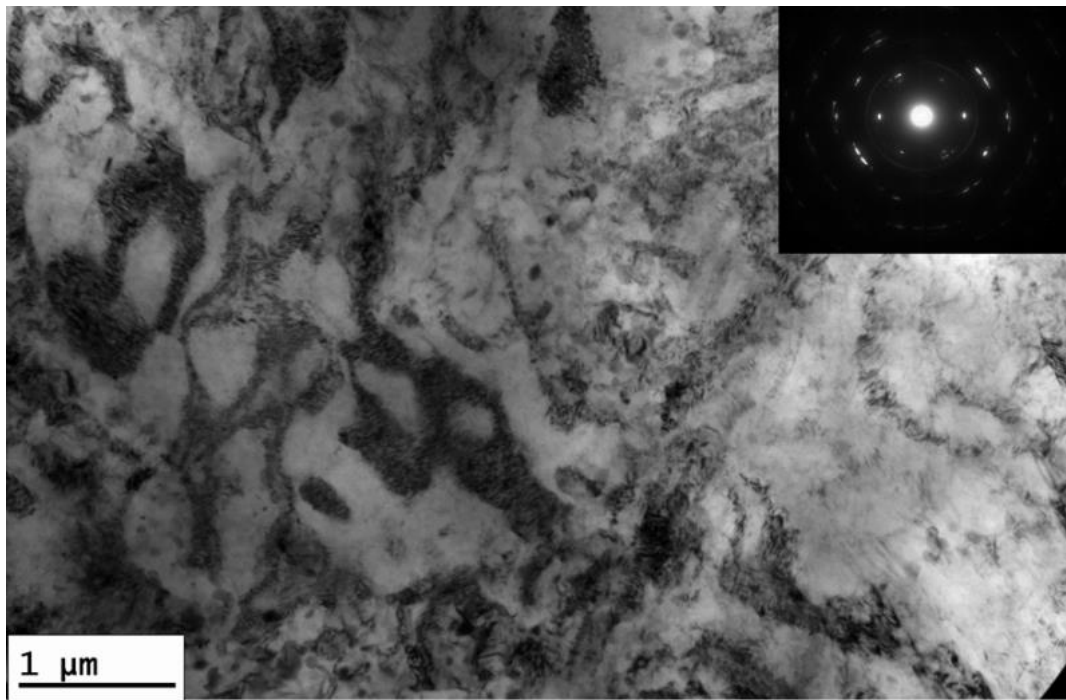
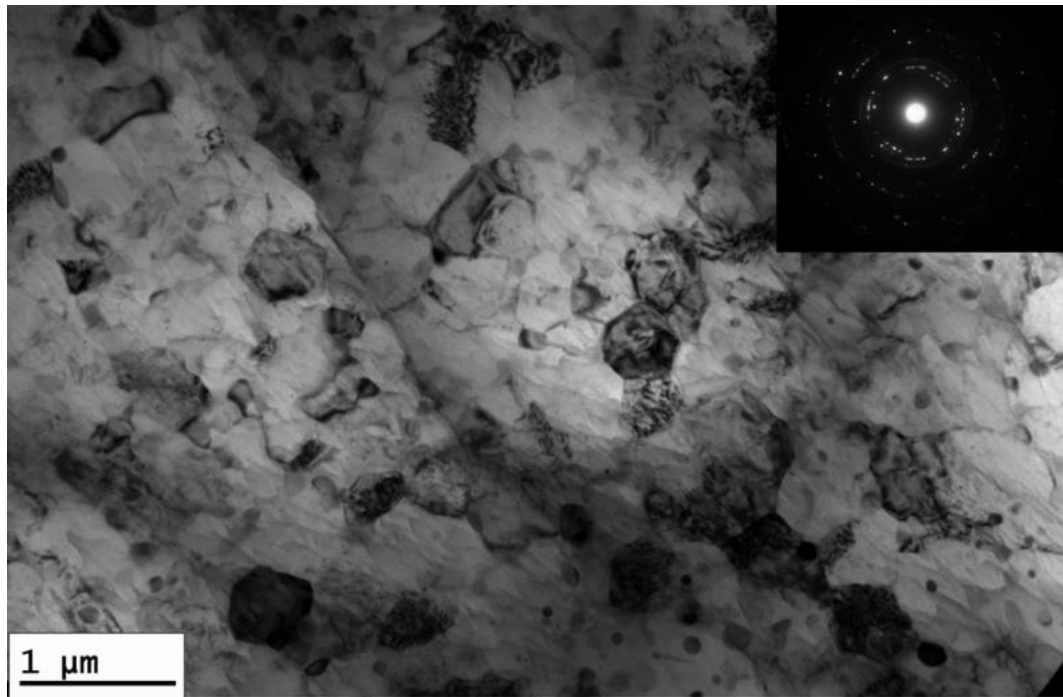


Figure 4.31 Optical images showing centre (left column) and edge (right column) after HPT processing at 473K through: (a, b) 3 turns; (c, d) 5 turns; and (e, f) 10 turns.

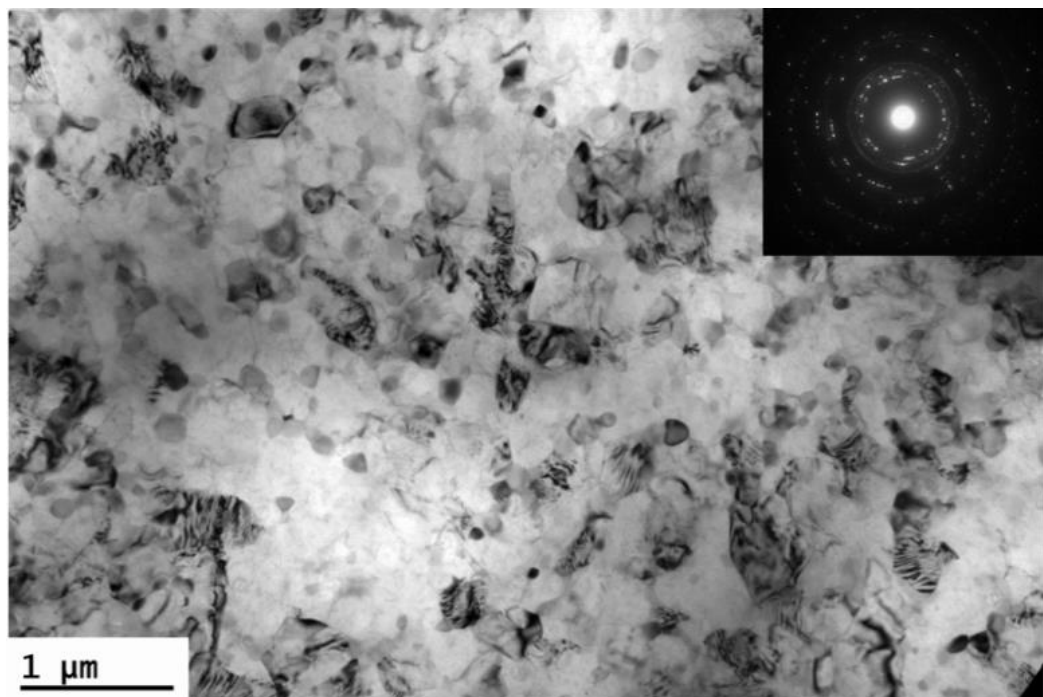
Figure 4.32 shows TEM images of the microstructure evolution of AZ80 magnesium alloy processed by HPT at 473 K. It is clear from Figure 4.32 (a) that the high dislocation density present in the microstructure is due to the HPT process imposing an extreme strain in the alloy. The dislocation cells in Figure 4.32 (a) will develop boundaries upon further straining. The microstructure at Figure 4.32 (b) starts to show some homogenous refined microstructure with increasing numbers of turns, up to 3 turns. The average grain size appears to be smaller than $\sim 1\ \mu\text{m}$, and after 10 turns of HPT at elevated temperature the microstructure illustrates a reasonable degree of equiaxed grains. The SAED patterns confirm the evolution of microstructure toward homogeneity by showing how the build-up of dots develop into almost a complete ring after 10 turns in Figure 4.32 (c). A well-defined ring indicates the presence of grain boundaries with high misorientation angles. The TEM images in Figure 4.32 (b) and (c) show that the average grain size at Figure 4.32 (b) after 3 turns of HPT was coarser than the average size in Figure 4.32 (c) after 10 turns of HPT. Increasing numbers of turns add further reduction to the average grain size and the resultant microstructure shows a UFG with an average grain size of $\sim 330\ \text{nm}$, as shown in Figure 4.32 (c).



(a) 1/4 turn



(b) 3 turns

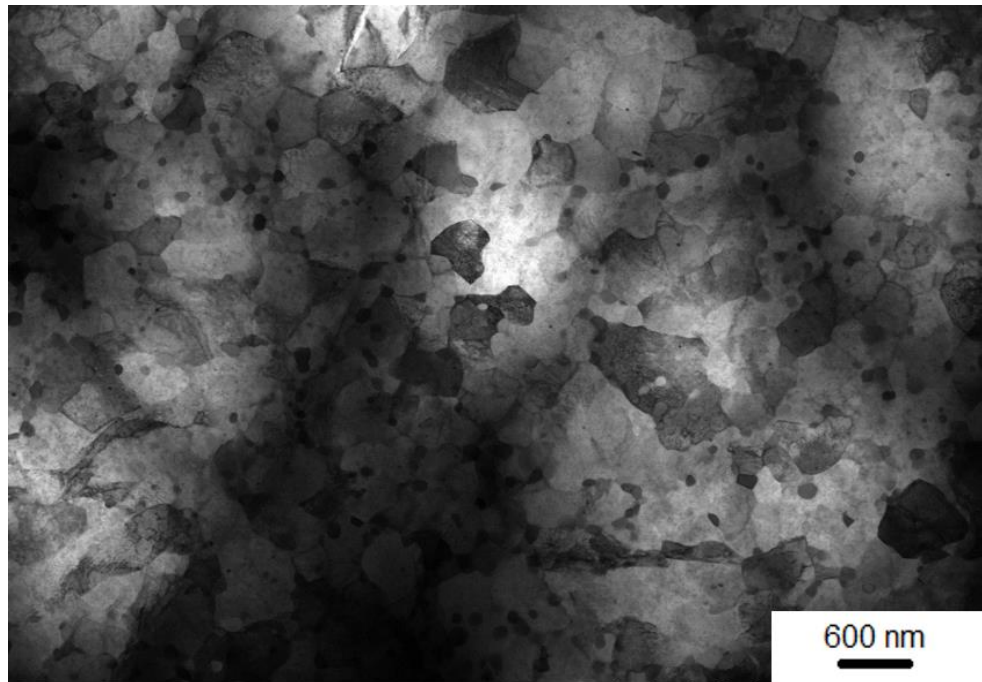


(c) 10 turns

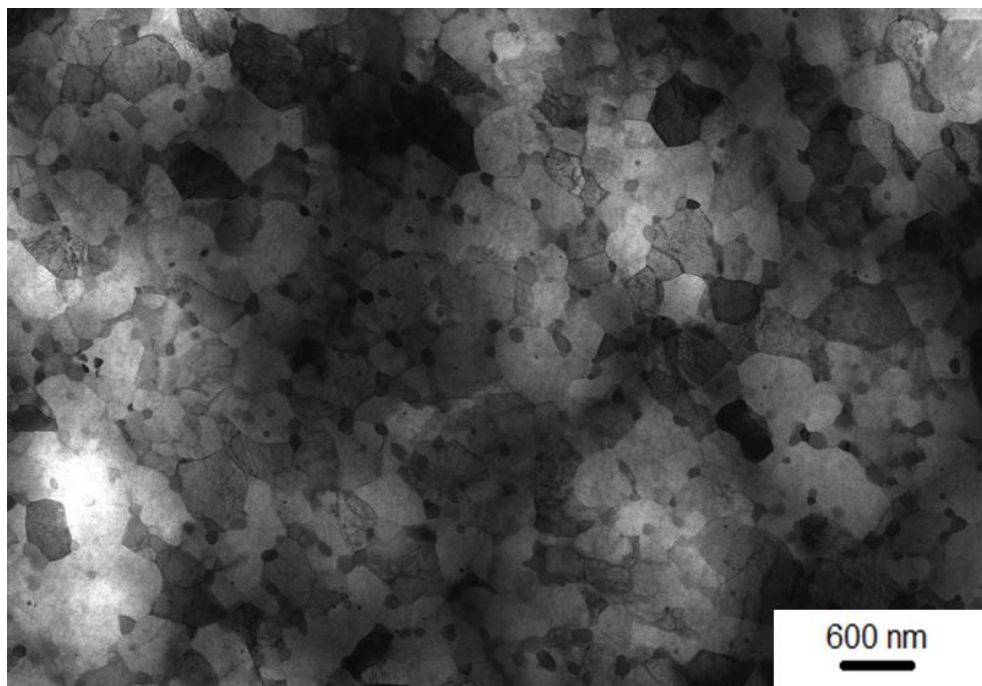
Figure 4.32 Images from TEM combined with the diffraction patterns for the AZ80 alloy after processing by HPT at 473 K for: (a) 1/4 turn; (3) 1 turn; and (d) 10 turns.

The microstructure starts to demonstrate reasonable homogeneity after 5 turns of HPT at elevated temperatures. Although the resultant average grain size is larger than the sample processed by HPT at room temperature, processing AZ80 by HPT at 473 K produced an ultra-fine grain. Figures 4.33 (a) and (b) a STEM images demonstrate the microstructure of samples processed by HPT at 473 K for 5 and 10 turns respectively, which display a reasonable homogeneity.

Figures 4.34 (a) and (b) summarizes the evolution of the precipitates during the HPT process at 473 K. Starting from the early stages of HPT, the precipitates fragment to a fine size in the nanometer range, as shown in the STEM images in Figure 4.34 (a). The process is conducted at elevated temperature, at which there is a high rate of recovery. For this reason, the rate of grain refinement is slower than when conducted at room temperature. This leads to a larger average grain size in the alloy in the early stages of HPT at 473 K than in alloy processed by HPT at room temperature, as it will be demonstrated in Figure 4.42 in comparison to Figure 4.25. This larger average grain size reduces the fraction of the triple junction and results in a random distribution of precipitates in the sample, as shown in Figure 4.34 (a). Inducing further strain by increasing the number of turns will introduce a further reduction in the alloy's average grain size and increase the fraction of the triple junction. This increment in the fraction of the triple junction allows the precipitates to be allocated to that space, as shown in Figure 4.34 (b) (indicated by yellow arrows). The distribution of the precipitates in samples processed for 1 and 5 turns is shown as a points count map in Figures 4.35 (a) and (b). Here, the matrix appears as a dark red point while the precipitates appear as brighter red points. It is clear from those images that there is a difference in the distribution of the precipitates: in samples processed for 1 turn less of the fraction of precipitates are located in the triple junction, while in samples processed for 5 turns more precipitates are located at the triple junction.

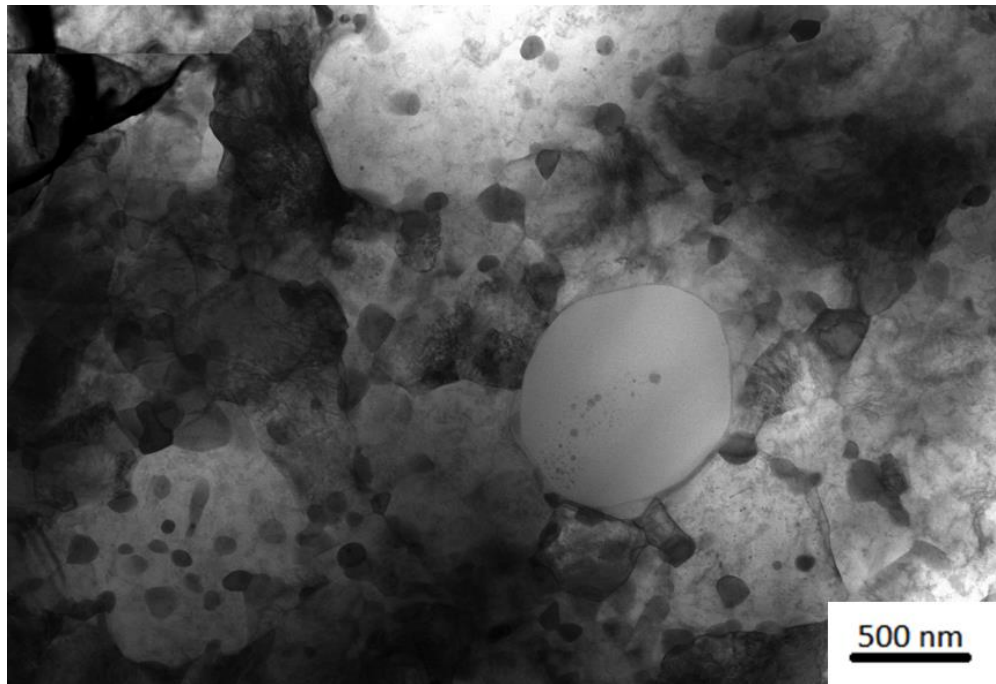


(a)

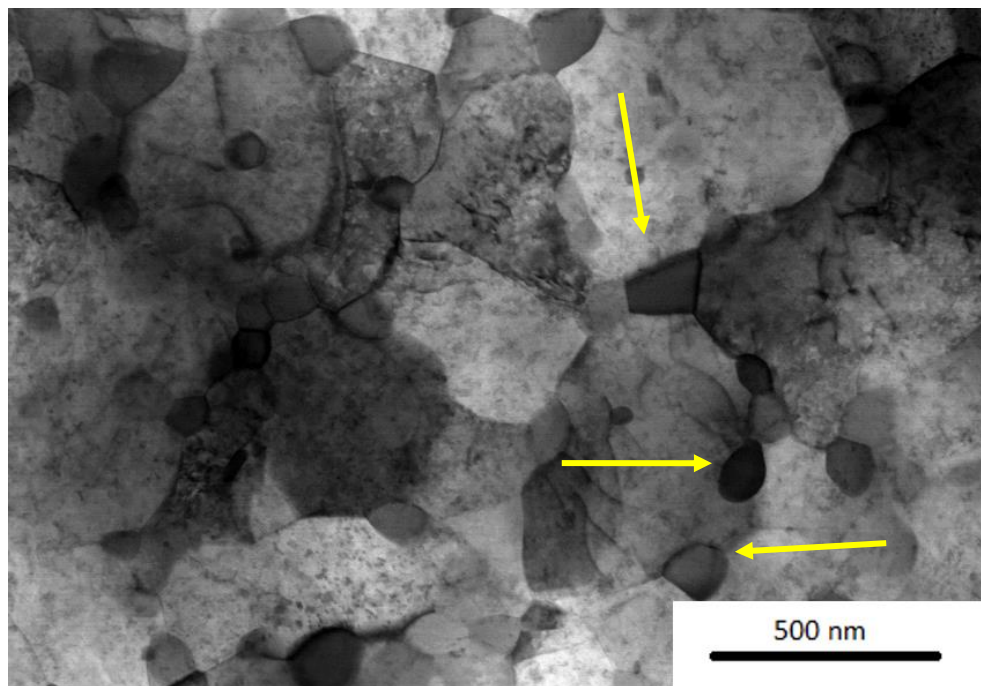


(b)

Figure 4.33 STEM images show a reasonably homogenous microstructure after: (a) 5 turns: and (b) 10 turns of processing by HPT at 473K.

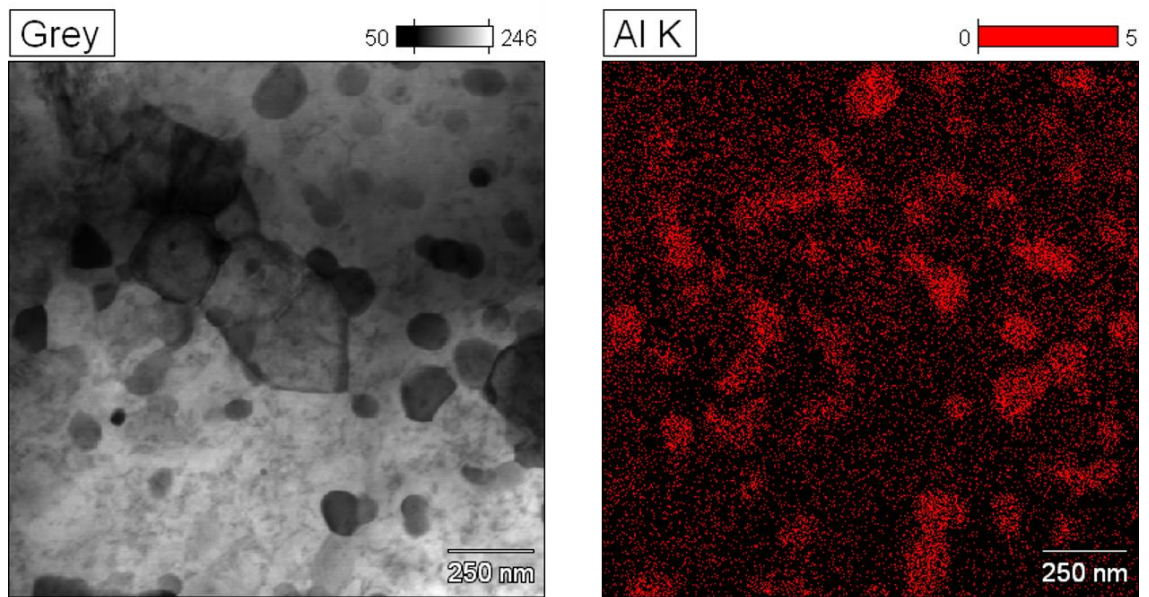


(a)

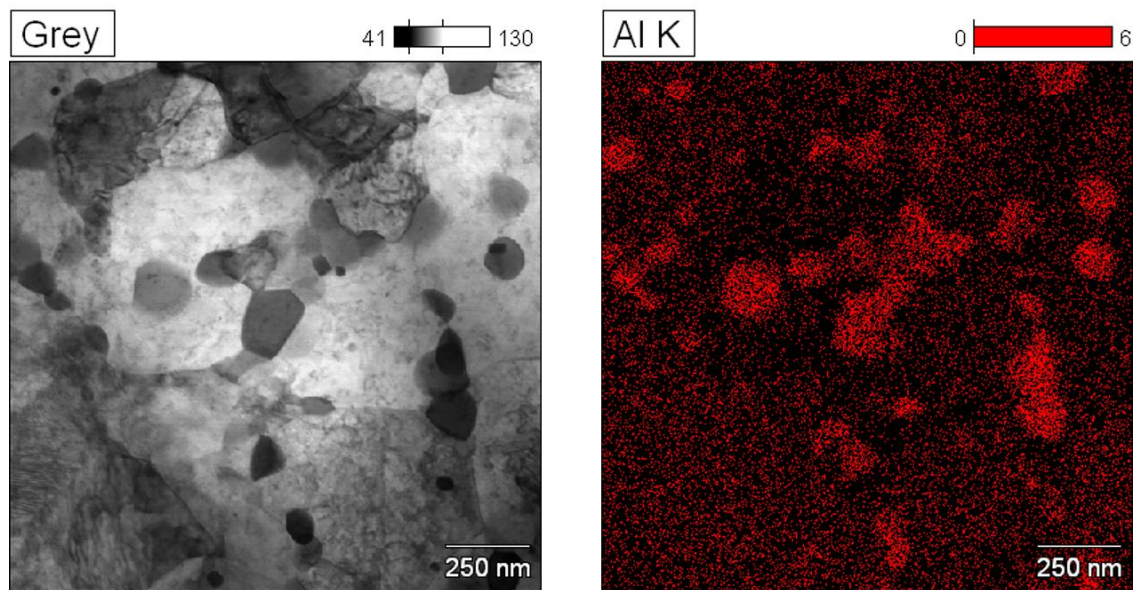


(b)

Figure 4.34 STEM images of the precipitate distribution in AZ80 alloy processed by HPT at 473 K for: (a) 1; and (b) 5 turns.



(a) 1 turn



(b) 5 turn

Figure 4.35 Points count maps to show the distribution of precipitates after processing by HPT at 473 K for: (a) 1 turn; and (b) 5 turns.

Figure 4.36 shows a TEM image of a sample processed by HPT for 10 turns at elevated temperatures. The microstructure shows a reasonable homogeneity with equiaxed UFG grains having an average grain size of ~ 330 nm.

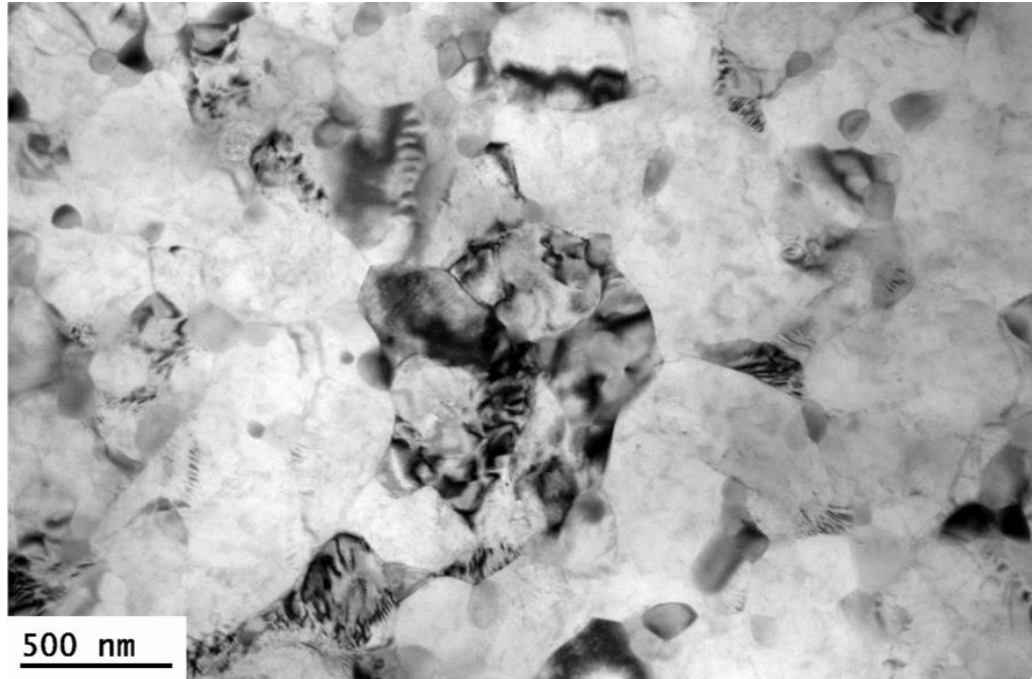


Figure 4.36 TEM image of AZ80 magnesium alloy processed by HPT at 473 K for 10 turns, showing equiaxed UFG grains with an average grain size of ~ 330 nm.

4.4.2 Microstructure observation through the disc thickness

Figure 4.37 (a), (b), (c), (d), (e) and (f) illustrate the development of the microstructure in the vertical section of the processed discs. Three AZ80 discs processed by HPT at 473 K for 1, 3 and 10 turns were examined. The microstructure development in these images is consistent with that at the disc surface. After one turn, the images showed greater refinement of the microstructure at the edge (Figure 4.37 (b)) than the disc centre (Figure 4.37 (a)). Although there is a higher fraction of fine grains at the edge of the disc, there is a notable fraction of coarse grains at the disc centre. This bi-modal microstructure continues at the disc centre in discs processed up to 3 turns, while the edge of the disc showed a higher degree of microstructure refinement without the presence of coarse grains. The disc processed for 10 turns showed a reasonably homogenous microstructure at both the centre (Figure 4.37 (e)) and edge (Figure 4.37 (f)).

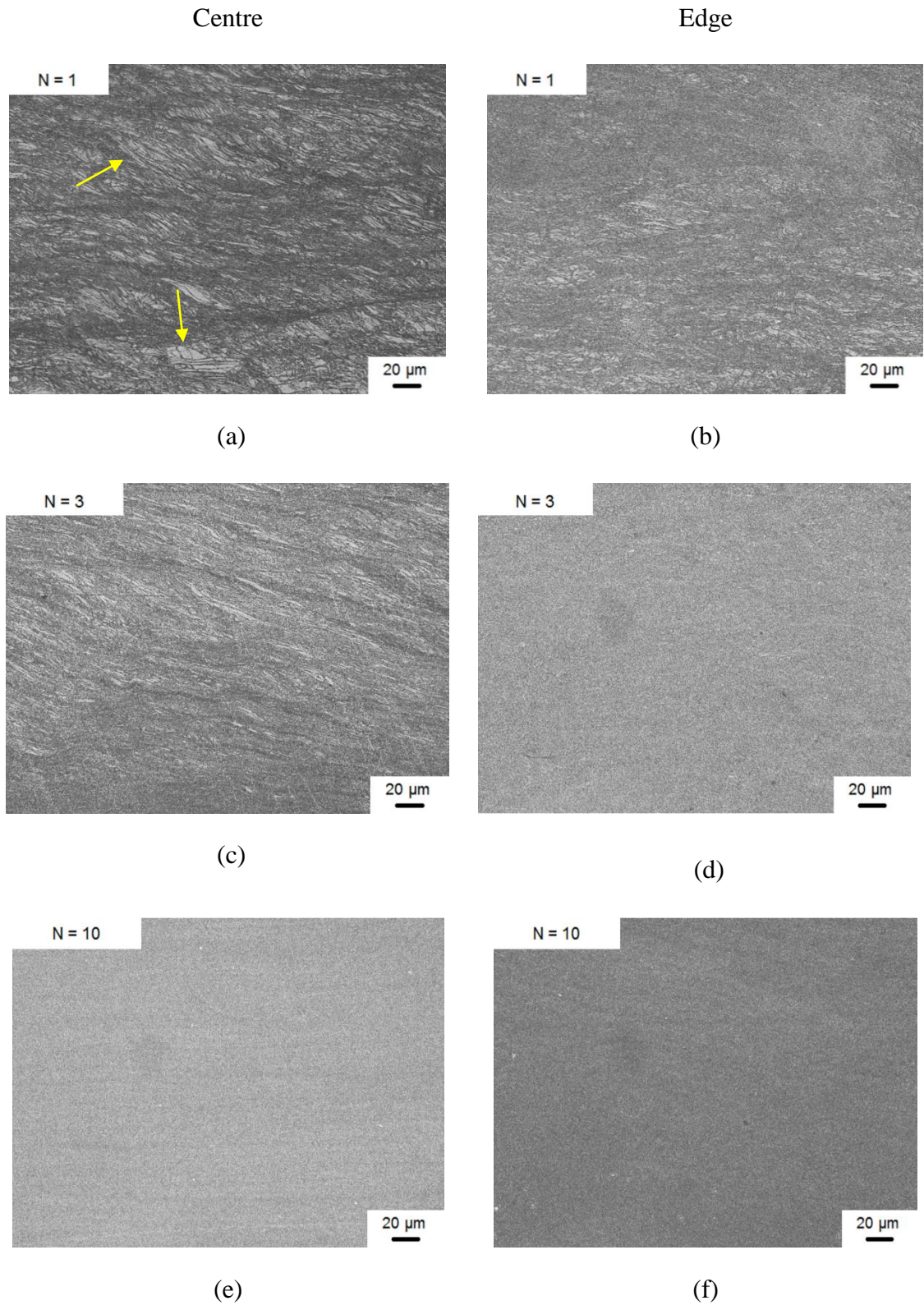


Figure 4.37 Optical images showing the centre (left column) and edge (right column) for the whole thickness after HPT processing at 473K through: (a, b) 1 turn; (c, d) 3 turns; and (e, f) 10 turns.

4.5 Microhardness evolution after HPT processing at 473 K

4.5.1 Microhardness along the disc diameter

Microhardness measurements for each disc processed by HPT at 473 K were taken along the diameter. The Vickers microhardness (Hv) results are depicted in Figure 4.38. The measurements along the disc diameter for various numbers of turns 1/4, 1, 3, 5 and 10, are shown using different symbols and colours in the figure: the $N = 0$ represents the disc pressed for one minute without rotation. The average hardness values are plotted as a function of distance (r) in mm from the centre of the disc. The lower dashed line symbolizes the average microhardness value obtained from the cross-diameter of the discs in the as-received condition of ~ 63 Hv. Processing the alloy by HPT was complicated by the variation in imposed strain along the disc diameter, dependent on the displacement from the disc centre and the number of HPT turns. The results verified a gradual evolution toward homogeneity with increasing numbers of turns up to 5 and 10 turns. This homogeneity was documented when the microhardness values reached the saturation level of ~ 110 Hv along the disc diameter.

As expected, the hardness values increase across the disc diameter, starting from the pressing stage when $N = 0$. A closer look at the hardness profile shows a rise in microhardness values up to ~ 90 Hv at the periphery when the disc was subjected to hydrostatic pressure only, without any rotation. This rapid increase at the disc periphery was not seen at the disc centre, which had a value of ~ 70 Hv. When the alloy was processed for 1/4 turn, the difference between the edges and the centre was reduced, and the average microhardness increased gradually at the disc centre with increasing numbers of turns. The evolution toward saturation level is continued with further rotation. When the alloy was processed for 5 and 10 turns, there were no significant differences in microhardness values, and the size of the error bars decreased with increasing displacement from the disc centre and an increasing number of turns. Saturation was achieved at Hv ~ 110 , at which hardness value the alloy showed reasonable homogeneity across the disc diameter.

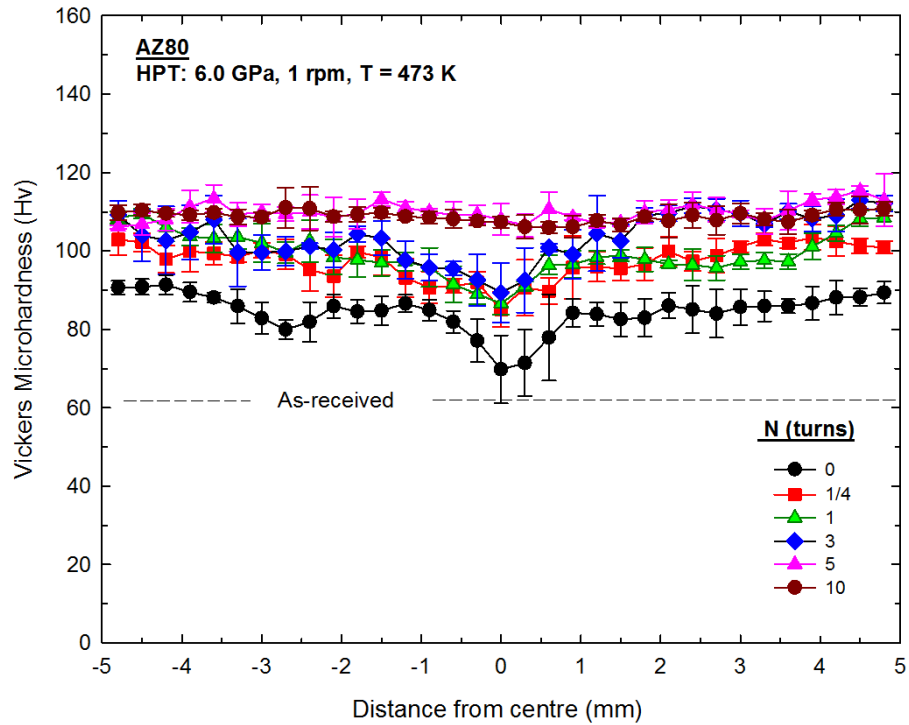


Figure 4.38 Vickers microhardness H_v , plotted as a function of position on discs processed by HPT at 473 K, using an applied pressure of 6.0 GPa through 0 to 10 turns: the lower dashed line at $H_v \sim 63$ shows the as-received condition.

Processing AZ80 magnesium alloy by HPT at elevated temperatures demonstrated strain-hardening behaviour. This is displayed in Figure 4.39 by plotting the microhardness values, H_v , against the calculated equivalent strain using the relationship in Equation 2.4. All the individual datum points plotted together essentially delineate a single curve. Thus, it can be seen from the graph that microhardness increases rapidly in the HPT early stages. This increase in microhardness values was a result of the increase in the imposed strain during the process. When the equivalent strain reaches the value of ~ 30 or higher, microhardness values remains reasonably constant up to equivalent strains of >200 . This indicates the development of a steady state, or saturation, condition.

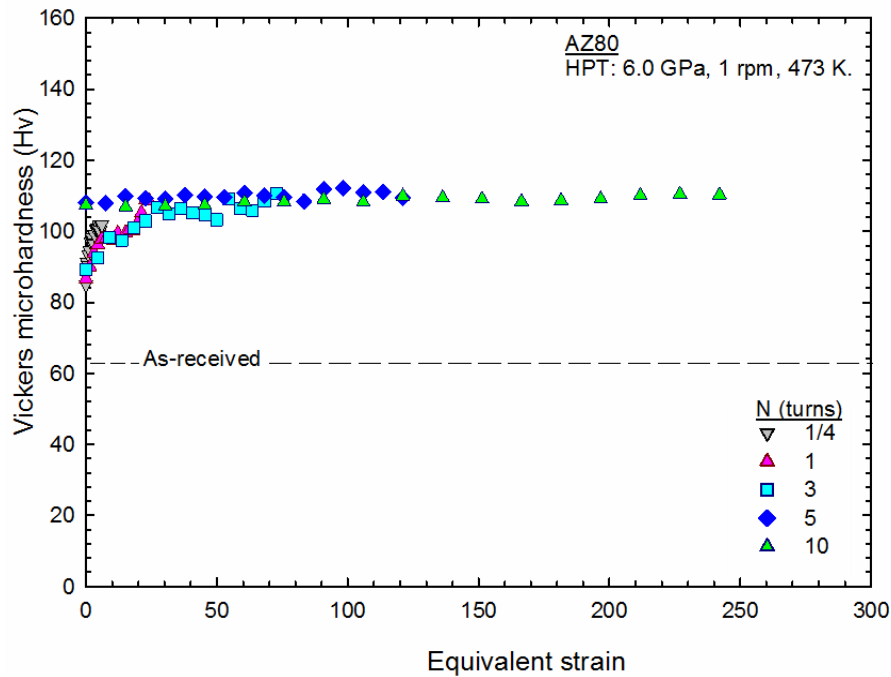


Figure 4.39 Vickers microhardness Hv, plotted against equivalent strain, showing the development of saturation condition at strains above ~ 30 of an AZ80 processed by HPT at 473 K.

To compare the evolution in microhardness values at the centre and the edge of the discs processed by HPT at elevated temperatures, the microhardness values at the centre and at the edge were plotted against the number of turns, as in Figure 4.40. There was a small increase in microhardness values at the pressing stage, especially at the disc centre. The edge of the disc demonstrated a higher value than the centre up to 3 turns. The difference in values between the centre and the edge was considerable. Increasing numbers of turns up to 5 turns decreased the difference and both area of the disc showed almost the same microhardness value Hv. This behaviour continued up to 10 turns of the HPT process, demonstrating a saturation level of microhardness values between 5 and 10 turns of HPT process at 473 K.

The average microhardness values are plotted against numbers of turns in Figure 4.41. The average was ~ 84 Hv at 0 turn. When the alloy was processed for 1/4 turn, the average was ~ 97 Hv. This large difference in average microhardness values decreases with increasing numbers of turns up to 3 turns, and the average was ~ 103 Hv. As the alloy was processed up to 5 and 10 turns, the average microhardness did not change and

was saturated at an average of ~ 110 Hv. This graph demonstrates the increase in average microhardness value along the disc diameter with increasing numbers of turns.

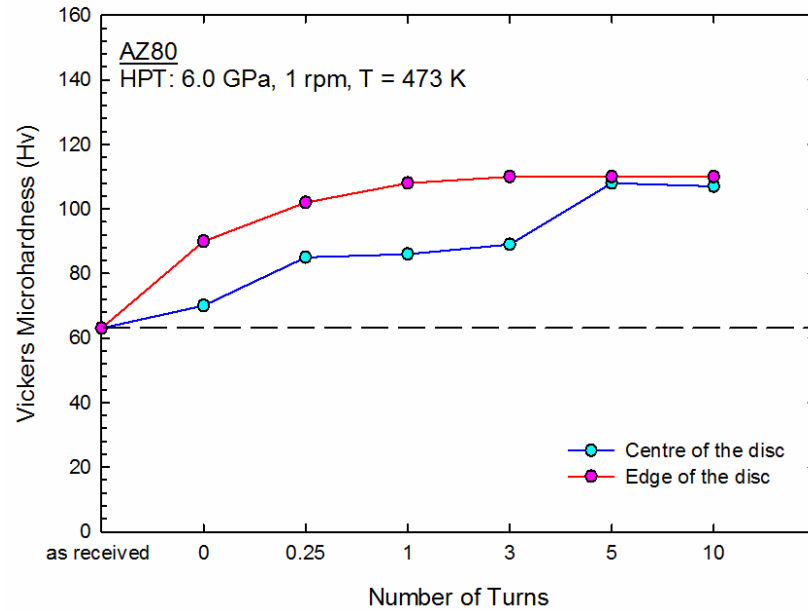


Figure 4.40 Comparison of hardness evolution between the centre and the edge of discs processed by HPT for up to 10 turns at 473 K.

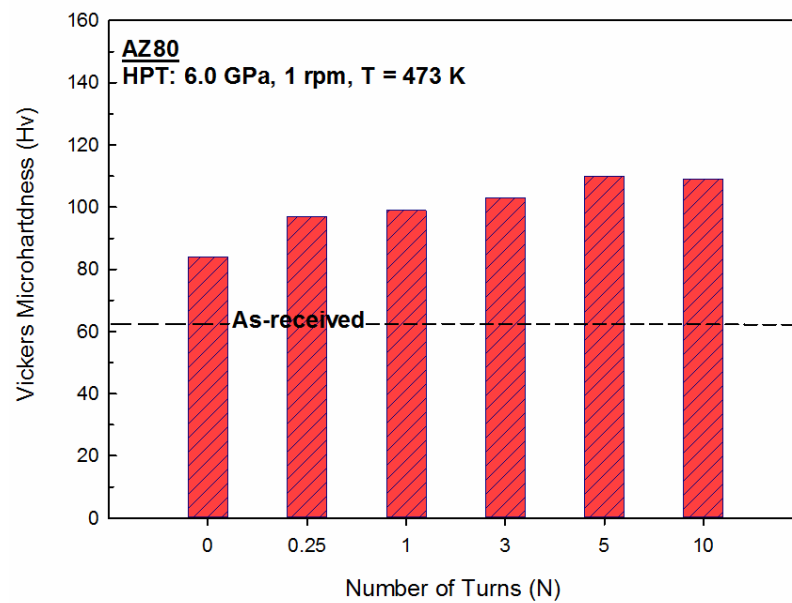


Figure 4.41 Variation in the average microhardness values Hv of AZ80 alloy processed by HPT at 473 K, plotted against numbers of HPT process turns N.

The measurement of average grain size against the average Vickers microhardness (Hv) for 1, 3, 5 and 10 processed turns is plotted in Figure 4.42. This illustrates the intense reduction in average grain size at low numbers of turns in the HPT process at 473 K. After one turn the average grain size was ~ 600 nm. Applying additional strain leads to a further reduction in average grain size, and saturation of average grain size was achieved when the alloy was processed by 10 turns, achieving an average grain size of ~330 nm.

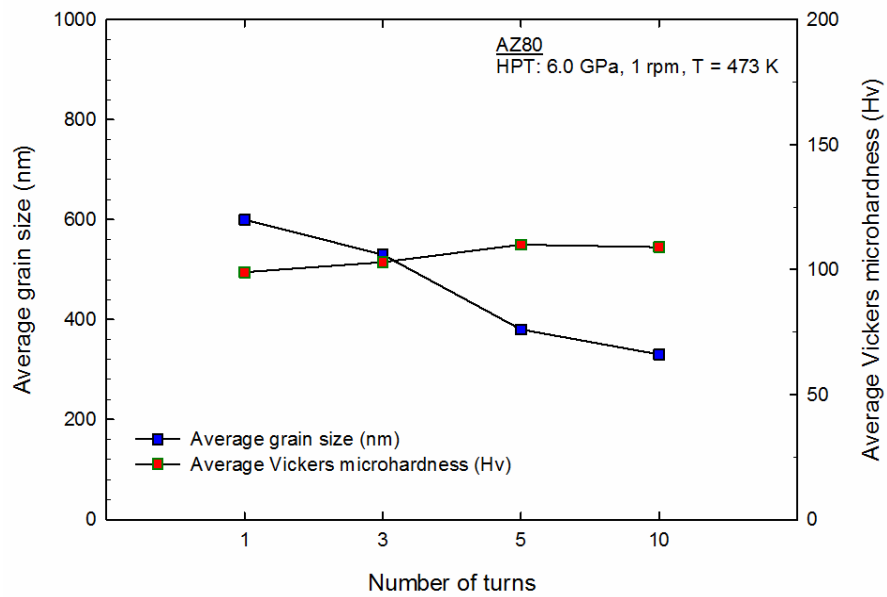


Figure 4.42 Average grain size and the average microhardness values of the alloy processed by HPT for different number of turns at 473 K.

The distribution of the microhardness values over the whole disc surface is displayed using colour-coded contour mapping, Figure 4.43 shows the overall homogeneity development of discs processed by HPT at 473 K for 1/4, 1 and 5 turns. The microhardness data were recorded using a rectilinear grid pattern with 0.3 mm spacing. The two perpendicular axes X and Y are marked in mm, where the position (0, 0) is the midpoint of each disc. The microhardness values are in the range of 80 to 140 Hv, represented by a series of coloured increases of 10 Hv.

The alloy shows a tendency toward structural homogeneity with increasing numbers of revolutions, even when processed at elevated temperatures. The alloy processed by a 1/4 turn exhibits a uniform distribution of microhardness values at the disc surface, with an average of ~100 Hv, apart from in a small area at the disc periphery where higher values

of Hv ~ 110 are displayed. The area of the higher microhardness values expanded toward the disc centre when the alloy was processed for 1 turn. Discs processed by up to 5 turns show an increase in microhardness values over the entire disc surface to an average value of ~ 117 Hv. The histogram in Figure 4.44 shows the increase in average microhardness value, and the data average shifted to the right side of the graph, where the microhardness values are higher.

AZ80

HPT: 6.0 GPa, 1 rpm, T =473 K

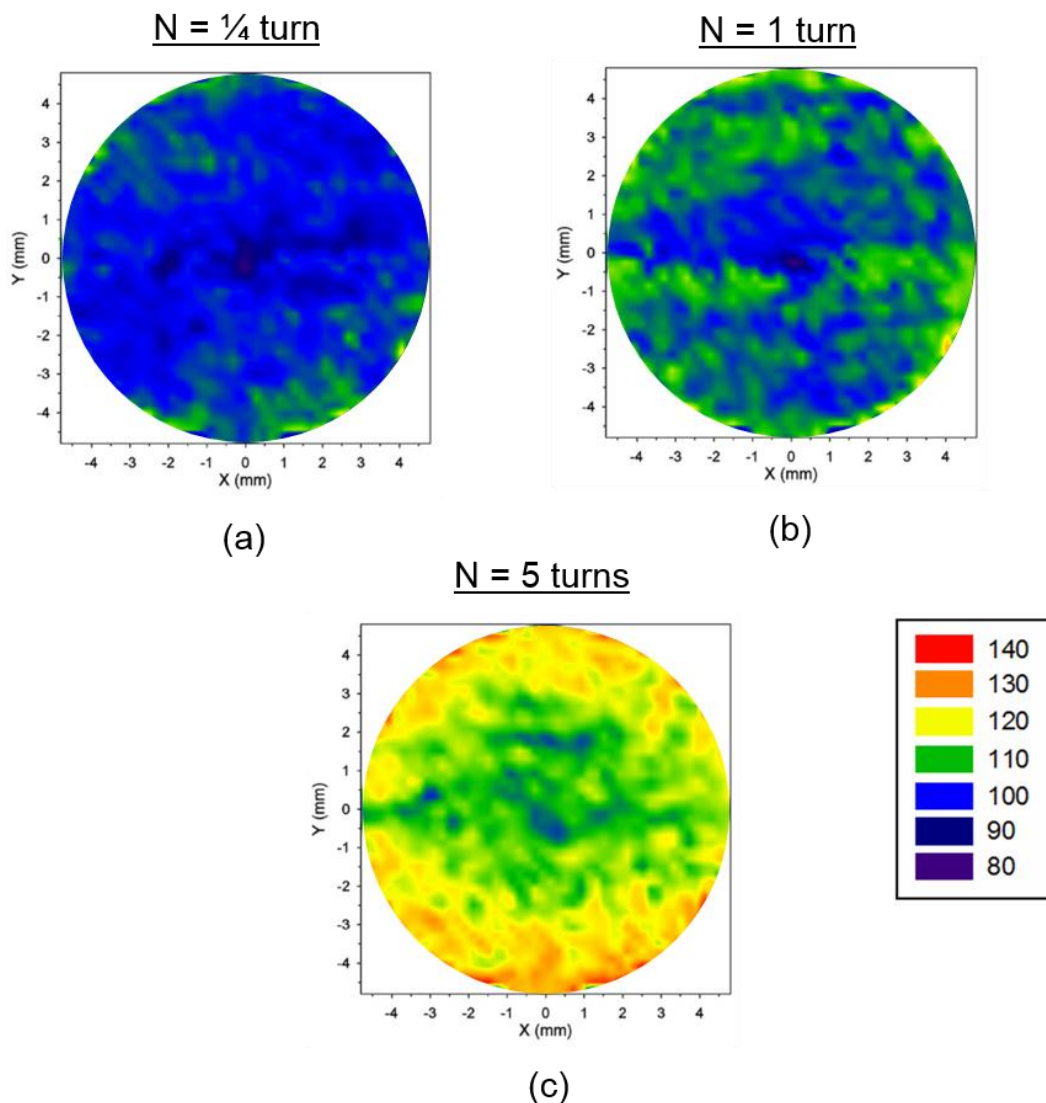
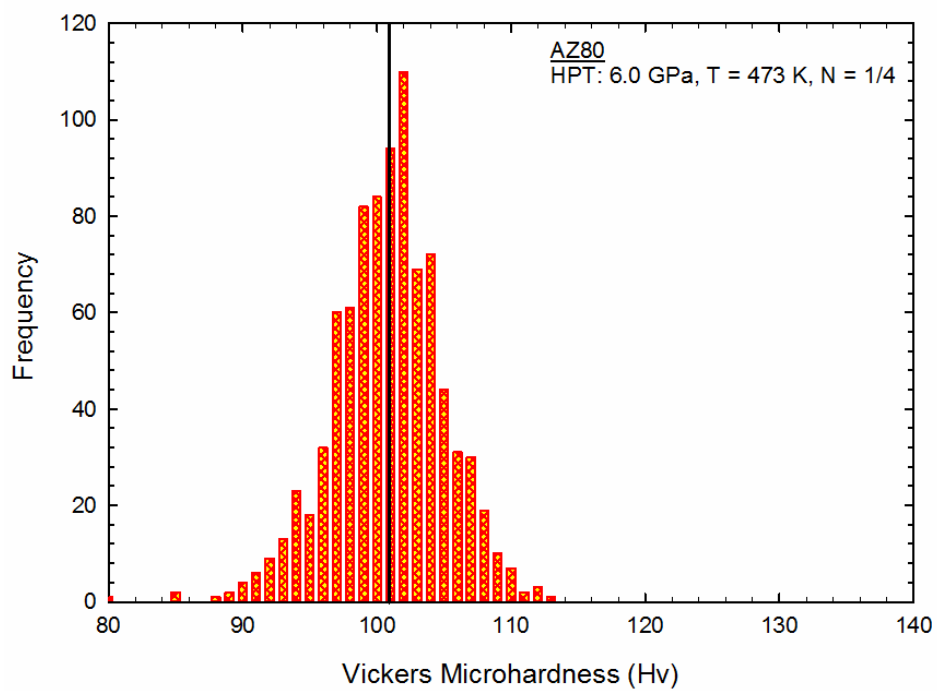
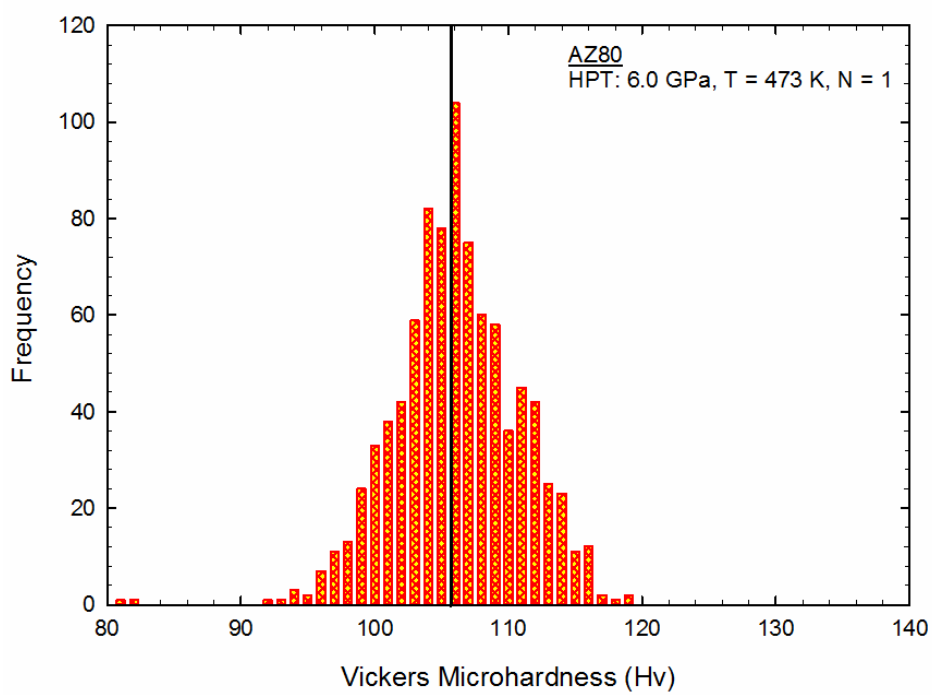


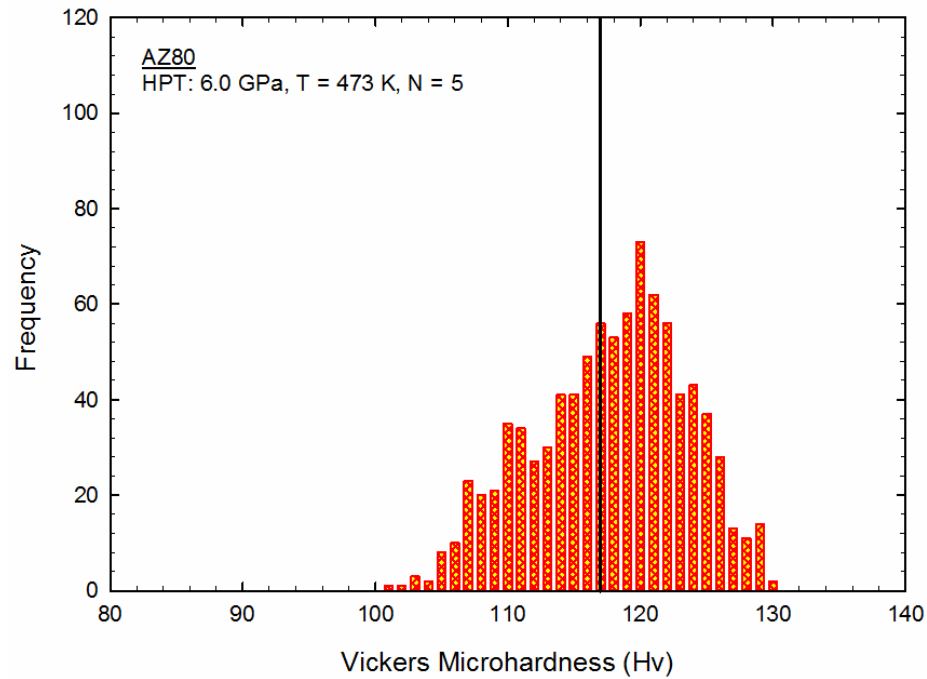
Figure 4.43 Colour-coded contour maps showing the distribution of the Vickers microhardness values at: (a) 1/4; (b) 1; and (c) 5 turns of processed AZ80 discs by HPT at 473 K.



(a)



(b)



(c)

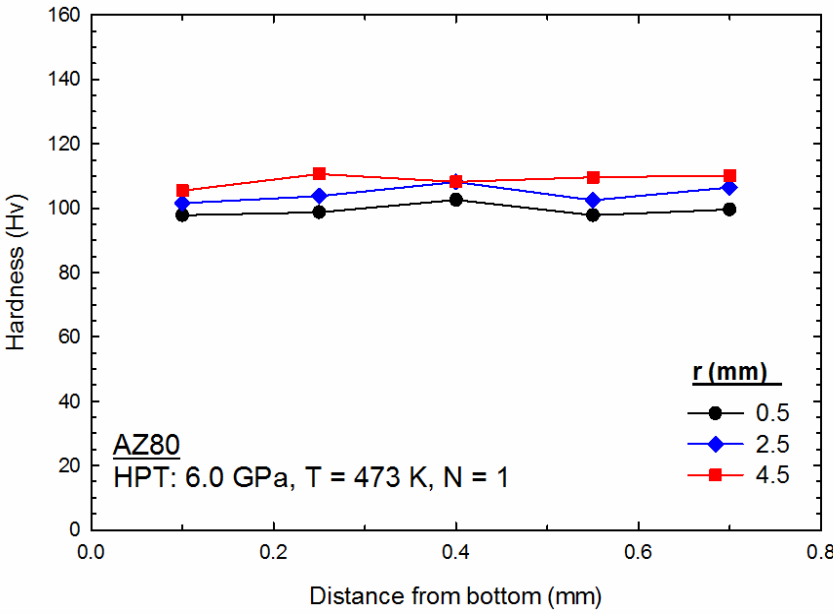
Figure 4.44 Histogram of Vickers microhardness values distributed at the whole disc surface after processing by HPT at 473 K through: (a) 1/4 turn; (b) 1 turn; and (c) 5 turns. Vertical lines denote the average value.

4.5.2 Microhardness through the disc thickness

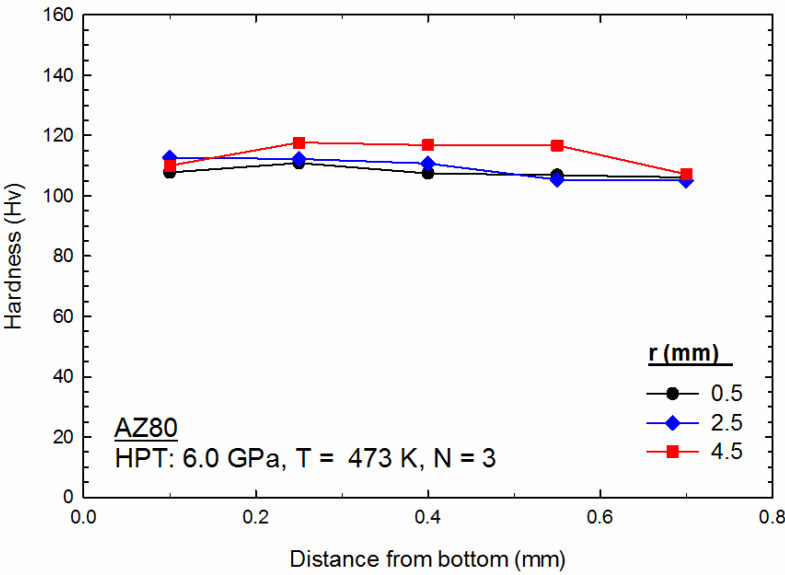
In order to compare the evolution of microhardness through a disc's thickness in the vertical direction when processed by HPT at elevated temperatures to those processed at room temperature, the investigation was carried out on discs processed by HPT at 473 K for the same number of turns as those processed at room temperature, namely 1, 3 and 10. The results of this investigation are shown in Figures 4.45 (a), (b) and (c).

The variation in microhardness values is not significant in discs processed by 1 and 3 turns. Higher values were recorded at both discs' periphery, with average values of ~105 and ~115 Hv respectively. The variation between the top and bottom surfaces of the disc was likewise insignificant. It can be noted that the distribution of microhardness values is consistent with the evolution of microstructure, as in Figure 4.45. More homogenous microhardness values are present in the disc processed for 10 turns, and

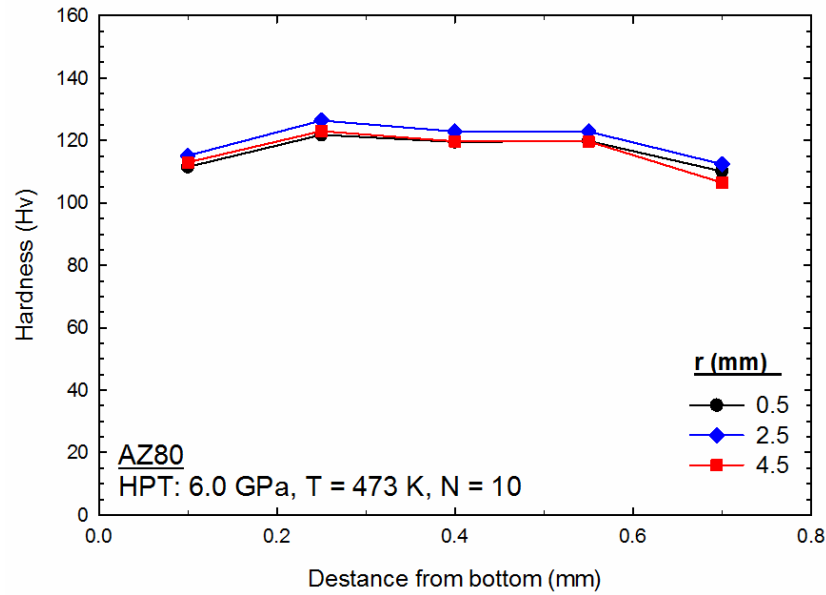
the graph shows a higher value at the mid-thickness area, with average values of ~120 Hv.



(a)



(b)



(c)

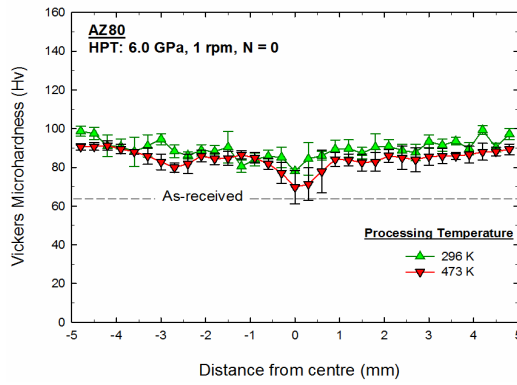
Figure 4.45 Microhardness values at different displacement from the centre as a function of distance from bottom to top of the disc processed by HPT at 473 K: (a) 1 turn; (b) 3 turns; and (c) 10 turns.

4.6 The evolution comparison in Microstructure and microhardness between alloy processed by HPT at 296 K and 473 K

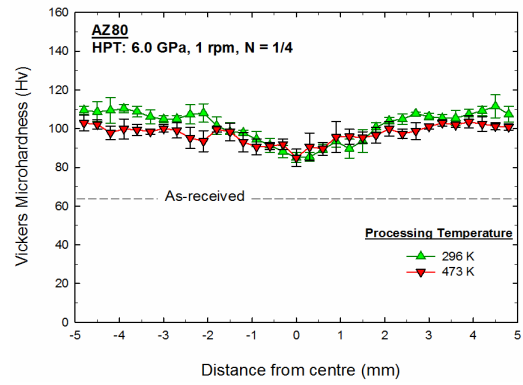
There were differences in the evolution of microstructure and microhardness during HPT process between samples processed at 296 K and 473 K. In Figures 4.6 and 4.7, the optical images show the deformation of the microstructure of samples processed at room temperature, with no obvious twinning at the surface of the disc or through the disc thickness, as seen in Figure 4.20. The only twinning was in a grain of ~ 50 nm, as shown in Figure 4.19. The STEM images in Figure 4.13 describe the microstructure evolution in samples processed at 296 K for 1/4, 1 and 10 turns. After 1/4 and 1 turn of HPT there was evidence of elongated grains, probably in the torsion direction, and the average grain size after 1 turn is smaller than ~ 500 nm, as shown in Figure 4.25. The precipitates are located mainly at the triple junction between the grains, as shown in Figure 4.11. Increasing numbers of turns result in a fairly homogenous microstructure with an average grain size of ~ 200 nm after 5 turn of HPT processing at room temperature, as shown in Figure 4.17. This was confirmed by the development of the SAED pattern to a fully ring in Figure 4.18.

By contrast, in samples processed at 473 K, twinning started from the compression stage at which the alloy was pressed by HPT facility for 60 seconds without torsion, as shown in the OM and SEM images in Figure 4.29. The grains' fragmentation by twinning is observed through the discs' thickness, as shown in Figure 4.37. The presence of the twinning continued during the HPT process until the alloy displayed a reasonable homogeneous UFG microstructure, as shown in Figures 4.31 (e) and (f). The evolution in samples processed by HPT at 473 K is illustrated by TEM images in Figures 4.32 (a), (b) and (c), where the alloy was processed for 1/4, 3 and 10 turns. The SAED in those figures developed a well-defined ring with increasing number of turns. The precipitates were randomly distributed within the matrix after a lower number of HPT process turns, as seen in Figures 4.34 (a) and 4.35 (a). By further reducing the average grain size through increasing the number of HPT turns up to 5, a larger fraction of precipitates is located at the triple junction, as seen in Figures 4.34 (b) and 4.35 (b). Processing the alloy up to 10 turns produced an equiaxed UFG grains with an average grain size ~ 330 nm, as shown by the TEM image in Figure 4.36.

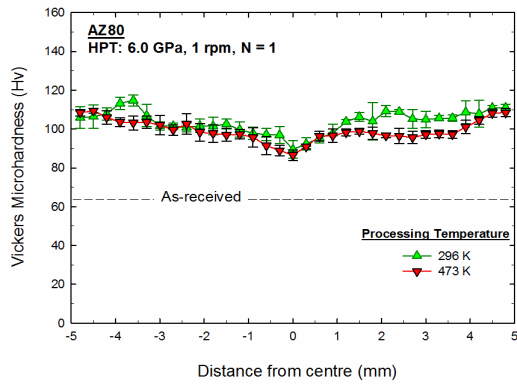
In order to compare the evolution in microhardness when processing the AZ80 magnesium alloy at both 296 K and 473 K, the Vickers microhardness values, H_v , are plotted individually for each processed turn. Figure 4.46 illustrates the results for: (a) $N = 0$; (b) $N = 1/4$; (c) $N = 1$; (d) $N = 3$; (e) $N = 5$; and (f) $N = 10$ at 296 and 473 K. For all numbers of turns, the microhardness values of samples processed at 296 K are higher than the microhardness values of samples processed at 473 K. There was an overlap in some areas of the discs processed for fewer numbers of turns, as shown in Figures 4.46 (a), (b) and (c). The microhardness values of discs processed at 473 K are higher in those areas than the microhardness values of samples processed at 296 K. After 3 turns, the gap between the microhardness values of both temperatures became larger, favouring the samples processed at room temperature. The variation in microhardness values between the edge and the centre of the disc seems to be less in discs processed at elevated temperature. In the graphs in Figures 4.22 and 4.39, the Vickers microhardness H_v , plotted against equivalent strain, demonstrates a slight difference between the steady-state hardness level that indicates a small difference in the rate of recovery when processing AZ80 magnesium alloy by HPT at 296 K and 473 K [196].



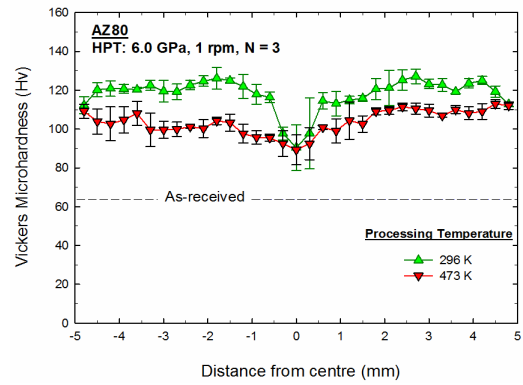
(a)



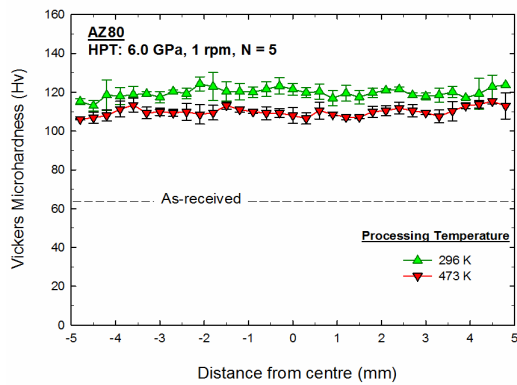
(b)



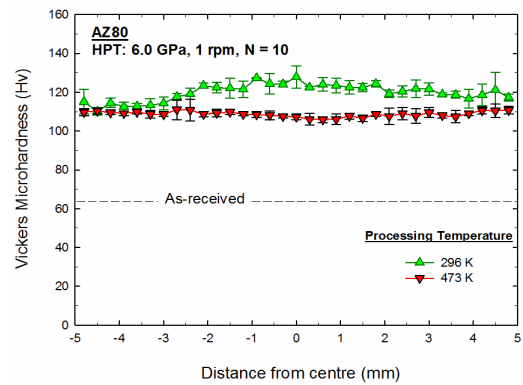
(c)



(d)



(e)



(f)

Figure 4.46 Results of Vickers microhardness values H_v , plotted individually for each processed turn at 296 K and 473 K for (a) $N = 0$, (b) $N = 1/4$, (c) $N = 1$, (d) $N = 3$, (e) $N = 5$ and (f) $N = 10$.

Figure 4.47 illustrates the average microhardness values along the discs' diameter against the number of HPT revolution at 296 K and 473 K. At both processing

temperatures the alloy shows an evolution of microhardness values with increasing number of turns toward saturation level after 5 and 10 turns.

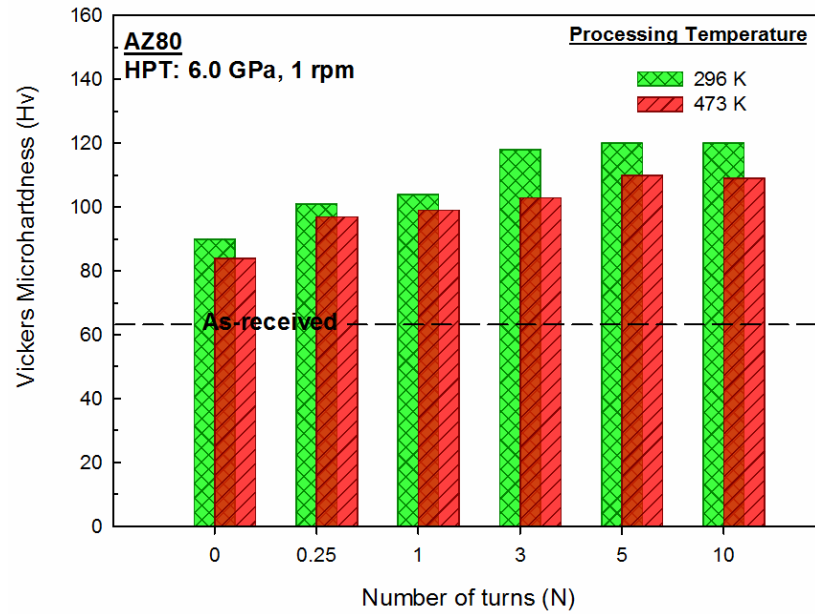


Figure 4.47 Average Hv values along the disc diameter against the number of HPT turns for sample processed by HPT at 296 and 473K.

4.7 Superplastic Behaviour of AZ80 Processed by HPT

The microstructure of the unprocessed AZ80 magnesium alloy shows an average grain size of $\sim 25 \mu\text{m}$. This microstructure has a Mg-rich phase and a β phase $\text{Mg}_{17}\text{Al}_{12}$. The β phase is located at the grain boundaries in granular form, as shown in Figure 4.4 (f), and with a lamellar form as shown in Figure 4.4 (a), (b), (c) and (d). After processing by HPT, these precipitates breakdown to nano-sized particles and were distributed at the triple junction within the ultra-fine grained microstructure (average grain size less than 500 nm) of the alloy, as shown in Figures 4.11 and 4.12. This grain size reduction and precipitate distribution helped to achieve better elongation when the alloy was tested in tension to fracture in a tensile test.

No study has reported either superplastic behaviour in AZ80 magnesium alloy exceeding 400%, or any elongation in ultra-fine grained AZ80 magnesium alloy processed by HPT (to the author's knowledge). This study is therefore the first to

describe the tensile behaviour of AZ80 magnesium alloy previously processed by HPT. Furthermore, this is the first successful attempt to achieve superplastic elongation exceeding 400% with this alloy. The alloy was first processed by HPT at room temperature for 1/4, 1, 5 and 10 turns, then pulled in tension to failure at strain rates of $1.4 \times 10^{-4} \text{ s}^{-1}$, $1.4 \times 10^{-3} \text{ s}^{-1}$, $1.4 \times 10^{-2} \text{ s}^{-1}$ and $1.4 \times 10^{-1} \text{ s}^{-1}$. The tensile test was carried out at temperatures of 473 K, 523 K and 573 K, corresponding to $\sim 0.53T_m$, $\sim 0.59T_m$ and $\sim 0.65T_m$ respectively, when the absolute melting temperature of AZ80 magnesium alloy is taken to be 883 K (610 °C), based on the Mg-Al binary phase diagram shown in Figure 2.33.

4.7.1 Stress-strain curves

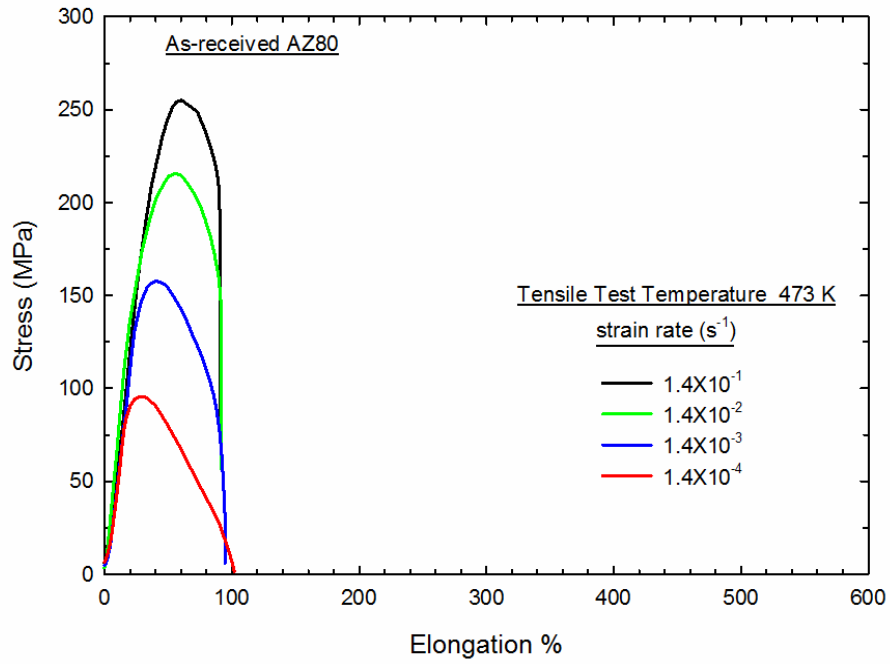
Figure 4.48 shows the stress–strain curves of the as-received condition of the samples tested in tension to failure using a tensile test. The tests were conducted at 473 K and 573 K for different strain rates of $1.4 \times 10^{-4} \text{ s}^{-1}$, $1.4 \times 10^{-3} \text{ s}^{-1}$, $1.4 \times 10^{-2} \text{ s}^{-1}$ and $1.4 \times 10^{-1} \text{ s}^{-1}$. The maximum elongation of the coarse-grained alloy was $\sim 190\%$ when the alloy was tested at temperature of 573 K using a strain rate of $1.4 \times 10^{-4} \text{ s}^{-1}$. At the same strain rate, but at lower testing temperatures 473 K, the elongation was $\sim 100\%$. From the graphs, it can be noted that the elongation increases with decreasing flow stress, increasing testing temperature and decreasing strain rate.

Figures 4.49, 4.50, 4.51 and 4.52 illustrate the stress-strain curves of AZ80 samples processed by HPT at room temperature and pulled in tension to failure using a strain rate of $1.4 \times 10^{-4} \text{ s}^{-1}$, $1.4 \times 10^{-3} \text{ s}^{-1}$, $1.4 \times 10^{-2} \text{ s}^{-1}$ and $1.4 \times 10^{-1} \text{ s}^{-1}$ at tensile testing temperatures of 473 K, 523 K and 573 K for $N = 1/4, 1, 5$, and 10 turns respectively. These curves describe the behaviour of ultra-fine grained AZ80 magnesium alloy. At a fast strain rate of $1.4 \times 10^{-1} \text{ s}^{-1}$ the alloy exhibits a high value of flow stress for any given number of turns and at any given tensile testing temperatures. By decreasing the strain rates, the maximum flow stress decreases, and this behaviour was found in all testing temperature. The alloy displays a contrary behaviour regarding the tensile testing temperature; by increasing the tensile testing temperature the maximum flow stress decreases at any given number of turns at any given strain rate.

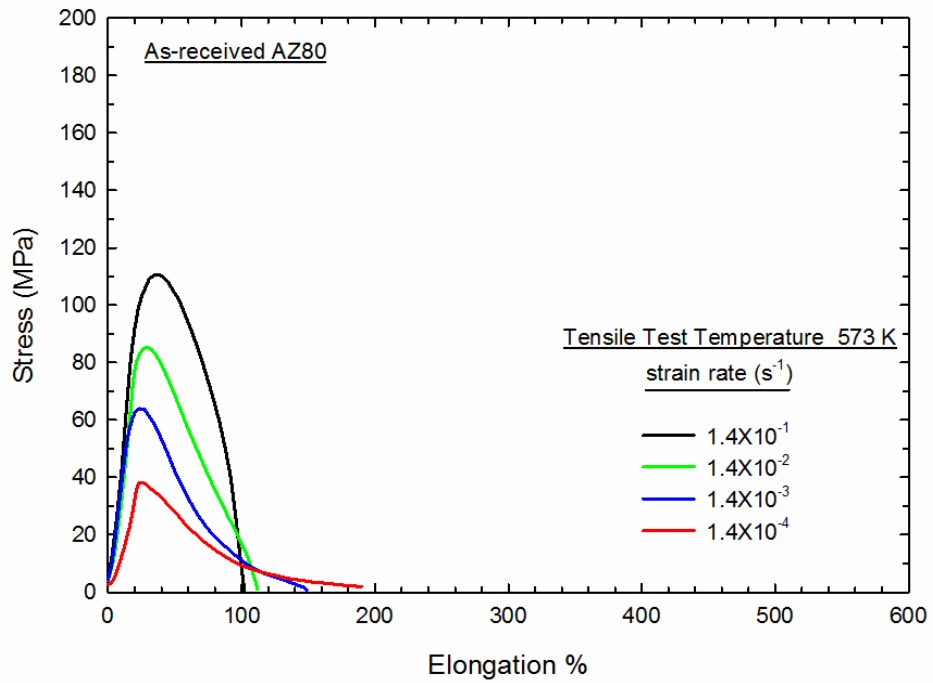
Superplastic elongation is clear in Figures 4.49 (b) and (c), 4.50 (a), (b) and (c), 4.51 (a), (b) and (c), and Figure 4.52 (a), (b) and (c), where the sample's elongation exceeded

400%. It is clear from the curves that elongation exceeding 400% was easily achieved when the alloy was tested at 523 K and 573 K. The higher the testing temperature, the greater the elongation. At all testing temperatures, the samples processed by HPT for 1 turn and tested at the slower strain rate of $1.4 \times 10^{-4} \text{ s}^{-1}$ showed the maximum elongation, and, for each sample tested for a given number of turns, the maximum elongation for a given testing temperature was achieved when the alloy was tested at the slower strain rate of $1.4 \times 10^{-4} \text{ s}^{-1}$. Figures 4.53 (a), (b) and (c) illustrate the maximum elongation for each number of turns of the HPT process against the strain rate at testing temperatures of 473 K, 523 K and 573 K respectively. The elongation of 645% was the maximum of all samples and was achieved in sample processed by HPT for 1 turn at a tensile testing temperature of 573 K at a strain rate of $1.4 \times 10^{-4} \text{ s}^{-1}$, as in Figure 4.53 (c), which corresponds to the higher testing temperature of $\sim 0.65T_m$ where the maximum elongation at the lower testing temperature of $\sim 0.53T_m$ was 423%, as in Figure 4.53 (a), was achieved in a sample processed by HPT for 1 turn at a strain rate of $1.4 \times 10^{-4} \text{ s}^{-1}$.

Despite these observations, the material successfully exceeded an elongation of 400% and achieved low temperature superplasticity (LTSP) in samples processed by HPT for 1, 5 and 10 turns when pulled to failure in tension at a strain rate of $1.4 \times 10^{-4} \text{ s}^{-1}$ at a testing temperature of 473 K, as shown in Figures 4.50 (a), 4.51 (a) and 4.52 (a), yet failed to do so in sample processed by HPT for 1/4 turn (Figure 4.49 (a)). It is clear from the figures that AZ80 magnesium alloy is sensitive to the testing temperature and the strain rate. The maximum elongation decreased with increasing strain rate and decreasing testing temperature. It can be noticed that the maximum elongation was achieved only after 1 turn of the HPT process, although a reasonably homogenous microstructure has not been achieved until now. Since extensive refinement of AZ80 magnesium alloy starts at a lower number of turns in HPT, all specimens of each given number of turns of the HPT process show an excellent elongation when tested to failure in tension with a strain rate of $1.4 \times 10^{-4} \text{ s}^{-1}$ and at a higher testing temperature of 573 K.

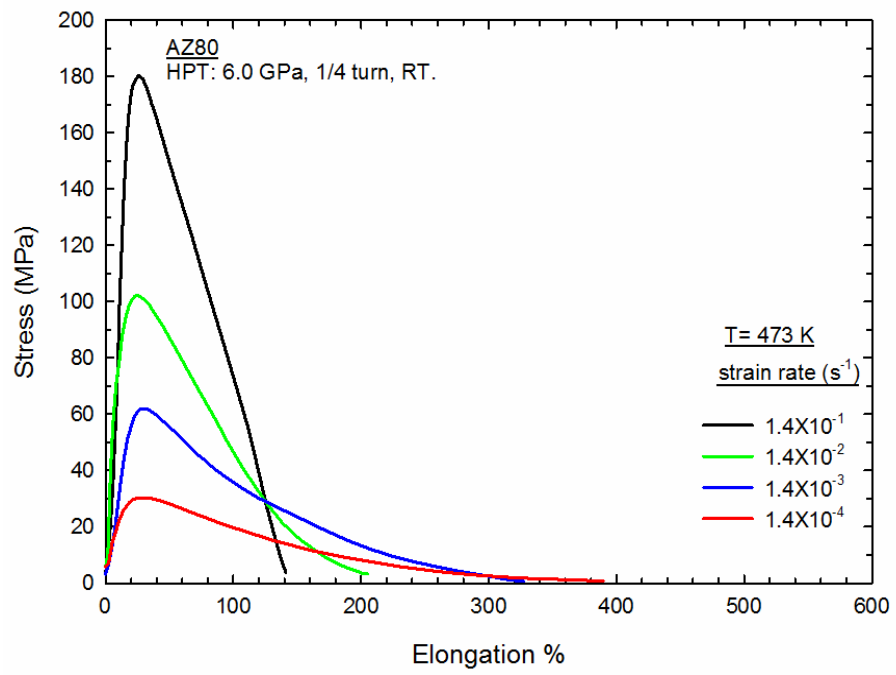


(a)

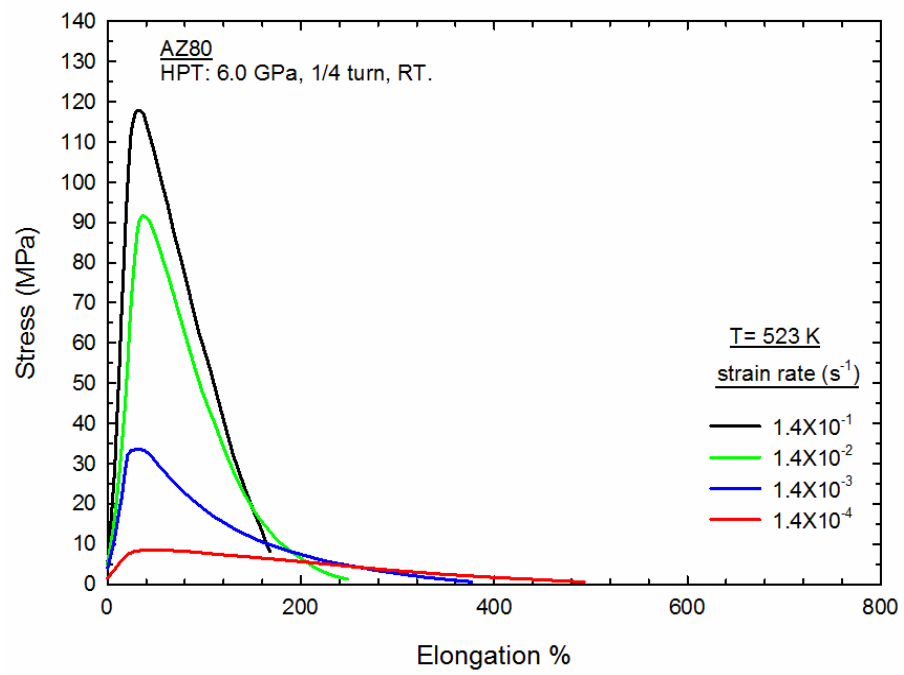


(b)

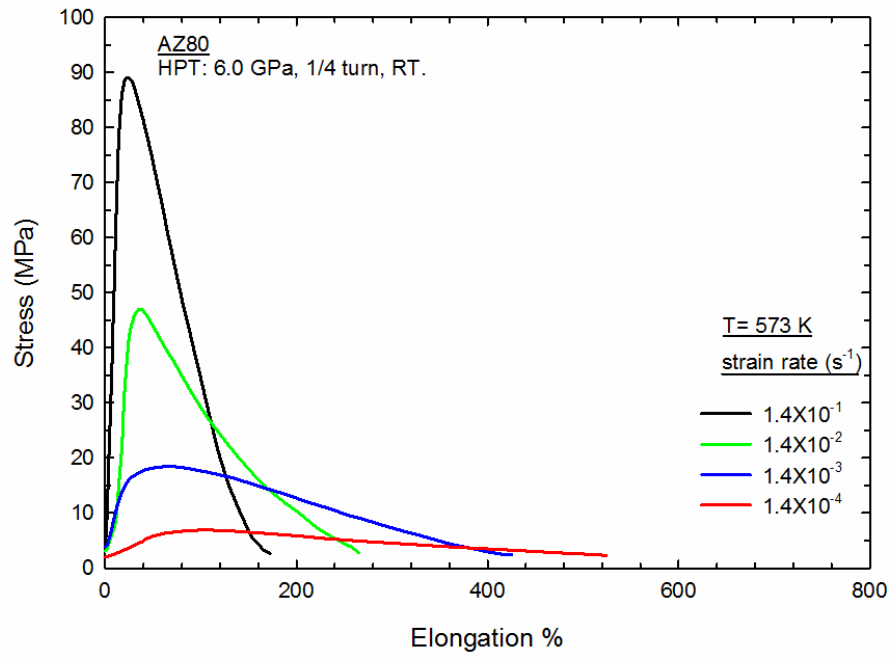
Figure 4.48 Stress-strain curve of the AZ80 in the as-received condition tested by tensile test in (a) at 473 K and (b) at 573 K for different strain rates.



(a)

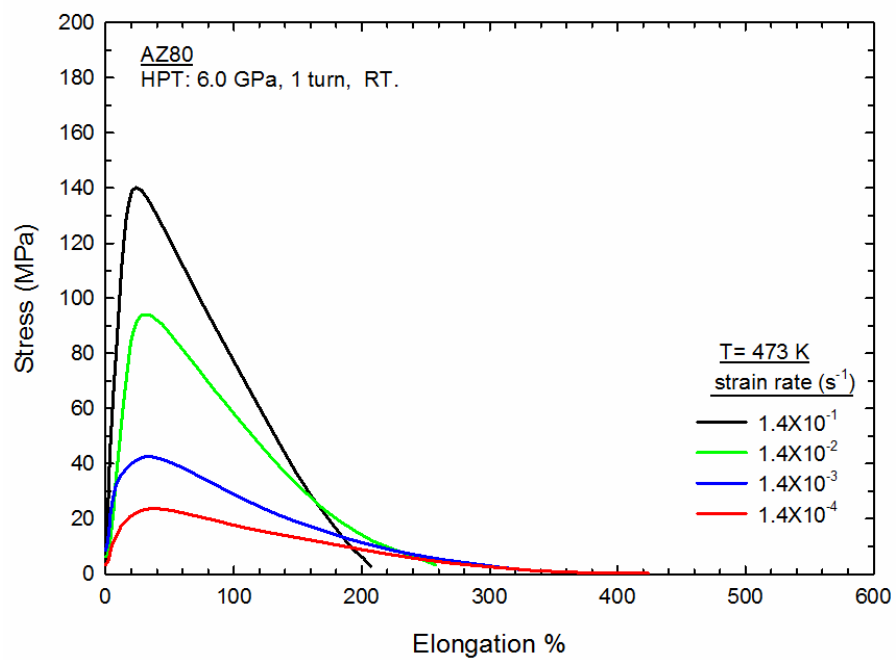


(b)

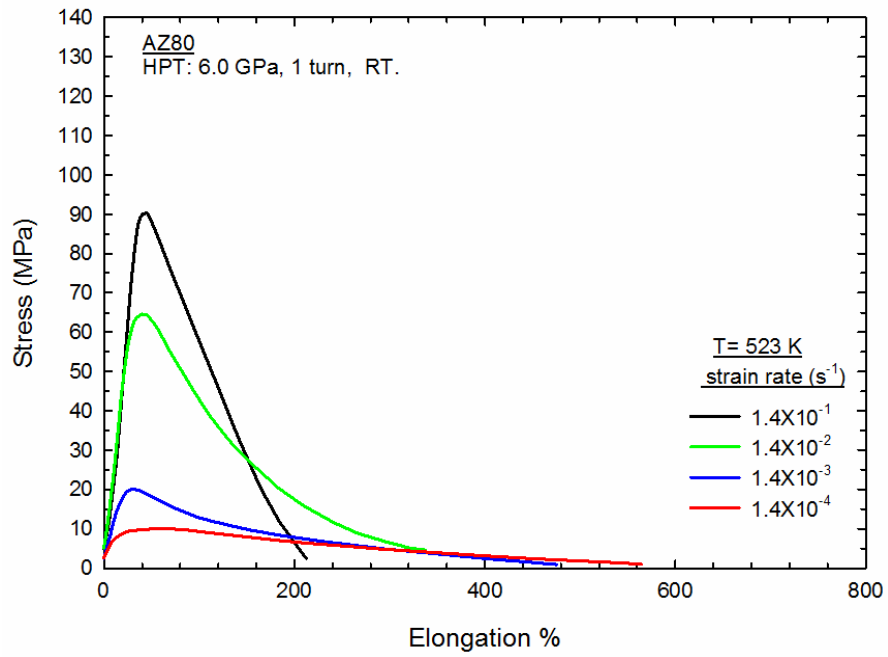


(c)

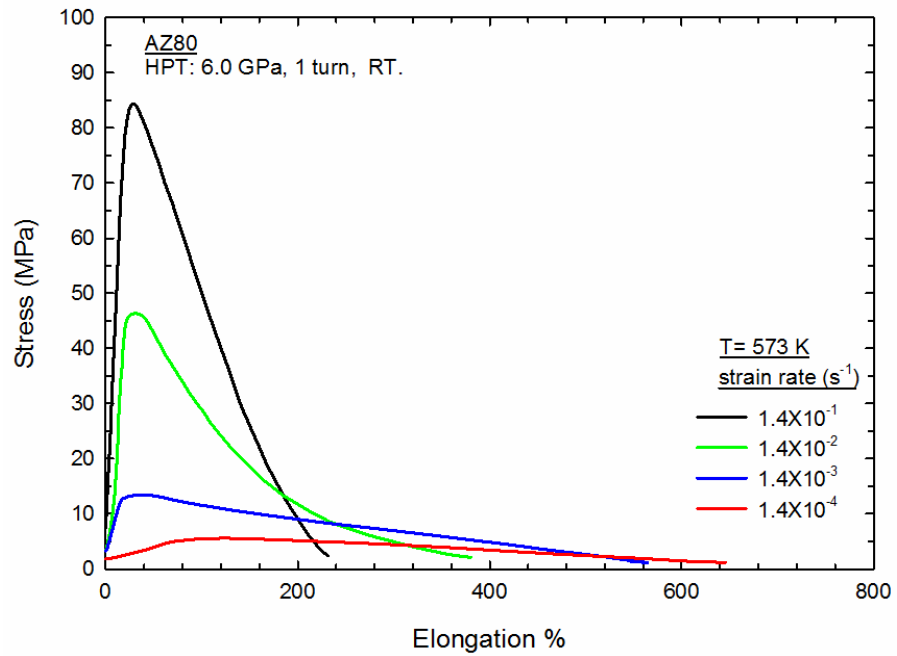
Figure 4.49 Stress-strain curve for the AZ80 alloy processed for $N = 1/4$ turn in HPT at room temperature using an applied pressure of 6.0 GPa and tested in tension for different strain rates at a testing temperature of 473 K at (a), 523 K at (b) and 573 K at (c).



(a)

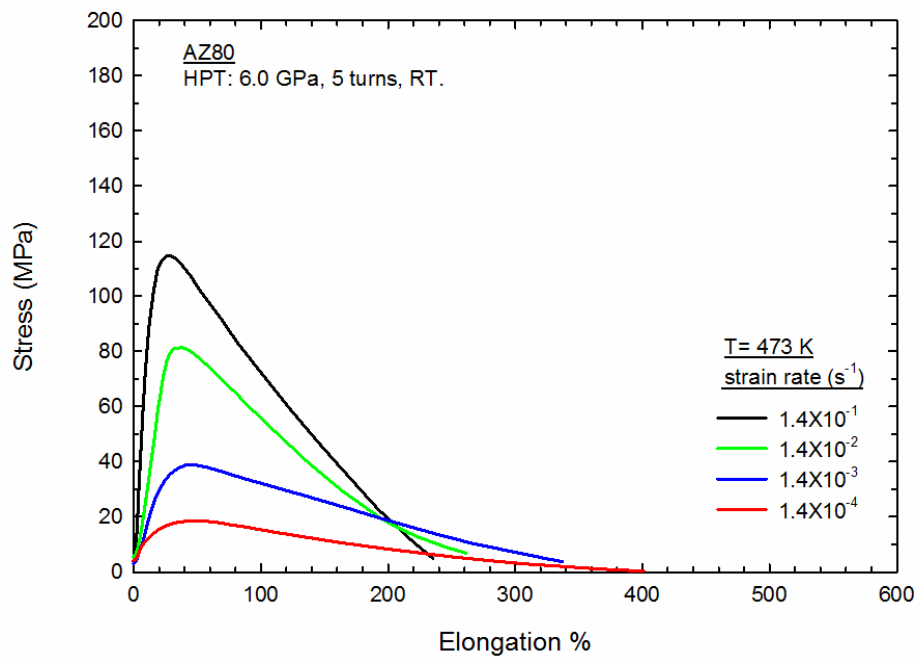


(b)

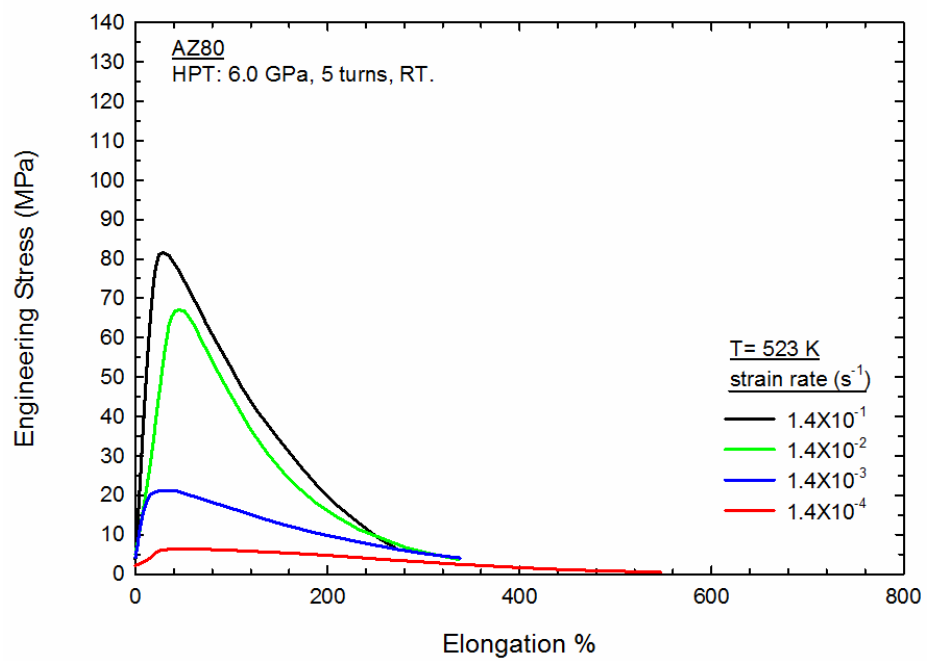


(c)

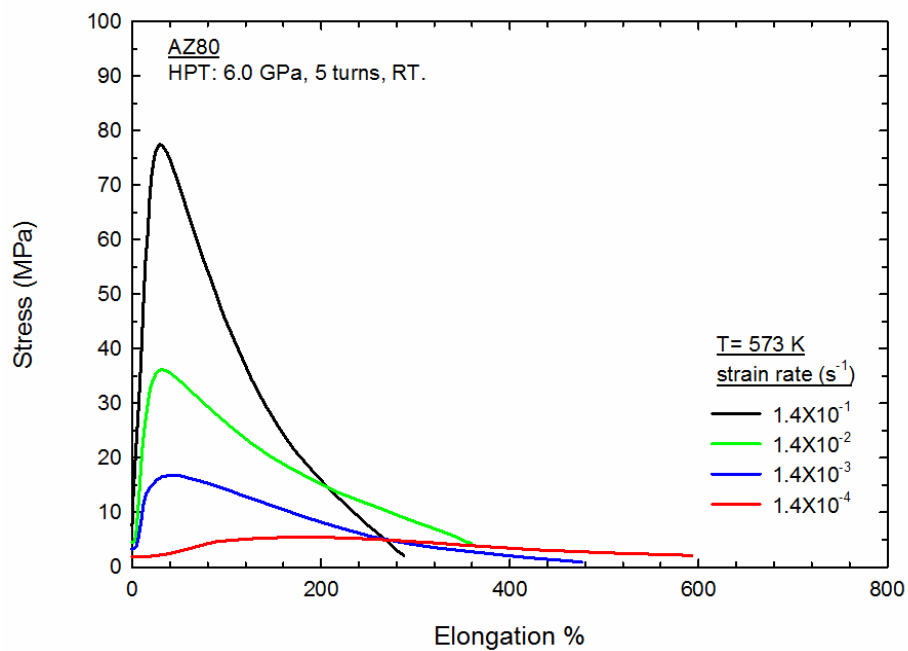
Figure 4.50 Stress-strain curve for the AZ80 alloy processed for $N = 1$ turn in HPT at room temperature using an applied pressure of 6.0 GPa and tested in tension for different strain rates at a testing temperature of 473 K at (a), 523 K at (b) and 573 K at (c).



(a)

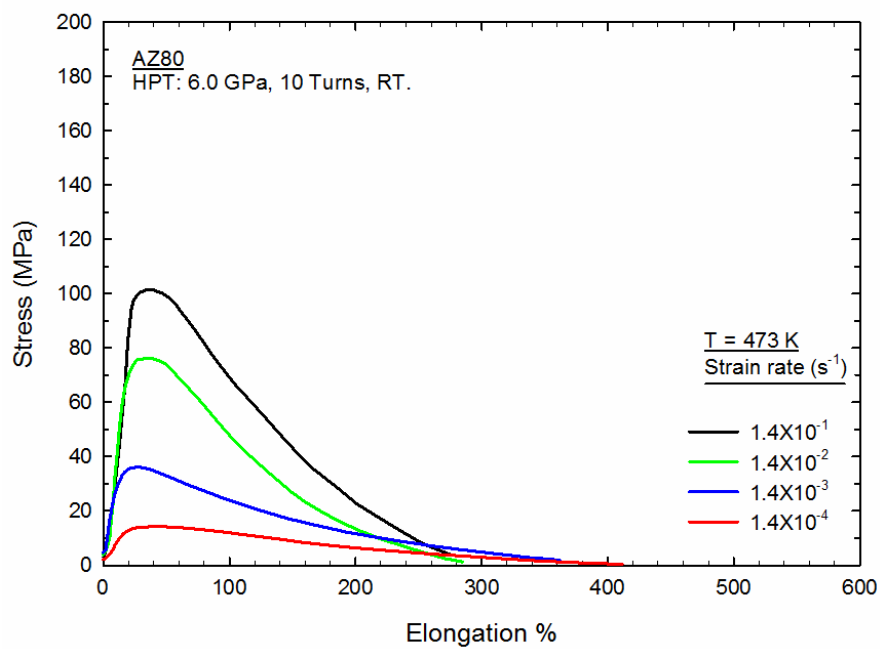


(b)

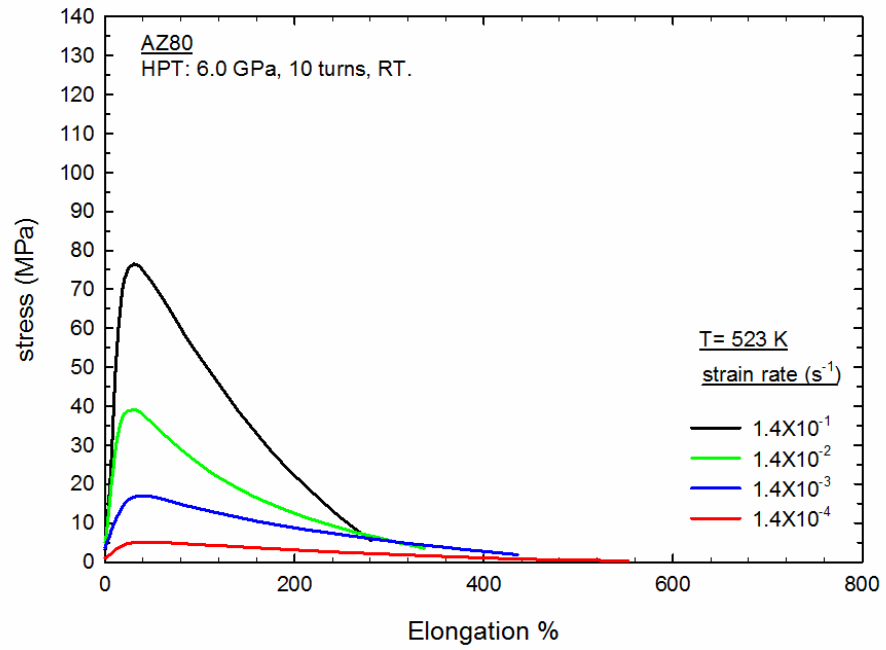


(c)

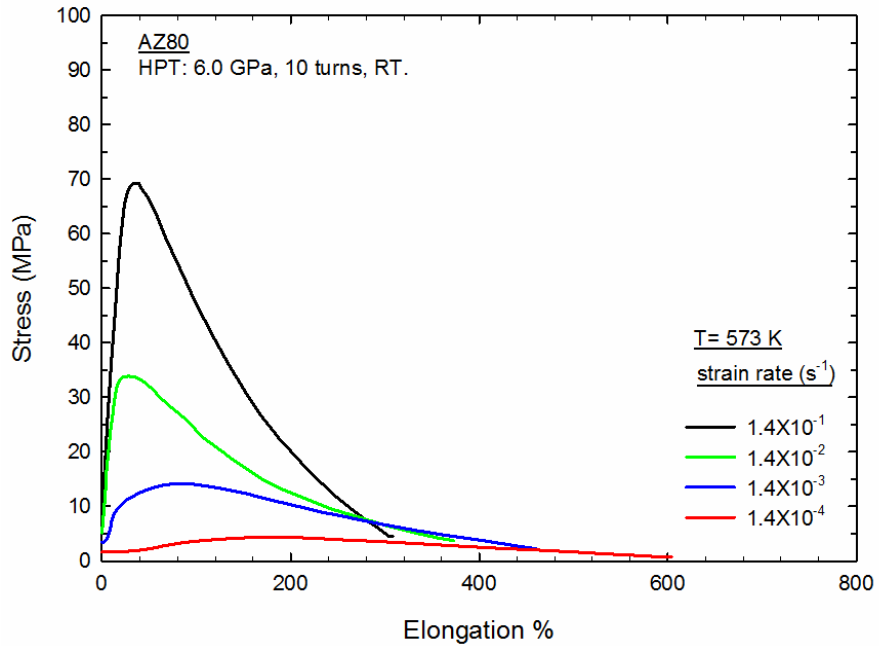
Figure 4.51 Stress-strain curve for the AZ80 alloy processed for $N = 5$ turn in HPT at room temperature using an applied pressure of 6.0 GPa and tested in tension for different strain rates at a testing temperature of 473 K at (a), 523 K at (b) and 573 K at (c).



(a)

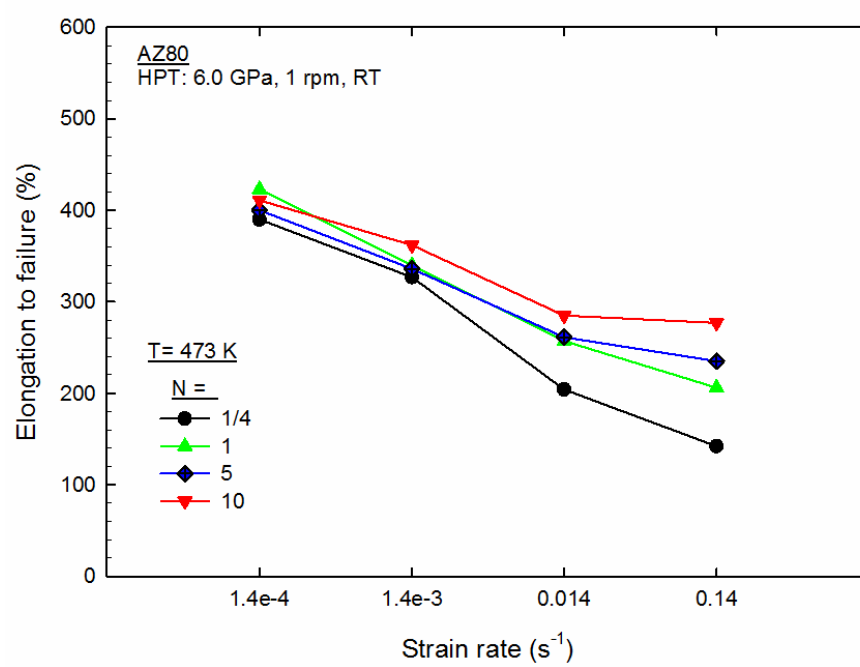


(b)

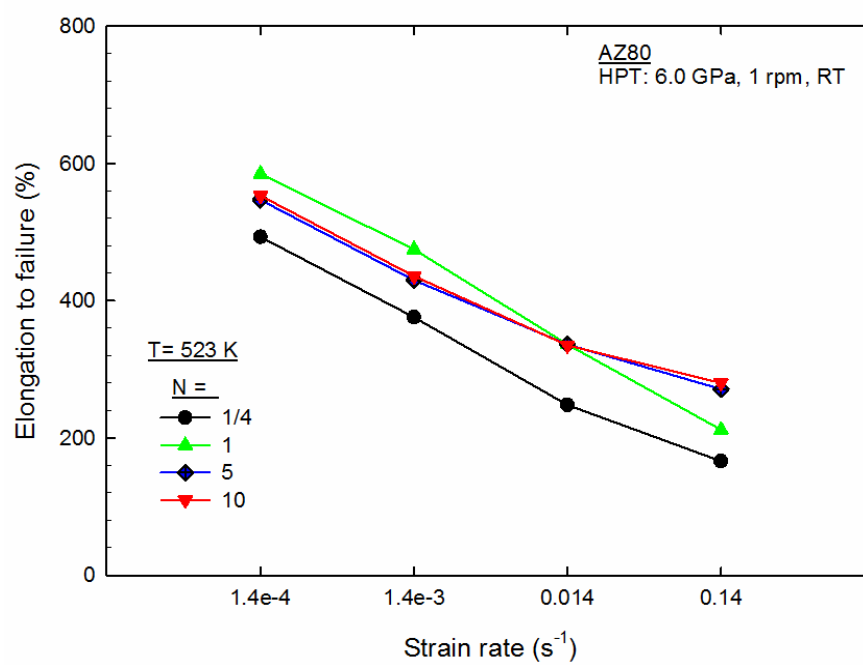


(c)

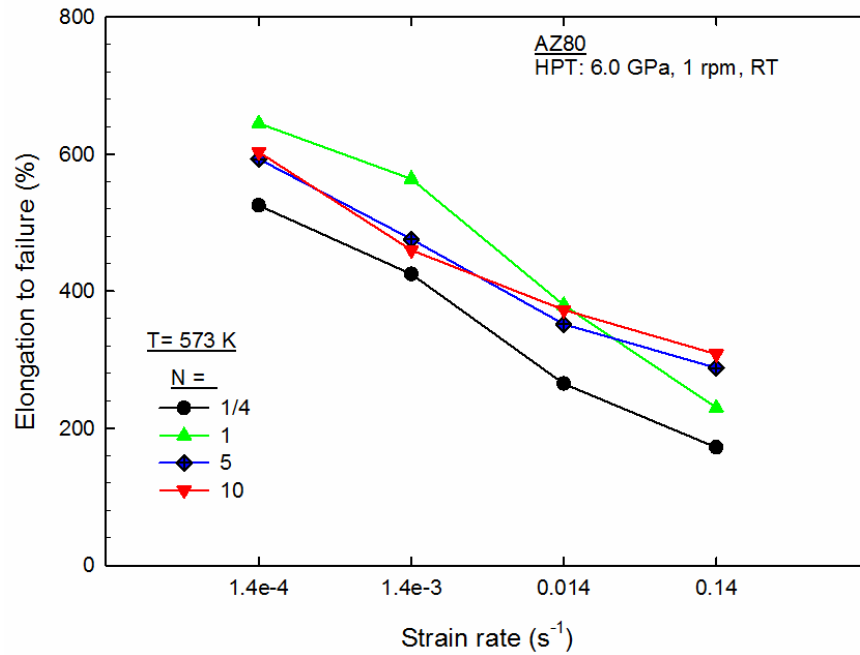
Figure 4.52 Stress-strain curve for the AZ80 alloy processed for N = 10 turn in HPT at room temperature using an applied pressure of 6.0 GPa and tested in tension for different strain rates at a testing temperature of 473 K at (a), 523 K at (b) and 573 K at (c).



(a)



(b)

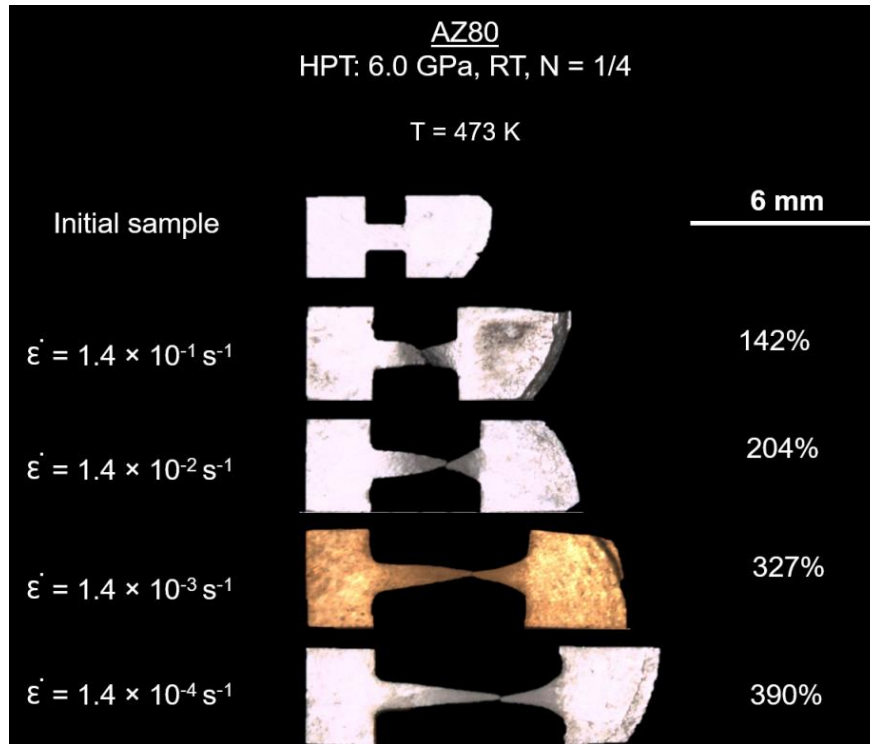


(c)

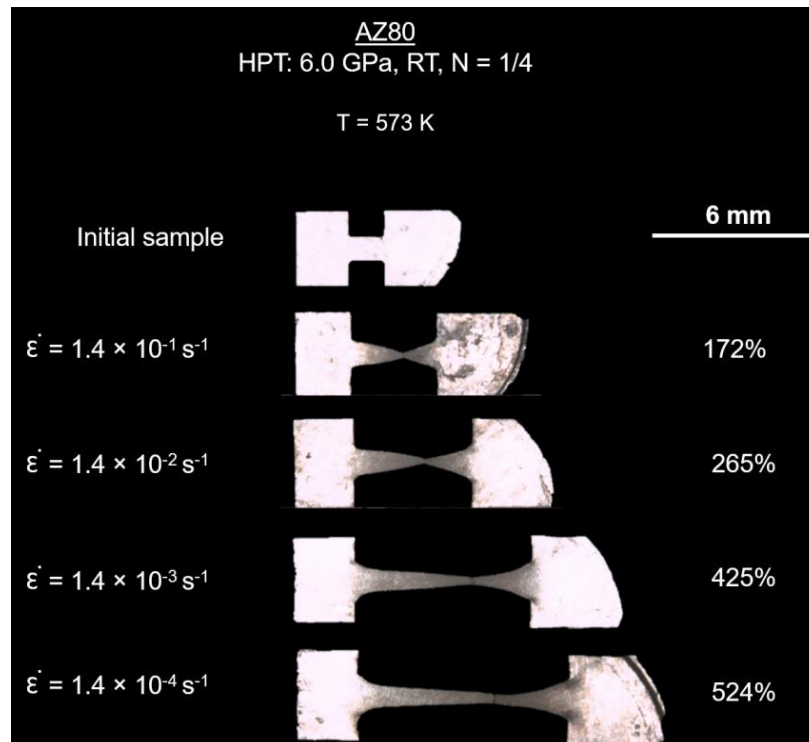
Figure 4.53 Elongation – strain rate curve for the AZ80 alloy processed for different number of turns in HPT at room temperature using an applied pressure of 6.0 GPa and tested in tension for different strain rates at a testing temperature of 473 K at (a), 523 K at (b) and 573 K at (c).

4.7.2 The appearance of AZ80 samples after tensile testing

Figures 4.54, 4.55, 4.56 and 4.57 show the appearance of the specimens after tensile testing at 473 K and 573 K. The unprocessed sample is at the top of the figure, and the processed samples are placed in the order of strain rates, from highest to lowest, from top to bottom. It is noticeable in these figures at both testing temperatures that the maximum elongation was achieved for any given number of turns of the HPT process when the sample was tested at the slower strain rate of $1.4 \times 10^{-4} s^{-1}$. Those samples of the maximum elongation showed a uniform deformation until fracture within the gauge length. This behaviour, and an absence of necking, provides additional evidence of superplastic behaviour [197].

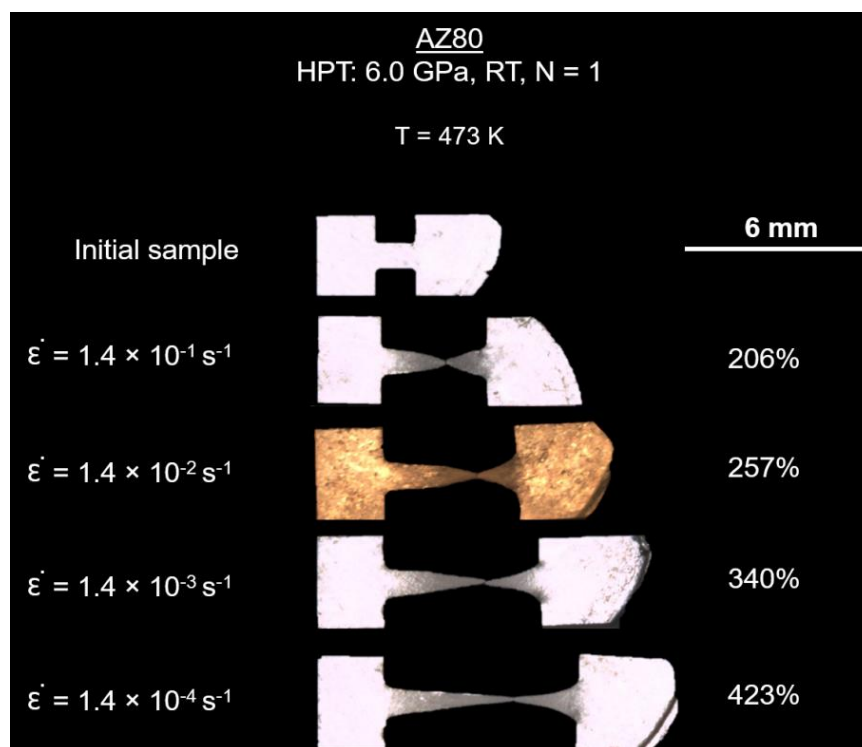


(a)

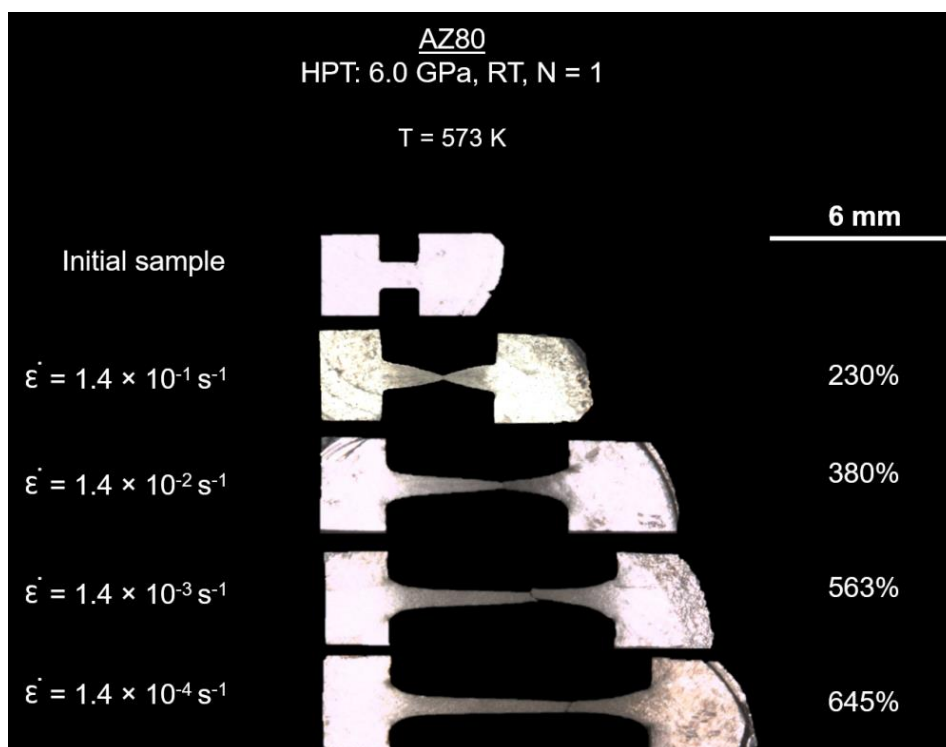


(b)

Figure 4.54 Appearance of AZ80 alloy tensile specimens processed by HPT at room temperature for N = 1/4 after tension to failure using different strain rates at testing temperature of 473K and 573 K, including the untested sample at the top.

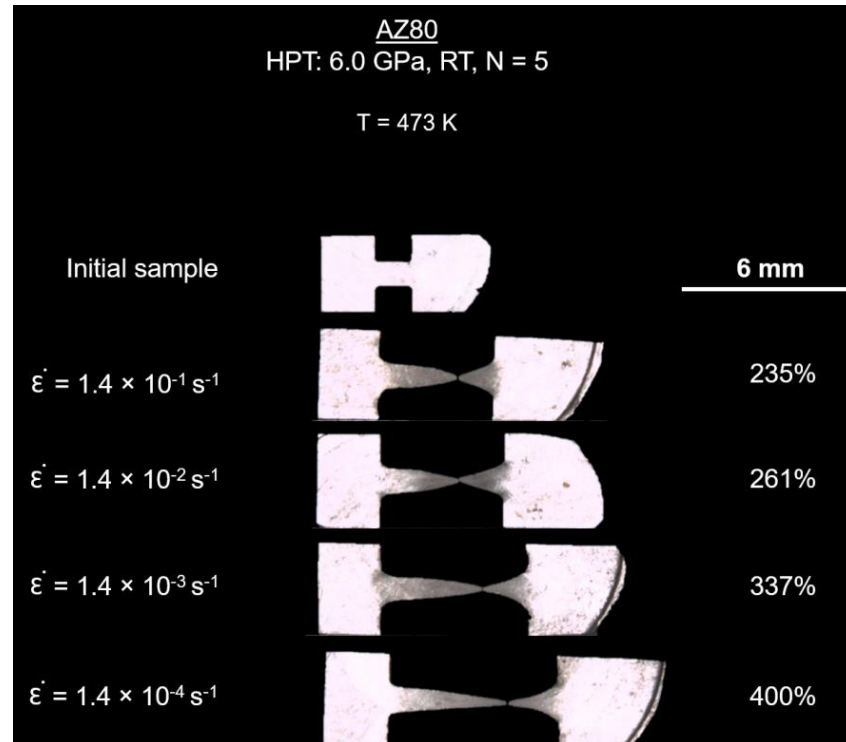


(a)

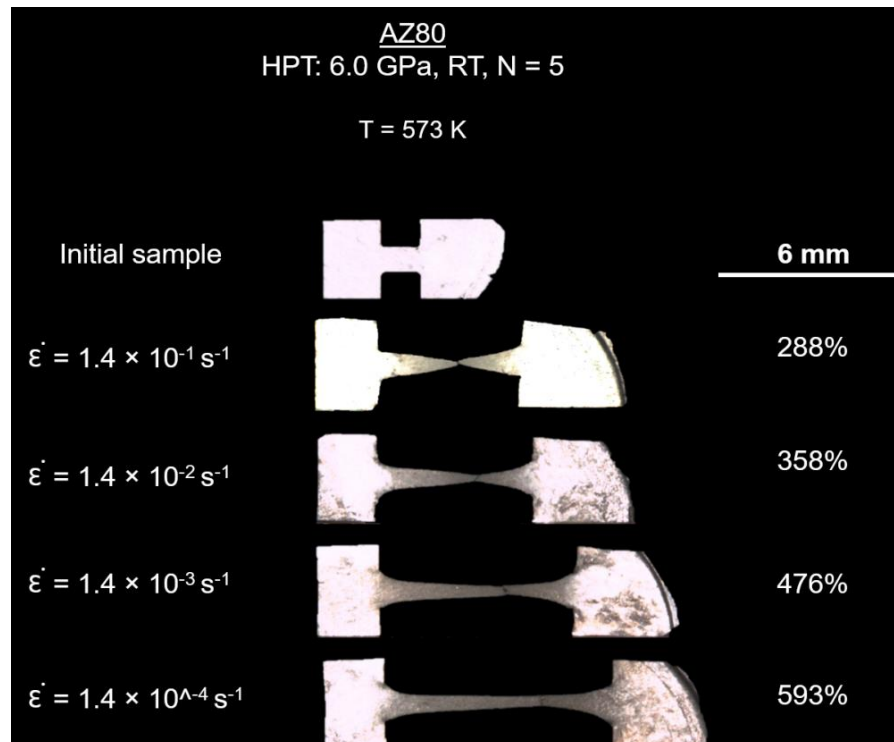


(b)

Figure 4.55 Appearance of AZ80 alloy tensile specimens processed by HPT at room temperature for N = 1 after tension to failure using different strain rates at testing temperature of 473 K and 573 K, including the untested sample at the top.

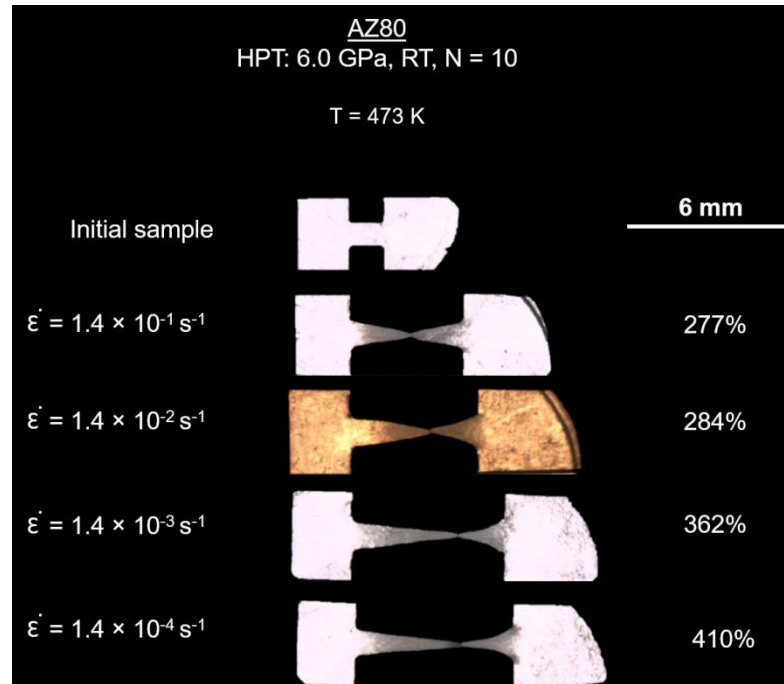


(a)

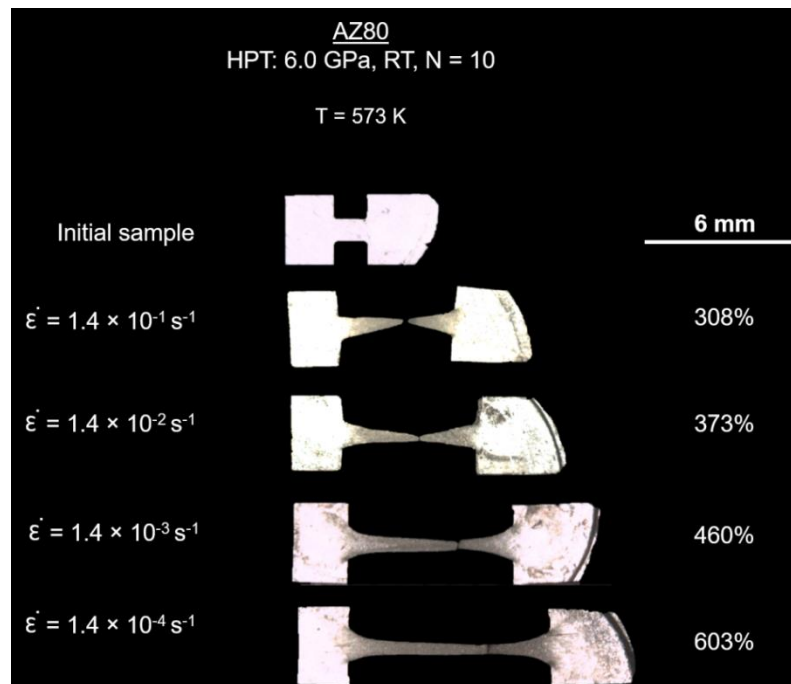


(b)

Figure 4.56 Appearance of AZ80 alloy tensile specimens processed by HPT at room temperature for N = 5 after tension to failure using different strain rates at testing temperature of 473 K and 573 K, including the untested sample at the top.



(a)



(b)

Figure 4.57 Appearance of AZ80 alloy tensile specimens processed by HPT at room temperature for $N = 10$ after tension to failure using different strain rates at testing temperature of 473 K and 573 K, including the untested sample at the top.

In Figures 4.58, 4.59, 4.60 and 4.61 and Figures 4.62, 4.63, 4.64 and 4.65, the appearance of the tested samples at 473 K and 573 K respectively are presented in a

different order, where the strain rate is constant and the number of turns increases from the top to the bottom. In these figures, it can be seen that at higher strain rates the sample with higher number of turns has the maximum elongation, while at slower strain rates the maximum elongation is achieved when the material is processed by HPT for 1 turn. The maximum elongation of all samples records an elongation of 645%. This elongation was achieved when the sample was processed by HPT for 1 turn and pulled in tension to failure at 573 K using a strain rate of $1.4 \times 10^{-4} \text{ s}^{-1}$. These results illustrate that AZ80 magnesium alloy does not follow the predicted trend of increasing superplasticity with increasing numbers of HPT process turns and decreasing average grain size, as described earlier for an AZ91 magnesium alloy [145]. In the earlier study, maximum elongation was achieved after 10 turns of torsional strain in HPT, while in the current study maximum elongation was achieved after only one turn, when a reasonably homogenous microstructure had not been achieved. There was a trend for Al–3% Mg–0.2% Sc alloy to show increased ductility in samples processed by ECAP with increasing number of passes through the die [198]. Similar behaviour to this study was reported earlier in ZK60 magnesium alloy processed by ECAP up to six passes, followed by the tensile test, and the maximum elongation was found in a sample processed by only two passes of ECAP [144].

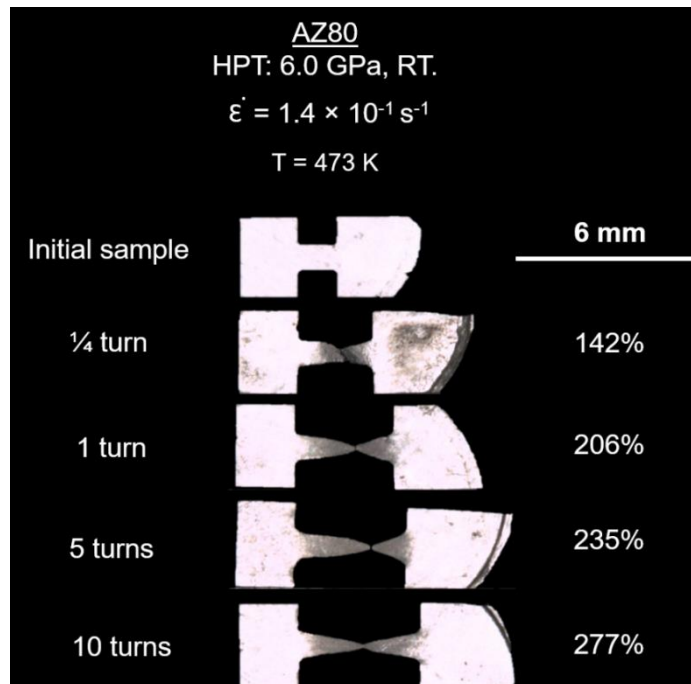


Figure 4.58 Appearance of AZ80 alloy tensile specimens processed by HPT at room temperature for different number of turns after tension to failure using strain rates of $1.4 \times 10^{-1} \text{ s}^{-1}$ at testing temperature of 473 K, including the untested sample at the top.

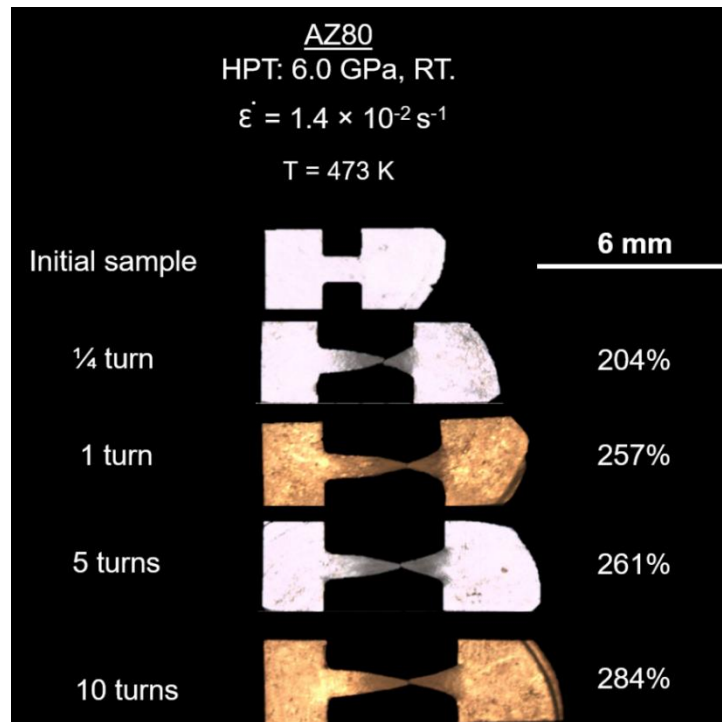


Figure 4.59 Appearance of AZ80 alloy tensile specimens processed by HPT at room temperature for different number of turns after tension to failure using strain rates of $1.4 \times 10^{-2} \text{ s}^{-1}$ at testing temperature of 473 K, including the untested sample at the top.

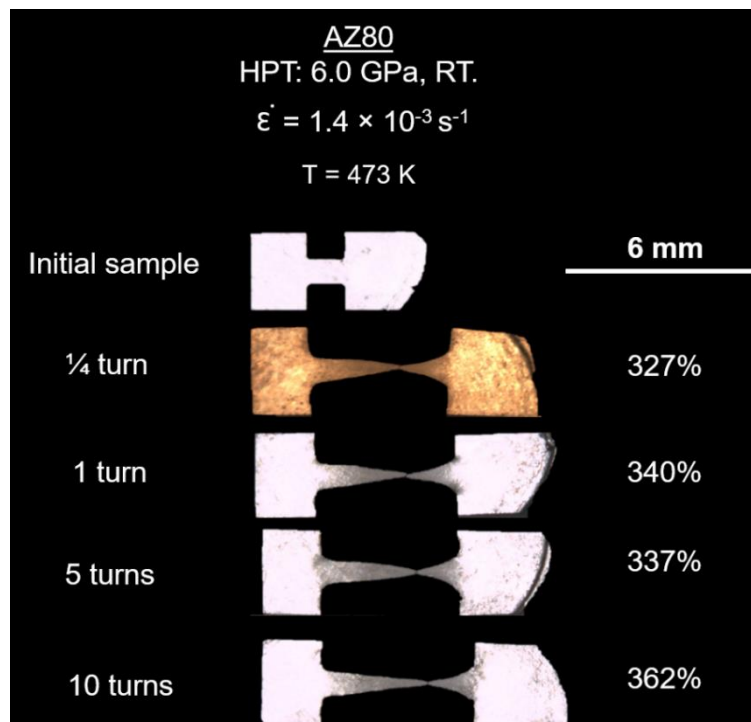


Figure 4.60 Appearance of AZ80 alloy tensile specimens processed by HPT at room temperature for different number of turns after tension to failure using strain rates of $1.4 \times 10^{-3} \text{ s}^{-1}$ at testing temperature of 473 K, including the untested sample at the top.

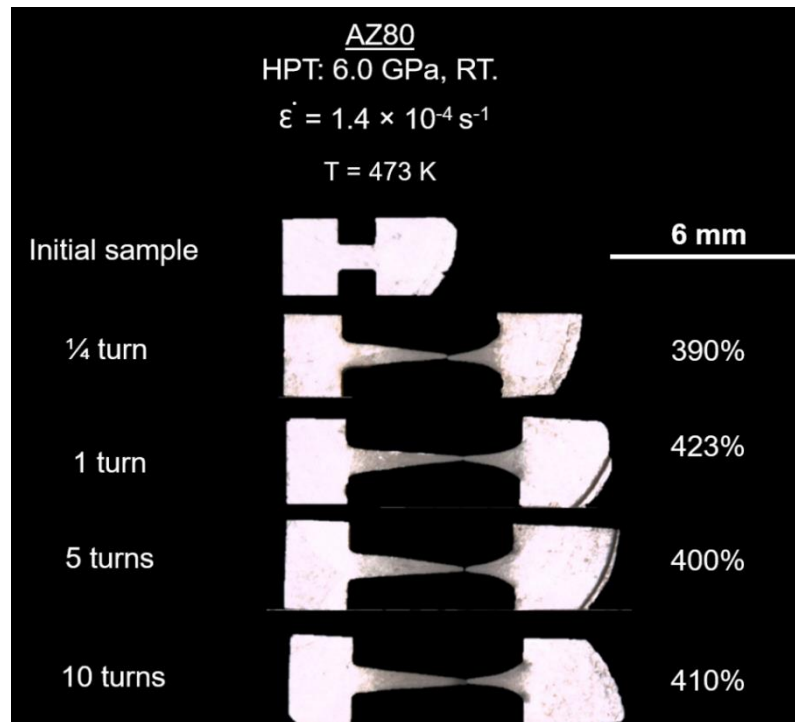


Figure 4.61 Appearance of AZ80 alloy tensile specimens processed by HPT at room temperature for different number of turns after tension to failure using strain rates of $1.4 \times 10^{-4} \text{ s}^{-1}$ at testing temperature of 473 K, including the untested sample at the top.

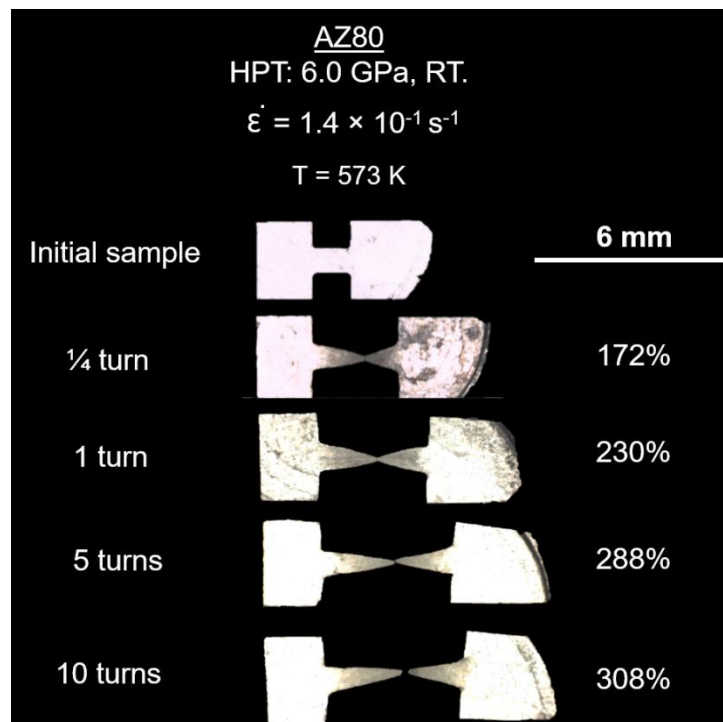


Figure 4.62 Appearance of AZ80 alloy tensile specimens processed by HPT at room temperature for different number of turns after tension to failure using strain rates of $1.4 \times 10^{-1} \text{ s}^{-1}$ at testing temperature of 573 K, including the untested sample at the top.

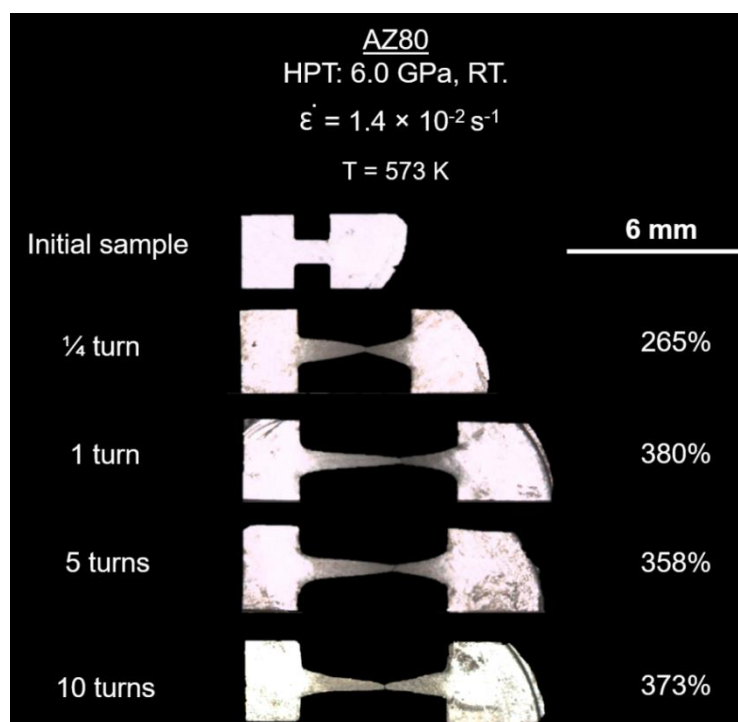


Figure 4.63 Appearance of AZ80 alloy tensile specimens processed by HPT at room temperature for different number of turns after tension to failure using strain rates of $1.4 \times 10^{-2} \text{ s}^{-1}$ at testing temperature of 573 K, including the untested sample at the top.

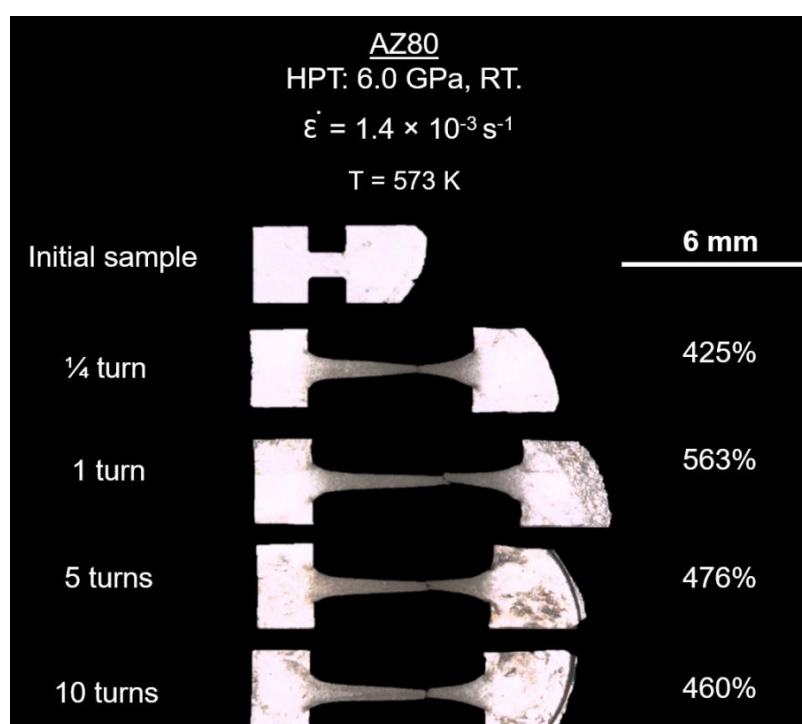


Figure 4.64 Appearance of AZ80 alloy tensile specimens processed by HPT at room temperature for different number of turns after tension to failure using strain rates of $1.4 \times 10^{-3} \text{ s}^{-1}$ at testing temperature of 573 K, including the untested sample at the top.

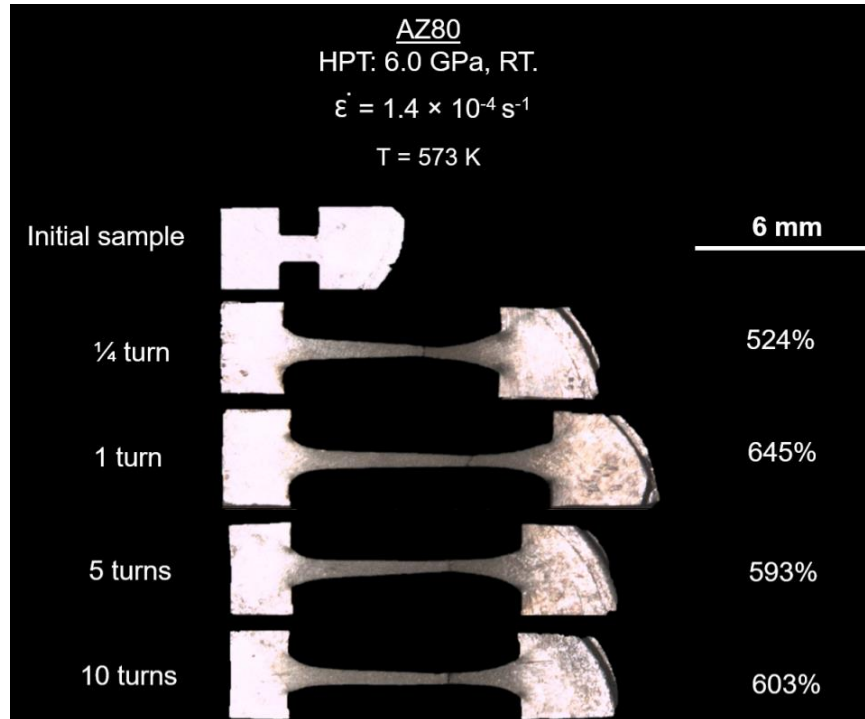
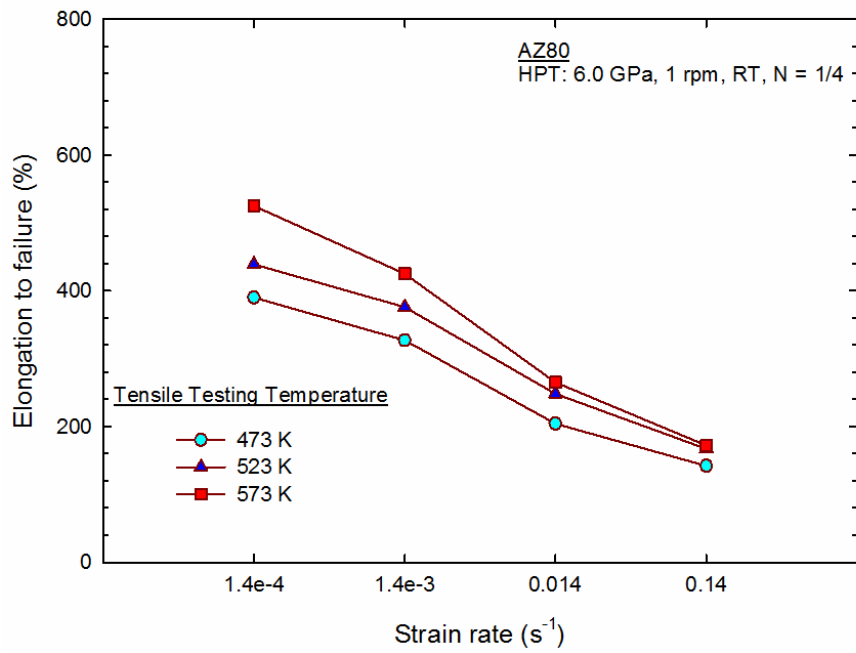


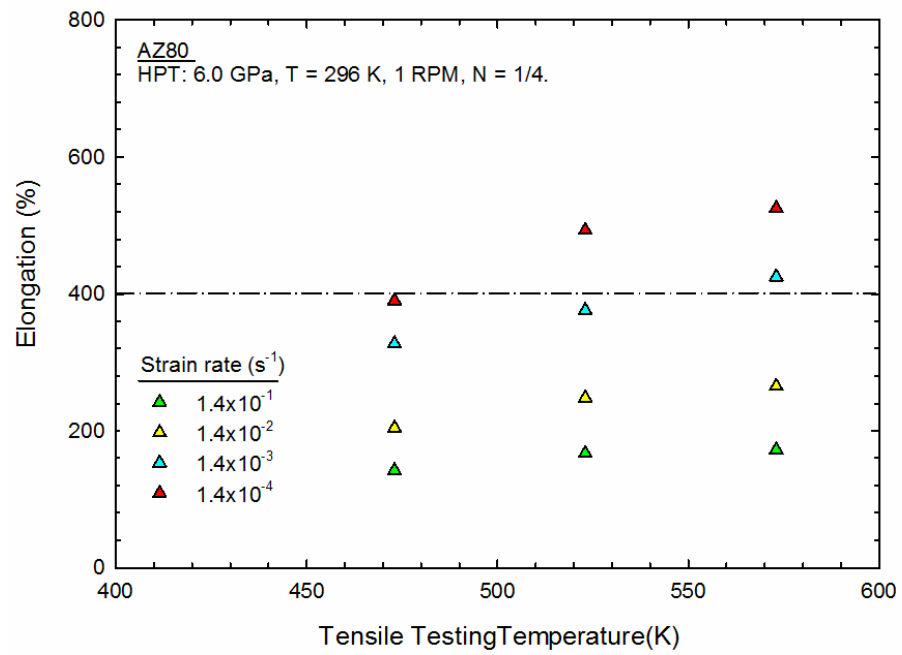
Figure 4.65 Appearance of AZ80 alloy tensile specimens processed by HPT at room temperature for different number of turns after tension to failure using strain rates of $1.4 \times 10^{-4} \text{ s}^{-1}$ at testing temperature of 573 K, including the untested sample at the top.

4.7.3 The effect of strain rate and tensile testing temperature on the final elongation

Figures 4.54 (b), 4.55 (b), 4.56 (b) and 4.57 (b) illustrate the effect of the testing strain rate on final elongation when samples were processed by HPT for 1/4, 1, 5 and 10 turns and pulled in tension to failure at 573 K using strain rates of $1.4 \times 10^{-4} \text{ s}^{-1}$ – $1.4 \times 10^{-1} \text{ s}^{-1}$. Although the sample tested at the high strain rate $1.4 \times 10^{-2} \text{ s}^{-1}$ – $1.4 \times 10^{-1} \text{ s}^{-1}$ shows good elongation, none of the samples exceeded an elongation of 400%, thus the alloy did not show high-strain rate superplasticity (HSRS) behaviour. On the other hand, all the samples tested at slower strain rates $1.4 \times 10^{-4} \text{ s}^{-1}$ – $1.4 \times 10^{-3} \text{ s}^{-1}$ achieved an elongation greater than 400%. Figures 4.66, 4.67, 4.68, 4.69 illustrate the effect of the strain rate and tensile testing temperature on the final elongation in part (a) of the figures. The effect of the strain rate can be seen: the slower the strain rate, the greater the final elongation. The dashed line in section (b) of these figures represents the point of 400% elongation. It can be seen that by increasing the tensile testing temperature, the more samples will exceed that line, and the greater their elongation.

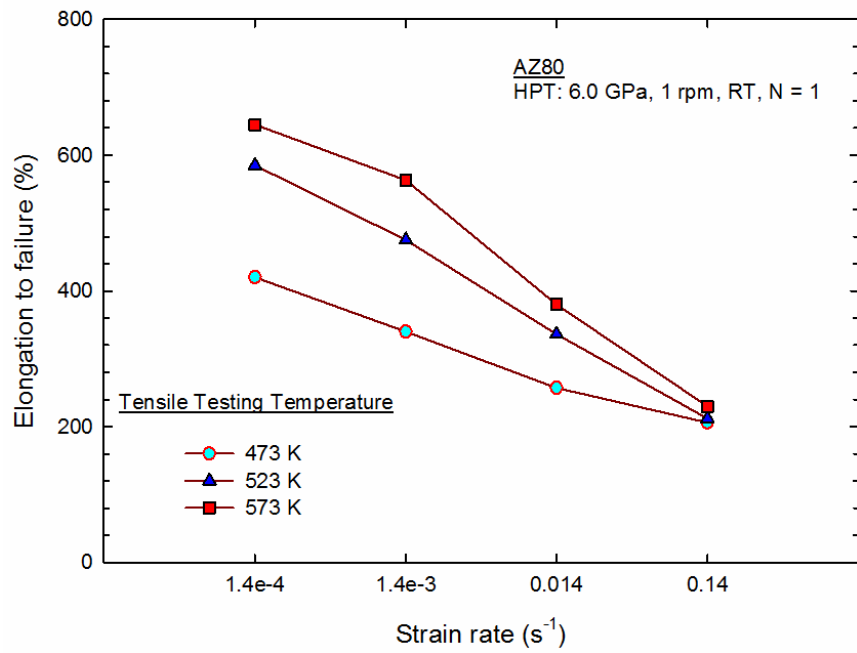


(a)

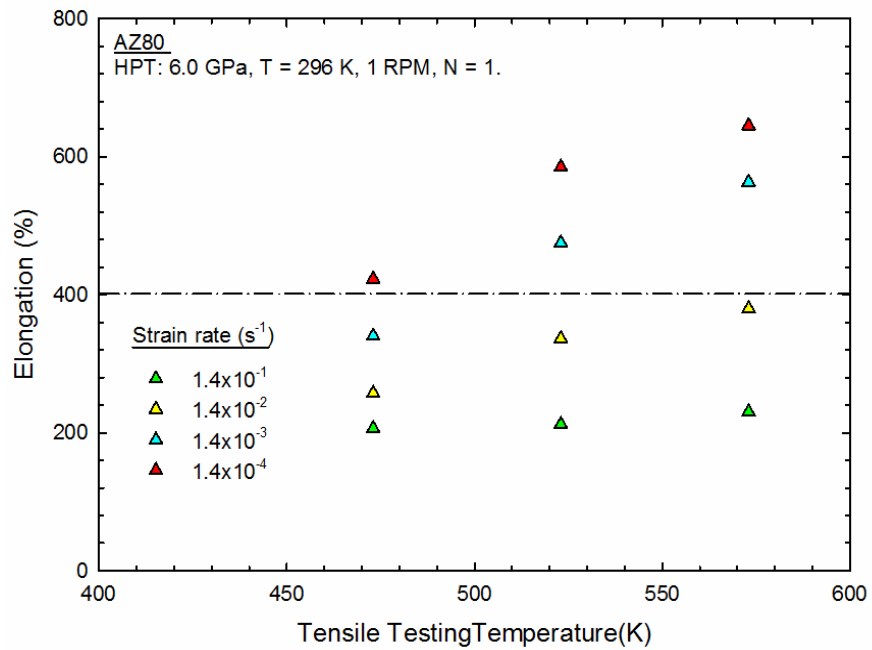


(b)

Figure 4.66 Elongation to failure comparison between HPT samples processed up to 1/4 turn at room temperature and tested to fracture using tensile test at different strain rates at (a) and different tensile testing temperatures at (b).

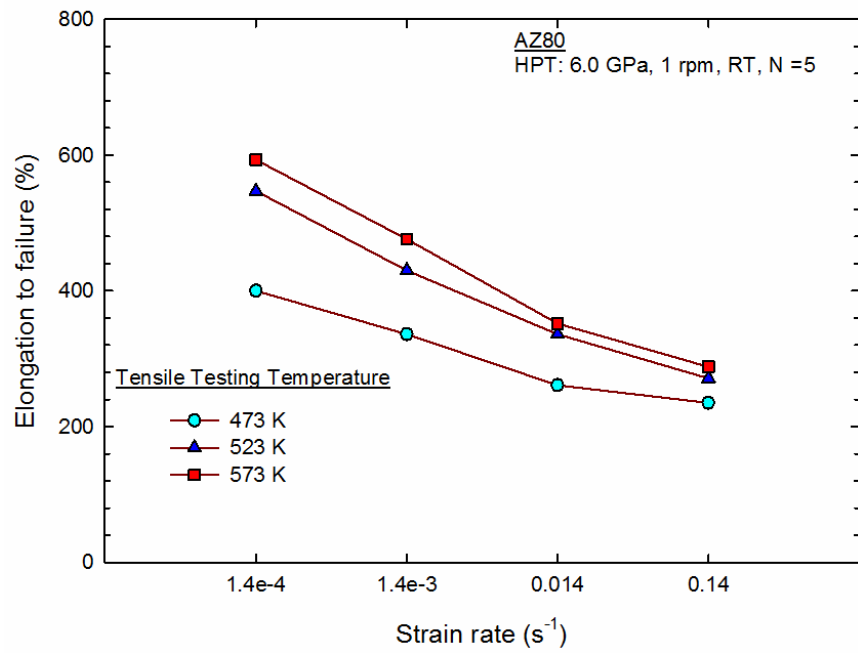


(a)

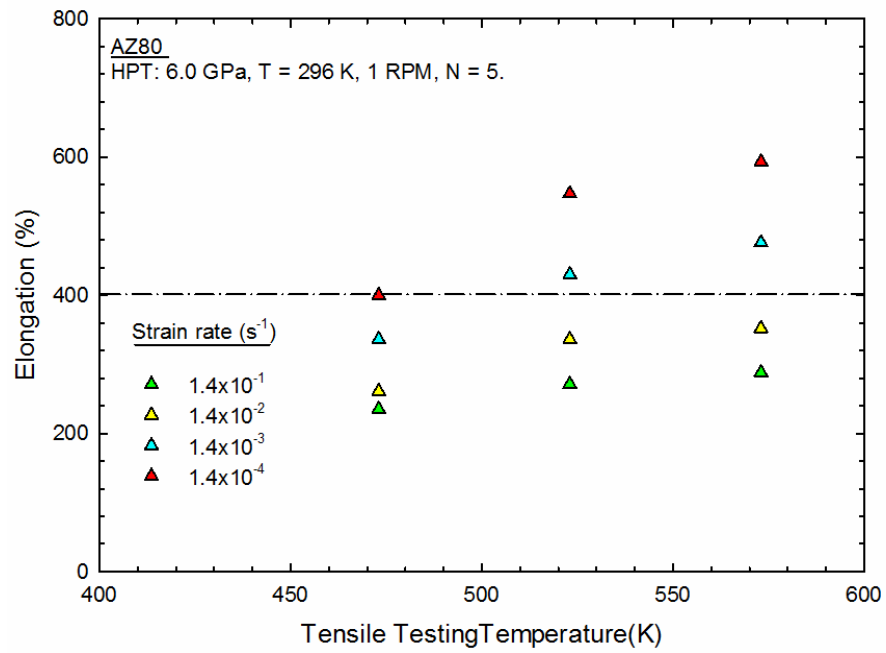


(b)

Figure 4.67 Elongation to failure comparison between HPT samples processed up to 1 turn at room temperature and tested to fracture using tensile test at different strain rates at (a) and different tensile testing temperatures at (b).

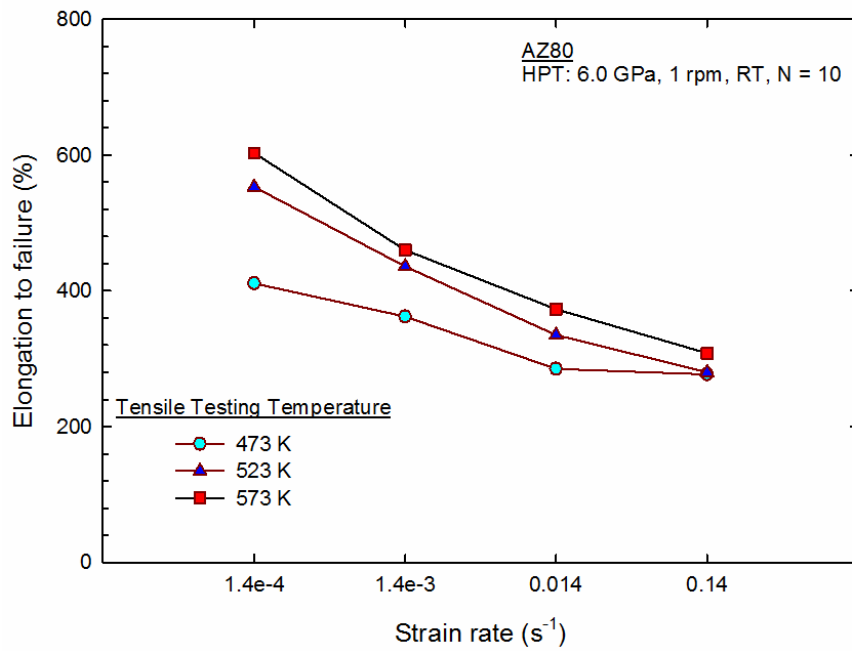


(a)

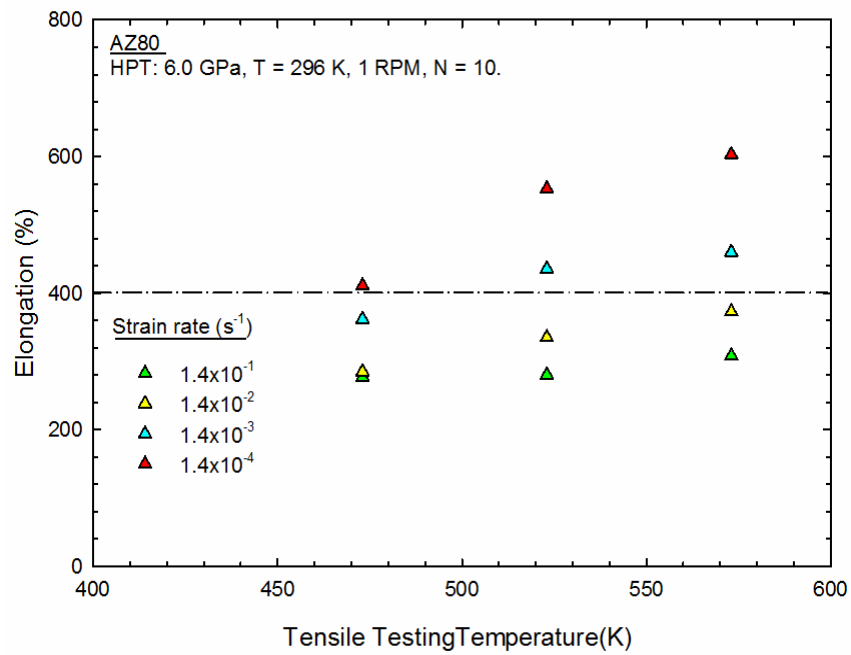


(b)

Figure 4.68 Elongation to failure comparison between HPT samples processed up to 5 turns at room temperature and tested to fracture using tensile test at different strain rates at (a) and different tensile testing temperatures at (b).



(a)



(b)

Figure 4.69 Elongation to failure comparison between HPT samples processed up to 10 turns at room temperature and tested to fracture using tensile test at different strain rates at (a) and different tensile testing temperatures at (b).

4.7.4 Strain rate sensitivity index (m) and the activation energy (Q)

The strain rate sensitivity index (m) values were calculated from the slope of (log-log) format stress-strain rate diagram (Equation 4.1)

$$m = \left(\frac{\partial \ln \sigma}{\partial \ln \dot{\epsilon}} \right) \quad 4.1$$

These values are shown in the flow stress against strain rate graphs in the as-received condition in Figure 4.70 and after HPT process in Figures 4.71, 4.72 and 4.73. These graphs represent the samples processed by HPT at room temperature for any given number of turns and pulled to fracture in tension at testing temperatures of 473 K, 523 K and 573 K respectively. A first look at these graphs shows that increasing tensile testing temperature will decrease the flow stresses and increase the value of strain rate sensitivity (m). This increase in the value of strain rate sensitivity (m) is associated with an increase in the maximum elongation achieved before fracture. The flow stress increases with increasing strain rate. It can be seen that a sample processed by HPT for one turn and tested in tension to fracture by tensile test at 573 K, where it shows maximum elongation for all processed samples at a strain rate of $1.4 \times 10^{-4} \text{ s}^{-1}$, has the highest strain rate sensitivity (m) of ~ 0.6 .

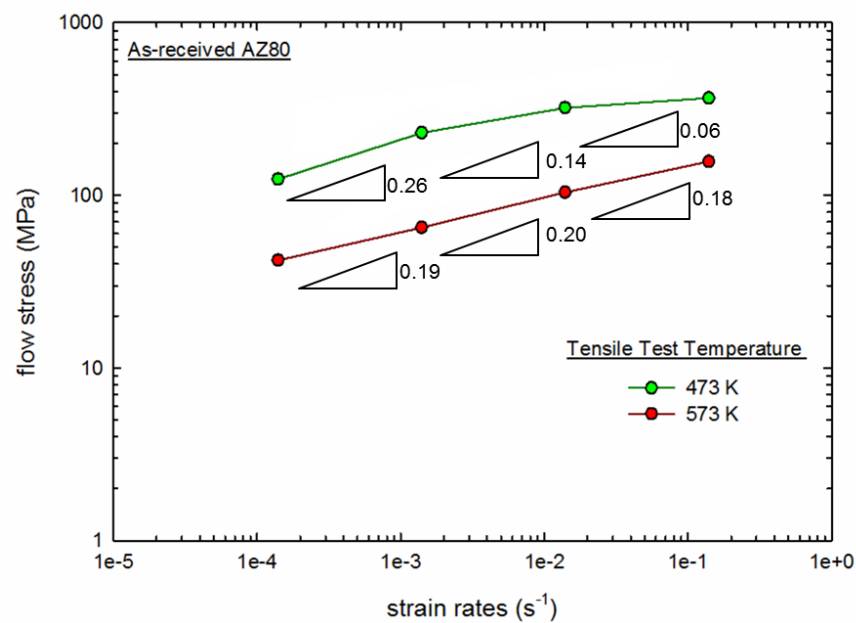
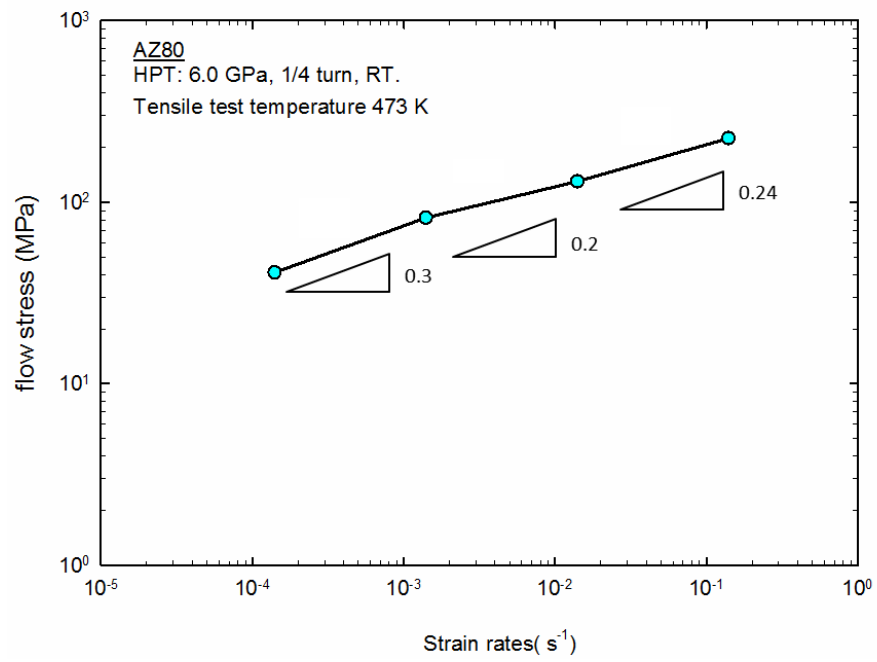
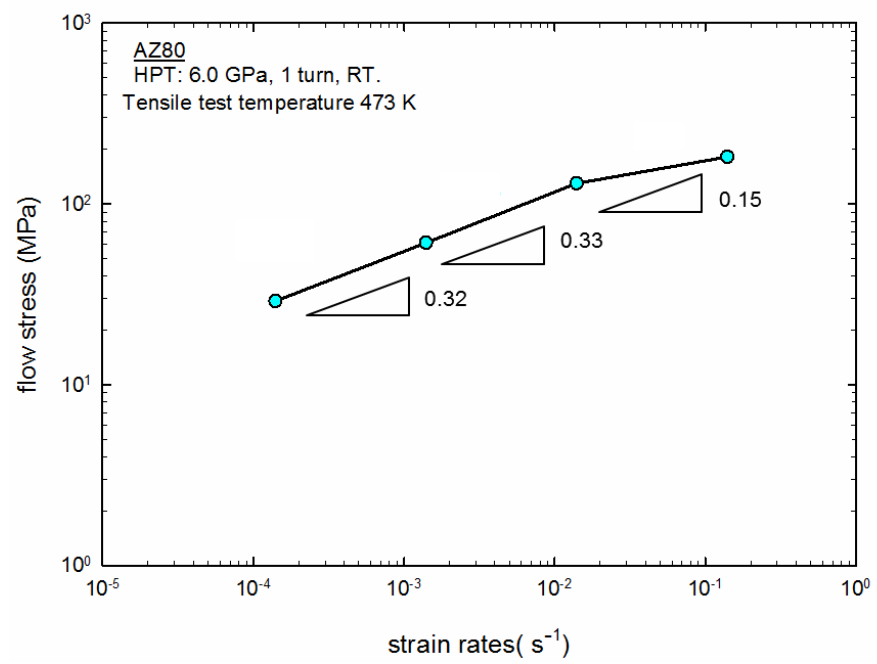


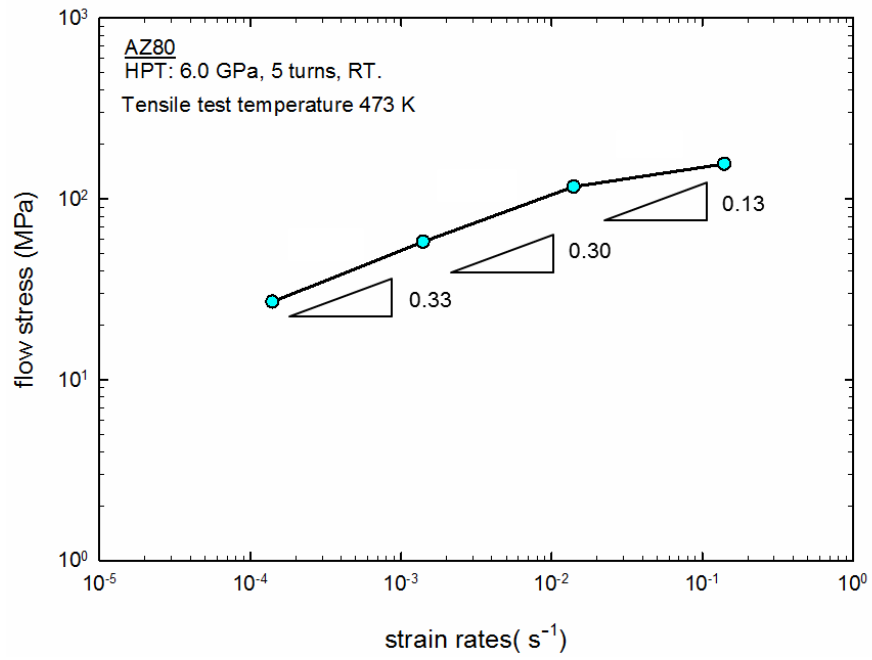
Figure 4.70 Strain rate sensitivity of AZ80 alloy in the as-received condition and tested in tension for different strain rates at a testing temperature of 473 K and 573 K.



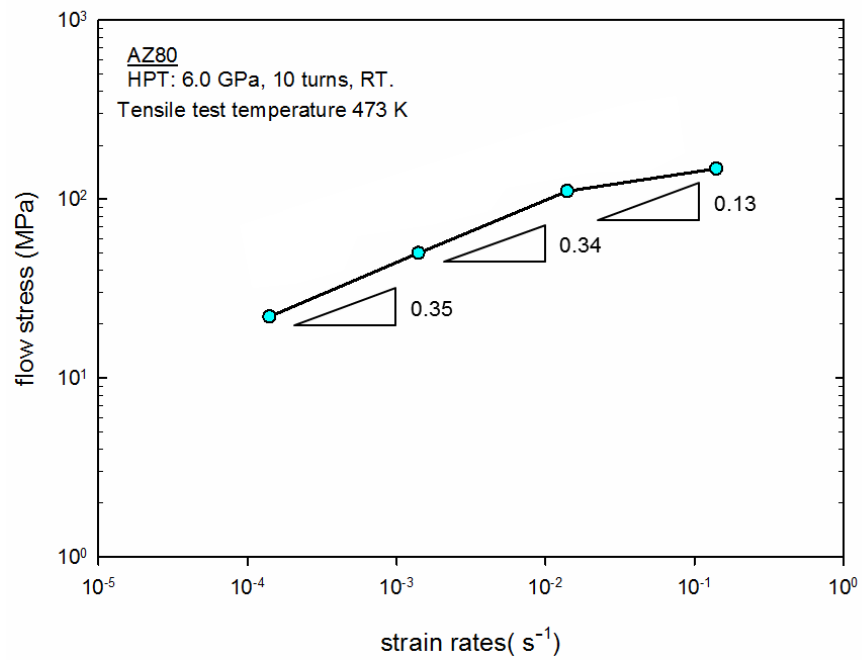
(a)



(b)

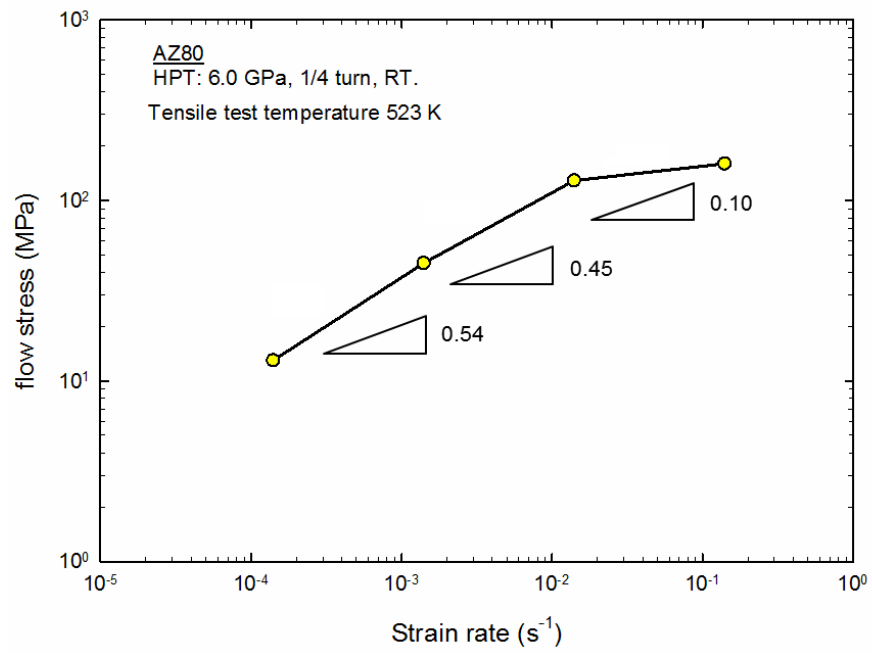


(c)

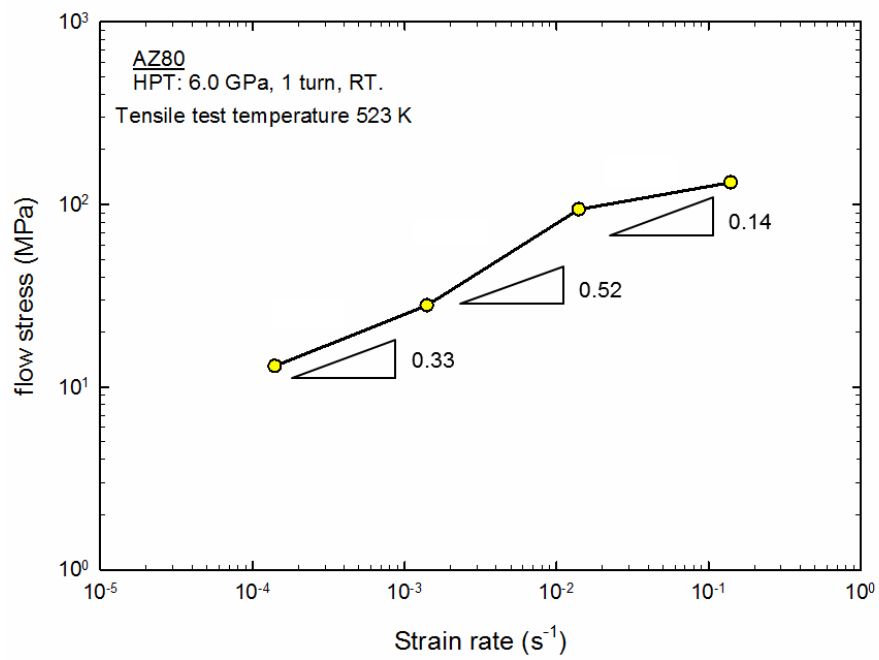


(d)

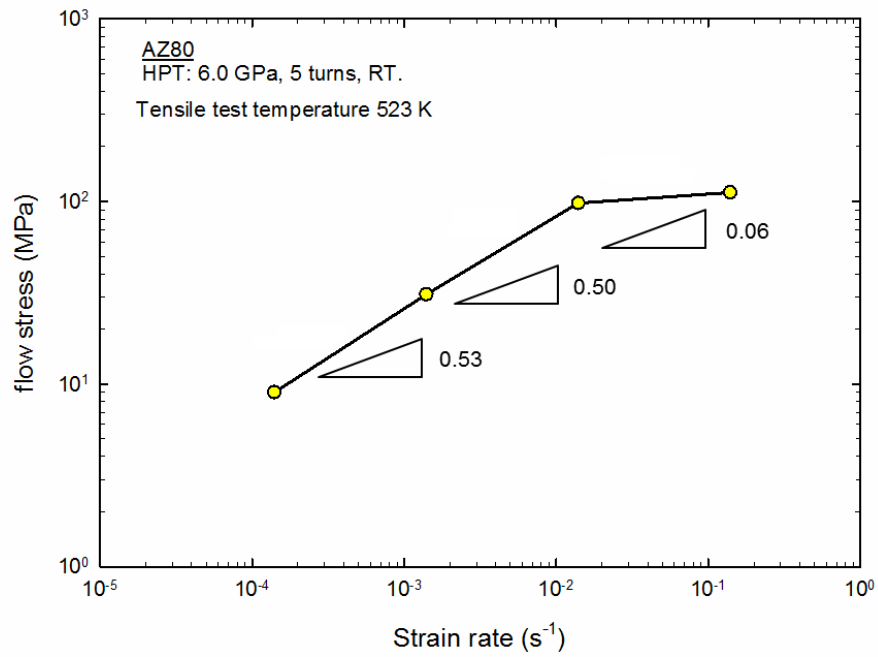
Figure 4.71 Strain rate sensitivity of AZ80 alloy processed for (a) $\frac{1}{4}$ turn, (b) 1 turn, (c) 5 turns and (d) 10 turns in HPT at room temperature using an applied pressure of 6.0 GPa and tested in tension for different strain rates at a tensile testing temperature of 473 K.



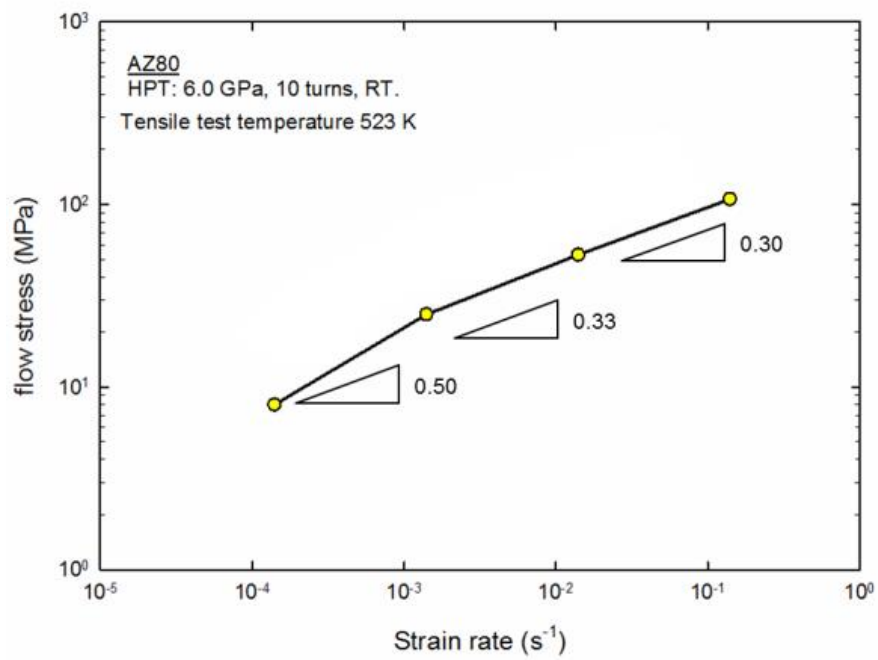
(a)



(b)

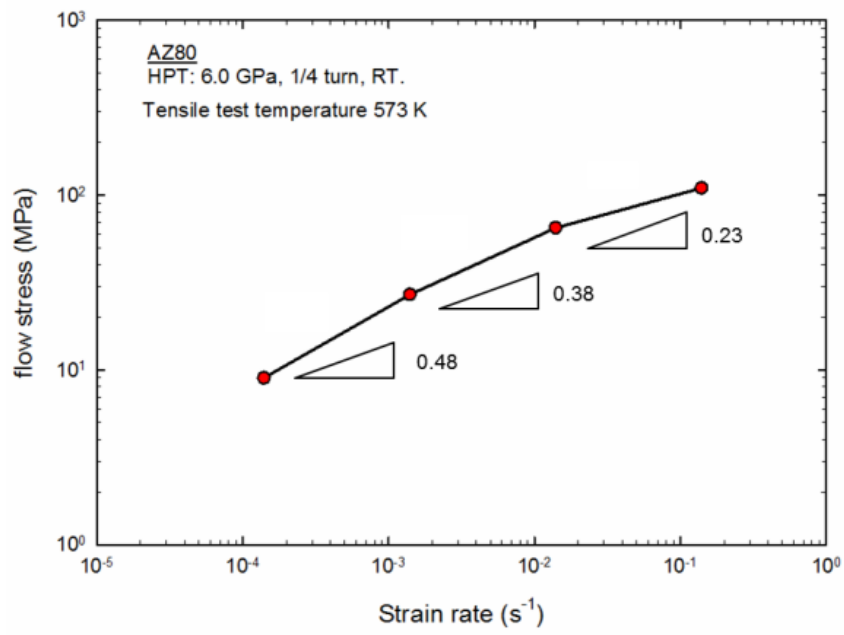


(c)

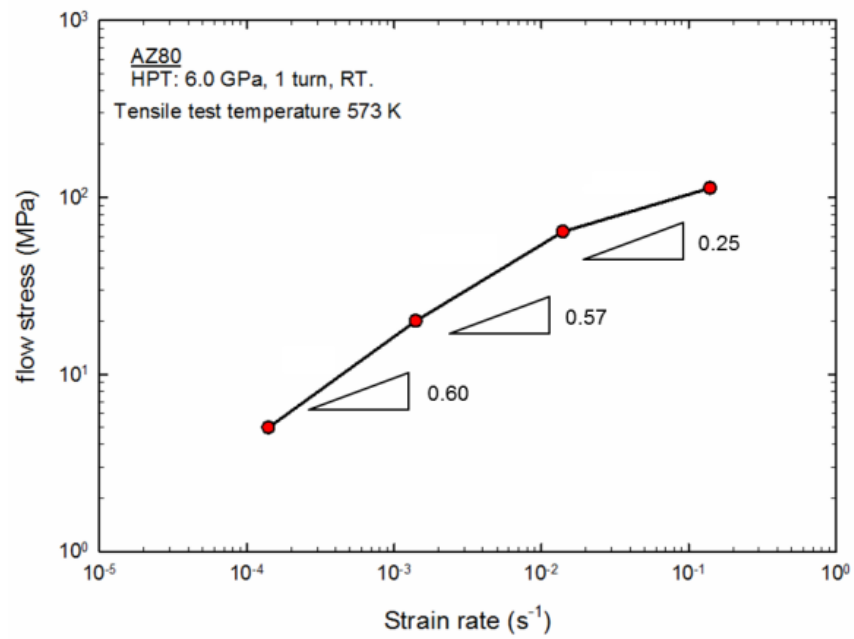


(d)

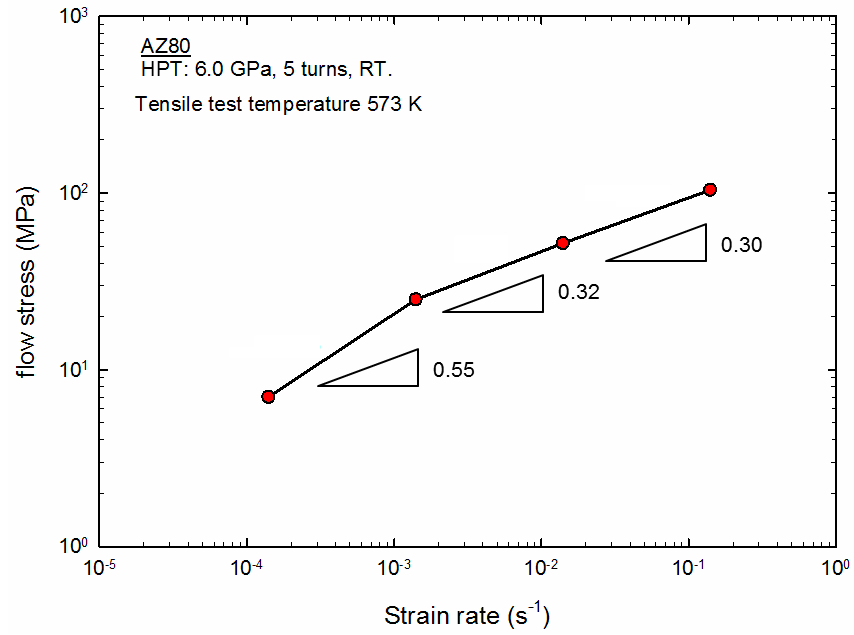
Figure 4.72 Strain rate sensitivity of AZ80 alloy processed for (a) $\frac{1}{4}$ turn, (b) 1 turn, (c) 5 turns and (d) 10 turns in HPT at room temperature using an applied pressure of 6.0 GPa and tested in tension for different strain rates at a tensile testing temperature of 523 K.



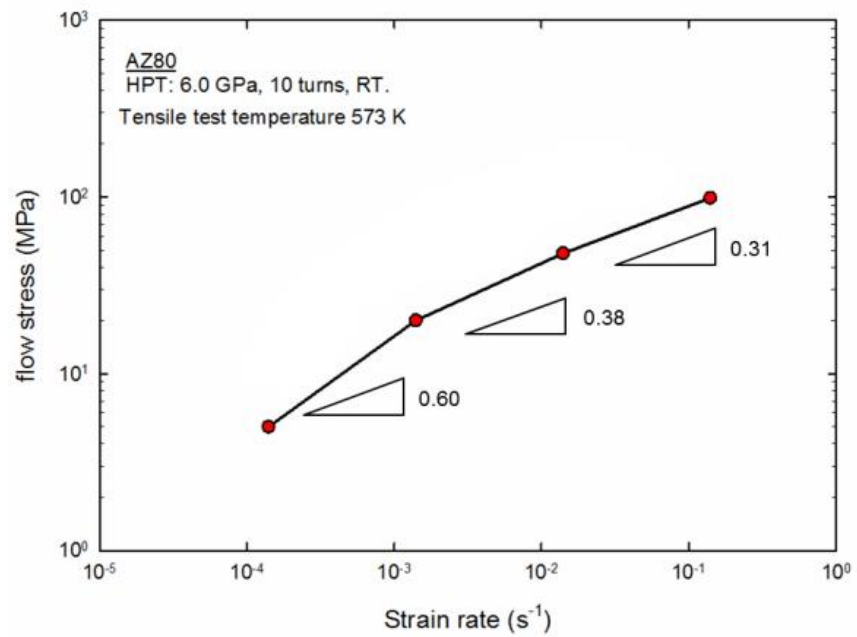
(a)



(b)



(c)



(d)

Figure 4.73 Strain rate sensitivity of AZ80 alloy processed for (a) $\frac{1}{4}$ turn, (b) 1 turn, (c) 5 turns and (d) 10 turns in HPT at room temperature using an applied pressure of 6.0 GPa and tested in tension for different strain rates at a tensile testing temperature of 573 K.

Since 1 turn has the maximum elongation in all tensile testing temperature when pulled in tension to fracture using a strain rate of $1.4 \times 10^{-4} \text{ s}^{-1}$, a graph of the variation in the flow stress of 1 turn against the reciprocal of tensile testing temperature was generated to calculate the activation energy (Q), as shown in Figure 4.74, using the following equation [199,200]:

$$Q = NR(\partial(\ln \sigma)/\partial(\frac{1}{T})) \quad 4.2$$

The activation energy was calculated at a fixed strain rate where Q is the activation energy, N is the stress exponent ($N = \frac{1}{m}$), R is the gas constant, σ is the flow stress, T is the absolute temperature, and $(\partial(\ln \sigma)/\partial(\frac{1}{T}))$ represents the slope of the graph. The activation energy was calculated for a sample processed by HPT for 1 turn at room temperature, and pulled in tension to failure at 473 K to 573 K under a strain rate of $1.4 \times 10^{-4} \text{ s}^{-1}$, since it has the most elongation of all samples. The apparent activation energy Q was 72.8 kJ/mol. This value is lower than the self-diffusion activation energy (135 kJ/mol) and grain boundary-diffusion activation (92 kJ/mol) for pure magnesium [201], but closer to the latter. This value indicates that the main deformation mechanism is GBS.

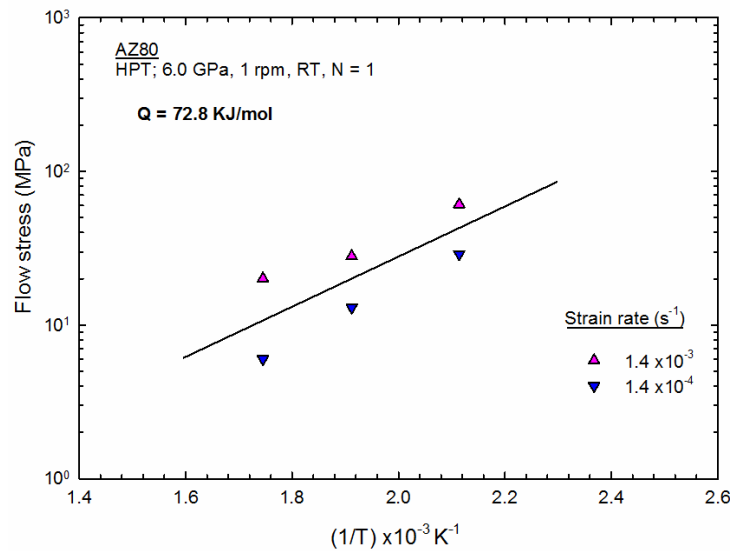
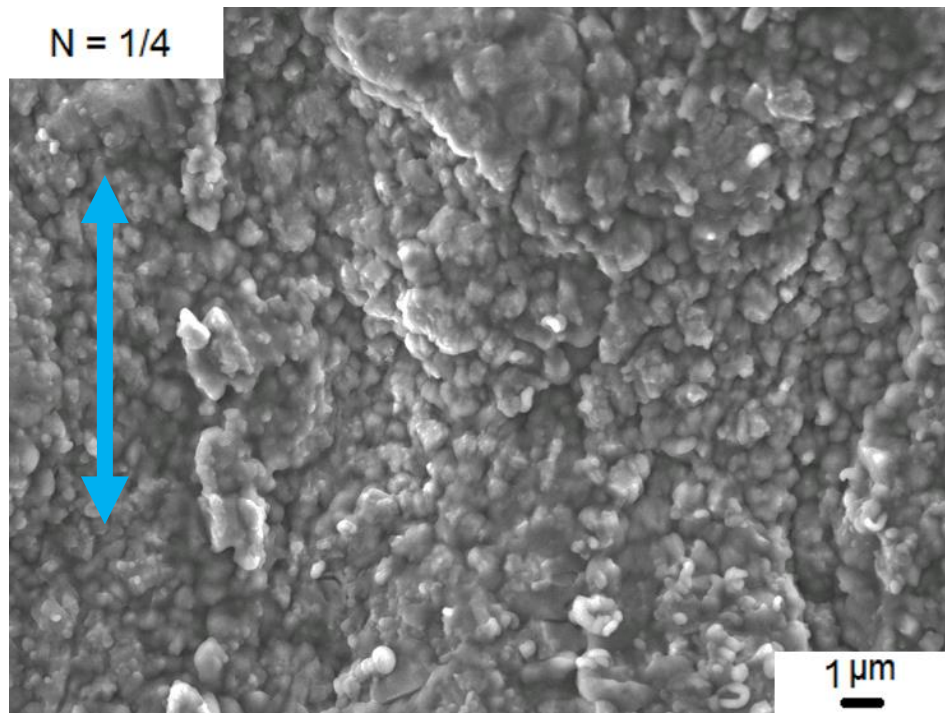


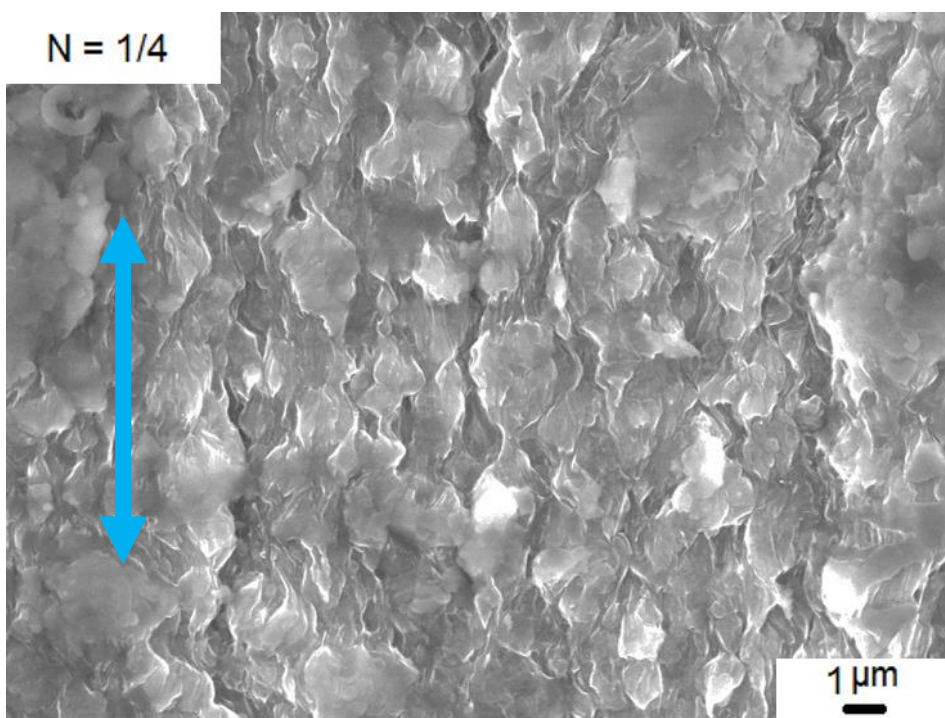
Figure 4.74 Difference in flow stresses with the reciprocal of the temperatures of samples processed by HPT for one turn and tested in tension at 473 K and 573 K using strain rates of $1.4 \times 10^{-4} \text{ s}^{-1}$ – $1.4 \times 10^{-3} \text{ s}^{-1}$ to determine the value of the activation energy (Q).

4.7.5 Microstructure observation at the gauge length

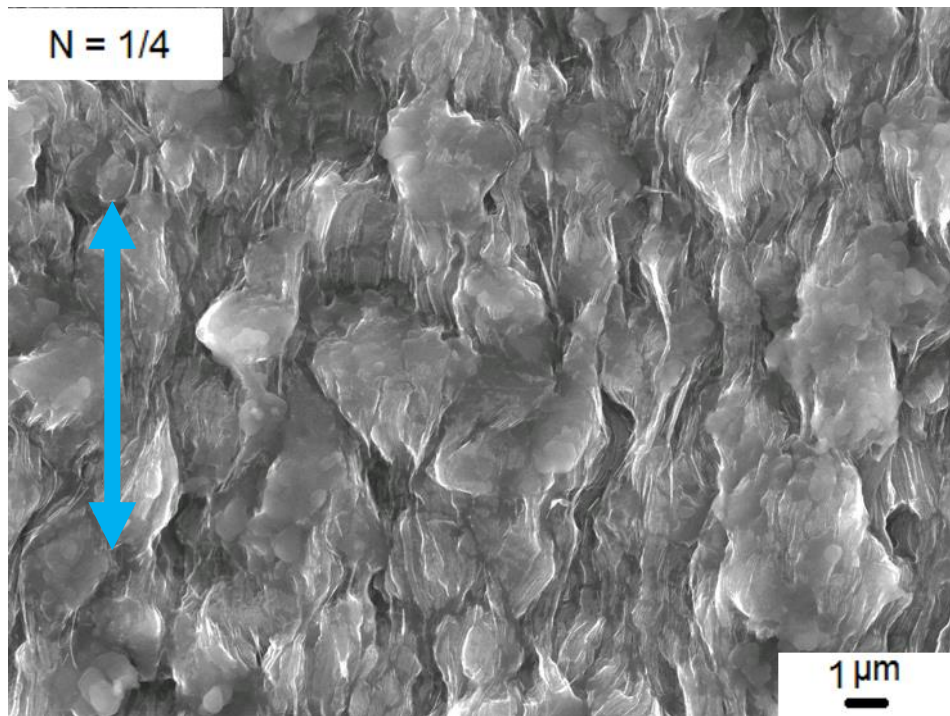
The SEM images in Figures 4.75, 4.76, 4.77 and 4.78 and Figures 4.79, 4.80, 4.81 and 4.82 show the microstructure on the gauge lengths after tensile test at 473 K and 573 K without any type of preparation of the samples. The grains are equiaxed and distributed homogeneously at the surface of the elongated specimen, with a number of cavities and interspaces between the grain boundaries, as pointed out by yellow arrows, and the existence of filaments, pointed out by red arrows between the grains. These indicate the presence of a high viscosity area along the grain boundaries [133]. This high viscosity area will tolerate a large number of cavities before the sample fractures. The filaments act to connect the grains by filling in the cavities and spaces between them. They are more observable when the alloy was tested at 573 K, as shown in Figures 4.79 (c), 4.80 (c), 4.81(c) and 4.82 (c). The second observation of the microstructure is that the grains of a sample processed by HPT and pulled in tension to failure at various temperature and strain rates appear coarser with increasing tensile test temperature and decreasing strain rate, as shown in the previous figures. Moreover, an interesting observation is that the grains in samples processed by HPT at room temperature and pulled in tension to failure at certain temperature, either 473 K or 573 K, show the following behaviour: at the faster strain rate $1.4 \times 10^{-2} \text{ s}^{-1}$ – $1.4 \times 10^{-1} \text{ s}^{-1}$; the grains of the sample processed by HPT for a higher number of turns (10 turns) are finer than for the sample processed by HPT for a lower number of turns (1 turn) and tensile tested at the same temperature, while when the alloy tested at a slower strain rate of $1.4 \times 10^{-4} \text{ s}^{-1}$, the grains in the sample processed by HPT for a higher number of turns (10 turns) are coarser than for the sample processed by HPT for a lower number of turns (1 turn) and tensile tested at the same temperature. The third observation is that the grains developed filaments at higher testing temperatures and slower strain rates. Tensile direction (TD) is indicated by the large blue arrow in the next images.



(a) $N = 1/4$, 473 K, $1.4 \times 10^{-2} \text{ s}^{-1}$

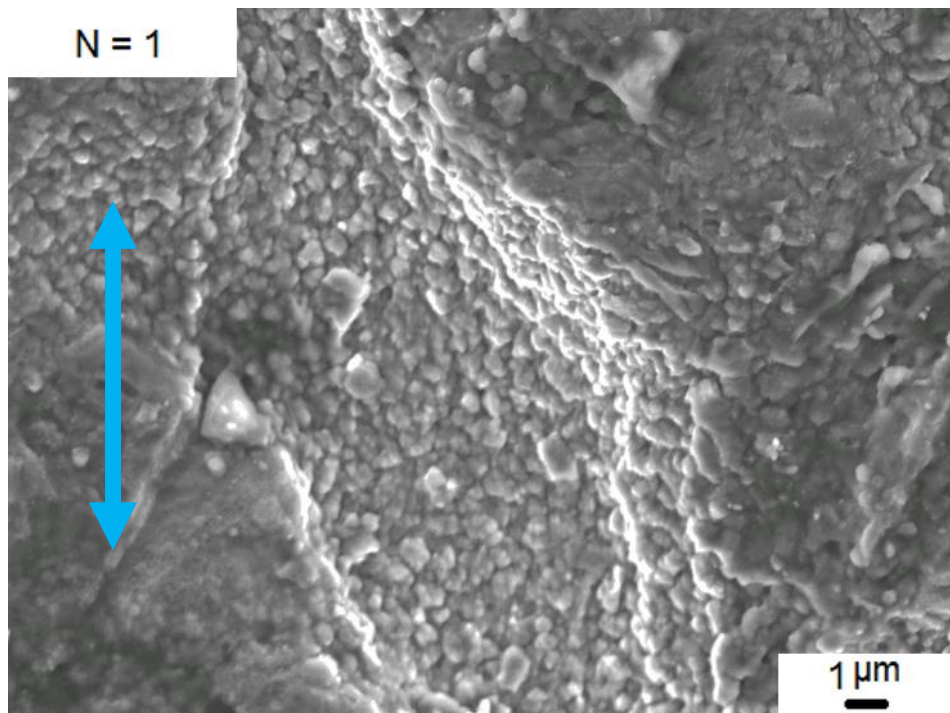


(b) $N = 1/4$, 473 K, $1.4 \times 10^{-3} \text{ s}^{-1}$

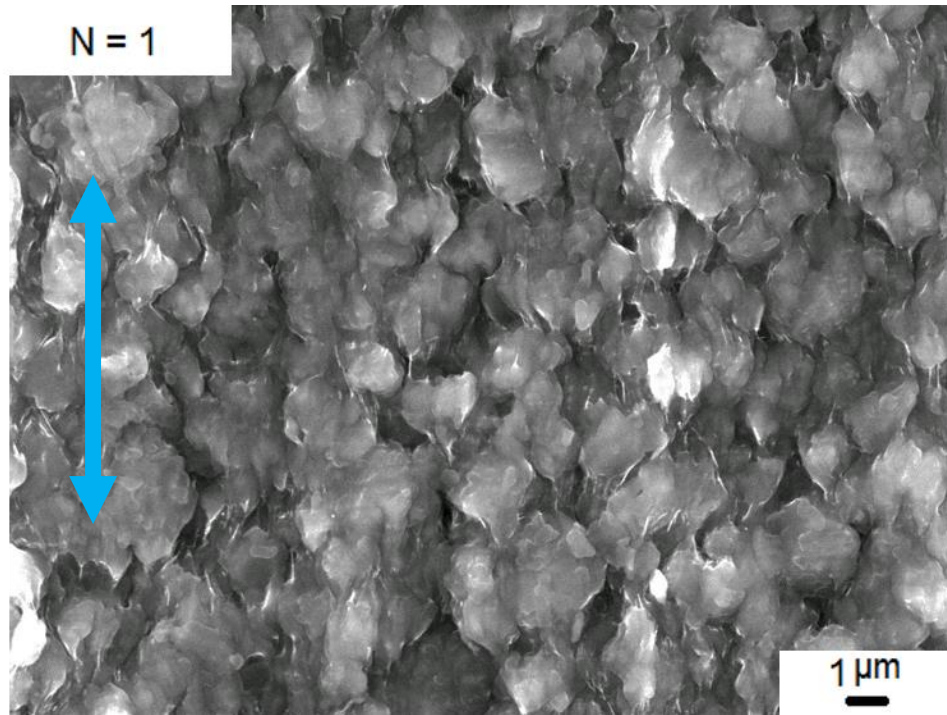


(c) $N = 1/4$, 473 K, $1.4 \times 10^{-4} \text{ s}^{-1}$

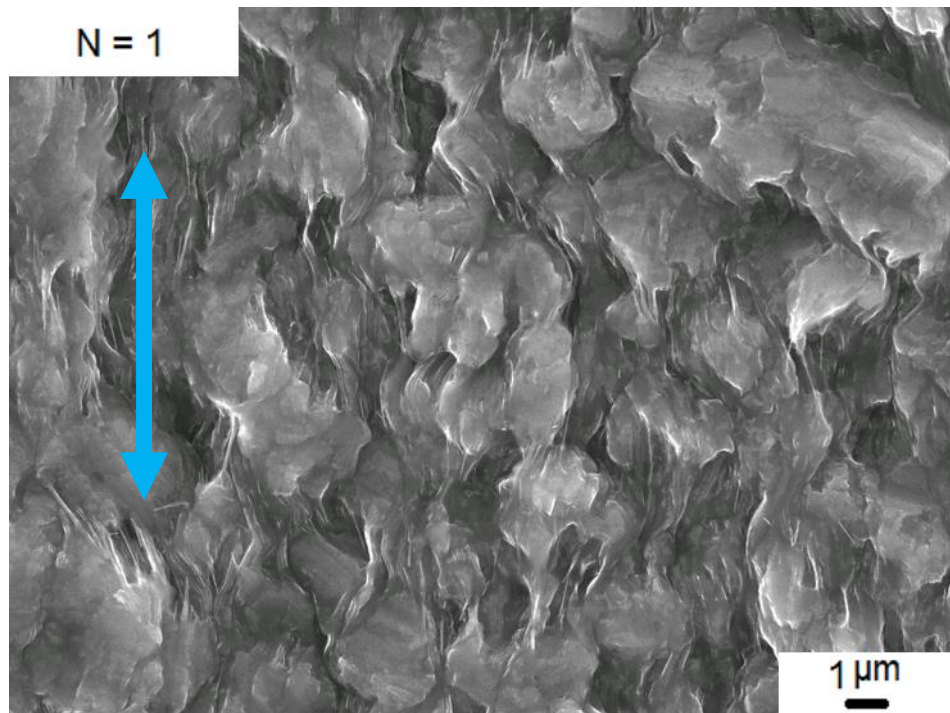
Figure 4.75 Surface morphology of the tested tensile samples at the gauge lengths for the AZ80 alloy processed for $N = 1/4$ turn in HPT at room temperature using an applied pressure of 6.0 GPa and tested in tension to failure for different strain rates at a testing temperature of 473 K.



(a) $N = 1$, 473 K, $1.4 \times 10^{-2} \text{ s}^{-1}$

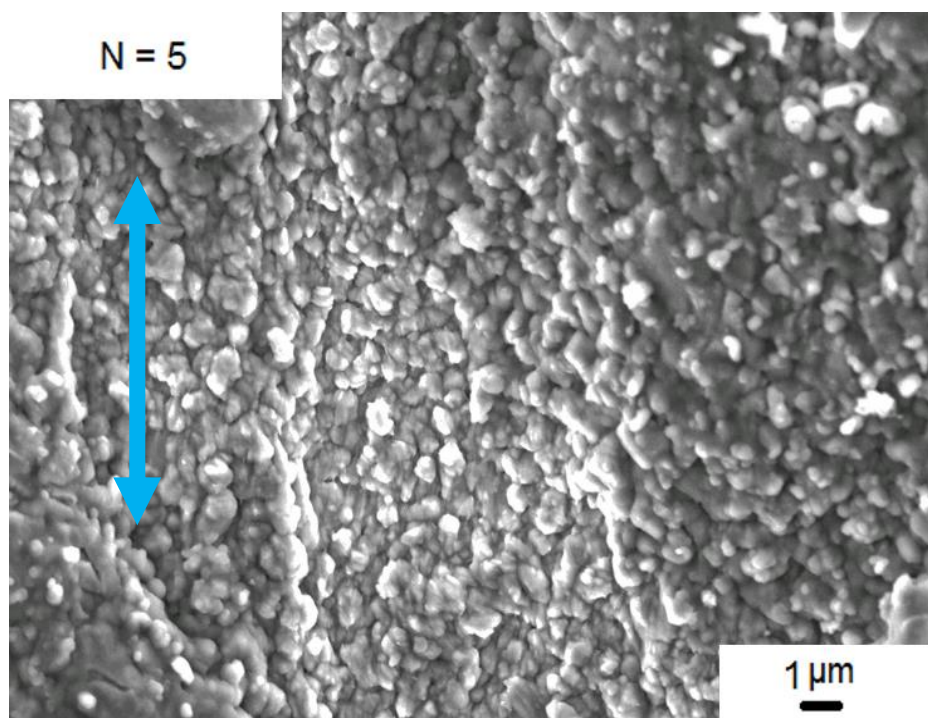


(b) $N = 1$, 473 K , $1.4 \times 10^{-3} \text{ s}^{-1}$

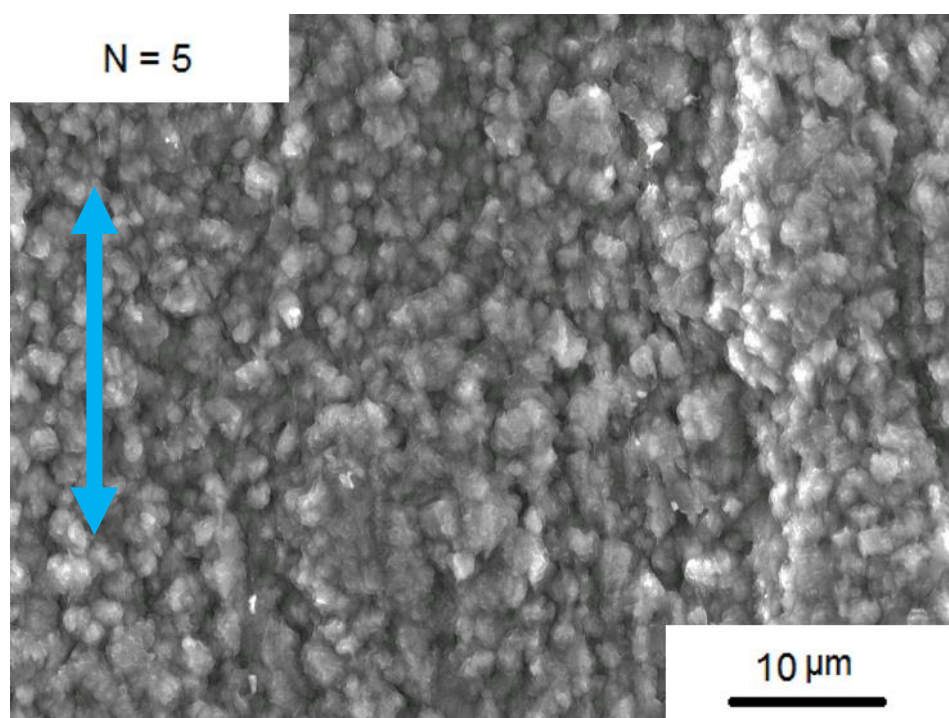


(c) $N = 1$, 473 K , $1.4 \times 10^{-4} \text{ s}^{-1}$

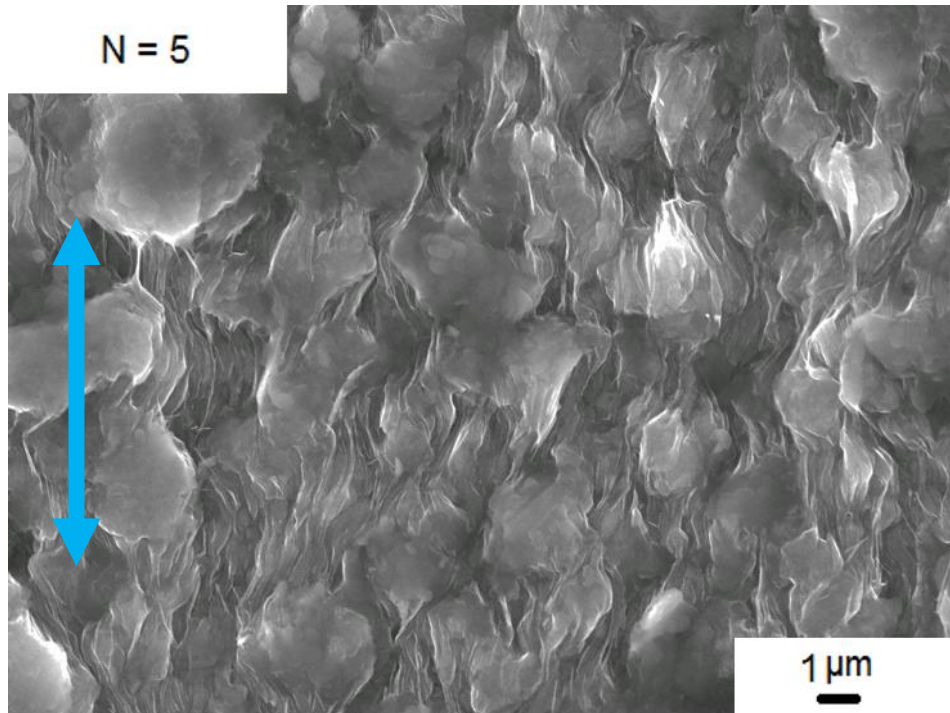
Figure 4.76 Surface morphology of the tested tensile samples at the gauge lengths for the AZ80 alloy processed for $N = 1$ turn in HPT at room temperature using an applied pressure of 6.0 GPa and tested in tension to failure for different strain rates at testing temperature of 473 K .



(a) $N = 5$, 473 K, $1.4 \times 10^{-2} \text{ s}^{-1}$

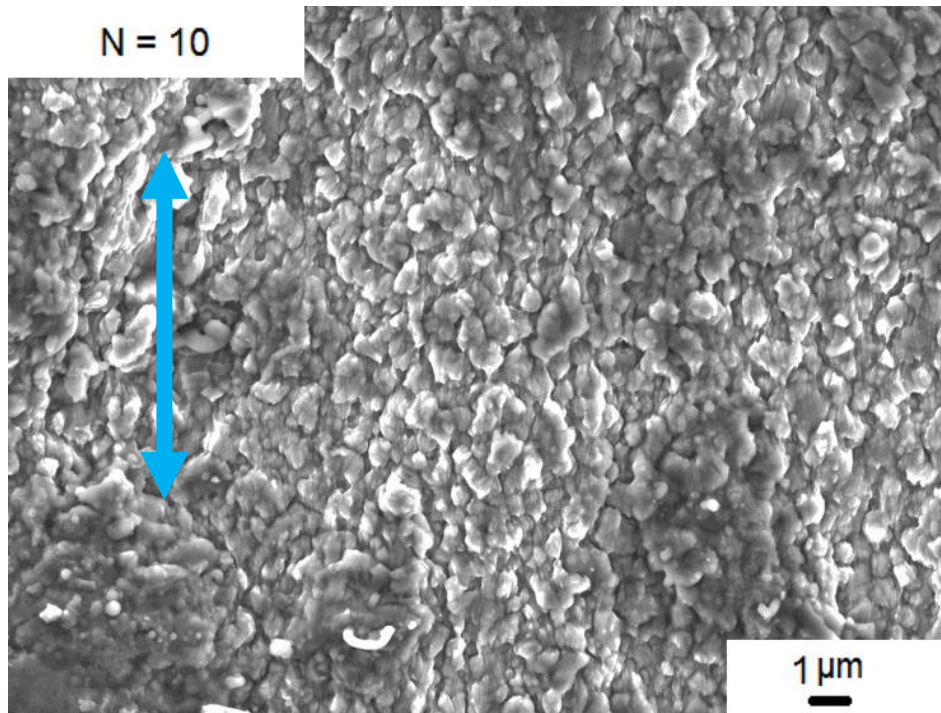


(b) $N = 5$, 473 K, $1.4 \times 10^{-3} \text{ s}^{-1}$

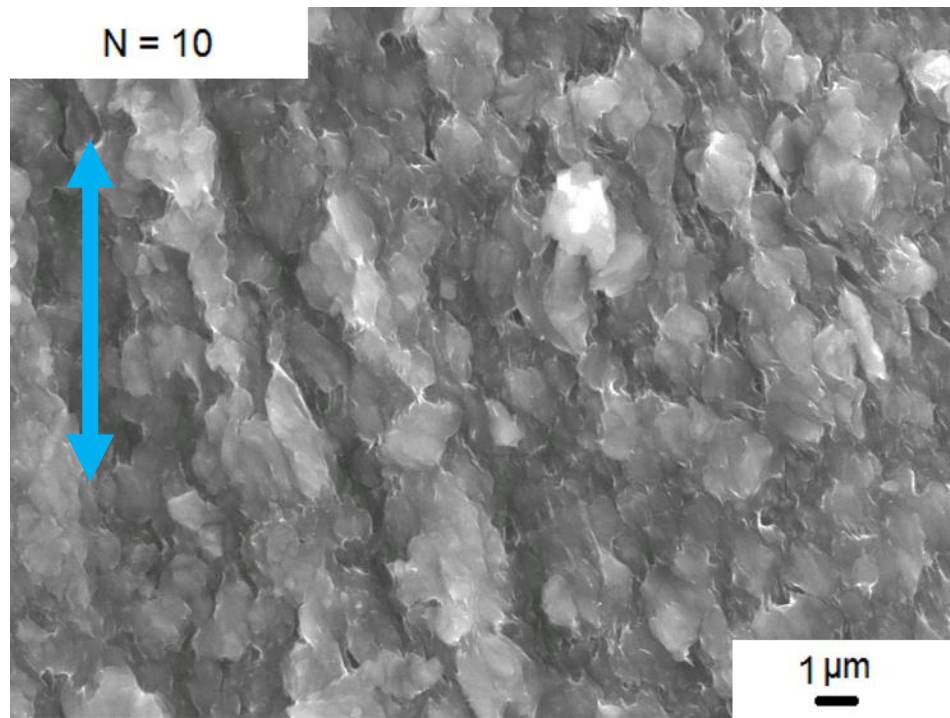


(c) $N = 5$, 473 K, $1.4 \times 10^{-4} \text{ s}^{-1}$

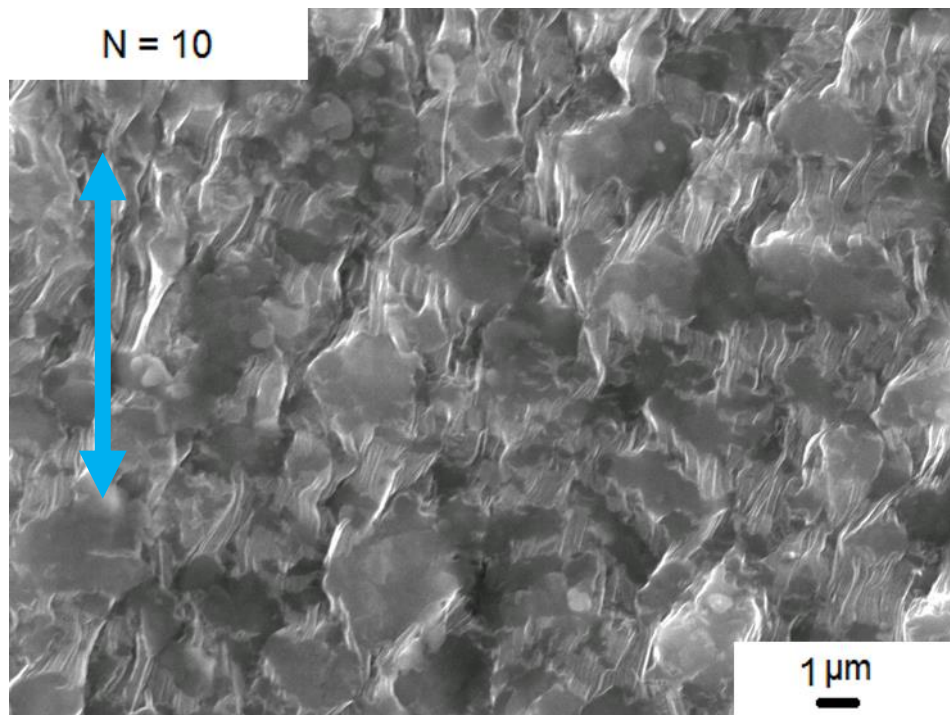
Figure 4.77 Surface morphology of the tested tensile samples at the gauge lengths for the AZ80 alloy processed for $N = 5$ turns in HPT at room temperature using an applied pressure of 6.0 GPa and tested in tension to failure for different strain rates at a testing temperature of 473 K.



(a) $N = 10$, 473 K, $1.4 \times 10^{-2} \text{ s}^{-1}$

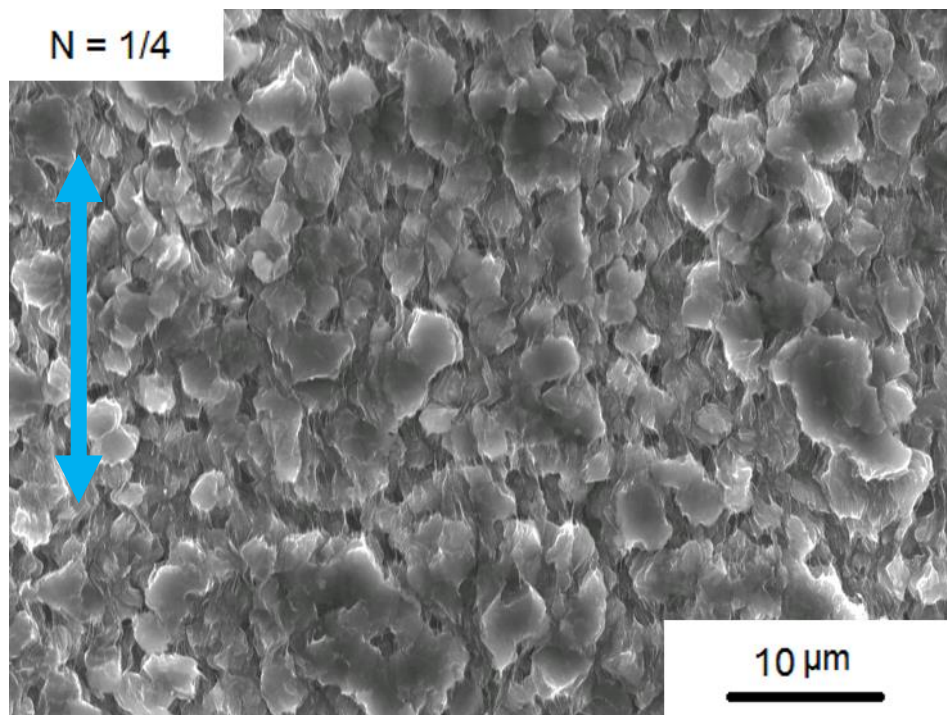


(b) $N = 10$, 473 K, $1.4 \times 10^{-3} \text{ s}^{-1}$

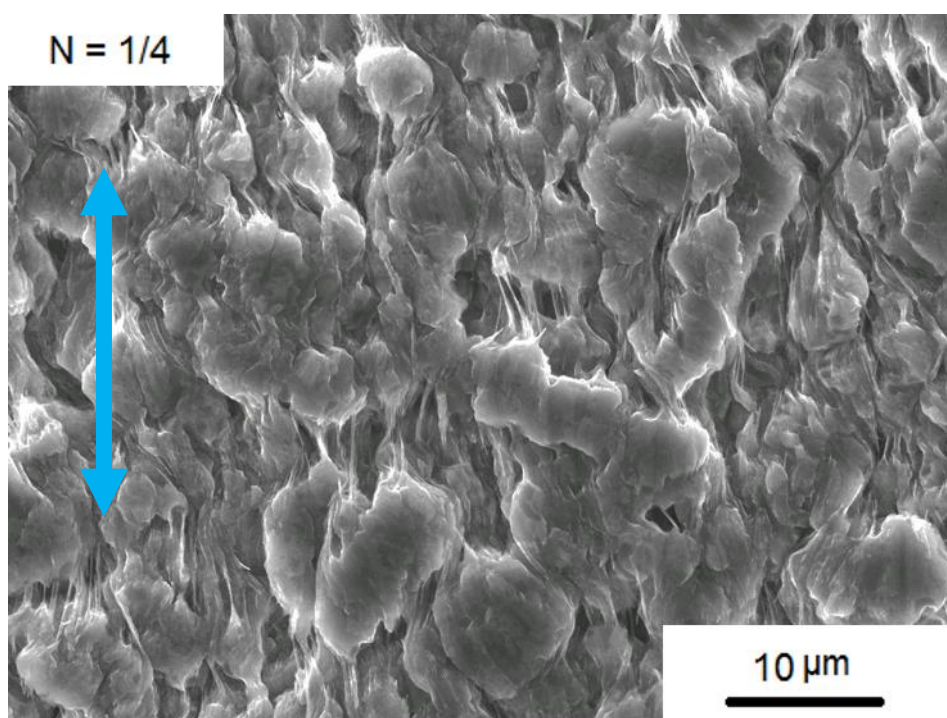


(c) $N = 10$, 473 K, $1.4 \times 10^{-4} \text{ s}^{-1}$

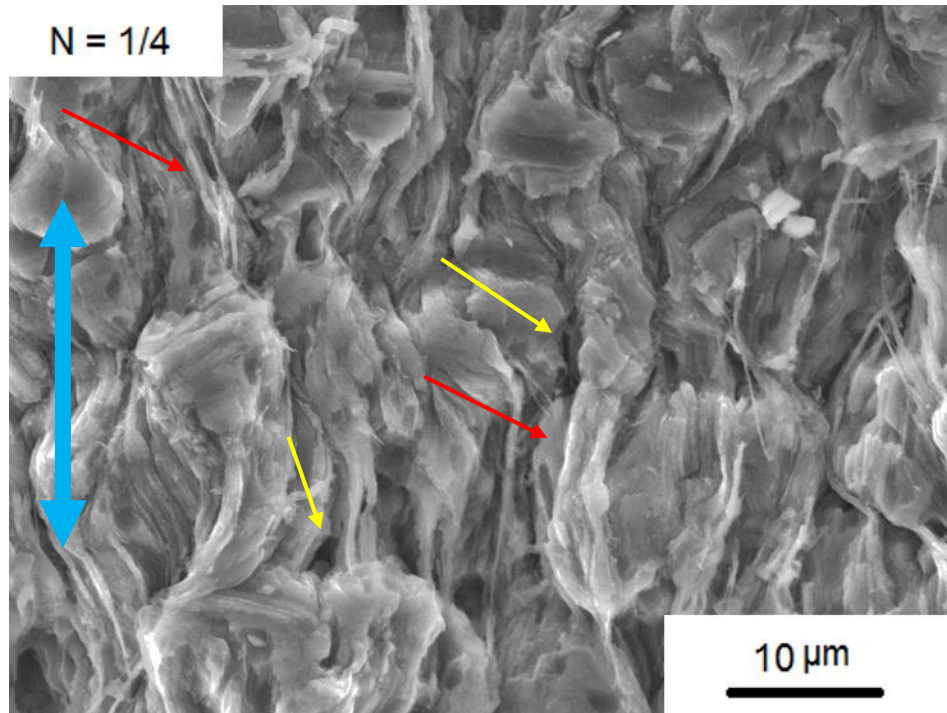
Figure 4.78 Surface morphology of the tested tensile samples at the gauge lengths for the AZ80 alloy processed for $N = 10$ turns in HPT at room temperature using an applied pressure of 6.0 GPa and tested in tension to failure for different strain rates at a testing temperature temperature of 473 K.



(a) $N = 1/4$, 573 K, $1.4 \times 10^{-2} \text{ s}^{-1}$

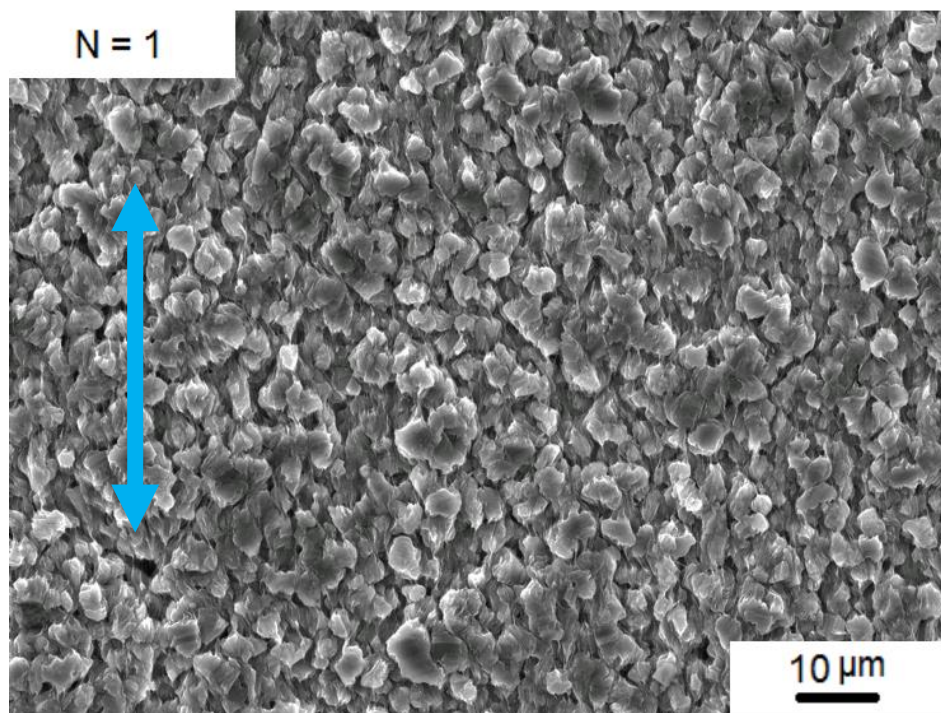


(b) $N = 1/4$, 573 K, $1.4 \times 10^{-3} \text{ s}^{-1}$

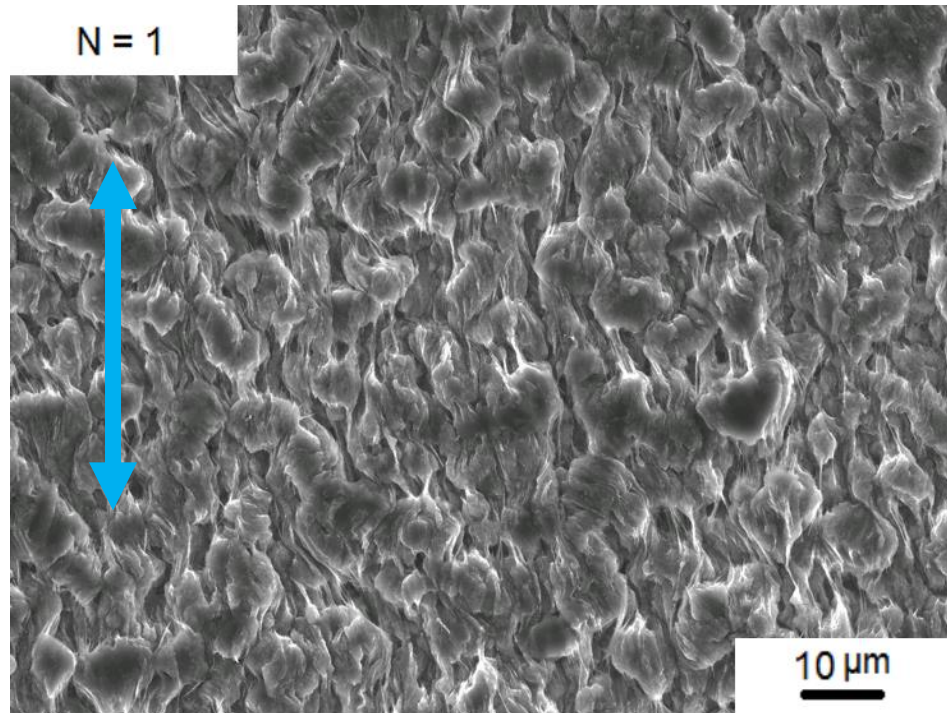


(c) $N = 1/4$, 573 K, $1.4 \times 10^{-4} \text{ s}^{-1}$

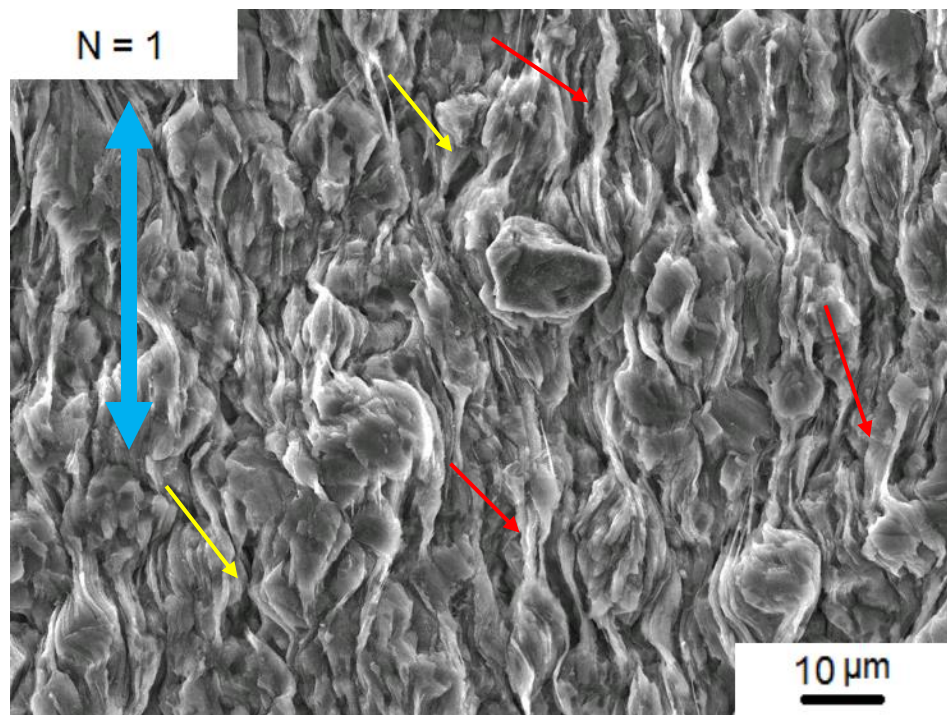
Figure 4.79 Surface morphology of the tested tensile samples at the gauge lengths for the AZ80 alloy processed for $N = 1/4$ turns in HPT at room temperature using an applied pressure of 6.0 GPa and tested in tension to failure for different strain rates at a testing temperature of 573 K.



(a) $N = 1$, 573 K, $1.4 \times 10^{-2} \text{ s}^{-1}$

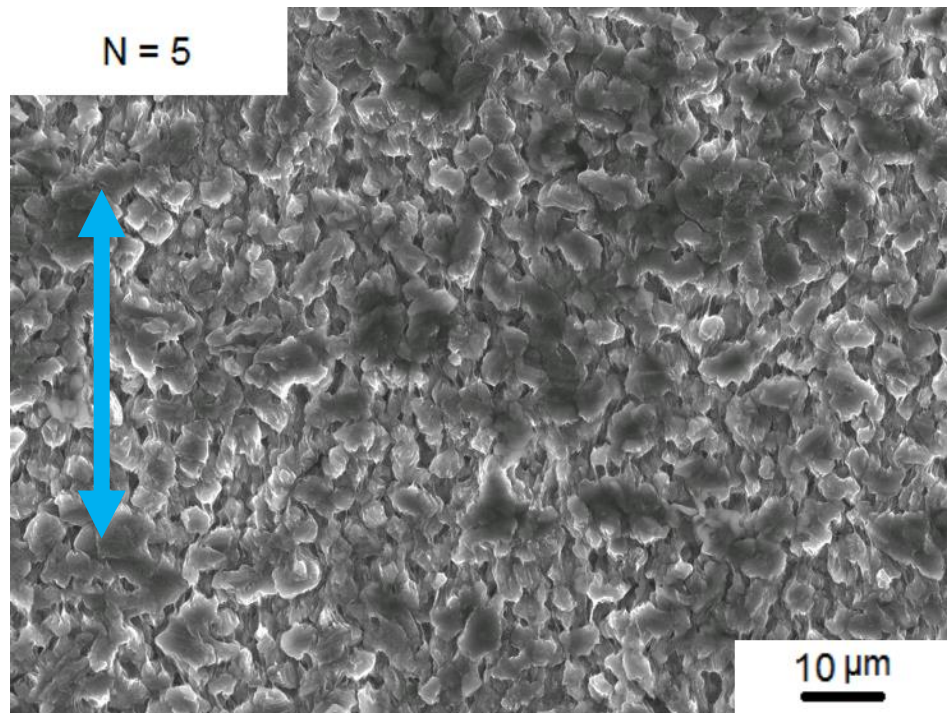


(b) $N = 1$, 573 K, $1.4 \times 10^{-3} \text{ s}^{-1}$

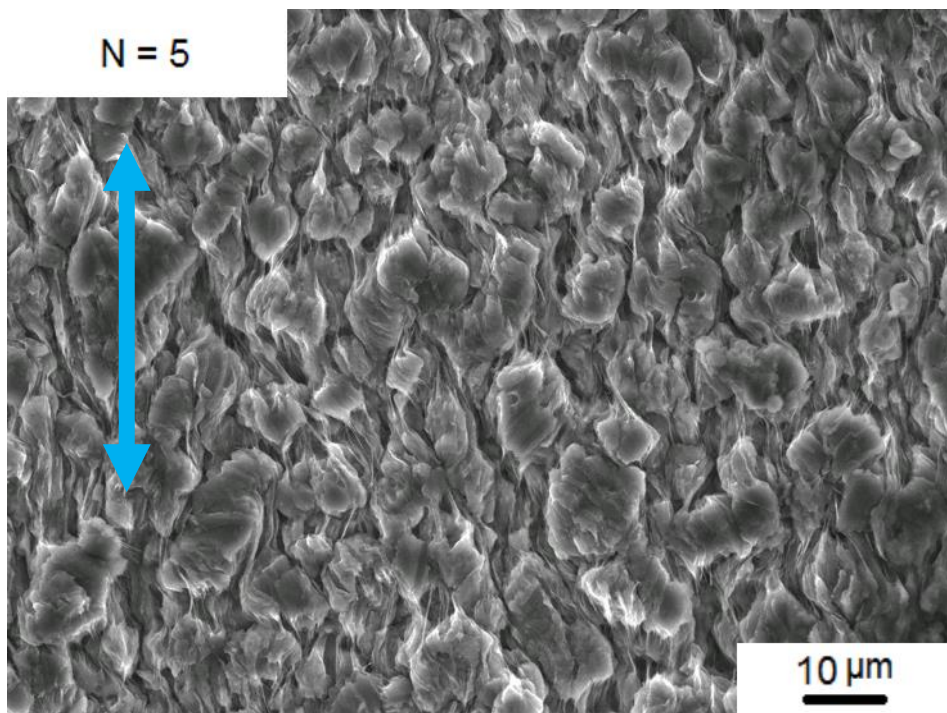


(c) $N = 1$, 573 K, $1.4 \times 10^{-4} \text{ s}^{-1}$

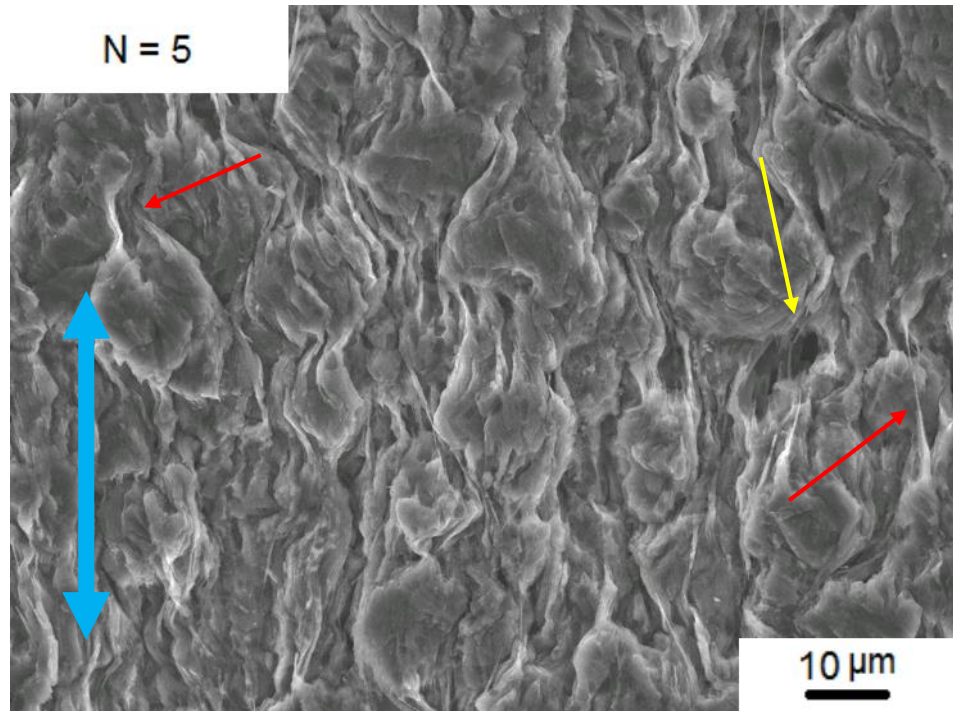
Figure 4.80 Surface morphology of the tested tensile samples at the gauge lengths for the AZ80 alloy processed for $N = 1$ turns in HPT at room temperature using an applied pressure of 6.0 GPa and tested in tension for different strain rates at a testing temperature of 573 K.



(a) $N = 5$, 573 K, $1.4 \times 10^{-2} \text{ s}^{-1}$

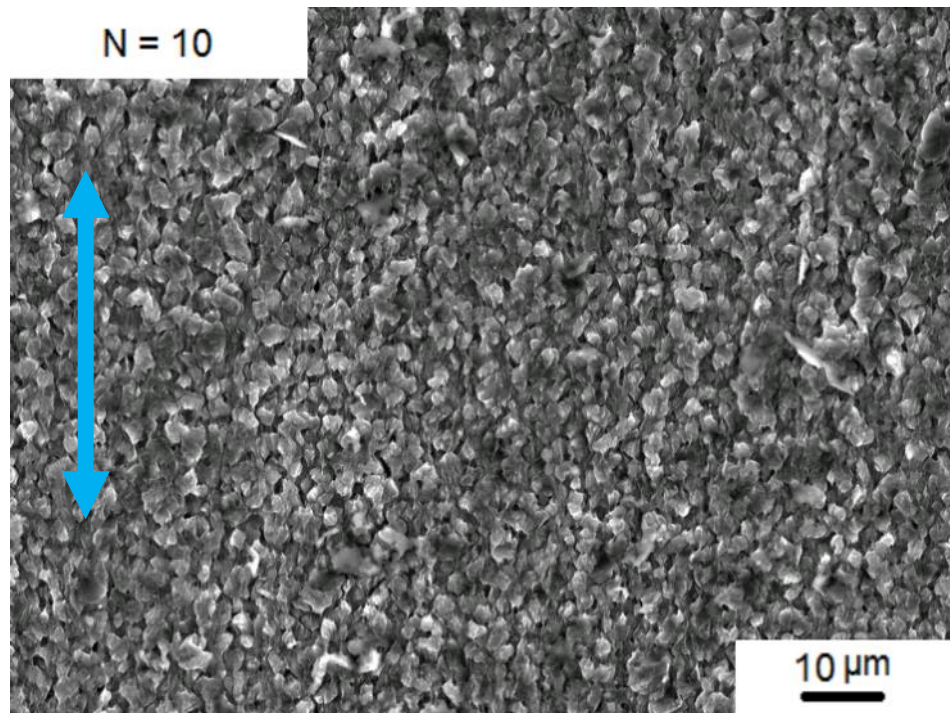


(b) $N = 5$, 573 K, $1.4 \times 10^{-3} \text{ s}^{-1}$

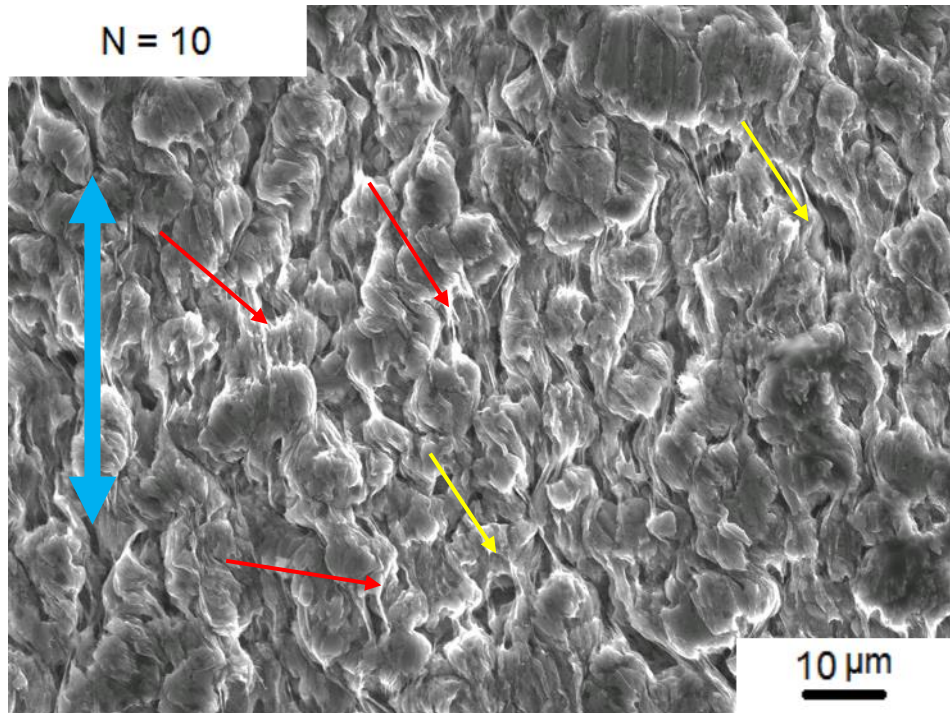


(c) $N = 5$, 573 K, $1.4 \times 10^{-4} \text{ s}^{-1}$

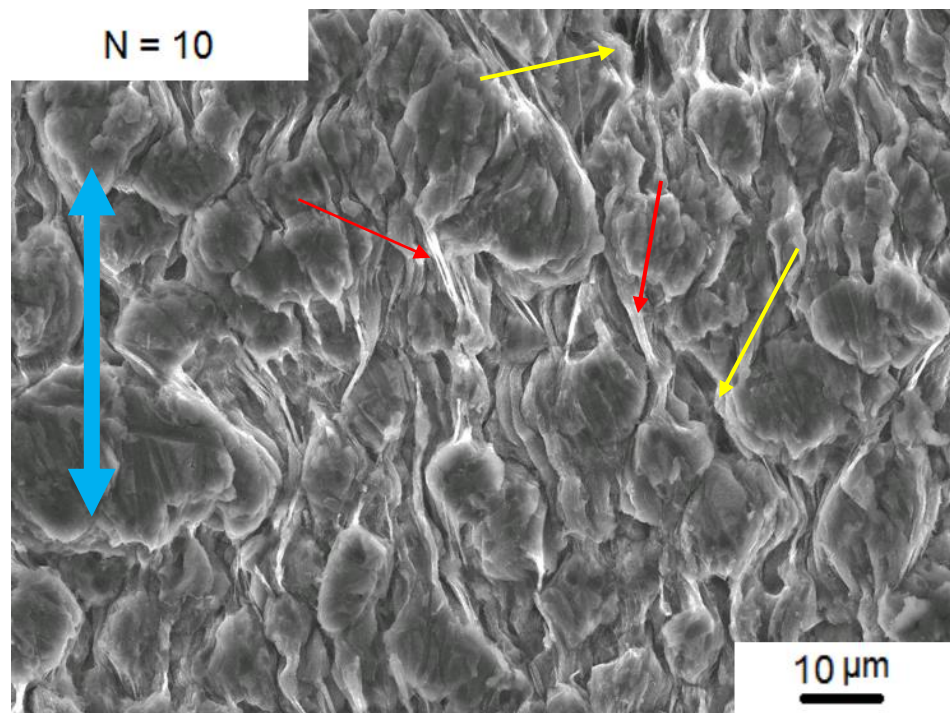
Figure 4.81 Surface morphology of the tested tensile samples at the gauge lengths for the AZ80 alloy processed for $N = 5$ turns in HPT at room temperature using an applied pressure of 6.0 GPa and tested in tension to failure for different strain rates at a testing temperature of 573 K.



(a) $N = 10$, 573 K, $1.4 \times 10^{-2} \text{ s}^{-1}$



(b) $N = 10$, 573 K, $1.4 \times 10^{-3} \text{ s}^{-1}$



(c) $N = 10$, 573 K, $1.4 \times 10^{-4} \text{ s}^{-1}$

Figure 4.82 Surface morphology of the tested tensile samples at the gauge lengths for the AZ80 alloy processed for $N = 10$ turns in HPT at room temperature using an applied pressure of 6.0 GPa and tested in tension to failure for different strain rates at a testing temperature of 573 K.

Figure 4.83 shows the SEM images at the gauge length for samples processed by HPT at room temperature for 1 and 10 turns, both tested to failure in a tensile test at 573 K. The selection of these samples and testing temperature is because at this temperature maximum elongation was achieved after 1 turn; 10 turns was the highest number of revolutions through which the alloy was processed by HPT; and the smallest average grain size was achieved by this process. The average grain size after the HPT process for 1 and 10 turns was ~ 370 nm and ~ 200 nm respectively. When the alloy was tested at a faster strain rate of $1.4 \times 10^{-2} \text{ s}^{-1}$, the grains of a sample processed by HPT for 10 turns were finer than for one turn, as in Figures 4.83 (a) and (b).

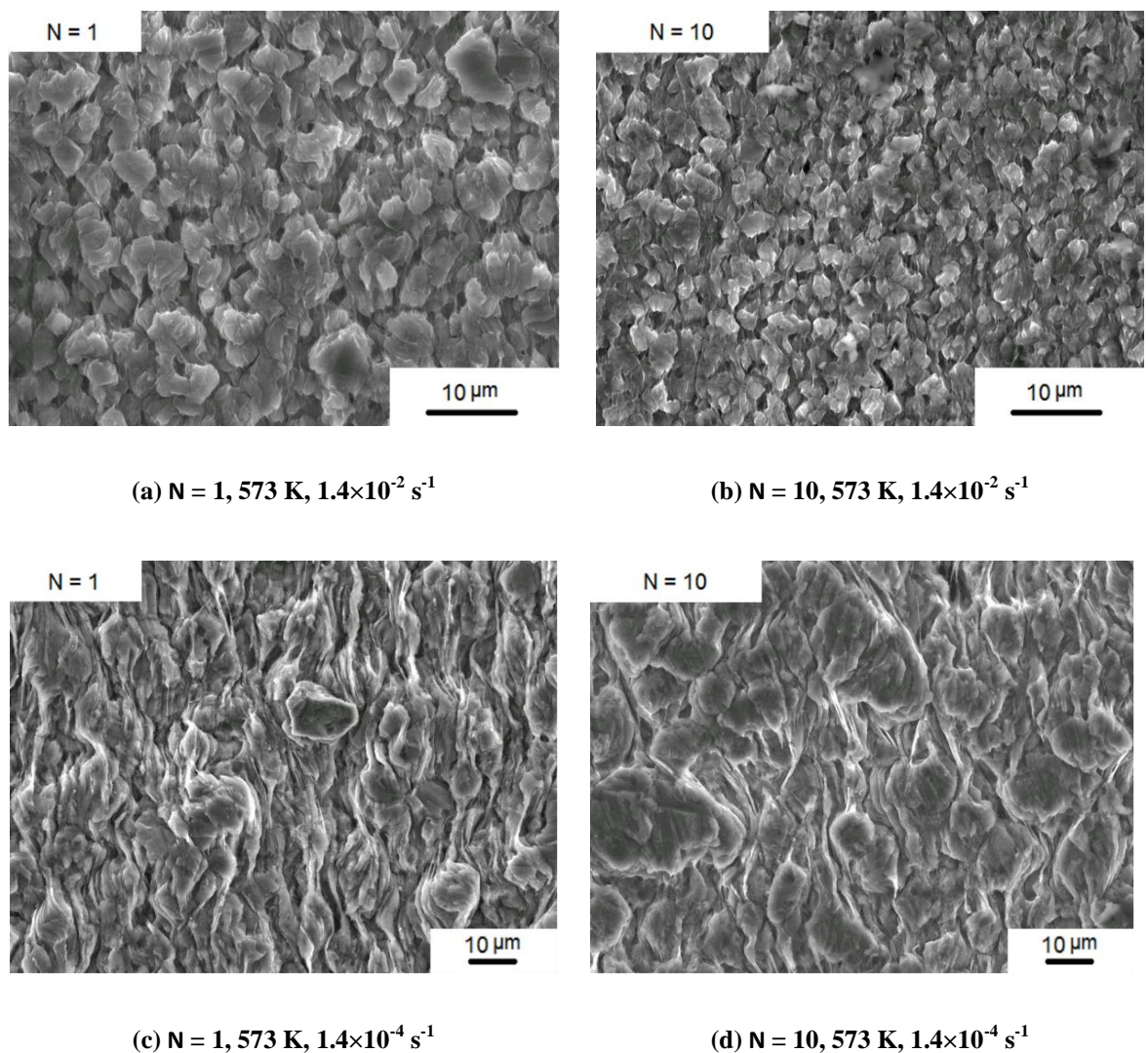


Figure 4.83 SEM images of the grains at the gauge length of the tensile tested samples at (a), (b), (c) and (d) . The average grain size shows greater growth in the sample processed by HPT for 10 turns and tested at 573 K using strain rate $1.4 \times 10^{-4} \text{ s}^{-1}$ than the sample processed by HPT for one turn and tested under the same conditions.

The anticipated microstructure changed when the alloy was tested at the slower strain rate $1.4 \times 10^{-4} \text{ s}^{-1}$, and it is obvious that the grains of the sample processed by HPT for 10 turns are coarser than for 1 turn, as in Figures 4.85 (c) and (d).

Figure 4.84 summarizes a comparison of all HPT samples processed for different numbers of turns at room temperature and tested to fracture using a tensile test at different strain rates and different testing temperatures. The graph clearly displays the effect of the strain rate and the tensile testing temperature on the final elongation of the tested samples, the higher the tensile testing temperature and the slower the strain rate, the greater the final elongation of the sample.

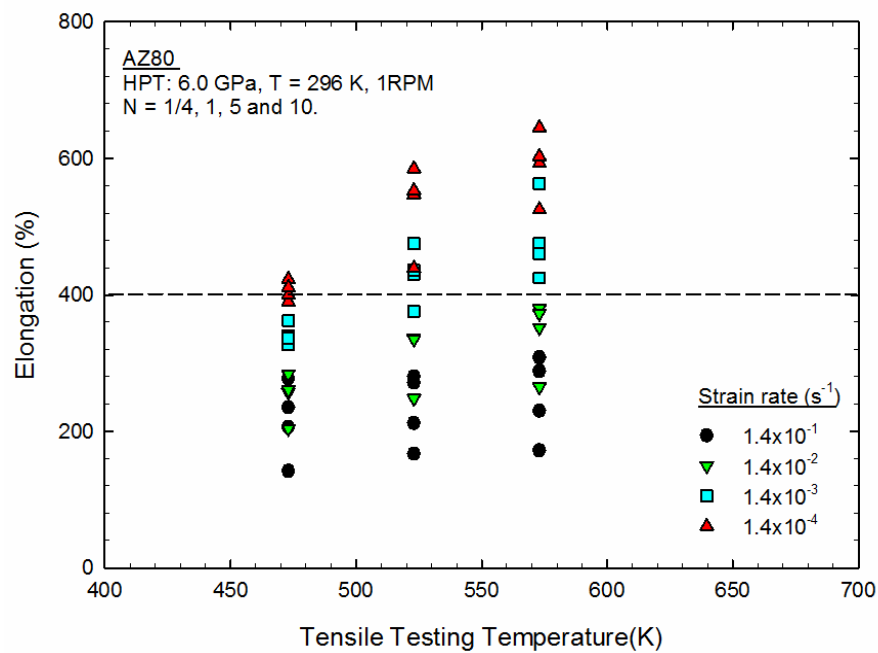


Figure 4.84 Elongation to failure comparison between HPT samples processed for different number of turns at room temperature and tested to fracture using tensile test at different strain rate and different testing temperatures.

5 Discussion

The results of this investigation demonstrate that the microstructure of AZ80 magnesium alloy was successfully refined without inducing any obvious cracking or segmentation into the samples up to 10 turns through HPT process at room temperature (296 K) and at an elevated temperature (473 K). These results cannot be achieved by ECAP, the other popular SPD technique, when processing at room temperature (296 K), without inducing cracks or segmentation [202]. This is due to the limited slip systems provided by HCP crystal structure, which do not satisfy the five independent slip systems required by von Mises for homogeneous plastic deformation. Although increasing the processing temperature can activate the non-basal slip system [203] and enhance the workability of AZ80, it is usually associated with dynamic recrystallization, if the processing temperature is about 400–600 K, where the formation of new fine grains along the grain boundaries or along the twin boundaries takes place [51,169], and grain growth.

The microstructure of the alloy in the as-received condition consists of fairly equiaxed grains and a uniform microstructure, as shown in Figures 4.1, 4.2 and 4.3, in which the microstructure consists of the α matrix and the β phase $\text{Mg}_{17}\text{Al}_{12}$ precipitates, which are rich in aluminium, as shown in Figures 4.4 and 4.5 (b). The average grain size of the alloy in the as-received condition before processing was $\sim 25\text{ }\mu\text{m}$ and the average length of the lamellar precipitates was between $\sim 1\text{--}4\text{ }\mu\text{m}$, after 10 turns of the HPT process the final average grain size was $\sim 200\text{ nm}$ when the alloy was processed at room temperature, 296 K, and $\sim 330\text{ nm}$ when processed at an elevated temperature of 473 K, the smaller the final average grain size in favour of processing at room temperature having been reported in earlier studies [14,15]. This reduction in size included the precipitates, with the average size of the precipitates being reduced to less than $\sim 100\text{ nm}$ for both processing temperatures of 296 K and 473 K. The HPT process resulted in an excellent reduction in grain size associated with significant strengthening of the material at both temperatures, as shown in Figures 4.25 and 4.42. The resultant hardness values as much as doubled, in some areas of the processed disc after 10 turns of HPT, as shown in Figures 4.21 and 4.38.

The development of the alloy microstructure towards homogeneity under the HPT process is influenced by two factors: the applied pressure and the imposed strain represented by the number of turns. In Equation 2.4, applied pressure is abandoned and the imposed strain is the dominant factor. The imposed strain in HPT varies with the displacement from the disc centre and with the number of turns applied to the sample.

5.1 Microstructure evolution after HPT process at room temperature

The excellent average grain size achieved after 10 turns of HPT at room temperature and elevated temperature was smaller than that of earlier reported investigations of deforming AZ80 magnesium alloy by ECAP at different temperatures [179,195]. Thus, it can be concluded that HPT is more effective than ECAP in producing an ultra-fine grained microstructure in AZ80 magnesium alloy. The resultant average grain size was larger than in earlier reports of processing heat-treated AZ80 by HPT up to 15 revolutions, in which the final grain size was ~100 nm [119]. However, a heat treatment process had been used in that study due to failure during processing of AZ80 by HPT without heat treatment at room temperature, when extensive cracking on the specimen was observed. By contrast, HPT in this study was successful when conducted at room temperature without any prior process or treatment. The evolution of microstructure and microhardness towards homogeneity was consistent with earlier reports of a gradual evolution of microstructure in magnesium alloy towards homogeneity when processed by HPT using an applied pressure of 6.0 GPa up to five turns [86]. Table 5.1 shows the initial and final average grain size in various reported studies on pure magnesium and magnesium alloys processed by HPT at room temperature, and the maximum Vickers microhardness achieved in those studies compared to the current study.

Table 5. 1 Final grain size and the maximum Vickers microhardness of pure magnesium and magnesium alloys processed by HPT at room temperature for different numbers of revolutions.

Magnesium and magnesium alloy	HPT processing		Grain size (μm)		Maximum Vickers microhardness, Hv	Reference
	Pressure (GPa)	No. of turns	Before HPT	After HPT		
Pure Mg 99.8% ^a	6.0	8	~ 50	~ 0.6	55	Qiao <i>et al.</i> [204]
AZ31 ^b	2.5	15	~ 150-200	0.15-0.2	113	Stráská <i>et al.</i> [9]
AZ31 ^c	6.0	5	~ 10	0.9-1.2	110	Huang <i>et al.</i> [15]
AZ61 ^d	3.0	5	~ 22	0.11	-	Harai <i>et al.</i> [66]
ZK60 ^e	2.0	5	~ 9.4	~1	124	Torbati-Sarraf & Langdon [86]
ZK60A ^f	6.0	5	~10	2-5	110	Lee <i>et al.</i> [109]
Mg-8%Li ^g	3.0	5	-	~ 0.5	63	Matsunoshita <i>et al.</i> [185]
Mg-9 wt% Al ^h	3.0	5	~ 12	~ 0.15	120	Kai <i>et al.</i> [14]
AZ80 ⁱ	3.0	15	~ 6-31	~ 0.1	125	Arpacay <i>et al.</i> [119]
AZ80 ^j	6.0	10	~ 25	~ 0.2	120	Current study

Material condition prior to HPT

^a Extruded at temperature of 350 °C prior to HPT.

^b Homogenized at 390 °C for 12h prior to HPT.

^{c d e f j} Extruded.

^g Extruded at temperature of 100 °C prior to HPT.

^h Extruded at temperature of 200 °C prior to HPT.

ⁱ Extruded at temperature of 300 °C then solution heat treated at 400 °C for 11 h prior to HPT, then water quenching.

In processing HCP metals and alloys at room temperature, basal slip system and mechanical twinning are the essential deformation systems in magnesium alloy. The basal slip system provides only two independent slip systems, so other deformation modes are needed to satisfy von Mises criteria. The twin system can provide up to 5 independent slip systems [152]. Due to the low critical resolved shear stress (CRSS) required to activate the basal slip system, the low stress required for twinning [205] basal slip system and mechanical twinning are the main deformation mechanisms at ambient temperatures in HCP metals and alloys. Non-basal slip systems require a higher CRSS of approximately 100 times greater than the basal slip system [152,157]. During the HPT process an extensive compression pressure is applied to the sample, with the geometry of the HPT anvils helping to build the hydrostatic pressure. When the sample is under compression, a small amount of the material will flow out of the anvils through the narrow gap but, due to friction, this amount will be restricted, generating a back pressure and induced hydrostatic pressure on the sample [82]. This high hydrostatic pressure was proven in an earlier study to activate the non-basal slip system [89,206]. The activation of non-basal slip system provides the five independent deformation slip systems and fulfils von Mises criteria for homogeneous plastic deformation. Furthermore, using compressive hydrostatic pressure prevents nucleation and propagation of cracks in the sample [32], improves the formability of magnesium alloy, enhances grain refinement and produces a material of finer grain size [61,89].

The grain refinement mechanism starts when a very high strain is imposed through the application of hydrostatic pressure. As predicted by Equation 2.4, in the early compression-torsion stage, after a few turns of HPT, the heterogeneous nature of the HPT process forces the deformation to occur rapidly at the edge of the disc, where the displacement is at a maximum from the disc centre, and therefore maximum imposed strain is applied compared to the centre of the disc. In the early stages of HPT processing at room temperature, grains tend to be elongated, probably in the torsion direction, as shown in the STEM Figures 4.13 (a) and (b) due to the monotonic HPT strain [207]. As shown by TEM in Figures 4.14 (a), (b) and (c), an intense dislocation is induced in the alloy in the early stages of HPT due to the extensive hydrostatic pressure applied to the alloy and to torsional strain, with these tangled dislocations evolving to elongated dislocation cells as shown in Figures 4.15 (a) and (b). With further strain these elongated dislocation cells become subdivided into more dislocations cells, as

shown in Figure 4.16. These dislocation cells evolve to subgrains, then to grains having high-angle boundaries as shown in Figures 4.17 (a) and (b).

A transitional stage of inhomogeneous microstructure is presented in the intermediate stage due to the variation of the strain introduced to the sample by HPT. This heterogeneous bi-modal microstructure is formed at lower numbers of turns in the HPT process and consists of multiple grain size. Since the average grain size of the alloy in the initial microstructure is larger than 10 μm , the development of bi-modal microstructure is to be anticipated [51,170]. This bi-modal microstructure has been reported earlier for Mg alloy processed by ECAP [169] and HPT [15]. Although there was a small fraction of large grains in the microstructure, as shown earlier in Figure 4.19 and seen in Figure 5.1, the extensive reduction in the average grain size introduced to the alloy only after one turn was excellent when processing AZ80 by HPT at room temperature. The bi-modal microstructure develops to a reasonably homogeneous ultrafine grain microstructure with the imposition of higher strain through increasing number of HPT turns [9,51].

There was no obvious twinning in the sample processed at room temperature and investigated by OM, as shown in Figures 4.6, 4.7 and 4.20 or investigated by SEM in Figure 4.8. Although AZ80 magnesium alloy has an HCP crystal structure with limited slip systems, it also has a low SFE and a low rate of recovery, and these determine the refinement mechanisms and influence the final average grain size. In materials with low SFE, twinning is an important mode of deformation and the material is suited to producing a smaller grain size [94,100]. As shown in Table 2.6, increasing the aluminium content in magnesium alloy lowers the SFE which, as a result, increases the tendency of the alloy to be deformed by twinning [208].

Twinning is usually activated at very low temperatures, and was not seen in the sample processed at room temperature, which relates to the initial average grain size of the alloy. It is well known that grain size in general has a major influence on deformation mechanisms [209–211] and that twinning formation, in particular, is sensitive to grain size [212]. Increasing the grain size in coarse-grained materials increases the activity of deformation twinning [213], and reducing the grain size will correspondingly decrease the tendency of such material to deformation by twinning [214,215]. It is well known that, in coarse-grained FCC metals and alloys, decreasing the grain size will make it

very difficult for twinning to be activated [216]. This behaviour has also been reported in HCP metals and alloys [214]. However, the effect of the changes on grain size in coarse-grained material on deformation by twinning has not been fully determined or classified, therefore needs further investigation [217].

Based on the previous literatures and OM, SEM and TEM images it can be seen that processing AZ80 coarse grains (average grain size $\sim 25\text{ }\mu\text{m}$) by HPT at room temperature does not produce any obvious twinning, which indicates that the average grain size was not optimum for twinning nucleation. Nevertheless, a close look at the TEM image in Figure 4.19 and STEM image in Figure 5.1 reveals the appearance of twinning at grain sizes smaller than $\sim 100\text{ nm}$, as reported in an earlier study [218]. Similar observations were found in HCP metals and alloys in other studies [219]. As stated earlier, the deformation behaviour of metals and alloys can be determined by the grain size [209–211]. The observations in previous studies were the foundation of the interpretation given for the existence of twinning in Figures 4.19 and 5.1; however there is a need for further investigation to assure it is not moiré fringe pattern. Moreover, it is proven that applying hydrostatic pressure can enhance the ductility of the alloy by activating the non-basal slip systems, so the von Mises criteria will be fulfilled [89]. Thus, deformation by dislocation slip was the dominant mechanism when processing AZ80 at room temperature.

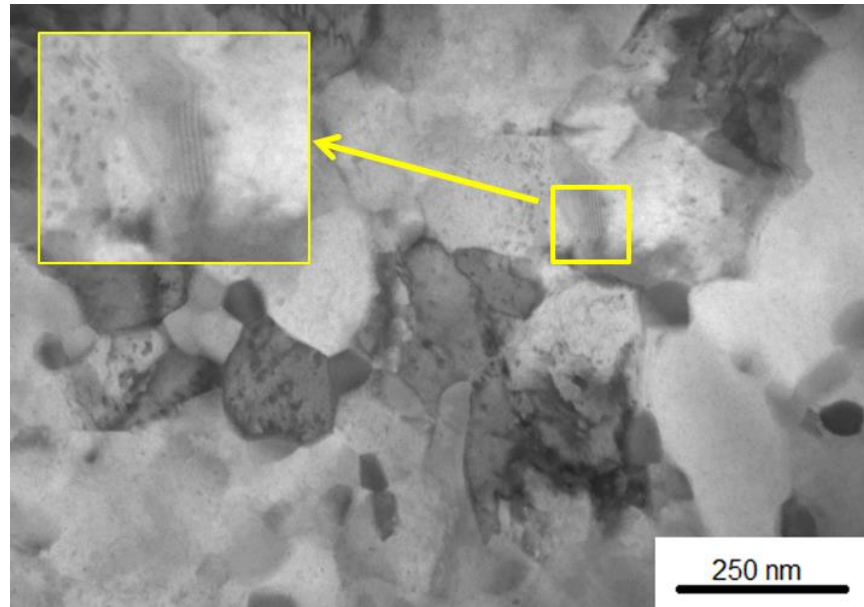


Figure 5.1 STEM image shows the bi-modal structure of the alloy after one turn of HPT at room temperature. The yellow arrow shows the formation of twinning in grains with a size smaller than ~100 nm.

Figures 4.6 (b) and (d) show that, at lower numbers of turns in HPT, deformation developed rapidly at the edge of the disc as expected, based on Equation 2.4, which demonstrates that imposed strain is at a maximum at the periphery of the disc and decreases toward the centre of the disc. The disc centre displays a microstructure of coarse grains, as shown in Figures 4.6 (a) and (c). This heterogeneity in microstructure was noted in earlier studies [75,91]. The deformation extended from the edge to the centre of the disc with increasing numbers of turns, as shown in Figure 4.7 (e), after processing by HPT for 10 turns. Earlier reports demonstrated that processing a material by HPT using an applied pressure of 6.0 GPa up to five turns and more will result in a microstructure with equiaxed grains. This reasonable degree of homogeneity has been confirmed for different metals and alloys [86,91].

Figure 5.2 represents the calculation of the imposed equivalent strain during the HPT process to the sample at three different displacement from the centre: 0.3 mm from the centre, at the half radius and at the disc periphery, based on Equation 2.4 and assuming a constant thickness of 0.83 mm to show the variation in imposed strain across the radius of the disc.

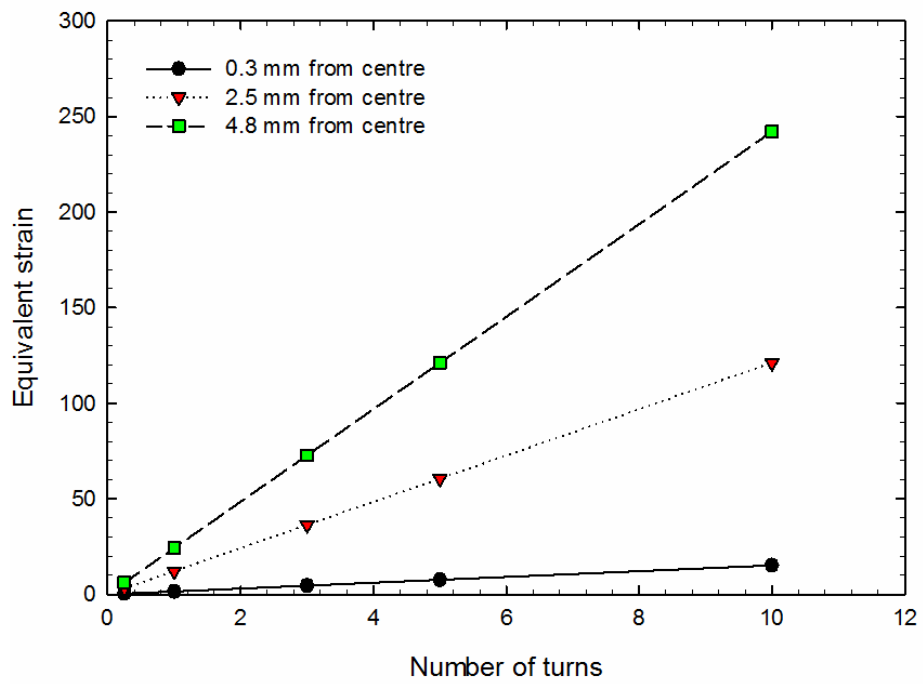


Figure 3.2 The equivalent strain near the centre, at the half-radius and periphery of a disc processed by HPT for a 1/4, 1, 3, 5 and 10 turns.

The evolution of microstructure from the edge towards the centre of the disc with reasonable homogeneity along the disc diameter was obvious after 5 and 10 turns of HPT process, as shown in Figure 4.21, in which the evolution in microhardness values H_v may indicate microstructural evolution during torsional straining. The results in this study go against the theoretical prediction, which assumes an area of zero imposed strain at $r = 0$. The results can be explained by different modelling studies. The ‘strain gradient plasticity’ model [106] predicts a two-stage microstructural development in materials. The first stage is when accumulated plastic strain is higher at the periphery of the disc and almost absent at the centre of the disc at the start of HPT torsion. This results in the creation of a high strain gradient. In the later stages, the region in which strain is zero gradually shrinks, and the region with minimum strain gradient shifts towards the centre of the disc where the strain gradient is higher. By increasing the strain, the rate of accumulated strain at the centre of the disc exceeds the rate of accumulated strain at the disc periphery, so a near homogeneity of strain distribution is obtained. A more recent study using finite element modelling shows that there is an increase in the value of effective strain at the disc centre, which is attributable to the continuous thickness reduction while torsion at high pressure [107].

5.2 Microstructure evolution after HPT processing at elevated temperature

In addition to the excellent grain refinement produced by processing AZ80 by HPT at room temperature, processing AZ80 at elevated temperature 473 K achieved a great reduction in average grain size and successfully produced an ultra-fine grained material, as shown in the STEM images in Figures 4.33 (a) and (b). The microstructure of the alloy processed at elevated temperature shows coarser grains than when processed at room temperature. The final average grain size after 10 turns of HPT process at 473 K was ~330 nm. Although the average grain size is significantly refined, processing AZ80 by HPT at room temperature has the advantage of introducing a finer average grain size, of ~ 200 nm, than processing it at elevated temperatures (473 K). This can be attributed to the effect of homologous temperature: by increasing the homologous temperature, the steady-state grain size increases [113]. Deforming the alloy at this high temperature in the range of dynamic recrystallization of magnesium alloys [51,169] leads to the formation of the these new grains, which reduces the amount of dislocation during the

deformation [220], leading to a coarser average grain size in comparison with same alloy processed by HPT at room temperature for the same number of turns.

In a previous study, AZ80 was processed by ECAP at two different temperatures, and the results showed a finer average grain size in favour of the lower processing temperature [179]. When AZ31, ZK61 and AZ91 magnesium alloys were processed by HPT at different temperatures, a microstructure investigation revealed that the smaller resultant average grain sizes were in the samples processed by HPT at the lower temperatures [66,104,196]. The microstructural and microhardness evolution towards homogeneity and saturation when processing the alloy at 473 K confirms earlier reports of a gradual evolution of microstructure in magnesium alloy towards homogeneity when processing by HPT using an applied pressure of 6.0 GPa up to five turns [86]. Even though the final grain size is larger than in earlier reported studies, the results show effective grain refinement when processing at elevated temperatures. Table 5.2 demonstrates the initial and final average grain size of various reported studies on magnesium alloys processed by HPT at elevated temperatures.

Table 5. 2 Final grain size of magnesium alloys processed by HPT at elevated temperature for different numbers of revolutions.

Magnesium and magnesium alloy	HPT processing		Grain size (μm)		HPT processing temperature (K)	Reference
	Pressure (GPa)	No. of turns	Before HPT	After HPT		
AZ31	6.0	5	~ 10	~ 2.6-4.2	473	Huang <i>et al.</i> [196]
AZ61	3.0	7	~22	~ 0.22	423	Harai <i>et al.</i> [66]
AZ91	3.0	10	~ 30	~ 0.25	473	AL-Zubaydi <i>et al.</i> [104]
Mg-9 wt% Al as cast	3.0	5	~ 30	~ 0.33	423	Kai <i>et al.</i> [14]
AZ80	6.0	10	~ 25	~ 0.33	473	Current study

Magnesium alloy is an HCP material that has a limited slip system. In deforming HCP metals and alloys at low temperature, twinning plays an important role, alongside the slip system. In this study, twinning was not clearly observed when processing the alloy at room temperature. It was only found in grains having an average size of less than ~100 nm. This observation was found earlier in FCC [218,221] and HCP materials [219]. It is well known that, when processing magnesium alloy at low temperature, below that required for activating the non-basal slip system, which is 225 °C [156], the deformation will be restricted to dislocation slip in the basal plane and twinning.

By contrast, twinning has been clearly observed when processing the alloy at 473 K, which represents 0.53 T_m according to the Mg-Al binary phase diagram in Figure 2.33. The microstructure observation through OM and SEM showed extensive twinning activity when the alloy was compressed for one minute without torsion at an elevated temperature, as shown in Figure 4.29. This indicates that twinning was introduced to the alloy at the compression stage. This participation of twinning in grain refinement due to the extensive level of stress achieved by SPD [222].

Figure 4.30 shows grain refinement accompanying twinning, starting from lower numbers of turns of HPT. A close look at the images shows much activity of twinning, with no significant difference between the edge and the centre of the disc. Increasing numbers of turns up to 3 turns leads to a pronounced bi-modal structure at the edge of the disc. Figure 4.31 (b) shows a heterogeneous microstructure in which there is a highly deformed area, with the presence of coarse grains at the edge of the disc. This fraction of large grains at the edge of the disc vanishes when the alloy was subjected to further strain by increasing the number of turns to 5. When the alloy was processed for 10 turns, a homogeneous microstructure was observed across the entire disc surface as shown in Figures 4.31 (e) and (f). Twin boundaries can strengthen the material, as do grain boundaries, by acting as a dislocation movement barrier [223,224].

This behaviour was reported in an earlier study when AZ91 magnesium alloy was processed by HPT at temperatures of 296 K, 423 K and 473 K [104]. It was concluded that twinning activity was more pronounced when the alloy was processed at 423 K and 473 K than at the ambient temperature. In another study, WE43 magnesium alloy was processed by HPT at room temperature, 473 K and 573 K. It was concluded that the deformation of the alloy by HPT was associated with twinning at all processing

temperatures [219]. When AZ61 magnesium alloy was deformed by cyclic bending at 623 K, the microstructure after deformation showed clear evidence of twinning [225]. When AZ31 magnesium alloy was processed by uniaxial compression at 523 K, the resultant microstructure displayed a high density of twinning [226]. The formation of twinning in the compression stage of the HPT process helps in the fragmentation of the coarse grains into a finer grain, as can be seen in Figure 4.29 and, since the process temperature lies within the range of dynamic recrystallization of magnesium alloy [51,169,227], new dynamically recrystallized grains nucleate at the original grain boundaries, as seen in Figure 5.3 (indicated by the yellow arrows). In addition to the fragmentation of coarse grains, twin boundaries act as sites where new recrystallized grains are created [196].

The microstructure developing from the dynamic recrystallization mechanism is a bi-modal necklace-like microstructure [124], which explains the more pronounced heterogeneity in the early stages of HPT processed at 473 K than at 296 K. Increasing the number of turns increases the imposed strain, causing the microstructure to evolve towards greater homogeneity by the consumption of larger grains by finer ones. The final average grain size after 10 turns (~ 330 nm) of HPT processing at 473 K was smaller than the final average grain size after one turn (~ 600 nm).

This result is contrary to earlier reports of AZ31 processed by HPT at 473 K for five turns [15], when the average grain size after five turns was larger than the average grain size after one turn. In that experiment, the microhardness profile shows that, when processing the alloy by HPT at elevated temperature, the microhardness values after five turns are lower than after one turn. This can be attributed to the lower proportion of aluminium in AZ31 (3 wt%) in comparison to AZ80 (8.7 wt%), which lowers the extent of precipitation in the alloy. Earlier studies revealed that the highly deformed particles of discontinuous precipitation of ($\text{Mg}_{17}\text{Al}_{12}$) with an average size of ~100 nm have an excellent pinning effect for grain growth in the new dynamically recrystallized grains [228–230], which explains the absence of the grain growth effect in AZ80 compared to AZ31 and the resultant excellent grain refinement in the current study. These two concurrent effects of twinning and formation of new recrystallized grains at the original grain boundaries and the twin boundaries have been reported in AZ31 magnesium alloy processed by ECAP and HPT at elevated temperatures [88,169].

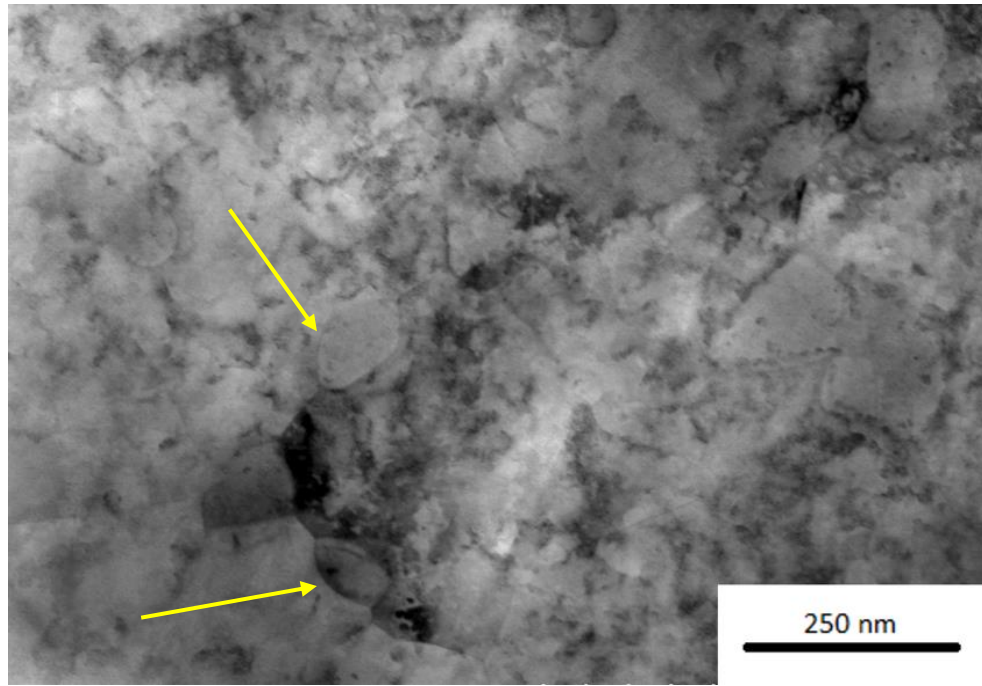


Figure 5.3 New recrystallized grains nucleate at the original grain indicated by the yellow arrows.

5.3 Microstructure evolution in vertical direction

Few studies describe the microstructural evolution of magnesium alloy throughout the disc thickness, and fewer still describe it when the material is processed at room temperature. Although the theoretical approach in Equation 2.4 assumes that the imposed strain is constant through the disc thickness because of the exact distance from the disc centre, varying only in the radial direction, in fact the observation and the results of this study are contrary to the prediction of Equation 2.4. They coincide with earlier results for magnesium alloys, showing that deformation is heterogeneous through the thickness of a disc processed by HPT at both room and high temperatures [12,102,118,192].

In order to derive a good understanding of the heterogeneity throughout the disc, it is best to observe plastic flow during two discrete stages of the HPT process: the compression stage and the compression-torsion stage. At the compression stage, the anvils apply an elevated hydrostatic pressure to the sample that creates a restricted flow region at the upper and lower surface of the disc, as illustrated in Figure 5.4 [231]. This region forces the plastic flow to be concentrated at the mid-thickness of the centre of the disc and increases the imposed strain near the lateral edges of the disc.

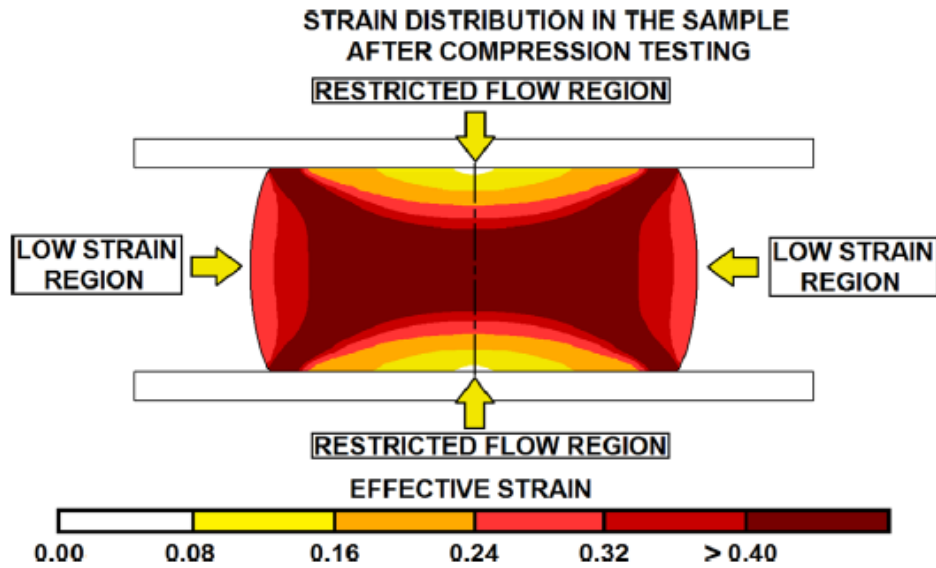


Figure 5.4 Simulation of a compression test showing the restricted flow region and the distribution of the effective strain [231].

This behaviour in Figure 5.4 is consistent with the observation of different grain size structure regions through the disc's thickness, and a sample processed by HPT for one turn follows the same behaviour, with a darker area representing the finer-grain structure that appears at the mid-thickness of the disc, as shown in Figure 4.20, when the samples are processed by HPT at room temperature. The depth of this darker area is less than the thickness of the sample, which indicates a plastic flow concentration in that area leading to heterogeneous deformation through the thickness of the disc. Discs processed by HPT at an elevated temperature of 473 K show this darker area at the mid-thickness of the sample processed for a lower number of turns when $N = 1$ at the centre of the disc. This heterogeneity, as revealed by the presence of the shear band and the distribution of coarse grains in the surrounding highly deformed grains, is shown in Figure 4.37 (a). The presence of twinning is illustrated in this image by a yellow arrow to show coarse grains fragmented by twinning. The grain refinement by HPT at this temperature can be considered similar to that described in earlier reports of grain refinement in magnesium alloy by ECAP at 473 K [41,51].

In the compression-torsion stage, the high pressure process of 6.0 GPa concentrates plastic flow in the mid-thickness area [232]. The area of darker appearance (finer grains) expanded in the vertical and the radial directions toward the disc centre with

increasing numbers of turns. The grain refinement involves dynamic recrystallization, besides twinning, when processing magnesium alloy at this temperature: the new recrystallized grains nucleate at the original grain and twin boundaries, and slowly consume the original coarse grains. This kind of deformation gives a necklace-like appearance consisting of coarse and fine grains [12]. The higher fraction of coarse grains are distributed randomly through the whole cross-section of the disc and become smaller at the edge of the disc, whereas the highly deformed area increases, indicating that the edge of the disc has been subjected to a higher level of plastic deformation than the centre, due to the variation in imposed strain by HPT [6]. This stage of bi-modal microstructure is considered a transitional stage, and by increasing the number of turns may develop into a more homogeneous microstructure [41].

Figure 4.37 shows optical images of cross-sections of samples processed by HPT at 473 K for 1, 3 and 10 turns. These optical images indicate a heterogeneous deformation at the lower number of turns, with variation in microstructure appearing in both radial and axial directions. By increasing the number of turns, the deformation expands to cover the whole area of the disc and through its cross-section, and the microstructure evolves to a more homogeneous microstructure, as shown in Figure 4.37 (e) and (f).

At a high number of turns, strain-hardening materials such as AZ80 will develop a steady state or saturation condition, after five turns, in this case. At that level, the strain-hardening materials promote their behaviour to perfect plastic behaviour [233]. This behaviour is found to have a high tendency for flow localization, increasing with the number of turns, and the plastic flow of the material will be concentrated in the mid-thickness near the disc periphery. This behaviour was clear in the disc processed by HPT at 296 K up to 10 turns, while the disc processed by HPT at 473 K up to 10 turns shows a lower degree of heterogeneity in comparison to the one processed at room temperature.

5.4 Precipitation evolution during HPT process at 296 K and 473 K

In the as-received condition, AZ80 magnesium alloy has a second phase β -phase $\text{Mg}_{17}\text{Al}_{12}$, in the form of coarse granular and lamellar discontinuous particles. This form of precipitates, due to the coarse size, has little influence on the material's strength due

their poor dislocation pinning [175]. The average length of these precipitates is ~1-4 μm . These precipitates have a lower melting point than the matrix, at 437 °C [234].

In the early stages of the HPT processing at lower numbers of turns, these precipitates start to fragment into small, fine particles, due to the extensive compression pressure and torsional strain, as shown in Figure 4.8. Earlier reports show that these fine particles start to align, probably in the torsional direction at lower number of HPT turns [104]. Although the intermetallic β phase has a BCC structure [159], that has a high number of slip systems [92], the literatures does not focus on the deformations mechanism of the intermetallic β phase. This might be due to the very little fraction of the second phase in comparison to the matrix or because of the differences in Young modulus the precipitates having a considerably higher modulus. Due to the extensive grain refinement and the great reduction in the average grain size after only one turn of HPT at room temperature, where average grain size is ~370 nm (see Figure 4.25), these particles start to precipitate at the triple junctions as seen in Figure 4.11 (a) and (b), and the average size of these precipitates reduces to lower than ~100 nm after one turn. This behaviour continues up to 10 turns, as shown in Figure 4.12, where the average size of these precipitates is reduced to ~ 40 nm.

The same results were observed when the process was conducted at an elevated temperature: the particles start to break down to an average size of ~150-200 nm at lower number of HPT turns as shown in Figure 4.34 (a). The particles appear to be distributed randomly within the microstructure and, because of the average grain size achieved at this stage after one turn, ~ 600 nm, the triple junction fraction is lower than when processed at room temperature. By increasing the number of turns, the volume fraction of the grain boundaries increases, thus the triple junction density increases and more precipitates are localised at these triple junctions, as seen in Figure 4.34 (b). These fine precipitates may participate in heterogeneous deformation by developing localized deformation zones and high misorientation grain boundaries within the area surrounding the precipitates [235]. Moreover, these fine precipitates enhance the strength of the material by providing resistance to dislocation slip [236]. The effect of these fine particles is substantial while deforming AZ80 at an elevated temperature: they act to inhibit grain growth, which helps in further grain size reduction [237].

5.5 Microhardness evolution after HPT processing at 296 K and 473 K

In the current study, the AZ80 magnesium alloy was processed by HPT for a number of revolutions using an applied compressive pressure of 6.0 GPa at 296 K and 473 K. Hardness measurements showed a significant rise after the HPT process. They almost doubled when processed at both room temperature and at elevated temperature. The gradual evolution towards homogeneity was obvious when the discs were processed by HPT at both temperatures for at least five turns. As shown in Figures 4.21 and 4.38, at this number of turns the alloy showed a reasonable degree of homogeneity along the disc diameter. The results concur with many earlier studies, signifying that processing a metal by HPT using applied pressure of 6.0 GPa for at least five turns produces a reasonably homogeneous ultra-fine grained microstructure [68,91].

The microhardness measurements correlate well with the microstructural observations of AZ80 magnesium alloy when processed for up to 10 turns, this increment in microhardness values being associated with excellent grain refinement as reported earlier, as shown in Figures 4.25 and 4.42. Although the results in this study reveal clear evidence of heterogeneous deformation across the diameter of the disc surfaces in the early stages of processing, at this stage the distribution of microhardness values is not uniform along the diameter, with lower values at the centre of the disc. Due to the lower SFE of the alloy, the evolution towards homogeneity follows the trend explained earlier in Figure 2.23, in that the central area of the disc has lower Hv values than the peripheral area, but these continue to rise with increasing imposed strain [87]. Increasing the number of HPT revolutions up to 5 and 10 turns leads to saturated high microhardness values of Hv ~120 and ~110 when processing at room and an elevated temperature respectively. The alloy at this stage shows reasonably homogeneous hardness values along the disc diameter. Table 5.1 demonstrates the maximum resultant values of Vickers microhardness Hv in pure magnesium and magnesium alloys processed by HPT at room temperature and compares them to the current study.

The size of the error bars indicates the evolution of the alloy towards homogeneity. At fewer numbers of turns there were significant differences in the size of the error bars between the centre and the disc periphery, in favour of the centre region, as shown in Figures 4.21 and 4.38, which indicates a more homogenous microstructure at the edge region in the early stages of HPT process due to the large imposed strain there [87].

Increasing numbers of turns lead to a gradual decrease in the error bars size in the centre region that indicates a gradual evolution towards homogeneity in the alloy [84].

The average microhardness value as a function of distance from the centre of the disc is plotted in Figures 4.21 and 4.38. The variation across the diameter of the disc demonstrates the strain hardening model in the material for both processing temperatures 296 K and 473 K [193]. This behaviour is consistent with the imposed equivalent strain, calculated using Equation 2.4, as shown in Figures 4.22 and 4.39. These figures illustrate an initial increment in the microhardness value H_v at the start of the process, when the equivalent strain is low, then, when the equivalent strain reaches a value of ~ 30 , the microhardness values tend to saturate. This behaviour was observed for both processing temperatures. The central region has lower microhardness values of H_v , with higher values at the disc periphery during the early stages of the HPT process. By continuing to increase the number of turns, the imposed equivalent strain will accumulate at the outer region of the disc then move inward to the centre. After five turns, the microhardness values along the disc diameter reach saturation level and the material becomes more homogeneous.

Since the AZ80 magnesium alloy shows increasing microhardness with increasing equivalent strain, it follows the most common model of hardness evolution in which strain hardening occurs. The variation of microhardness values in Figures 4.21 and 4.38 is plotted against the calculated equivalent strain after HPT for 1/4, 1, 3, 5 and 10 turns, as displayed in Figures 4.22 and 4.39, where the lower dashed line represents the microhardness values in the as-received condition, demonstrating strain hardening behaviour. The as-received microhardness values increases after HPT processing for a lower number of turns, especially at the edge of the disc, with increasing equivalent strain, finally becoming saturated at a high value of $H_v \sim 120$ and ~ 110 for processing at room temperature and at elevated temperature respectively, at an equivalent strain of ~ 30 . After this point, increments in equivalent strain are not accompanied by any increase in microhardness values, and they remain approximately constant even at high equivalent strain. This type of behaviour is similar to most metals and alloy reveal in the absence of or with little dynamic recovery [193,194].

The evaluation of measured microhardness values with increasing values of calculated equivalent strain based on Equation 2.4 is an effective approach to understanding and

categorizing microhardness evolution during the HPT process and correlating it with microstructural evolution. The first application of this approach was in the study of austenitic steel processed by HPT using an applied pressure of 5.3 GPa for a number of different turns [75]. Subsequently, this approach was applied to different materials in various studies in which three behavioural types of microhardness evolution to homogeneity in hardness have been experimentally observed. These depend on the nature of recovery during the HPT process [87,116,193,194].

Figures 4.23 and 4.40 demonstrate the differences in microhardness values between the centre and the edge of the discs until saturation after 5 and 10 turns. This hardness homogeneity after five turns was predicted, as it has been established by many studies [87,117,238]. Microhardness development towards homogeneity is also consistent with a theoretical approach based on strain gradient plasticity modelling [106], and a recent study using three-dimensional finite element modelling confirmed the increment of plastic deformation with increasing distance from the disc centre and the number of turns in a material exhibiting strain hardening behaviour [232].

Colour-coded contour mapping demonstrates the variation and the evolution in microhardness across the entire disc surface, as shown in Figures 4.26 and 4.43. A set of colour keys represents the individual values of microhardness H_v , from 80 to 140, in increments of 10. These confirm the trend for microhardness evolution, explained earlier by strain gradient plasticity modelling [106] and three-dimensional finite element modelling [232]. Where plastic deformation increases with distance from the centre of the disc and with increasing numbers of revolutions, this region of higher hardness values H_v will expand towards the centre of the disc with increasing number of turns, creating a reasonable degree of homogeneity after five turns. Figures 4.27 and 4.44 show the frequency distribution of the microhardness values of the total disc surface. For low numbers of turns, it appears that there is a wide range of microhardness values, indicating heterogeneous deformation on the disc surface in the early stages of HPT. With increasing numbers of turns, the wide range of microhardness values becomes narrower, indicating the evolution of microhardness towards homogeneity. The average H_v values rise with increasing number of turns, as shown in Figures 4.24 and 4.41: the hardness of the material is enhanced.

5.6 Hardness measurements through the thickness of the disc

Hardness measurements through the thickness of the disc were recorded as the average of five separate points, plotted as a function of distance from the bottom of the disc through the thickness of the disc, as shown in Figure 3.4. The discs processed by HPT for 1, 3 and 10 turns were selected for processing temperatures of 296 K and 473 K.

The results confirmed the heterogeneity of deformation through the thickness of the disc, being more noticeable for discs processed at room temperature than at an elevated temperature, as shown in Figures 4.28 and 4.45. Several studies on various magnesium alloys at room and elevated temperatures have demonstrated a similar behaviour through the thickness of the disc [12,102,118]. These results are contrary to the theoretical and experimental expectation of imposed strain according to Equation 2.4, which correlates the degree of deformation to the radial distance from the disc centre and assumes a constant distribution of strain through the thickness of the disc.

A more pronounced variation in microhardness values was evident at different axial positions from the radial direction. This variation demonstrates the inhomogeneous deformation through the thickness of the disc. The higher microhardness values were mainly in the mid-thickness area at ~ 0.4 mm from the bottom. Although an increasing number of turns reduced the heterogeneity of microhardness distribution between the bottom, mid-thickness and top surface, the imposed strain after 10 turns was not enough to produce reasonable homogeneity in the axial direction. In fact, a study using finite element modeling predicts the development of microstructural and microhardness heterogeneity due to flow localization during the HPT processing in strain-hardening materials, especially at high numbers of turns [233]. Although the microhardness value increased with increasing number of turns for both processing temperatures, there were differences in the values in favour of processing at the lower temperature, as reported in an earlier study [12].

5.7 Superplastic behaviour of AZ80

The HPT processing of the AZ80 magnesium alloy conducted at 296 K was successful. An ultra-fine grained microstructure of reasonable homogeneity was achieved, of an average grain size of ~200 nm. Similar grain refinement has been reported for AZ80, AZ31 and AZ91 magnesium alloys processed by HPT in earlier studies [9,119,145]. In

the early stages of HPT processing, the microstructure contained both fine and coarse grains, as in Figure 5.1 in the TEM images, due to the variation of imposed strain along the disc diameter, even though the microstructure developed gradually to a reasonably uniform ultra-fine grained structure after five turns of HPT processing.

The morphology and distribution of the second phase can play a part in material strengthening. An intermetallic β phase was precipitated in the initial condition at the grain boundaries with an average length of several microns, as in Figures 4.4 and 4.5. This coarse precipitate is not efficient in restraining dislocation [175]. During the HPT process, the precipitates are broken down and highly deformed into fine particles with an average size of less than ~ 100 nm. These fine particles are located at the triple junctions, as shown in Figures 4.11 and 4.12. These fine precipitates enhance the strength of the material by providing resistance to dislocation slip [236]. When the material is pulled in tension to failure at elevated temperatures, these fine particles act as a grain-growth inhibitor to improve the magnitude of the superplasticity [237]. In superplastic deformation, it is important to prevent grain growth [239].

Figure 4.48 shows the stress-elongation curve of the as-received condition and, as stated above, the average grain size of the as-received alloy is ~ 25 μm . This coarse-grained alloy shows good ductility with elongation of $\sim 190\%$ at a high testing temperature of 573 K and slower strain rate $1.4 \times 10^{-4} \text{ s}^{-1}$. Testing the alloy in the as-received condition at a lower testing temperature of 473 K shows higher flow stress and less elongation than at the higher temperature, and this behaviour was reported earlier in AZ80 [240]. Increasing the elongation with increasing testing temperatures can be attributed to the activation of the non-basal slip systems [186]. It is well known that increasing the temperature above ~ 225 $^{\circ}\text{C}$ will activate additional slip systems, other than the basal slip system [156] and, by increasing the temperature, the critical resolved shear stress of the non-basal systems decreases, resulting in a participation of these slip systems in the deformation [241]. Since the tensile test was conducted at 573 K these non-basal systems were activated. This enhanced the formability and the ductility of the alloy and explains the large decrease in the flow stress when processing the alloy at 573 K rather than at 473 K. The reduced elongation of the alloy at 473 K can be due to the limited number of slip systems at testing temperatures below 225 $^{\circ}\text{C}$, where the deformation of magnesium alloy is restricted to the basal slip system or twinning. Figure 4.70 shows

the decrease in the flow stress with increasing testing temperature and decreasing strain rate. The average strain rate sensitivity value (m) of the as-received condition was ~ 0.2 , and this lower strain rate sensitivity indicates that dislocation creep plays a major part in contributing to better ductility at higher temperature in a coarser grained magnesium alloy [240].

In addition to the good ductility achieved by the coarse-grained alloy, the samples processed by HPT and then pulled in tension to fracture by tensile test show superplastic behaviour in which their elongation exceeded 400% at different testing temperatures and strain rates, while the samples in the as-received condition had a maximum elongation of less than 200%. This is clear evidence of improved ductility in AZ80 magnesium alloy through processing by HPT. Earlier reports have shown that ECAP, the other common SPD technique, improved the ductility of AZ31 magnesium alloy and a maximum elongation was achieved of more than 1000%, compared to less than 500% in the as-received condition [183].

After HPT at room temperature, miniature specimens of each processed number of HPT turns of $N = 1/4, 1, 5$ and 10 turns were tested at temperatures of 473 K, 523 K and 573 K, corresponding to $\sim 0.53T_m$, $\sim 0.59T_m$ and $\sim 0.65T_m$ respectively, where the absolute melting temperature of AZ80 magnesium alloy is taken to be 883 K (610 °C), according to the Mg-Al binary phase diagram in Figure 2.33, and strain rates of $1.4 \times 10^{-4} \text{ s}^{-1}$, $1.4 \times 10^{-3} \text{ s}^{-1}$, $1.4 \times 10^{-2} \text{ s}^{-1}$ and $1.4 \times 10^{-1} \text{ s}^{-1}$ for each testing temperature.

Figures 4.49, 4.50, 4.51 and 4.52 show the elongation to failure of the alloy plotted against stress when the ultra-fine grained AZ80 magnesium alloy is pulled in tension to failure at 473 K, 523 K and 573 K respectively. These curves illustrate the effect of lowering the strain rate on the final elongation of the samples. Testing the alloy at the slower strain rate of $1.4 \times 10^{-4} \text{ s}^{-1}$ achieves the maximum elongation at each given number of HPT process turns. In addition, increasing the testing temperature leads to the same results accompanying both procedures, with a decrease in flow stress due to the strain softening that can be attributed to the activation of the non-basal slip systems [186] and to dynamic recrystallization [242]. At higher strain rates, the flow stress increases because of dislocation accumulation at the grain boundaries at that relatively fast strain rate [243]. By decreasing the strain rate, the tensile testing time increases, allowing for new grains to nucleate and grow due to dynamic recrystallization (DRX).

Since the tensile test temperatures of 473 K, 523 K and 573 K are in the range of DRX for magnesium alloy [51,169], this formation of new grains reduces both the amount of dislocation and the flow stress [220]. On the other hand, increasing the strain rates and decreasing the testing temperature leads the alloy to display strain hardening behaviour by increasing the maximum stress [244].

The appearance of the specimens after tensile testing at 473 K and 573 K is shown in Figures 4.54 (a) and (b), 4.55 (a) and (b), 4.56 (a) and (b), and 4.57 (a) and (b). The unprocessed sample is at the top in each figure, and the processed samples are placed in the order of strain rates, from highest to lowest, from top to bottom, for any given number of HPT process turns. In these figures, it can be seen that the maximum elongation for any given number of HPT process turns is when the alloy was processed at the slower strain rate of $1.4 \times 10^{-4} \text{ s}^{-1}$. Increasing the testing temperature increases the maximum elongation achieved by the samples. It is clear from the appearance of the specimens that the elongation was smooth and uniform, with no obvious necking. This neck-free deformation is evidence of superplastic behaviour [197].

In Figures 4.58, 4.59, 4.60 and 4.61, 4.62, 4.63, 4.64, and 4.65 the samples are shown in a different order. Each of these represents fixed strain rate from the highest $1.4 \times 10^{-1} \text{ s}^{-1}$ to the lowest $1.4 \times 10^{-4} \text{ s}^{-1}$ for tensile testing temperatures of 473 K and 573 K respectively. At higher strain rates of $1.4 \times 10^{-2} \text{ s}^{-1}$ – $1.4 \times 10^{-1} \text{ s}^{-1}$, at both testing temperatures of 473 K and 573 K, the maximum elongation was in the samples that had the maximum number of turns in HPT process (10 turns). At the slower strain rate of $1.4 \times 10^{-4} \text{ s}^{-1}$, the superplastic elongation was found to be enhanced in the samples processed by HPT for one turn when tested at both temperatures. The finer-grained structure in samples processed for a higher number of HPT turns showed less elongation than the sample processed for one turn when tested at the slower strain rate. The maximum elongation of all processed samples was 645% when the sample was processed by HPT for one turn and tested at a strain rate of $1.4 \times 10^{-4} \text{ s}^{-1}$.

These results can be attributed to a number of different causes. The first main factor is grain size stability. The finer grain size in samples processed for a higher number of HPT turns and subjected to higher imposed strain retained the smaller size when the alloy was tested at a higher strain rate, but at a slower strain rate the finer grains lost their thermal stability, and grain growth in AZ80 processed by HPT for a higher number

of turns took place when the sample was exposed to elevated temperatures for a longer time. Moreover, samples with more imposed strain have the ability to start to recrystallize at a lower temperature [245]. This leads to a rapid growth in grain size in samples processed for a higher number of HPT turns, as shown in Figure 4.83. An early investigation of ZK60 magnesium alloy processed by ECAP supports this trend. The maximum elongation of 3050% was found after two passes of ECAP, while after six passes the maximum elongation was 930% when samples were tested at strain rate of 10^{-4}s^{-1} and 473 K [144]. The trend does not follow the predicted trend of increasing ductility with increasing number of passes in ECAP [198], or with increased number of turns in HPT [14,135,145]. The second main factor is grain-boundary sliding, the main deformation mechanism for superplastic deformation. This mechanism needs to be accompanied by an ‘accommodation mechanism’ to avoid cavity development [133]. It has been reported earlier that intergranular slip can act as an accommodation mechanism to grain-boundary sliding [239]. Furthermore, previous investigations have shown that bi-modal microstructure can facilitate dislocation movement due to the ease of generating slip in a coarser grains [246]. In addition, several previous studies have reported a transition microstructure consisting of fine and coarse grains in the early stages of HPT processing [15]. This bi-modal microstructure was confirmed earlier in this study and can be seen in Figure 5.1. All these factors contribute to achieving the maximum elongation of AZ80 when the sample was processed by one turn of HPT.

The results of the AZ80 magnesium alloy show good ductility at the low processing temperature of 473 K and at higher strain rate of $1.4\times 10^{-2}\text{s}^{-1}$ - $1.4\times 10^{-1}\text{s}^{-1}$. Figures 4.66 (a), 4.67 (a), 4.68 (a) and 4.69 (a) illustrate the elongation to fracture versus the strain rate of samples for each given number of HPT turns and tested at 473 K, 523 K and 573 K respectively. The results show that decreasing the strain rate as well as increasing the testing temperature will increase the maximum elongation for each given number of HPT process turns. In (b), these figures illustrate the elongation to fracture versus the testing temperature for each given number of HPT turns at strain rates of $1.4\times 10^{-4}\text{s}^{-1}$, $1.4\times 10^{-3}\text{s}^{-1}$, $1.4\times 10^{-2}\text{s}^{-1}$ and $1.4\times 10^{-1}\text{s}^{-1}$. These figures also reveal superplastic behaviour of the alloy for the first time at higher testing temperatures of 523 K and 573 K and at slower strain rates of $1.4\times 10^{-4}\text{s}^{-1}$ - $1.4\times 10^{-3}\text{s}^{-1}$. The horizontal dashed line represents elongation of 400%.

The maximum elongation of 645% was achieved at 573 K, which corresponds to the higher testing temperature of $\sim 0.65T_m$ at which the maximum elongation at the lower testing temperature of $\sim 0.53T_m$ was 423%. Other magnesium alloys such as AZ91 processed by HPT and pulled in tension to failure at $\sim 0.62T_m$ exhibit an excellent elongation of 810% [184] and 1308% at $\sim 0.74T_m$ [145].

The results, for the first time in AZ80 alloy, exceeded an elongation of 400%. No previous study has either reported superplastic behaviour in AZ80 magnesium alloy exceeding 400% or described elongation in ultra-fine grain AZ80 magnesium alloy processed by HPT (to the author's knowledge). For comparison, other elongation results have been 239% for an extruded AZ80 with an average grain size of $\sim 35\mu\text{m}$ tested at 703 K and a strain rate of $6.56 \times 10^{-4} \text{s}^{-1}$ [186], and 246% for an extruded AZ80 with an average grain size of $\sim 26\mu\text{m}$ tested at 623 K and a strain rate of 10^{-4}s^{-1} [187].

Despite the large sample size used in previous studies, a gauge length of 25 mm with a diameter of 5 mm was used for the former study, and a gauge length of 10 mm and a gauge width and thickness of 5 mm for the latter. The ultra-fine grain of AZ80 successfully exceeded the elongation required for it to be categorized as superplastic elongation (400%). The current research used a small specimen size (a gauge length 1.1 x 1.0 mm width). Normally, larger tensile specimens would display greater elongation due to the greater volume of material involved in the deformation process. The results of this investigation surpass the elongation achieved by previous studies even at high strain rates, when the minimum elongation achieved was 265% for samples processed by 1/4 turn by HPT and tested to failure at a strain rate of $1.4 \times 10^{-2} \text{s}^{-1}$ at 573 K. Again, a sample processed by HPT for 10 turns and tested to failure in tension at 473 K and a strain rate of $1.4 \times 10^{-1} \text{s}^{-1}$ achieved an elongation of 277%.

Figures 4.71, 4.72 and 4.73 show flow stress plotted against strain rate. The strain rate sensitivity (m) values were calculated from the slope of (log-log) format. It has been observed that increasing the tensile testing temperature will decrease the flow stresses and increase the value of strain rate sensitivity (m). This increase in the value of strain rate sensitivity (m) is associated with an increase in the maximum elongation achieved before fracture. In previous studies, it has been shown that elongation in tension will increase with increasing strain rate sensitivity (m) [247]. The AZ80 sample that recorded the highest elongation of 645% in current research had a highest strain rate sensitivity (m) of

~ 0.6 . This relatively high value of strain rate sensitivity (m) indicates that grain-boundary sliding is indeed the main deformation mechanism [248], and it is close to the theoretical value of strain rate sensitivity is $m \sim 0.5$ for superplastic flow [249].

Using Equation 4.2 [199,200], the activation energy was calculated for a fixed strain rate. The activation energy was calculated for samples processed by HPT for one turn at room temperature, and tested to failure in tension at 473 K, 523 K and 573 K under a fixed strain rate of $1.4 \times 10^{-4} \text{ s}^{-1}$, since one turn has the greatest elongation of all the samples, as shown in Figure 4.74. The apparent activation energy Q was 72.8 kJ/mol. This value is lower than the self-diffusion activation energy (135 kJ/mol) and grain boundary diffusion (92 kJ/mol) for pure magnesium [201], but closer to the latter. This value indicates that the main deformation mechanism is grain-boundary sliding.

Figures 4.75, 4.76, 4.77, 4.78, 4.79, 4.80, 4.81, and 4.82 show SEM images of the microstructure on the gauge lengths after tensile testing at 473 K and 573 K. The grains associated with the superplastic elongation are equiaxed with a grain size below 10 μm , which is within the range required for superplasticity. The grain size was maintained when testing the material at an elevated temperature until failure, and this insignificant grain growth, with equiaxed rather than elongated grains, points to grain-boundary sliding as the main deformation mechanism for superplastic deformation in AZ80 magnesium alloy [249].

Figures 4.79 (c), 4.80 (c), 4.81 (c) and 4.82 (b) and (c) show the microstructure of samples tested to fracture by tension at 573 K, the red arrows pointing to the filament and the yellow arrows to the cavities within the gauge length of the tested samples. In general, fracture in superplastic alloy takes place due to the interlinkage between cavities: ‘cavitation failure’ [197]. These cavities can be developed by stress concentration at the triple junction of grain boundaries [250]. The presence of filaments indicates the presence of an area of high viscosity along the grain boundaries [133]. The filaments are formed during the separation of the grain boundaries, with the presence of high viscosity area during the plastic deformation, and it has been proven that increasing the testing temperature can change the morphology of the filament so it becomes longer, denser and coarser [133]. The filaments are aligned in the direction of tension and act as connectors between the separated grains by filling in the cavities and spaces between them, and a large number of cavities can be tolerated before the sample fractures and

relaxes the stress concentration areas. The presence of filaments connecting separated grains is evidence of grain movement, which might be due to grain-boundary sliding [133].

There is a relatively high value of strain rate sensitivity m and microstructure showing an equiaxed grains at the gauge of the specimens. Furthermore, there are cavities and interspaces between the grain boundaries, and the formation of refining filaments linking the disconnected grains' boundaries. All these observations and the calculation of the activation energy indicate that the primary deformation mechanism in the superplastic behaviour of AZ80 magnesium alloy processed by HPT could be grain-boundary sliding [251,252].

6 Summary and conclusions

- AZ80 magnesium alloy was successfully processed through SPD using the HPT technique at 296 K and 473 K. HPT processing conditions were quasi-constrained, using an applied pressure of 6.0 GPa with 1 rpm rotation speed for different numbers of turns: 1/4, 1, 3, 5 and 10.
- The evolution of microstructure and microhardness during HPT was examined both on the surface of the discs and through their thickness. Using Vickers microhardness tests, optical microscopy (OM), scanning electron microscopy (SEM) and transmission electron microscopy (TEM), the investigation revealed many results explaining the evolution of the material during HPT at both tested temperatures 296 K and 473 K.
- Following the HPT at room temperature, a tensile test was conducted at three different temperatures of 473 K, 523 K and 573 K using a strain rate of $1.4 \times 10^{-4} \text{ s}^{-1}$, $1.4 \times 10^{-3} \text{ s}^{-1}$, $1.4 \times 10^{-2} \text{ s}^{-1}$ and $1.4 \times 10^{-1} \text{ s}^{-1}$ for each testing temperature and for samples produced from discs processed for $N = 1/4, 1, 5$ and 10 turns. After the tensile test, the microstructure of the samples was observed using SEM at the gauge surface near the tip of the fracture without any further grinding or polishing. OM images of the tensile tested samples were used to calculate the final elongation.
- HPT resulted in good grain refinement, reducing the average grain size from the initial value of $\sim 25 \text{ }\mu\text{m}$ in the as-received condition to an ultra-fine grain with an average grain size of ~ 200 and $\sim 330 \text{ nm}$ when processed at 296 K and 473 K respectively. The evolution in microstructure and microhardness started at the compression stage and continued through the compression-torsion stage. Because of its low SFE, in the early stages of HPT processing the evolution showed significant refinement at the edges of the disc and coarse grains at the centre of the disc. This behaviour was more obvious in samples processed at elevated temperatures. This confirmed the theoretical approach of maximum imposed strain at the edge of the disc and the heterogeneous deformation through HPT. This created a strain gradient between the centre and the edge of

the disc. By increasing the number of turns, the strain gradient shifted towards the centre of the disc and the material showed reasonable homogeneity after 5 turns at both testing temperatures. There was no obvious twinning in samples processed at room temperature, whereas in samples processed at 473 K the contribution of twinning in the deformation was observable. The microhardness measurement confirmed the microstructure evolution, whereby at a lower number of turns the periphery of the disc had the highest microhardness values and the lower values were at the centre of the disc.

- The microhardness results demonstrate a gradual evolution to reasonable homogeneity, and this took place concurrently with strain hardening to saturation level. The material established a saturation level of microhardness after processing by 5 turns, at a value of ~120 and ~110 Hv when processed at 296 K and 473 K respectively. Increasing the number of turns to 10 had no further value in terms of strengthening the material. The final strength of the material processed by HPT was approximately twice that of the as-received condition. The high aluminium content (8.7 %) in AZ80 might play an important part in achieving high microhardness values and excellent average grain size refining when processing the alloy at elevated temperatures by inhibiting grain growth. Through its thickness, the material showed more heterogeneity in the axial than the radial direction.
- Superplastic elongation was investigated in AZ80 magnesium alloy processed by HPT at 296 K. The tensile test was conducted at different strain rates of $1.4 \times 10^{-4} \text{ s}^{-1}$, $1.4 \times 10^{-3} \text{ s}^{-1}$, $1.4 \times 10^{-2} \text{ s}^{-1}$ and $1.4 \times 10^{-1} \text{ s}^{-1}$ and temperatures of 473 K, 523 K and 573 K. The results showed an excellent superplasticity at slower strain rates and higher testing temperatures. Moreover, many samples exceeded an elongation of 400% using various strain rates and testing temperatures. This is the first time (to the author's knowledge) that superplastic behaviour exceeding 400% has been reported in this alloy. AZ80 magnesium alloy does not show the predicted behaviour of increasing ductility with increased imposed strain and decreased average grain size during HPT processing. The superplastic elongation of 645% achieved by a sample processed for one turn and tested in tension to fracture at 573 K at a strain rate of $1.4 \times 10^{-4} \text{ s}^{-1}$, was the greatest

elongation recorded for the alloy. Microstructure observation and activation energy calculation both point to grain-boundary sliding as the main mechanism for plastic deformation.

- After the HPT process, the coarse precipitates had been refined to a nano-sized ultra-fine particles with an average size of less than 100 nm, and their effect in strengthening the alloy has been promoted by pinning the dislocation motion. When processing AZ80 at elevated temperatures, these fine precipitates act as a barrier for grain growth that explains the finer average grain size after a higher number of turns after processing the alloy by HPT at 473 K. Furthermore, it helps the samples tested in tension to failure by tensile test to achieve better elongation.

7 Future Work

- Investigate the superplasticity potential of AZ80 processed by HPT at elevated temperatures (473 K), using the tensile test at various temperatures 473 K, 523 K and 573 K and strain rates of $1.4 \times 10^{-4} \text{ s}^{-1}$, $1.4 \times 10^{-3} \text{ s}^{-1}$, $1.4 \times 10^{-2} \text{ s}^{-1}$ and $1.4 \times 10^{-1} \text{ s}^{-1}$. Moreover, the elongation behaviour of the alloy will describe the effect of the dynamic recrystallization during HPT on the maximum elongation. Investigate the potential for high strain rate superplasticity under these conditions and compare the results with the results achieved earlier in this study.
- Process the AZ80 by HPT at 323 K, 373 K and 423 K for the same number of turns: 0, 1/4, 1, 3, 5, and 10, to investigate the effect of processing temperature on twinning formation during HPT process.
- Process the AZ80 by ECAP using a die with an angle of 110° at room temperature, and using a die with an angle of 90° and at 473 K, both using a route B_C for 2, 4 and 6 passes. This is to study the effect of variation in testing temperature, ECAP die angles and number of passes on the final microstructure and microhardness values, since there is a lack of information about AZ80 magnesium alloy processed by ECAP, and compare the results with the results achieved in this study by processing the alloy with HPT.
- Process the AZ80 by ECAP with an angle of 110° and a route B_C for 4 passes at room temperature to produce a finer equiaxed grain with a high angle of misorientation then by HPT for various numbers of turns, both at room temperature, to study the effect of reducing average grain size before HPT on the final microstructure and microhardness values.
- Investigate the superplasticity potential of AZ80 processed by ECAP by tensile testing at various temperatures 473 K, 523 K and 573 K and strain rates of $1.4 \times 10^{-4} \text{ s}^{-1}$, $1.4 \times 10^{-3} \text{ s}^{-1}$, $1.4 \times 10^{-2} \text{ s}^{-1}$ and $1.4 \times 10^{-1} \text{ s}^{-1}$, to study the effect of sample size produced by SPD on final elongation and the potential for high strain rate superplasticity.

References

- [1] E.O. Hall, Proc R Soc B (1951) 747–753.
- [2] N.J. Petch, J Iron Steel Inst (1953) 25–28.
- [3] H. Gleiter, Acta Mater. 48 (2000) 1–29.
- [4] Y.T. Zhu, T.C. Lowe, T.G. Langdon, Scr. Mater. 51 (2004) 825–830.
- [5] R.Z. Valiev, T.G. Langdon, Prog. Mater. Sci. 51 (2006) 881–981.
- [6] A.P. Zhilyaev, T.G. Langdon, Prog. Mater. Sci. 53 (2008) 893–979.
- [7] A.P. Zhilyaev, C. Xu, M. Furukawa, Z. Horita and T.G. Langdon, "Principles of High-Pressure Torsion and Equal-Channel Angular Pressing: A Comparison of Microstructural Characteristics," Ultrafine Grained Materials III (Y.T. Zhu, T.G. Langdon, R.Z. Valiev, S.L. Semiatin, D.H. Shin and T.C. Lowe, eds.), pp. 75–80. The Minerals, Metals and Materials Society, Warrendale, PA (2004).
- [8] M. Janeček, J. Čížek, J. Gubicza, J. Vrátná, J. Mater. Sci. 47 (2012) 7860–7869.
- [9] J. Stráská, M. Janeček, J. Gubicza, T. Krajňák, E.Y. Yoon, H.S. Kim, Mater. Sci. Eng. A 625 (2015) 98–106.
- [10] B. Mordike, T. Ebert, Mater. Sci. Eng. A302 (2001) 37–45.
- [11] Y. Uematsu, K. Tokaji, M. Matsumoto, Mater. Sci. Eng. A 517 (2009) 138–145.
- [12] R.B. Figueiredo, M.T.P. Aguilar, P.R. Cetlin, T.G. Langdon, Metall. Mater. Trans. A 42 (2011) 3013–3021.
- [13] R. Valiev, Nat. Mater. 3 (2004) 511–516.
- [14] M. Kai, Z. Horita, T.G. Langdon, Mater. Sci. Eng. A 488 (2008) 117–124.
- [15] Y. Huang, R.B. Figueiredo, T. Baudin, F. Brisset, T.G. Langdon, Adv. Eng. Mater. 14 (2012) 1018–1026.
- [16] R.Z. Valiev, Y. Estrin, Z. Horita, T.G. Langdon, M.J. Zehetbauer, Y.T. Zhu, JOM 58(4) (2006) 33–39.
- [17] R.Z. Valiev, A.P. Zhilyaev, T.G. Langdon, Bulk Nanostructured Materials: Fundamentals and Applications, Wiley, Hoboken, NJ, USA, 2014.
- [18] H. Jiang, Y.T. Zhu, D.P. Butt, I. V. Alexandrov, T.C. Lowe, Mater. Sci. Eng. A 290 (2000) 128–138.
- [19] H.-J. Lee, S.K. Lee, K.H. Jung, G.A. Lee, B. Ahn, M. Kawasaki, T.G. Langdon, J. Mater. Sci. Eng. A 630 (2015) 90–98.
- [20] R.Z. Valiev, R.K. Islamgaliev, I. V Alexandrov, Prog. Mater. 45 (2000) 103–189.
- [21] Y. Saito, H. Utsunomiya, N. Tsuji, T. Sakai, Acta Mater. 47 (1999) 579–583.
- [22] J.A. Chapman, D. V. Wilson, J Inst Met 91 (1962) 39–40.
- [23] P.W. Bridgman, Phys Rev 48 (1935) 825.
- [24] P.W. Bridgman, J. Appl. Phys. 14 (1943) 273.
- [25] V.M. Segal, V.I. Reznikov, A.E. Drobyshevskiy, Kopylov V.I., Russ Met. (1981) 99.

- [26] T.G. Langdon, *Acta Mater.* 61 (2013) 7035–7059.
- [27] B. Chen, D.-L. Lin, L. Jin, X.-Q. Zeng, C. Lu, *Mater. Sci. Eng. A* 483–484 (2008) 113–116.
- [28] Y. Chen, Y. Li, L. He, C. Lu, H. Ding, Q. Li, *Mater. Lett.* 62 (2008) 2821–2824.
- [29] S.V. Dobatkin, J.A. Szpunar, A.P. Zhilyaev, J.-Y. Cho, A.A. Kuznetsov, *Mater. Sci. Eng. A* 462 (2007) 132–138.
- [30] P. Kumar, C. Xu, T.G. Langdon, *J. Mater. Sci.* 44 (2009) 3913–3916.
- [31] C. Xu, K. Xia, T.G. Langdon, *Mater. Sci. Eng. A* 527 (2009) 205–211.
- [32] K. Xia, J.T. Wang, X. Wu, G. Chen, M. Gurvan, *Mater. Sci. Eng. A* 410–411 (2005) 324–327.
- [33] P.K. Chaudhury, B. Cherukuri, R. Srinivasan, *Mater. Sci. Eng. A* 410–411 (2005) 316–318.
- [34] Z. Horita, T. Fujinami, T.G. Langdon, *Mater. Sci. Eng. A* 318 (2001) 34–41.
- [35] R.Z. Valiev, I.P. Semenova, V.V. Latysh, H. Rach, T.C. Lowe, J. Petruzelka, L. Dluhos, D. Hrusak, J. Sochova, *Adv. Eng. Mater.* (2008) B15.
- [36] Y. Huang, T.G. Langdon, *Mater. Today* 16 (2013) 85–93.
- [37] Y. Iwahashi, J. Wang, Z. Horita, M. Nemoto, T.G. Langdon, *Scr. Mater.* 35 (1996) 143–146.
- [38] K. Nakashima, Z. Horita, M. Nemoto, T.G. Langdon, *Acta Mater.* 46 (1998) 1589–1599.
- [39] C. Xu, Z. Horita, T.G. Langdon, *Mater. Sci. Eng. A* 528 (2011) 6059–6065.
- [40] Y. Estrin, S.B. Yi, H.-G. Brokmeier, Z. Zuberova, S.C. Yoon, H.S. Kim, R.J. Hellmig, *Int. J. Mater. Res.* 99 (2008) 50–55.
- [41] R.B. Figueiredo, T.G. Langdon, *Int. J. Mater. Res.* 100 (2009) 1638–1646.
- [42] M. Nemoto, Z. Horita, M. Furukawa, T.G. Langdon, *Met. Mater.* 4 (1998) 1181–1190.
- [43] Z. Horita, M. Furukawa, M. Nemoto, T.G. Langdon, *Mater. Sci. Technol.* 16 (2000) 1239–1245.
- [44] M. Furukawa, Z. Horita, T.G. Langdon, *Mater. Int* 9 (2003) 141–149.
- [45] K. Oh-Ishi, Z. Horita, M. Nemoto, M. Furukawa, T.G. Langdon, *Metall. Mater. Trans. A* 29 (1998) 2011–2013.
- [46] T.G. Langdon, *Mater. Sci. Eng. A* 462 (2007) 3–11.
- [47] M. Furukawa, Y. Iwahashi, Z. Horita, M. Nemoto, T.G. Langdon, *Mater. Sci. Eng. A* 257 (1998) 328–332.
- [48] M. Furukawa, Z. Horita, T.G. Langdon, *Mater. Sci. Eng. A* 332 (2002) 97–109.
- [49] Y. Iwahashi, Z. Horita, M. Nemoto, T.G. Langdon, *Acta Mater.* 46 (1998) 3317–3331.
- [50] R.B. Figueiredo, P.R. Cetlin, T.G. Langdon, *Acta Mater.* 55 (2007) 4769–4779.
- [51] R.B. Figueiredo, T.G. Langdon, *J. Mater. Sci.* 44 (2009) 4758–4762.

- [52] K. Furuno, H. Akamatsu, K. Oh-ishi, M. Furukawa, Z. Horita, T.G. Langdon, *Acta Mater.* 52 (2004) 2497–2507.
- [53] F. Djavanroodi, M. Ebrahimi, *Mater. Sci. Eng. A* 527 (2010) 1230–1235.
- [54] A. Yamashita, Z. Horita, T.G. Langdon, *Mater. Sci. Eng. A* 300 (2001) 142–147.
- [55] Y.C. Chen, Y.Y. Huang, C.P. Chang, P.W. Kao, *Acta Mater.* 51 (2003) 2005–2015.
- [56] W.H. Huang, C.Y. Yu, P.W. Kao, C.P. Chang, *Mater. Sci. Eng. A* 366 (2004) 221–228.
- [57] P. Malek, M. Cieslar, R.K. Islamgaliev, *J. Alloy. Compd* 378 (2004) 237.
- [58] A. Goloborodko, O. Sitdikov, R. Kaibyshev, H. Miura, T. Sakai, *Mater. Sci. Eng. A* 381 (2004) 121–128.
- [59] M. Furui, H. Kitamura, H. Anada, T.G. Langdon, *Acta Mater.* 55 (2007) 1083–1091.
- [60] R.Z. Valiev, I.V. Alexandrov, T.C. Lowe, Y.T. Zhu, *J. Mater. Res.* 17 (2002) 5–8.
- [61] N.X. Zhang, H. Ding, J.Z. Li, X.L. Wu, Y.L. Li, K.N. Xia, *Mater. Sci. Forum* 667–669 (2010) 547–552.
- [62] N. Krasilnikov, *Russ Met.* 3 (2005) 35.
- [63] A. Yamashita, D. Yamaguchi, Z. Horita, T.G. Langdon, *Mater. Sci. Eng. A* 287 (2000) 100–106.
- [64] K. Nakashima, Z. Horita, M. Nemoto, T.G. Langdon, *Mater. Sci. Eng. A* 281 (2000) 82–87.
- [65] Y. Huang, P. Prangnell, *Scr. Mater.* 56 (2007) 333–336.
- [66] Y. Harai, M. Kai, K. Kaneko, Z. Horita, T.G. Langdon, *Mater. Trans.* 49 (2008) 76–83.
- [67] R.Z. Valiev, R.K. Islamgaliev, I. V Alexandrov, *Prog. Mater. Sci.* 45 (2000) 103–189.
- [68] A.P. Zhilyaev, G.V. Nurislamova, B.-K. Kim, M.D. Baró, J.A. Szpunar, T.G. Langdon, *Acta Mater.* 51 (2003) 753–765.
- [69] N. Maury, N.X. Zhang, Y. Huang, A.P. Zhilyaev, T.G. Langdon, *Mater. Sci. Eng. A* 638 (2015) 174–182.
- [70] A.P. Zhilyaev, T.R. McNelley, T.G. Langdon, *J. Mater. Sci.* 42 (2007) 1517–1528.
- [71] B. Srinivasarao, a. P. Zhilyaev, T.G. Langdon, M.T. Pérez-Prado, *Mater. Sci. Eng. A* 562 (2013) 196–202.
- [72] Z.C. Duan, X.Z. Liao, M. Kawasaki, R.B. Figueiredo, T.G. Langdon, *J. Mater. Sci.* 45 (2010) 4621–4630.
- [73] P.B. Prangnell, J.R. Bowen, P.J. Apps, *Mater. Sci. Eng. A* 375–377 (2004) 178–185.
- [74] C. Xu, Z. Horita, T.G. Langdon, *Acta Mater.* 56 (2008) 5168–5176.
- [75] A. Vorhauer, R. Pippan, *Scr. Mater.* 51 (2004) 921–925.
- [76] A.P. Zhilyaev, T.R. McNelley, T.G. Langdon, *J. Mater. Sci.* 42 (2007) 1517–1528.

- [77] R.Z. Valiev, Y. V Ivanisenko, E.F. Rauch, B. Baudelet, *Acta Mater.* 44 (1996) 4705–4712.
- [78] F. Wetscher, A. Vorhauer, R. Stock, A. Pippan, *Mater. Sci. Eng. A* 387–389 (2004) 809–816.
- [79] F. Wetscher, R. Pippan, S. Sturm, F. Kauffmann, C. Scheu, G. Dehm, *Metall. Mater. Trans. A* 37 (2006) 1963–1968.
- [80] J. Zhang, N. Gao, M.J. Starink, *Mater. Sci. Eng. A* 527 (2010) 3472–3479.
- [81] J. Zhang, M.J. Starink, N. Gao, W. Zhou, *Mater. Sci. Eng. A* 528 (2011) 2093–2099.
- [82] A. Hohenwarter, A. Bachmaier, B. Gludovatz, S. Scheriau, R. Pippan, *Int. J. Mater. Res.* 100 (2009) 1653–1661.
- [83] P. Bazarnik, B. Romelczyk, Y. Huang, P. Bazarnik, T.G. Langdon, *J. Alloys Compd.* 688 (2016) 736–745.
- [84] J. Wongsang-ngam, M. Kawasaki, T.G. Langdon, *J. Mater. Sci.* 47 (2012) 7782–7788.
- [85] A.P. Zhilyaev, K. Oh-ishi, T.G. Langdon, T.R. McNelley, *Mater. Sci. Eng. A* 410–411 (2005) 277–280.
- [86] S.A. Torbati-Sarraf, T.G. Langdon, *J. Alloys Compd.* 613 (2014) 357–363.
- [87] C. Xu, Z. Horita, T.G. Langdon, *Acta Mater.* 55 (2007) 203–212.
- [88] Y. Huang, R.B. Figueiredo, T. Baudin, A.-L. Helbert, F. Brisset, T.G. Langdon, *Mater. Res.* 16 (2013) 577–585.
- [89] F. Kang, J.Q. Liu, J.T. Wang, X. Zhao, *Scr. Mater.* 61 (2009) 844–847.
- [90] J. Wongsang-ngam, M. Kawasaki, Y. Zhao, T.G. Langdon, *Mater. Sci. Eng. A* 528 (2011) 7715–7722.
- [91] A. Zhilyaev, S. Lee, G. V Nurislamova, R.Z. Valiev, T.G. Langdon, *Scr. Mater.* 44 (2001) 2753–2758.
- [92] J. William D. Callister, *Materials Science and Engineering An Introduction*, Wiley, USA, 2007.
- [93] J.A. Yasi, T. Nogaret, D.R. Trinkle, Y. Qi, J.L.G. Hector, W.A. Curtin, *Model Simul Mater Sci Eng* 17 (2009) pp13.
- [94] Y.T. Zhu, X.Z. Liao, S.G. Srinivasan, E.J. Lavernia, *J. Appl. Phys.* 98 (2005) 34319.
- [95] Y.T. Zhu, X.Z. Liao, R.Z. Valiev, *Appl. Phys. Lett.* 86 (2005) 103112.
- [96] G.E. Dieter, *Mechanical Metallurgy*, McGraw-Hill, Singapore, 1988.
- [97] L. Balogh, T. Ungár, Y. Zhao, Y.T. Zhu, Z. Horita, C. Xu, T.G. Langdon, *Acta Mater.* 56 (2008) 809–820.
- [98] J.P. Hirth, J. Lothe, *Theory of Dislocations*, second ed, McGraw-Hill, New York, 1968.
- [99] Y.H. Zhao, X.Z. Liao, Y.T. Zhu, Z. Horita, T.G. Langdon, *Mater. Sci. Eng. A* 410–411 (2005) 188–193.

- [100] Y.H. Zhao, Y.T. Zhu, X.Z. Liao, Z. Horita, T.G. Langdon, *Mater. Sci. Eng. A* 463 (2007) 22–26.
- [101] C. Xu, A.P. Zhilyaev, Z. Horita, T.G. Langdon, *Mater. Sci Forum* 586 (2008) 3–8.
- [102] A. Al-Zubaydi, R.B. Figueiredo, Y. Huang, T.G. Langdon, *J. Mater. Sci.* 48 (2013) 4661–4670.
- [103] A.Y. Khereddine, F. Hadj Larbi, H. Azzeddine, T. Baudin, F. Brisset, A.-L. Helbert, M.-H. Mathon, M. Kawasaki, D. Bradai, T.G. Langdon, *J. Alloys Compd.* 574 (2013) 361–367.
- [104] A.S.J. Al-Zubaydi, A.P. Zhilyaev, S.C. Wang, P. Kucita, P.A.S. Reed, *J. Mater. Sci.* 51 (2016) 3380–3389.
- [105] L.R.C. Malheiros, R.B. Figueiredo, T.G. Langdon, *J. Mater. Res. Technol.* 4 (2015) 14–17.
- [106] Y. Estrin, a. Molotnikov, C.H.J. Davies, R. Lapovok, *J. Mech. Phys. Solids* 56 (2008) 1186–1202.
- [107] D.J. Lee, E.Y. Yoon, L.J. Park, H.S. Kim, *Scr. Mater.* 67 (2012) 384–387.
- [108] R.B. Figueiredo, P.R. Cetlin, T.G. Langdon, *Mater. Sci. Eng. A* 528 (2011) 8198–8204.
- [109] H.-J. Lee, B. Ahn, M. Kawasaki, T.G. Langdon, *J. Mater. Res. Technol.* 4 (2015) 18–25.
- [110] Y.C. Wang, T.G. Langdon, *J. Mater. Sci.* 48 (2013) 4646–4652.
- [111] Y. Ito, Z. Horita, *Mater. Sci. Eng. A* 503 (2009) 32–36.
- [112] K. Edalati, A. Yamamoto, Z. Horita, T. Ishihara, *Scr. Mater.* 64 (2011) 880–883.
- [113] K. Edalati, Z. Horita, *Mater. Sci. Eng. A* 528 (2011) 7514–7523.
- [114] M. Kawasaki, B. Ahn, T.G. Langdon, *Acta Mater.* 58 (2010) 919–930.
- [115] N.X. Zhang, M. Kawasaki, Y. Huang, T.G. Langdon, *J. Mater. Sci.* 48 (2013) 4582–4591.
- [116] M. Kawasaki, B. Ahn, T.G. Langdon, *Mater. Sci. Eng. A* 527 (2010) 7008–7016.
- [117] M. Kawasaki, R.B. Figueiredo, T.G. Langdon, *Acta Mater.* 59 (2011) 308–316.
- [118] R.B. Figueiredo, T.G. Langdon, *Mater. Sci. Eng. A* 528 (2011) 4500–4506.
- [119] D. Arpacay, S.B. Yi, M. Janeček, A. Bakkaloglu, L. Wagner, *Mater. Sci. Forum* 584–586 (2008) 300–305.
- [120] G. Sakai, K. Nakamura, Z. Horita, T.G. Langdon, *Mater. Sci. Eng. A* 406 (2005) 268–273.
- [121] Y. Harai, Y. Ito, Z. Horita, *Scr. Mater.* 58 (2008) 469–472.
- [122] M. Kawasaki, H.-J. Lee, B. Ahn, A.P. Zhilyaev, T.G. Langdon, *J. Mater. Res. Technol.* 3 (2014) 311–318.
- [123] A.P. Zhilyaev, B.-K. Kim, G.V. Nurislamova, M.D. Baró, J.A. Szpunar, T.G. Langdon, *Scr. Mater.* 46 (2002) 575–580.
- [124] Y.J. Chen, Y.J. Li, J.C. Walmsley, N. Gao, H.J. Roven, M.J. Starink, T.G. Langdon, *J.*

- Mater. Sci. 47 (2012) 4838–4844.
- [125] J.T. Wang, C. Xu, Z.Z. Du, G.Z. Qu, T.G. Langdon, 411 (2005) 312–315.
 - [126] R.Z. Valiev, Mater. Sci. Eng. A 234–236 (1997) 59–66.
 - [127] Z. Horita, T.G. Langdon, Mater. Sci. Eng. A 410–411 (2005) 422–425.
 - [128] T.G. Langdon, Metall. Trans. A 13 (1982) 689–701.
 - [129] G.J. Davies, J.W. Edington, C.P. Culter, K.A. Padmanabhan, J. Mater. Sci. 5 (1970) 1091–1102.
 - [130] T.G. Langdon, Mater. Sci. Eng. A 174 (1994) 225–230.
 - [131] M. Kawasaki, T.G. Langdon, J. Mater. Sci. 51 (2015) 19–32.
 - [132] T.G. Langdon, J. Mater. Sci. 41 (2006) 597–609.
 - [133] C.L. Chen, M.J. Tan, Mater. Sci. Eng. A 298 (2001) 235–244.
 - [134] M. Kawasaki, T.G. Langdon, Mater. Trans. 49 (2008) 84–89.
 - [135] M. Kawasaki, T.G. Langdon, Mater. Sci. Eng. A 528 (2011) 6140–6145.
 - [136] F.A. Mohamed, M.M.I. Ahmed, T.G. Langdon, Metall. Trans. A 8 (1977) 933–938.
 - [137] J. Koike, R. Ohyama, T. Kobayashi, M. Suzuki, K. Maruyama, Mater. Trans. 44 (2003) 445–451.
 - [138] T. Mukai, M. Yamanoi, H. Watanabe, K. Higashi, Scr. Mater. 45 (2001) 89–94.
 - [139] Y.N. Wang, J.C. Huang, Scr. Mater. 48 (2003) 1117–1122.
 - [140] Y. Miyahara, K. Matsubara, Z. Horita, T.G. Langdon, Metall. Mater. Trans. A 36 (2005) 1705–1711.
 - [141] A.J. Barnes, J. Mater. Eng. Perform. 16 (2007) 440–454.
 - [142] K. Higashi, M. Mabuchi, T.G. Langdon, ISIJ Int. 36 (1996) 1423–1438.
 - [143] R.Z. Valiev, D. a Salimonenko, N.K. Tsenev, P.B. Berbon, T.G. Langdon, Scr. Mater. 37 (1997) 1945–1950.
 - [144] R.B. Figueiredo, T.G. Langdon, Adv. Eng. Mater. 10 (2008) 37–40.
 - [145] A.S.J. Al-Zubaydi, A.P. Zhilyaev, S.C. Wang, P.A.S. Reed, Mater. Sci. Eng. A 637 (2015) 1–11.
 - [146] A. Loucif, R.B. Figueiredo, M. Kawasaki, T. Baudin, F. Brisset, R. Chemam, T.G. Langdon, J. Mater. Sci. 47 (2012) 7815–7820.
 - [147] E. Aghion, B. Bronfin, D. Eliezer, J. Mater. Process. Technol. 117 (2001) 381–385.
 - [148] K.U. Kainer, Magnesium – Alloys and Technology, Wiley, Germany, 2003.
 - [149] T. Al-Samman, G. Gottstein, Mater. Sci. Eng. A 488 (2008) 406–414.
 - [150] M.R. Barnett, Metall. Mater. Trans. A 34 (2003) 1799–1806.
 - [151] A. Styczynski, C. Hartig, J. Bohlen, D. Letzig, Scr. Mater. 50 (2004) 943–947.
 - [152] M.H. Yoo, Metall. Trans. A 12 (1981) 409–418.
 - [153] S. Balasubramanian, L. Anand, Acta Mater. 50 (2002) 133–148.
 - [154] M. Niewczas, Acta Mater. 58 (2010) 5848–5857.

- [155] A. Staroselsky, L. Anand, *Int. J. Plast.* 19 (2003) 1843–1864.
- [156] T. Al-Samman, G. Gottstein, *Mater. Sci. Eng. A* 490 (2008) 411–420.
- [157] R. Reed-Hill, W. Robertson, *J. Met.* 9 (1957) 496–502.
- [158] K. Máthis, K. Nyilas, a. Axt, I. Dragomir-Cernatescu, T. Ungár, P. Lukáč, *Acta Mater.* 52 (2004) 2889–2894.
- [159] P. Palai, N. Prabhu, P.D. Hodgson, B.P. Kashyap, *J. Mater. Eng. Perform.* 23 (2014) 77–82.
- [160] H. Yabe, T. Kuji, *Alloy. Compd.* 433 (2007) 241–245.
- [161] X. Li, F. Jiao, T. Al-Samman, S. Ghosh Chowdhury, *Scr. Mater.* 66 (2012) 159–162.
- [162] T.J. Chen, R.Q. Wang, Y. Ma, Y. Hao, *Mater. Res.* 14 (2011) 532–540.
- [163] H. Somekawa, K. Hirai, H. Watanabe, Y. Takigawa, K. Higashi, *Mater. Sci. Eng. A* 407 (2005) 53–61.
- [164] ASM, *Metallography and Microstructures and Its Alloy*, ASM International, Materials Park, OH, 2004.
- [165] K.H. Matucha, *Materials Science and Technology, Volume 8, Structure and Properties of Nonferrous Alloys*, VCH Weinheim, 1996.
- [166] F. Kang, J.T. Wang, Y. Peng, *Mater. Sci. Eng. A* 487 (2008) 68–73.
- [167] S.L. Semiatin, D.P. Delo, *Mater. Des.* 21 (2000) 311–322.
- [168] V. V Stolyarov, R. Lapovok, G. brodova I, P.F. Thomson, *Mater. Sci. Eng. A* 357 (2003) 159–167.
- [169] R.B. Figueiredo, T.G. Langdon, *J. Mater. Sci.* 45 (2010) 4827–4836.
- [170] R.B. Figueiredo, T.G. Langdon, *Mater. Sci. Eng. A* 501 (2009) 105–114.
- [171] M. Janeček, M. Popov, M.G. Krieger, R.J. Hellmig, Y. Estrin, *Mater. Sci. Eng. A* 462 (2007) 116–120.
- [172] Y. He, Q. Pan, Y. Qin, X. Liu, W. Li, *J. Mater. Sci.* 45 (2010) 1655–1662.
- [173] K. Matsubara, Y. Miyahara, Z. Horita, T.G. Langdon, *Acta Mater.* 51 (2003) 3073–3084.
- [174] Y. Huang, R.B. Figueiredo, T.G. Langdon, *Rev. Adv. Mater. Sci.* 31 (2012) 129–137.
- [175] P. Yang, L. Wang, Q. Xie, J. Li, H. Ding, L. Lu, *Int. J. Miner. Metall. Mater.* 18 (2011) 338–343.
- [176] Z. Wang, Y. Yang, B. Li, Y. Zhang, Z. Zhang, *Mater. Sci. Eng. A* 582 (2013) 36–40.
- [177] D. Zhao, Z. Wang, M. Zuo, H. Geng, *Mater. Des.* 56 (2014) 589–593.
- [178] I.A. Yakubtsov, B.J. Diak, C.A. Sager, B. Bhattacharya, W.D. MacDonald, M. Niewczas, *Mater. Sci. Eng. A* 496 (2008) 247–255.
- [179] D.L. Yin, L.K. Weng, J.Q. Liu, J.T. Wang, *Kov. Mater* 49 (2011) 37–42.
- [180] R.B. Figueiredo, I.J. Beyerlein, A.P. Zhilyaev, T.G. Langdon, *Mater. Sci. Eng. A* 527 (2010) 1709–1718.

- [181] P. Serre, R.B. Figueiredo, N. Gao, T.G. Langdon, *Mater. Sci. Eng. A* 528 (2011) 3601–3608.
- [182] M. Mabuchi, H. Iwasaki, K. Yanase, *Scr. Mater.* 36 (1997) 681–686.
- [183] R.B. Figueiredo, T.G. Langdon, *J. Mater. Sci.* 43 (2008) 7366–7371.
- [184] M. Kai, Z. Horita, T.G. Langdon, *Mater. Sci. Eng. A* 488 (2008) 117–124.
- [185] H. Matsunoshita, K. Edalati, M. Furui, Z. Horita, *Mater. Sci. Eng. A* 640 (2015) 443–448.
- [186] W. Zhongjun, W. Zhaojing, Z. Jing, *Adv. Mater. Lett.* 2 (2011) 113–117.
- [187] L. Ren, J. Wu, G. Quan, *Mater. Sci. Eng. A* 612 (2014) 278–286.
- [188] G. Vander Voort, *Tech-Notes* 4 (2004).
- [189] M. Kawasaki, T.G. Langdon, *Mater. Sci. Eng. A* 498 (2008) 341–348.
- [190] Z. Wang, Y. Yang, B. Li, Y. Zhang, Z. Zhang, *Mater. Sci. Eng. A* 582 (2013) 36–40.
- [191] C. Wang, R. Xin, D. Li, B. Song, M. Wu, Q. Liu, *Mater. Sci. Eng. A* 680 (2017) 152–156.
- [192] R.B. Figueiredo, T.G. Langdon, *Mater. Sci. Forum* 667–669 (2011) 247–252.
- [193] M. Kawasaki, *J. Mater. Sci.* 49 (2013) 18–34.
- [194] M. Kawasaki, R.B. Figueiredo, Y. Huang, T.G. Langdon, *J. Mater. Sci.* 49 (2014) 6586–6596.
- [195] L. Tang, Y. Zhao, R.K. Islamgaliev, C.Y.A. Tsao, R.Z. Valiev, E.J. Lavernia, Y.T. Zhu, *Mater. Sci. Eng. A* 670 (2016) 280–291.
- [196] Y. Huang, R.B. Figueiredo, T. Baudin, A.-L. Helbert, F. Brisset, T.G. Langdon, *J. Mater. Sci.* 47 (2012) 7796–7806.
- [197] T.G. Langdon, *Met. Sci.* 16 (1982) 175–183.
- [198] S. Komura, M. Furukawa, Z. Horita, M. Nemoto, T.G. Langdon, *Mater. Sci. Eng. A* 297 (2001) 111–118.
- [199] J.B. Wen, F.X. Chen, K.K. Zhang, Y.S. Yang, *Mater. Sci. Forum* 551–552 (2007) 341–345.
- [200] X. Wu, Y. Liu, *Scr. Mater.* 46 (2002) 269–274.
- [201] H.J. Frost, M.. Ashby, *Deformation-Mechanism Maps: The Plasticity and Creep of Metals and Ceramics*, UK: pergamon press, 1982.
- [202] R.B. Figueiredo, P.R. Cetlin, T.G. Langdon, *Metall. Mater. Trans. A* 41 (2010) 778–786.
- [203] F. Kang, Z. Li, J. Tao, (2012) 7854–7859.
- [204] X.G. Qiao, Y.W. Zhao, W.M. Gan, Y. Chen, M.Y. Zheng, K. Wu, N. Gao, M.J. Starink, *Mater. Sci. Eng. A* 619 (2014) 95–106.
- [205] P.G. Partridge, *Met. Rev. Inst. Met.* 118 (1967) 169.
- [206] F. Kang, Z. Li, J.T. Wang, P. Cheng, H.Y. Wu, *J. Mater. Sci.* 47 (2012) 7854–7859.
- [207] A.A. Mazilkin, B.B. Straumal, S.G. Protasova, S. V. Dobatkin, B. Baretzky, J.

- Mater. Sci. 43 (2008) 3800–3805.
- [208] G. Frommeyer, U. Brück, P. Neumann, ISIJ Int. 43 (2003) 438–446.
 - [209] D.H. Shin, I. Kim, J. Kim, Y.S. Kim, S.L. Semiatin, Acta Mater. 51 (2003) 983–996.
 - [210] N. Stanford, U. Carlson, M.R. Barnett, Metall. Mater. Trans. A Phys. Metall. Mater. Sci. 39 A (2008) 934–944.
 - [211] X.Z. Liao, Y.H. Zhao, Y.T. Zhu, R.Z. Valiev, D. V. Gunderov, J. Appl. Phys. 96 (2004) 636–640.
 - [212] M.R. Barnett, Z. Keshavarz, A.G. Beer, D. Atwell, Acta Mater. 52 (2004) 5093–5103.
 - [213] M.A. Meyers, O. Vohringer, V.A. Lubarda, Acta Mater. 49 (2001) 4025–4039.
 - [214] N. V. Ravi Kumar, J.J. Blandin, C. Desrayaud, F. Montheillet, M. Suéry, Mater. Sci. Eng. A 359 (2003) 150–157.
 - [215] A. Ghaderi, M.R. Barnett, Acta Mater. 59 (2011) 7824–7839.
 - [216] M.A. Meyers, U.R. Andrade, A.H. Chokshi, Metall. Mater. Trans. A 26 (1995) 2881–2893.
 - [217] Y.T. Zhu, X.Z. Liao, X.L. Wu, Prog. Mater. Sci. 57 (2012) 1–62.
 - [218] Z.W. Wang, Y.B. Wang, X.Z. Liao, Y.H. Zhao, E.J. Lavernia, Y.T. Zhu, Z. Horita, T.G. Langdon, Scr. Mater. 60 (2009) 52–55.
 - [219] E.A. Lukyanova, N.S. Martynenko, I. Shakhova, A.N. Belyakov, L.L. Rokhlin, S. V. Dobatkin, Y.Z. Estrin, Mater. Lett. 170 (2016) 5–9.
 - [220] S.E. Ion, F.J. Humphreys, S.H. White, Acta Metall. 30 (1982) 1909–1919.
 - [221] X.Z. Liao, Y.H. Zhao, S.G. Srinivasan, Y.T. Zhu, R.Z. Valiev, D. V. Gunderov, Appl. Phys. Lett. 84 (2004) 592–594.
 - [222] I. Karaman, G.G. Yapici, Y.I. Chumlyakov, I.V. Kireeva, Mater. Sci. Eng. A 410–411 (2005) 243–247.
 - [223] I. Karaman, H. Sehitoglu, H.J. Maier, Y.I. Chumlyakov, Acta Mater. 49 (2001) 3919–3933.
 - [224] I. Karaman, H. Sehitoglu, K. Gall, Y.I. Chumlyakov, H.J. Maier, Acta Mater. 48 (2000) 1345–1359.
 - [225] Y. Jiang, X. Yang, L. Zhang, Mater. Sci. Forum 667–669 (2011) 623–627.
 - [226] Y. Chen, L. Jin, J. Dong, Z. Zhang, F. Wang, Mater. Charact. 118 (2016) 363–369.
 - [227] J.C. Tan, M.J. Tan, Mater. Sci. Eng. A 339 (2003) 124–132.
 - [228] S.W. Xu, N. Matsumoto, S. Kamado, T. Honma, Y. Kojima, Scr. Mater. 61 (2009) 249–252.
 - [229] S.W. Xu, S. Kamado, T. Honma, Scr. Mater. 63 (2010) 293–296.
 - [230] S.W. Xu, N. Matsumoto, S. Kamado, T. Honma, Y. Kojima, Mater. Sci. Eng. A 523 (2009) 47–52.
 - [231] P.H.R. Pereira, R.B. Figueiredo, P.R. Cetlin, T.G. Langdon, Mater. Sci. Eng. A 631 (2015) 201–208.

- [232] R.B. Figueiredo, G.C. V. Faria, P.R. Cetlin, T.G. Langdon, *J. Mater. Sci.* 48 (2013) 4524–4532.
- [233] R.B. Figueiredo, M.T.P. Aguilar, P.R. Cetlin, T.G. Langdon, *Mater. Sci.* 47 (2012) 7807–7814.
- [234] S. Celotto, T.J. Bastow, *Acta Mater.* 49 (2001) 41–51.
- [235] P.J. Apps, J.R. Bowen, P.B. Prangnell, *Acta Mater.* 51 (2003) 2811–2822.
- [236] M.-S. Tsai, P.-L. Sun, P.-W. Kao, C.-P. Chang, *Mater. Trans.* 50 (2009) 771–775.
- [237] S.W. Xu, S. Kamado, N. Matsumoto, T. Honma, Y. Kojima, *Mater. Sci. Eng. A* 527 (2009) 52–60.
- [238] K. Edalati, T. Fujioka, Z. Horita, *Mater. Trans.* 50 (2009) 44–50.
- [239] A. Bussiba, A. Ben Artzy, A. Shtechman, S. Ifergan, M. Kupiec, *Mater. Sci. Eng. A* 302 (2001) 56–62.
- [240] J. Qiao, F. Bian, M. He, Y. Wang, *Trans. Nonferrous Met. Soc. China* 23 (2013) 2857–2862.
- [241] A. Galiyev, R. Kaibyshev, G. Gottstein, *Acta Mater.* 49 (2001) 1199–1207.
- [242] R. Lapovok, P.F. Thomson, R. Cottam, Y. Estrin, *Mater. Sci. Eng. A* 410–411 (2005) 390–393.
- [243] Q. Guo, H.G. Yan, H. Zhang, Z.H. Chen, Z.F. Wang, *Mater. Sci. Technol.* 21 (2005) 1349–1354.
- [244] W. Lu, G. Quan, C. Yu, L. Zhao, J. Zhou, *Trans. Nonferrous Met. Soc. China* 22 (2012) S650–S655.
- [245] F.J. Humphreys, M. Hatherly, *Recrystallization and Related Annealing Phenomena*, Elsevier, Amsterdam, The Netherlands, 2004.
- [246] R. Lapovok, Y. Estrin, M.V. Popov, T.G. Langdon, *Adv. Eng. Mater.* 10 (2008) 429–433.
- [247] T.G. Langdon, *Scr. Met.* 11 (1977) 997.
- [248] O.D. Sherby, J. Wadsworth, *Prog. Mater. Sci.* 33 (1989) 169–221.
- [249] T.G. Langdon, *Acta Metall. Mater.* 42 (1994) 2437–2443.
- [250] D.H. Shin, K.T. Park, *Mater. Sci. Eng. A* 268 (1999) 55–62.
- [251] L. Clarisse, A. Bataille, Y. Pennec, J. Crampon, R. Duclos, *Ceram. Int.* 25 (1999) 389–394.
- [252] T. Mohri, M. Mabuchi, M. Nakamura, T. Asahina, H. Iwasaki, T. Aizawa, K. Higashi, *Mater. Sci. Eng. A* 290 (2000) 139–144.